

THÈSE DE DOCTORAT

Soutenue à Aix-Marseille Université
le 1^{er} décembre 2023 par

Witold Podlejski

Variabilité des algues sargasses de l'Océan Atlantique tropical
nord

Discipline

Science de l'environnement

Spécialité

Océanographie

École doctorale

ED 251 SCIENCES DE L'ENVIRONNEMENT

Laboratoire/Partenaires de recherche

Institut Méditerranéen d'Océanologie - MIO
Marine Biodiversity Exploitation and Conservation - MARBEC

Institut de Recherche pour le Développement
- IRD

Composition du jury

Ronan FABLET IMT Atlantique - Lab-STICC	Rapporteur
Jean-Olivier IRISSON Sorbonne Université - LOV	Rapporteur
Laure PECQUERIE IRD - LEMAR	Examinateuse
Frédéric MENARD IRD - MIO	Président du jury
Christophe LETT IRD - MARBEC	Co-Directeur de thèse
Léo BERLINE AMU - MIO	Directeur de thèse

Affidavit

Je soussigné, Witold Podlejski, déclare par la présente que le travail présenté dans ce manuscrit est mon propre travail, réalisé sous la direction scientifique de Christophe Lett et Léo Berline, dans le respect des principes d'honnêteté, d'intégrité et de responsabilité inhérents à la mission de recherche. Les travaux de recherche et la rédaction de ce manuscrit ont été réalisés dans le respect à la fois de la charte nationale de déontologie des métiers de la recherche et de la charte d'Aix-Marseille Université relative à la lutte contre le plagiat.

Ce travail n'a pas été précédemment soumis en France ou à l'étranger dans une version identique ou similaire à un organisme examinateur.

Fait à Marseille le 5/09/2023



Cette œuvre est mise à disposition selon les termes de la [Licence Creative Commons Attribution - Pas d'Utilisation Commerciale - Pas de Modification 4.0 International](#).

Liste de publications et participation aux conférences

Liste des publications réalisées dans le cadre du projet de thèse :

1. PODLEJSKI, W., DESCLOITRES, J., CHEVALIER, C., MINGHELLI, A., LETT, C., & BERLINE, L. (2022). Filtering out false sargassum detections using context features. *Frontiers in Marine Science*, 9. <https://doi.org/10.3389/fmars.2022.960939>
2. PODLEJSKI, W., BERLINE, L., NERINI, D., DOGLIOLI, A., & LETT, C. (2023). A new sargassum drift model derived from features tracking in modis images. *Marine Pollution Bulletin*, 188, 114629. <https://doi.org/https://doi.org/10.1016/j.marpolbul.2023.114629>
3. JOUANNO, J., MOQUET, J.-S., BERLINE, L., RADENAC, M.-H., SANTINI, W., CHANGEUX, T., THIBAUT, T., PODLEJSKI, W., MÉNARD, F., MARTINEZ, J.-M., AUMONT, O., SHEINBAUM, J., FILIZOLA, N., & N'KAYA, G. D. M. (2021b). Evolution of the riverine nutrient export to the tropical atlantic over the last 15 years: is there a link with sargassum proliferation? *Environmental Research Letters*, 16(3), 034042. <https://doi.org/10.1088/1748-9326/abell1a>
4. CHANGEUX, T., BERLINE, L., PODLEJSKI, W., GUILLOT, T., STIGER-POUVREAU, V., CONNAN, S., & THIBAUT, T. (2023). Variability in growth and tissue composition (cnp, natural isotopes) of the three morphotypes of holopelagic sargassum. *Aquatic Botany*, 187, 103644

Participation aux conférences et écoles d'été au cours de la période de thèse :

1. Improving *Sargassum* observation using aggregations context. **Talk.***European Geoscience Union*, avril 2022, à distance.
2. Improving *Sargassum* observation using aggregations context. **Poster.***Living Planet Symposium*, avril 2022, Bonn, Allemagne.
3. Estimating the effect of wind and surface current on *Sargassum* drift. **Poster.***Association for the Sciences of Limnology and Oceanography*, juin 2023, Palma, Espagne.

Résumé

Les algues sargasses dites pélagiques, *Sargassum fluitans* et *Sargassum natans*, apparaissent à la fois comme un refuge pour la biodiversité en océan ouvert et, depuis plus d'une décennie maintenant, comme un fléau écologique, économique et sanitaire pour les zones côtières touchées par leurs échouements massifs. Ces impacts néfastes sur les écosystèmes et les activités humaines, disséminés du golfe de Guinée jusqu'au golfe du Mexique, suscitent un effort de recherche international afin de comprendre et prévoir l'invasion de ces algues. La présente thèse s'inscrit dans cette dynamique en se focalisant sur la distribution spatiale et temporelle des algues sargasses ainsi que sur leur grande variabilité interannuelle. Ces travaux s'attachent à cartographier puis modéliser leur cycle saisonnier en prenant en compte à la fois leur dérive passive et leur croissance. Il y est d'abord question de la télédétection des sargasses, usant de l'imagerie satellite MODIS pour permettre une cartographie quantitative et journalière à large échelle de leur distribution spatiale. L'apport de cette thèse en la matière se concentre sur le filtrage des erreurs de détection en employant un algorithme d'apprentissage automatisé sur les caractéristiques spatiales de ces algues. Dans un second temps, la dérive des sargasses, mal quantifiée jusqu'alors, est observée dans des images satellites successives en extrayant des trajectoires d'agrégats de sargasse. Basé sur l'évaluation des vitesses d'agrégats résultantes, un modèle approfondi de la dérive des sargasses est proposé en fonction des courants et du vent environnants. En dernière partie de cette thèse, ce nouveau modèle de dérive, utilisé dans une approche Lagrangienne, est mis en synergie avec un modèle biogéochimique de la croissance des sargasses afin de reproduire l'évolution annuelle des quantités d'algues et de leur répartition. L'analyse des résultats de ce modèle de dérive et de croissance révèle la spatialisation de la croissance et dégénérescence des sargasses et permet également d'éclairer les principaux facteurs limitants environnementaux. Cette dernière analyse met, par ailleurs, en lumière une caractéristique climatique cruciale qui, par le réchauffement des températures de surface de l'océan au nord du Brésil, stoppe le développement saisonnier des biomasses de sargasses. Aussi, la temporalité de cette caractéristique climatique pourra être surveillée afin de mieux prévoir l'accroissement annuel des sargasses et dans le but d'alerter les pays sur les futurs risques d'échouements.

Mots clés : Sargasses, séries temporelles, télédétection, dérive, modèle Lagrangien, apprentissage automatisé, modèle de croissance.

Abstract

Pelagic *Sargassum* algae, *Sargassum fluitans* and *Sargassum natans*, are both a refuge for biodiversity in open oceans and, for over a decade now, an ecological, economic and health scourge for coastal areas affected by their massive stranding. These harmful impacts on ecosystems and human activities, scattered from the Gulf of Guinea to the Gulf of Mexico, have prompted an international research effort to warn of and predict the invasion of these algae. The present thesis is part of this dynamic, focusing on the spatial and temporal distribution of Sargassum seaweed, as well as its great inter-annual variability. The aim is to map and then model their seasonal cycle, taking into account both their passive drift and their growth. The first focus is on remote sensing of *Sargassum*, using satellite imagery to provide large-scale, quantitative, daily mapping of its spatial distribution. The contribution of this thesis in this area focuses on filtering detection errors using automated learning algorithms based on the spatial characteristics of these algae. In a second step, *Sargassum* drift, previously lacking tangible measurements, is observed in successive satellite images by extracting trajectories of *Sargassum* aggregates. Based on the assessment of the resulting aggregate velocities, an in-depth model of *Sargassum* drift is proposed as a function of surrounding wind and currents. In the final part of this thesis, this new drift model, used in a Lagrangian approach, is associated to a biogeochemical model of Sargassum growth in order to best reproduce the annual evolution of algae quantities and distribution. Analysis of the results of this double model reveals the spatialization of Sargassum growth and decay, and sheds light on the predominant environmental factors that limit it. This latest analysis also highlights a crucial climatic characteristic which, through warming ocean surface temperatures in the north of Brazil, stops the seasonal development of *Sargassum* biomasses. Thus, the temporality of this climatic event can be monitored in order to better predict the annual growth of *Sargassum* and to alert countries about the risks of future strandings.

Keywords: *Sargassum*, time series, drift, Lagrangian model, machine learning, growth model.

Remerciements

Ma première pensée va aux nombreux camarades de travail qui m'ont accompagné tout au long de cette thèse et qui ont rendu agréables et humains les temps passés dans mes deux laboratoires d'accueil. Ces doctorants, stagiaires et postdocs sont, grâce à leurs réflexions scientifiques, philosophique et politique tout autant que leur humour et leur bonne humeur, une des motivations majeures qui m'ont attirées vers le milieu de la recherche et qui mit font rester. Je voudrais ainsi remercier tout le groupe convivial formé au MIO avec Marine, Nadège, Thomas, Théo, Emilie, Claire, Mattéo, Floriane et beaucoup d'autres pour les deux ans passés ensemble et l'amitié qui en a découlé. De même, merci à Amaël, Adrien, Vincent, Maya, Constance, Ioluène, Paul, Anaïs, Davide et Jade du MARBEC pour leur accueil chaleureux dans ce deuxième lieu de ma thèse et pour les bons moments partagés. Merci aussi aux amis, hors contexte professionnel, qui ont agrémenté mon quotidien par leur présence et leur sympathie. Merci à Benoît, Arthur, Romane, Julie, Sofía, Gustave, Emma et Antoine qui ont souvent peuplés les weekends et soirées de ma thèse.

J'aimerais remercier ensuite les personnes avec lesquelles j'ai plus directement travaillé. Pour la plupart plus âgées et expérimentées, elles m'ont toutes traité comme leur égal dans nos travaux communs, me permettant ainsi de m'épanouir pleinement dans ma démarche de recherche. Je remercie donc Audrey, Jacques, Nicolas, David, Jean-Christophe, Andréa et Julien pour leur bienveillance, leur soutien et leurs enseignements. Je remercie bien sûr mes deux encadrants de thèse, Léo et Christophe, qui ont su se montrer très présent tout au long de cette thèse. Ça a été un plaisir de travailler avec vous et je vous remercie sincèrement pour la simplicité avec laquelle nous avons pu nouer des relations de travail saines et stimulantes.

Mes dernières pensées vont à mes proches, en particulier mes parents qui m'ont longuement hébergé en pleine pandémie et qui m'ont accueilli non plus comme l'enfant que j'étais, mais comme l'adulte que je devenais. Merci pour votre tendresse, twój syn, który cię kocha. Merci enfin à la femme que j'aime et qui m'a soutenu sur tous les aspects de mes trois ans de vie de doctorant, merci Iris.

Table des matières

Affidavit	2
Liste de publications et participation aux conférences	3
Résumé	4
Abstract	5
Remerciements	6
Table des matières	7
Table des figures	10
Liste des tableaux	14
Liste des acronymes	16
1. Introduction	21
2. Revue de littérature	34
2.1. Écologie	35
2.2. Biologie et facteurs de croissance	36
2.3. Morphotypes	37
2.4. Échouements et conséquences	38
2.5. Fixation du carbone	39
2.6. Composition chimique	39
2.7. Valorisation	40
2.8. Détection des sargasses	41
2.9. Études à large échelle du transport et de la croissance des sargasses	45
3. Filtrage des détections MODIS avec des attributs de contexte	47
3.1. Abstract	50
3.2. Introduction	50
3.3. Materials and Methods	52
3.3.1. Approach overview	52
3.3.2. <i>Sargassum</i> dataset : SAREDA	54
3.3.3. Learning dataset, "expert truth"	56
3.3.4. Aggregations characterisation : spatial features extraction	57
3.3.5. Classification algorithms selection and tuning	58

3.3.6. Time series production	60
3.4. Results	61
3.5. Discussion	68
3.5.1. Interpretation of features used in the classification	68
3.5.2. Accuracy of the classification and generalisation	69
3.5.3. Limits of the method and potential improvements	70
3.5.4. Uncertainties in the <i>Sargassum</i> estimates	70
3.5.5. <i>Sargassum</i> dynamics over 2016-2020	71
3.6. Conclusions	72
3.7. Appendices	72
3.7.1. Neighbours indices calibration	72
4. Suivi des agrégats de sargasses et modélisation de leur dérive	74
4.1. Abstract	77
4.2. Introduction	77
4.3. Materials and Methods	78
4.3.1. Overview	78
4.3.2. Images matching to derive <i>Sargassum</i> velocity	79
4.3.3. Current and wind velocities	80
4.3.4. Statistical analyses	80
4.4. Results	82
4.5. Discussion	86
4.5.1. General drift patterns	86
4.5.2. Extraction of <i>Sargassum</i> velocities : method limitations	86
4.5.3. Physical and statistical approximations	87
4.5.4. Geostrophic component of <i>Sargassum</i> drift	87
4.5.5. Windage and Ekman component of <i>Sargassum</i> drift	88
4.5.6. Proposed model of <i>Sargassum</i> drift	88
4.6. Appendices	89
4.6.1. Collocation between <i>Sargassum</i> and drifter	89
4.6.2. Matching on SIFT key points	89
4.6.3. Complex linear regression	90
4.6.4. Bootstrapped confidence intervals for parameters	91
4.6.5. Regressions using Ekman-corrected currents	91
4.6.6. Wind regressions	92
5. Modélisation Lagrangienne et biogéochimique du transport et de la croissance des sargasses	94
5.1. Abstract	97
5.2. Introduction	97
5.3. Materials and Methods	98
5.3.1. Satellite observation dataset	98
5.3.2. <i>Sargassum</i> drift model	99
5.3.3. <i>Sargassum</i> growth model	99

5.3.4. Model inputs : currents, wind, solar irradiation and nutrients	101
5.3.5. Simulations setup	102
5.4. Results	104
5.5. Discussion	110
5.5.1. Drift parameters variability	110
5.5.2. Main drivers of growth	111
5.5.3. Identified regions for growth and decay of <i>Sargassum</i> algae	112
5.6. Appendices	113
5.7. Interannual variability of time to double biomass values	113
5.8. Limitation factors of growth	114
5.9. Biomass time series analysis	114
6. Discussion générale	117
6.1. Masques des données satellites	119
6.2. Échelles spatiale et temporelle des images composites	120
6.3. Incertitude des mesures	123
6.4. Variabilité de la dérive	124
6.5. Modèles Lagrangien et Eulérien	125
6.6. Variabilité interannuelle de la distribution des sargasses	127
Bibliographie	130
ANNEXES	154
A. Apports en nutriments des grands fleuves et prolifération des sargasses	154
B. Croissance différenciée des trois morphotypes de sargasses	163

Table des figures

1.1.	Accumulation massive d'algues sargasses aux îles Vierges britanniques (Photo : YACHT SHOTS BVI).	21
1.2.	Thalle de <i>Sargassum natans</i> et ses organes spécialisés.	23
1.3.	Types de radeaux de sargasses (Schéma : ODY et al., 2019).	24
1.4.	Carte historique de la mer des Sargasses par Justus Perthes (1871). . . .	25
1.5.	Série temporelle des couvertures de sargasses sur l'océan Atlantique entier (M. WANG et al., 2019a).	26
1.6.	Télédétection des sargasses grâce à leur réflectance dans l'infrarouge (schéma : Anouk Ody).	27
1.7.	Spectre de réflectance des algues sargasses (SHIN et al., 2021). Le zoom de droite montre la bande d'absorbance vers 632 nm caractéristique des pigments de chlorophylle c et donc des algues brunes.	28
1.8.	Courants de surface de l'Océan Atlantique tropical nord, ils constituent les routes par lesquels transitent les algues sargasses au cours de leur cycle annuel (JOUANNO et al., 2021a). Les surfaces brunâtres correspondent aux biomasses de sargasses observées par satellite et l'échelle de couleur verte la concentration chlorophylle a (phytoplancton). . . .	29
1.9.	Spirale d'Ekman et le courant de surface résultant du vent (JAUD, 2011).	30
1.10.	Effet du vent (windage) sur la dérive dépendant de l'immersion d'un objet flottant (Schéma : National Oceanic and Atmospheric Administration)	30
1.11.	Facteurs physiques et biogéochimiques nécessaires à la croissance des algues sargasses.	32
2.1.	Nombre annuel de publications scientifiques portant sur les sargasses pélagiques ou les organismes qui y sont associés (jusqu'en juin 2023). .	34
2.2.	L'écosystème sargasse et différents organismes associés (Photo : NOAA (National Oceanic and Atmospheric Administration)).	35
2.3.	Culture des algues sargasses avec un courant artificiel permanent (Photo : MAGAÑA-GALLEGOS et al., 2023a).	36
2.4.	Les trois morphotypes majoritaires des sargasses (Photo : Thierry Thibaut, Sandrine Ruitton).	38
2.5.	L'impact des échouements sur l'écosystème côtier au Mexique (schéma : CHÁVEZ et al., 2020).	39
2.6.	Les voies de valorisation des sargasses (schéma : AMADOR-CASTRO et al., 2021).	40
2.7.	Agrégat de sargasses vu par le satellite MERIS (image : J. GOWER et KING, 2008)	43

3.1. Filtering method diagram. The daily images are processed to extract spatial and context features. These features feed the filtering model that discriminates between true and false detections. The manual labelling and algorithm selection are performed once (indicated in dotted line) to build the model.	53
3.2. SAREDA work flow. Intermediate step of the data are indicated in bold.	55
3.3. Examples of true and false detections for 2020 in 2° by 2° boxes. The colour bar indicates the AFAI deviation from the background (the AFAI detection threshold is indicated in red), masked pixels : either clouds, clouds shadows sunglint or shallow waters (<500 m depth) are represented in dark grey and land in light grey. The bottom right panel shows the average of Rayleigh-corrected reflectance spectra (Rrc) of each case and the background spectrum. Rrc was averaged over the detected pixels (not-detected pixel in the case of background) for each MODIS band in the range (400 nm - 800 nm). The bands used in the AFAI computation (667, 748, 869 nm) are shown as dashed blue lines.	56
3.4. Map of true (A) and false (B) <i>Sargassum</i> aggregations from the learning dataset over 5 years. All labelled aggregations were displayed at their location, with possible overlaps.	61
3.5. Learning curve of the random forest algorithm. The dataset fraction allocated for training increases from 3% to 90%, the remaining 10% of the data are used for testing. The displayed curves are the average on 30 computed curves. The blue curve shows the overall accuracy and the red curve the generalisation accuracy (i.e. training without a year and testing on it). Similar results were observed with the recall and precision scores.	63
3.6. Monthly composite of FC for June 2020 at 1 km and 50 km resolution for unfiltered (left) and filtered (right) data. The top panel is a zoom of the region shown on middle panel.	64
3.7. Filtered FC of monthly composites for 2020 at 50 km resolution.	65
3.8. <i>Sargassum</i> biomass time series averaged in different boxes during the time period 2016-2020. The top panel displays the 2020 aggregated data in 1 km-resolution and the boxes used for the biomass computation. Panel A presents the biomass time series in the same box as M. WANG et al., 2019b and compare it to their data (available until 2018 only). Panel B and C are the retrieved <i>Sargassum</i> filtered biomass for Eastern and Western Atlantic Ocean (boxes B and C on the map). The black lines on the bar-plots indicate the annual mean of filtered data computed over the five years.	66
3.9. Annual composites of biomass at 50 km for 2016-2020 associated with the envelope of the area of high <i>Sargassum</i> concentration. The normalised area with respect to 2018 is indicated. The last panel shows all the envelopes, its intersection (dotted line) and its union (dashed line).	68

4.1. Workflow of the <i>Sargassum</i> aggregates velocity extraction process, with data sources indicated in blue, results in green and processes in white. \mathbf{W} , \mathbf{U}_d , \mathbf{U}_S , \mathbf{U}_G are wind, drifter, <i>Sargassum</i> and geostrophic current velocities, respectively.	79
4.2. Example of image matching of January 6th 2021 for a collocated case with SIFT key points extracted from Terra and Aqua 100 x 100 pixels images. The five consistent matches are shown as linked pairs of points. The colorbar refers to AFAI deviation from background (PODLEJSKI et al., 2022), the white area is the mask. The collocated drifter is located at the centre of each image (not shown).	83
4.3. Collocated <i>Sargassum</i> /drifter pairs ($n = 192$) distribution in space and time, split into drogued (orange) and undrogued (blue) drifters.	83
4.4. Wind-rose of velocities for the detected <i>Sargassum</i> aggregates, collocated drifters (drogued and undrogued), and interpolated geostrophic current and wind at the time and location of the collocated drifters. Colours indicate the speed, and bar lengths the frequency. Note that all velocity directions are expressed in terms of vector azimuth, i.e. the direction toward which the vectors lead.	84
5.1. Workflow of the simulation setup. The example shown is for 1-month simulations, but an identical approach was used for longer simulations (3 months, 1 year).	103
5.2. TSS values computed between simulated monthly composites maps of <i>Sargassum</i> presence after 1 month of simulation and corresponding satellite images with windage set to 1%, current to 100% and deviation angle of windage to 0°. The orange curve shows the persistence, i.e. the TSS value computed between the previous satellite composite and the current one. The area between orange and blue curves gives the gain brought by the model. The red curve is the average fractional coverage in percent over of total area.	105
5.3. Drift model skill assessment for different sets of windage and current factors in four oceanic regions. Color and values refer to the number of occurrences where the parameters set was the best performing over simulations aggregated annually. The deflection angle was here set to 0°	106
5.4. Results of the drift and growth simulation starting in January 2017. The first row shows the monthly composites at 50 km resolution from satellite (left) and from the model after 6 months of simulation (right). The time series below show the evolution of <i>Sargassum</i> biomass in the four areas displayed on the top panel from satellite (black lines) and the simulation (colored lines).	107
5.5. Comparison between biomass (millions of tons) estimated with satellite observation (black lines) and simulated biomass (colored lines). Colors refer to the oceanic regions shown in Fig. 5.4.	108

5.6. Time to double biomass for <i>Sargassum</i> particles seeded at that location (left). Biogeochemical limitation factor according to the quotas of nitrogen or phosphorus in the tissues ($\min(f(Q_N), f(Q_P))$). Physical limitation factor according to temperature, irradiance and salinity ($f(T).f(S).f(I)$)	109
5.7. Sample of simulated trajectories that cross the Caribbean arc (left) and corresponding biomass time series (right) for the years 2016 (top) and 2018 (bottom). The black vertical lines indicate the approximate average date of the biomass maximum among the time series, and the location corresponding to this date is displayed for each particle with a black star on the maps.	110
5.8. The time to double biomass for years 2016 to 2020 and months May to August. The low time to double biomass values (yellow) between the North of Brazil and the Gulf of Mexico appeared in early May for 2016, in June for 2017 and 2020, in July for 2019 and in August for 2020 (rounded at the date of appearance).	113
5.9. Spatial and seasonal variability of the five limitation factors to <i>Sargassum</i> growth used in our model. T, I, S, Qn and Qp stand for temperature, irradiance, salinity, nitrogen quota and phosphorus quota, respectively.	114
5.10. The biomass time series dynamics classes for simulations starting in April, May or June. The right panel is the mean of the time series of biomass normalized according to Gaussian classes, the envelope of the curve refers to the variance. The central panel is a kernel density estimate (KDE) of the barycenter of the trajectories. The left panel is the mean biomass distribution in the class. The classes are numbered from 1 to 10 with indication of their corresponding fraction of the data set (n_total = 58920).	115
6.1. Carte des fréquences d'observation des sargasses sur les zones non masquées avec MODIS à 1 km de résolution, année 2017, non filtrée. Les contours indiquent le taux moyen d'observabilité (surface sans masque) journalière en pourcentage (Figure : Madjid Hadjal).	120
6.2. Comparaison de la couverture de sargasses sous forme de composites mensuels résultant de simulations Lagrangiennes sans croissance sur des durées de 1, 2 et 3 mois. L'initialisation est basée sur une image satellite mensuelle avec les particules lâchées le 15 ^{ème} jour du premier mois pour la colonne de gauche. Pour la colonne de droite, les particules sont lâchées le jour d'observation des détections satellites journalières correspondantes.	122
6.3. Composites mensuels des biomasses de sargasses sur l'année 2018 obtenus avec une simulation de 6 mois du transport et de la croissance des sargasses. De gauche à droite, composites mensuels observés par satellite, issus du modèle Lagrangien, issus du modèle Eulérien	126

Liste des tableaux

2.1. Études scientifiques pour la valorisation économique des sargasses.	41
2.2. Caractéristiques des capteurs principaux utilisés pour la détection des sargasses (LAZCANO-HERNANDEZ et al., 2023).	44
3.1. Labelled aggregations per year. The aggregations were obtained by the export of FC images in vector format. The labelling was performed over the Atlantic (100°West to 15°East, 15°South to 50°North).	57
3.2. Algorithms performance computed with a k-fold operation (k=50). No particular tuning were previously performed.	60
3.3. Feature frequency of use (%) for the final classifier (random forest). The frequencies were averaged over 30 generated forests. The radius used for the metrics NNI, PersI and NNAI were respectively 700 km, 50 km and 700 km.	62
3.4. Algorithms performance scores in percentage. The computation is made 30 times to https://fr.overleaf.com/project/62971c689b31d47b1bfe53ca reduce random effect. The standard deviation is indicated after the scores. The generalisation scores correspond to the weighted mean of the five annual tests.	64
3.5. Accuracy scores according to the pair of radii used for NNI-NNAI and PersI. The overall accuracy was obtained with a k-fold cross-validation on the whole dataset, the generalisation accuracy was computed by excluding a year from the training dataset and testing on it (this operation was done on each of the five years and the scores were averaged). The pair of radii yielding the best overall accuracy is indicated in blue while the pair of radii maximising the generalisation accuracy is indicated in red. Similar results were observed with overall and generalisation scores for recall and precision.	73
4.1. Number of collocation cases per year at different steps of the method. First after selection of the daily scenes with detections on Terra and Aqua, second after performing matching algorithms and finally after manual validation.	82

4.2. Regression models between measured velocities and environmental variables. \mathbf{U}_S , $\mathbf{U}_{D,d}$, $\mathbf{U}_{D,u}$, \mathbf{U}_G and \mathbf{W} are velocities for the detected <i>Sargassum</i> aggregates, collocated drogued/undrogued drifters, and interpolated geostrophic current and wind at the time and location of the <i>Sargassum</i> aggregates. Variables and estimated parameters are complex numbers, here displayed in exponential notation with angles in degrees anticlockwise. Depending on the regression model, some parameters are forced to real values (zero). The norm and the argument are associated with a standard deviation estimated over 5000 bootstrapped datasets. All regressions were statistically significant ($p < 0.01$), negative R^2 is due to model constraint (no intercept)	85
4.3. Regression models for <i>Sargassum</i> velocity using drifters velocity as explaining variable. Same as Table 4.2	85
4.4. Same as table 4.2 except that the velocities \mathbf{U}_S , $\mathbf{U}_{D,d}$ and $\mathbf{U}_{D,u}$ are corrected from Ekman current at either 0 or 15 meter depth.	92
4.5. Same as Fig. 4.2 with cases where the wind is lower than 3 m s^{-1}	92
4.6. Same as Fig. 4.2 with cases where the wind is greater than 3 m s^{-1}	93
5.1. Parameters used in the <i>Sargassum</i> growth model. All came from Jouanno et al. (in prep) except the K_m which was adapted here to the Lagrangian approach.	101

Liste des acronymes

ABI

Advanced Baseline Imager.

AFAI

Alternative Floating Algae Index.

AMM

Atlantic Meriodional Mode.

ANR

Agence National de Recherche.

CC

Caribbean Current.

CNES

Centre National d'Etudes Spatiales.

CNRS

Centre national de la recherche scientifique.

CSDI

Coast Shortest Distance Index.

ECMWF

European Centre for Medium-Range Weather Forecasts.

FAI

Floating Algae Index.

FC

Fractional Coverage.

FORESEA

FOREcasting seasonal Sargassum Events in the Altantic.

FPCA

Functional Principal Component Analysis.

GASB

Great Atlantic *Sargassum* Belt.

GDP

Global Drifter Program.

GLOH

Gradient Location and Orientation Histogram.

GOES

Geostationary Operational Environmental Satellite.

GPS

Global positioning System.

GTB

Gradient Tree Boosting.

IRD

Institut de Recherche pour le Développement.

ITCZ

Intertropical Convergence Zone.

KDE

Kernel Density Estimate.

LDA

Linear Discriminant Analysis.

LEGOS

Laboratoire d'Etudes en Géophysique et Océnographie Spatiales.

LIS

Laboratoire d'Informatique et des Systèmes.

MCI

(Maximum Chlorophyl Index.

MERIS

Medium Resolution Imaging Spectrometer.

MIO

Mediterranean Institute of Oceanography.

MODIS

Moderate-Resolution Imaging Spectroradiometer.

MSI

MultiSpectral Instrument.

NASA

National Aeronautics and Space Administration.

NB

Naive Bayes classifier.

NBC

North Brazil Current.

NDVI

Normalized Difference Vegetation Index.

NEC

North Equatorial Current.

NECC

North Equatorial CounterCurrent.

NEMO

Nucleus for European Modelling of the Ocean.

NIR

Near-InfraRed.

NNAI

Nearest Neighbours Area Index.

NNI

Nearest Neighbours Index.

NOAA

National Oceanic and Atmospheric Administration.

OF

Optical Flow.

OLCI

Ocean and Land Colour Instrument.

OLI

Operational Land Imager.

PersI

Persistence Index.

PISCES

Pelagic Interaction Scheme for Carbon and Ecosystem Studies.

RANSAC

RANDom SAMple Consensus.

RF

Random Forest.

SAREDA

SArgassum Evolving Distribution in the Atlantic.

SEC

South Equatorial Current.

SIFT

Scale Invariant Feature Transform.

SVM

Support Vector Machine.

SVP

Surface Velocity Program.

TSS

True Skill Statistic.

Liste des acronymes

UTC

Universal Time Clock.

VIIRS

Visible Infrared Imaging Radiometer Suite.

1. Introduction

Avec 70% de couverture de la surface terrestre, les océans apportent une contribution fondamentale aux grands équilibres planétaires. Par leurs échanges avec l'atmosphère, leur inertie thermique et leur circulation interne, ils jouent un rôle primordial dans la régulation de la température du globe et du CO₂ atmosphérique. Berceau et refuge de la biodiversité, on y dénombre 34 phyla riches de ressources pour l'alimentation humaine. Du fait du changement climatique, auquel s'ajoutent les pressions anthropiques locales, l'équilibre des océans et de la biodiversité associée est constamment mis en péril et l'on observe une augmentation alarmante des perturbations des écosystèmes. Parmi celles-ci, l'apparition d'espèces invasives est fréquemment un facteur de premier plan de ces déséquilibres. Le plus souvent introduites par l'homme, elles entraînent généralement une diminution de la biodiversité et la disparition de certaines espèces indigènes. De nombreuses espèces d'algues pluricellulaires se sont avérées invasives lorsqu'elles ont changé d'écosystème (VERLAQUE et al., 2015), qu'elles soient benthiques comme *Rugulopteryx okamurae*, côtières comme les Ulves ou pélagiques comme les algues sargasses, objet de la présente étude. En effet, ces dernières, auparavant limitées à de faibles quantités en mer des Sargasses, sont devenues un fléau régulier pour les côtes de divers pays (comme le Mexique, l'Angleterre, les USA ou la France) en causant de dramatiques épisodes d'échouement massif sur leurs plages (Figure 1.1).



FIGURE 1.1. : Accumulation massive d'algues sargasses aux îles Vierges britanniques (Photo : YACHT SHOTS BVI).

Les algues sargasses pélagiques

Ces échouements d'algues sargasses se composent actuellement de deux espèces différentes, *Sargassum natans* et *Sargassum fluitans*. Toutes deux incluses dans le genre *Sargassum*, elles font partie de la classe des algues brunes (*Phaeophyceae*) qui se caractérise par l'utilisation de la chlorophylle c pour capter l'énergie solaire. Parmi les autres espèces de sargasses, celles-ci ont pour spécificité de ne jamais être attachées à aucun substrat, d'où leur attribut de "pélagique". Elles flottent à la surface de l'océan durant leur cycle de vie entier et seuls leur échouement ou leur submersion en profondeur causent généralement leur dégradation. Une seule autre espèce de sargasse leur est comparable : *Sargassum horneri*. Évoluant en mer Jaune de Chine, cette dernière pousse fixée au fond de la mer (espèce benthique) mais des événements météo intenses peuvent décrocher une grande quantité de ces algues qui continuent à vivre à la surface de l'eau comme les sargasses pélagiques. À l'instar des autres algues, les sargasses n'ont pas à proprement parler de tissus différenciés, mais elles comportent néanmoins des organes spécialisés répartis sur leur thalle (organisme). Le stipe joue le rôle structurant assimilable à celui d'une tige en reliant les différents organes sans pour autant assurer une fonction circulatoire. Les frondes ou lames sont similaires à des feuilles qui augmentent la surface d'absorption de la lumière, et les pneumatocystes (flotteurs) assurent la flottaison de l'ensemble (Figure 1.2). Cette anatomie est partagée par toutes les sargasses pélagiques qui se déclinent en différents morphotypes. Au nombre de trois à l'heure actuelle, ils se distinguent par leur caractère plus ou moins touffu, la taille et le nombre de leurs frondes et pneumatocystes, ainsi que par leurs caractéristiques biologiques comme leur taux de croissance.

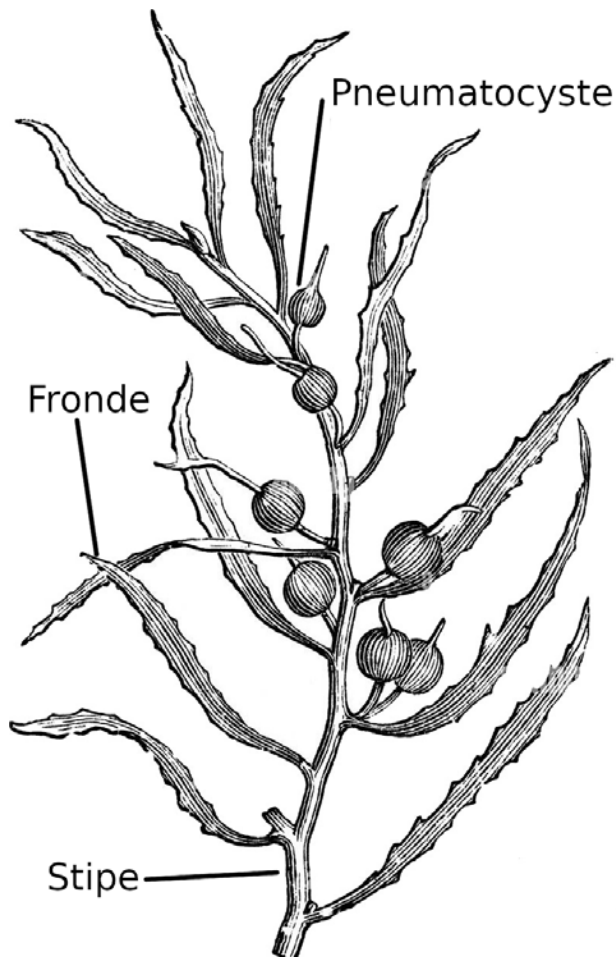


FIGURE 1.2. : Thalle de *Sargassum natans* et ses organes spécialisés.

Ces organismes se reproduisent par la fragmentation et la multiplication végétative majoritairement. Si bien que les populations d'un même morphotype sont très homogènes et comparables à un seul gigantesque clone (DIBNER et al., 2022). Du fait des courants et du vent, les populations d'algues se regroupent plus ou moins en radeaux compacts. Notamment, la circulation de Langmuir (tourbillons de surface dus au vent) génère des structures allongées particulières nommées andains (windrow en anglais) du fait leur similitude avec le fourrage après la moisson. Dans de plus rares cas, il se forme également des amas de taille variable pouvant aller jusqu'à 100 mètres de diamètre (Figure 1.3). Ces radeaux ont une épaisseur comprise entre quelques dizaines de centimètres et quelques mètres et sont le plus souvent clairsemés. Les vents influent de surcroît sur la profondeur des radeaux, à l'affleurement par vent calme, ils sont mélangés dans la couche d'eau superficielle jusqu'à quelques mètres de profondeur lorsque le vent et l'état de la mer se déchaînent.

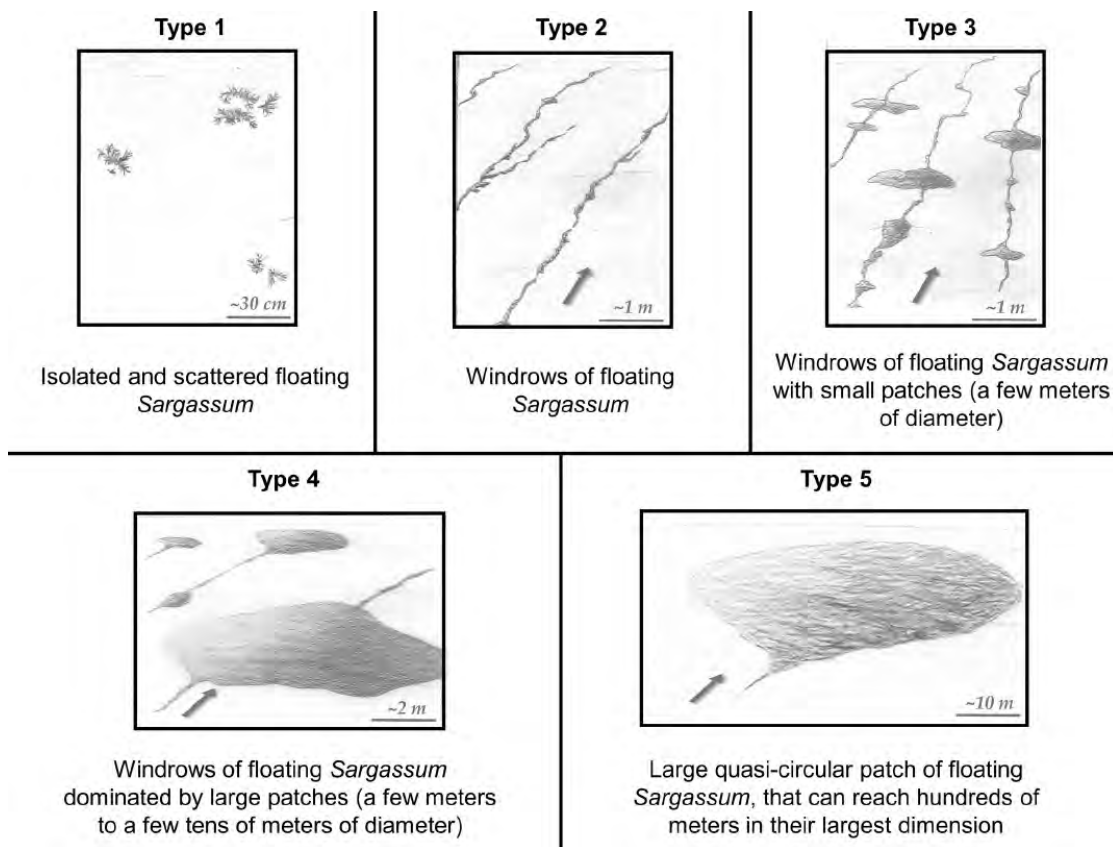


FIGURE 1.3. : Types de radeaux de sargasses (Schéma : ODY et al., 2019).

Les algues sargasses pélagiques sont bien connues des navigateurs et des scientifiques puisque leur première observation répertoriée remonte à la traversée de l'Atlantique par Christophe Colomb. Depuis lors, elles n'ont été l'objet que d'un intérêt marginal par la communauté scientifique et par les pêcheurs qui s'intéressent aux populations de poissons vivant parmi ces algues. Les sargasses n'ont été observées tout au long du dernier demi-millénaire que dans la mer qui porte leur nom, la mer des Sargasses (Figure 1.4).

1. Introduction

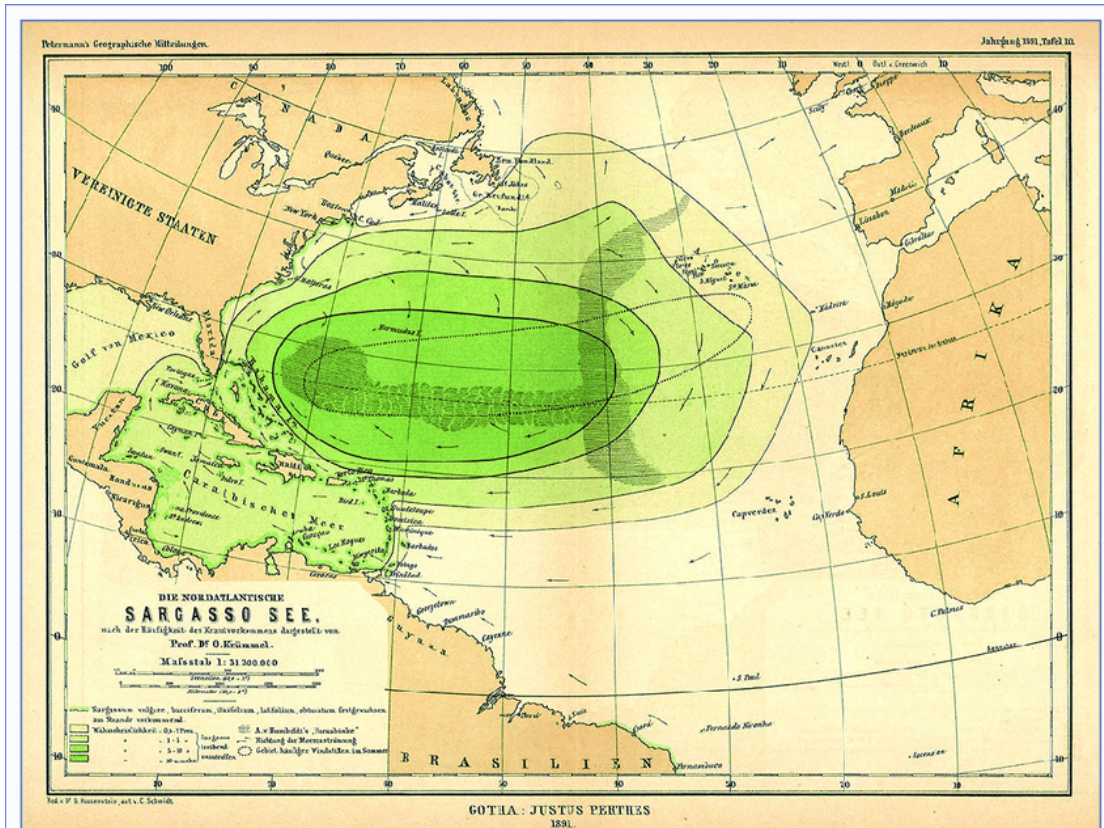


FIGURE 1.4. : Carte historique de la mer des Sargasses par Justus Perthes (1871).

Cette situation d'équilibre a perduré jusqu'au début des années 2010 qui ont été marquées par un changement radical de la distribution et de la dynamique des algues sargasses. Selon JOHNS et al., 2020, c'est suite à un événement climatique inhabituel et des vents violents en 2010 que les algues ont vraisemblablement été transportées loin à l'est de la mer des sargasses, jusqu'aux côtes des Canaries à partir desquelles elles ont été advectées vers le golfe de Guinée pour s'implanter durablement dans une nouvelle zone située vers 5° nord. À présent, on les trouve réparties sur toute l'étendue est-ouest de l'océan Atlantique, depuis le golfe de Guinée où elles sont abondantes en début d'année jusqu'à la mer des Caraïbes et le golfe du Mexique qu'elles envahissent durant l'été. Ce changement géographique s'est accompagné d'un accroissement décuplé des algues sargasses, leur couverture spatiale et les quantités de biomasses observées à l'heure actuelle sont sans commune mesure avec celles mesurées précédemment (Figure 1.5).

1. Introduction

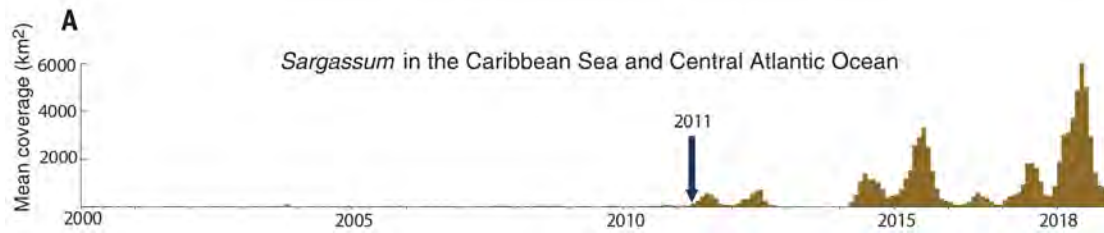


FIGURE 1.5. : Série temporelle des couvertures de sargasses sur l'océan Atlantique entier (M. WANG et al., 2019a).

Ces concentrations phénoménales d'algues s'étalent sur des centaines de kilomètres carrés et sont transportées aux abords des côtes de nombreux pays. Lorsque la combinaison du courant et du vent converge vers les plages, d'importantes quantités d'algues s'échouent sur le rivage et s'accumulent dans les eaux littorales. Leur présence, et à plus forte raison leur pourrissement, sont à la fois néfastes pour l'environnement côtier et pour les activités humaines, notamment touristiques. D'une part, l'eutrophisation de l'eau et l'obstruction de la lumière entraînent une mortalité importante des producteurs et consommateurs primaires de l'écosystème côtier. D'autre part, les dégazements nauséabonds et toxiques des algues en putréfaction font barrage au tourisme balnéaire et les pays touchés essuient de lourdes pertes économiques. Parmi ces derniers, on trouve le Mexique, dont les côtes du Yucatán sont sévèrement impactées par les échouements, ainsi que les USA avec la Floride et Porto Rico, régulièrement submergés d'algues sargasses. La France est également touchée au niveau de la Guadeloupe et de la Martinique dont les revenus touristiques, principal secteur économique de ces îles, sont considérablement dévalorisés. <https://www.senat.fr/questions/base/2018/qSEQ18030304S.html>.

Ces dégâts économiques, écologiques et sanitaires ont rendu nécessaire l'amélioration des connaissances scientifiques sur ces algues afin de mieux comprendre leur évolution et de permettre une meilleure gestion de leurs échouements. La présente thèse s'inscrit dans cette dynamique de recherche promue notamment par les organismes français. Le projet ANR (Agence Nationale de la Recherche) **FORESEA** (FOREcasting seasonal Sargassum Events in the Atlantic), par lequel cette thèse est financée, se propose ainsi d'observer, modéliser et prévoir la distribution spatiale des sargasses à l'échelle du bassin. Plus spécifiquement, il va s'agir ici d'explorer les facteurs déterminants du cycle saisonnier des sargasses afin d'élucider leur grande variabilité interannuelle, que ce soit au niveau des quantités de biomasse observées ou de leur distribution.

Observation des sargasses

Préalablement à l'étude des variations interannuelles des sargasses, il est indispensable d'améliorer nos connaissances sur leur distribution spatiale depuis leur récent changement d'aire de répartition. Malheureusement, ces algues se développent sur une zone d'une telle étendue (20 millions de km²) qu'il est impossible d'en faire le suivi exhaustif par des campagnes en mer et des mesures *in-situ*. Afin de contourner cette limitation, il est possible d'utiliser des outils de télédétection qui permettent d'étudier leur distribution à partir d'images globales. La télédétection est une approche très largement utilisée pour l'observation des phénomènes à large échelle comme les algues marines. Utilisée sur un objet d'étude (sargasses), elle donne accès à des informations (localisation, quantité, forme) transportées par un média (lumière) et reçues par un capteur sensible à ce média (spectroradiomètre, figure 1.6). Ces capteurs sont généralement portés par un aéronef (avion, ballon-sonde, etc) ou par des satellites. Ce sont ces derniers qui conviennent le mieux à l'observation des sargasses en permettant des prises de vue très étendues et régulières grâce à leur orbite stable.

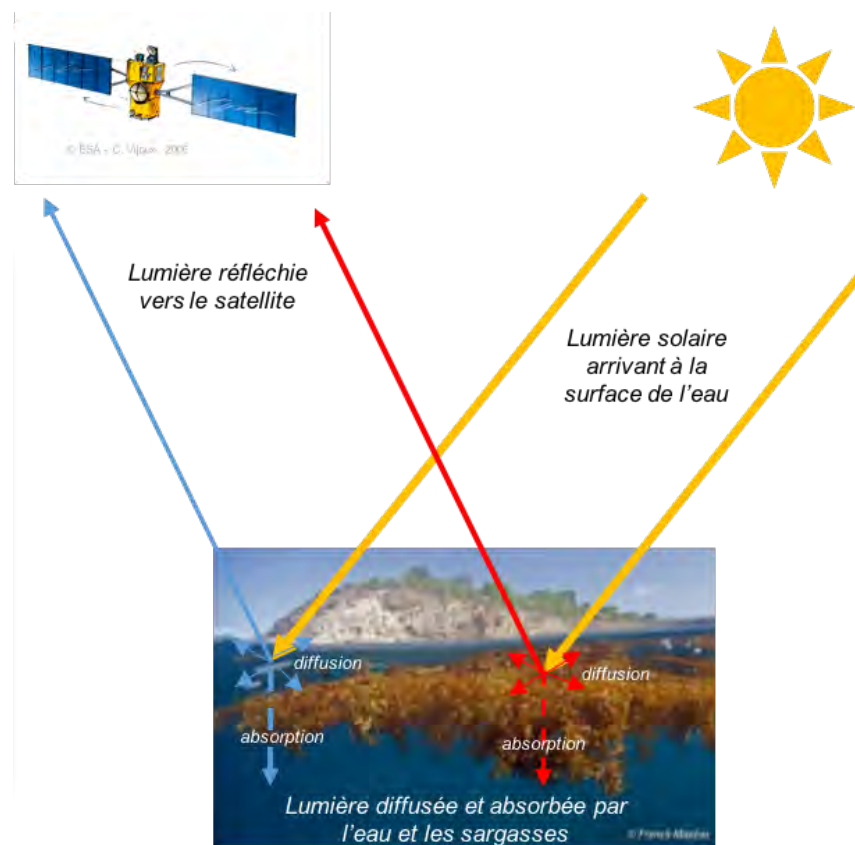


FIGURE 1.6. : Télédétection des sargasses grâce à leur réflectance dans l'infrarouge (schéma : Anouk Ody).

S'il suffit de disposer d'un capteur fixé à un satellite pour observer la surface de l'océan au sein duquel se trouvent les sargasses, il est en revanche bien plus complexe de les différencier de l'eau. En effet, leur couleur brunâtre caractéristique n'est pas distinguable depuis l'espace du fait de l'atmosphère et de toutes les particules qui y sont présentes (épaisseur optique). Par chance, les organismes chlorophylliens comme les plantes ou les algues sont très bien discernables dans le proche infrarouge (1000-2000 nm) grâce à leur forte réflectance dans ce domaine. Ainsi, un capteur sensible à ces longueurs d'onde parvient à correctement différencier les sargasses de l'eau de mer environnante et même à les quantifier en fonction de l'intensité du signal reçu. Cependant, les algues sargasses ne sont pas les seules à réfléchir la lumière du proche infrarouge et d'autres objets comme les nuages, leurs ombres, le reflet du soleil dans l'eau ou bien d'autres algues comme le *Trichodesmium* peuvent être confondus avec les sargasses. C'est pourquoi il a fallu construire des indices radiométriques (combinaison linéaire ou ratios de différentes longueurs d'onde) plus spécifiques à l'observation des sargasses, par exemple en ciblant la bande d'absorption vers 632 nm des sargasses due à leur chlorophylle c (Figure 1.7).

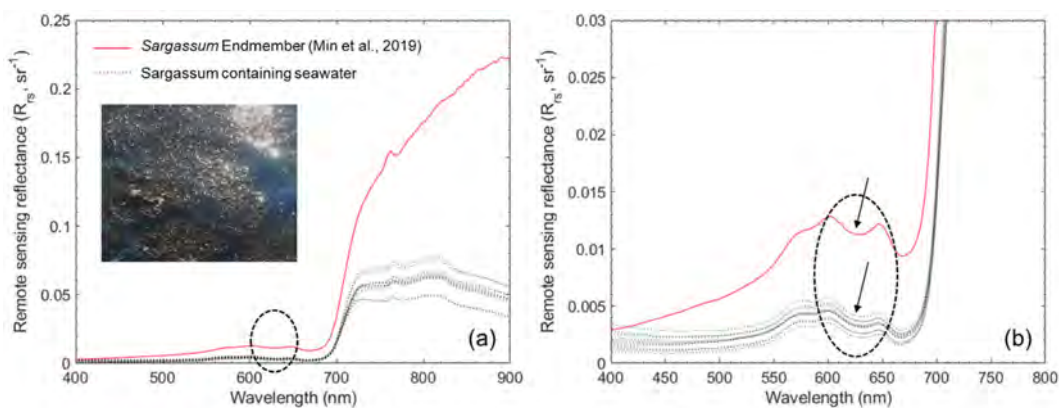


FIGURE 1.7. : Spectre de réflectance des algues sargasses (SHIN et al., 2021). Le zoom de droite montre la bande d'absorbance vers 632 nm caractéristique des pigments de chlorophylle c et donc des algues brunes.

Cette méthode permet de localiser et quantifier précisément les sargasses avec néanmoins des erreurs résiduelles (faux positifs) non négligeables dues à des objets de réflectances similaires. Le traitement de ces scories sera le sujet abordé par le chapitre 3 de la présente thèse afin d'obtenir un jeu de données le plus fidèle possible rendant compte de la distribution spatiale des sargasses. Une fois ce dernier obtenu, il sera possible de commencer à étudier le cycle saisonnier des sargasses grâce à ces nouvelles informations. Afin d'appréhender un phénomène physique ou biologique, une approche privilégiée par la démarche scientifique consiste à établir un modèle décrivant ledit phénomène. En ce qui concerne les algues sargasses, il sera ici nécessaire de définir à la fois une modélisation de leur dérive et de leur croissance. Ce sont ces deux modèles et leur synergie qui seront l'objet des travaux dans les chapitres 4 et 5 de cette thèse.

Principaux moteurs de la dérive des sargasses

Les radeaux de sargasses se situant à l'interface air-océan, leur dérive est principalement affectée par deux phénomènes physiques, le courant et le vent. Ceux-ci génèrent une force d'entraînement sur les algues et une bonne compréhension de leur interaction combinée sur les sargasses devrait permettre de prévoir leur déplacement. La nouvelle zone de distribution des algues sargasses se situe à la convergence de nombreux courants à grande échelle qui définissent la circulation générale des océans (Figure 1.8). On trouve notamment le courant nord équatorial (NEC) ainsi que son pendant saisonnier, le contre-courant nord équatorial (NECC). Mais il y a également le courant sud équatorial (SEC), le courant nord Brésil (NBC) et le courant Caribéen (CC). Tous ces courants sont en partie responsables du cycle saisonnier des sargasses en les entraînant dans leur trajet aller et retour en Atlantique.

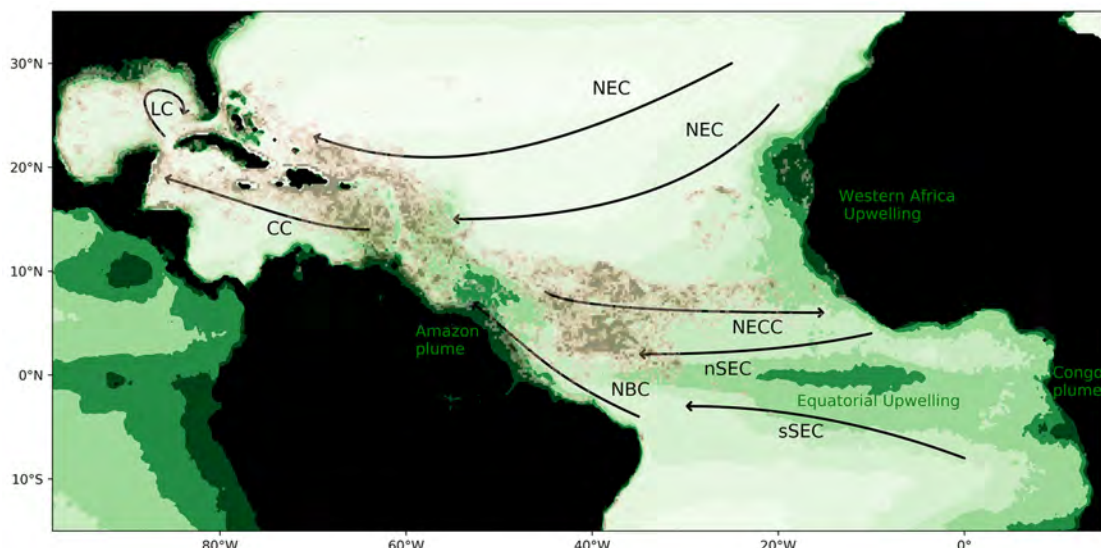


FIGURE 1.8. : Courants de surface de l'Océan Atlantique tropical nord, ils constituent les routes par lesquels transitent les algues sargasses au cours de leur cycle annuel (JOUANNO et al., 2021a). Les surfaces brunâtres correspondent aux biomasses de sargasses observées par satellite et l'échelle de couleur verte la concentration chlorophylle a (phytoplancton).

Le courant de surface peut être approximé en deux termes. En premier lieu, on trouve le courant géostrophique qui résulte de l'équilibre entre les gradients de pression et la force de Coriolis. À celui-ci s'ajoutent les courants hors équilibre ou agéostrophique, notamment ceux induits par le vent et l'état de la mer. Ces derniers sont généralement colinéaires et se déduisent du vent de surface. Le courant induit par le vent est en particulier appelé courant d'Ekman et en surface il est dévié de 45° vers la droite de la direction du vent (hémisphère nord) du fait de la force de Coriolis (Figure 1.9).

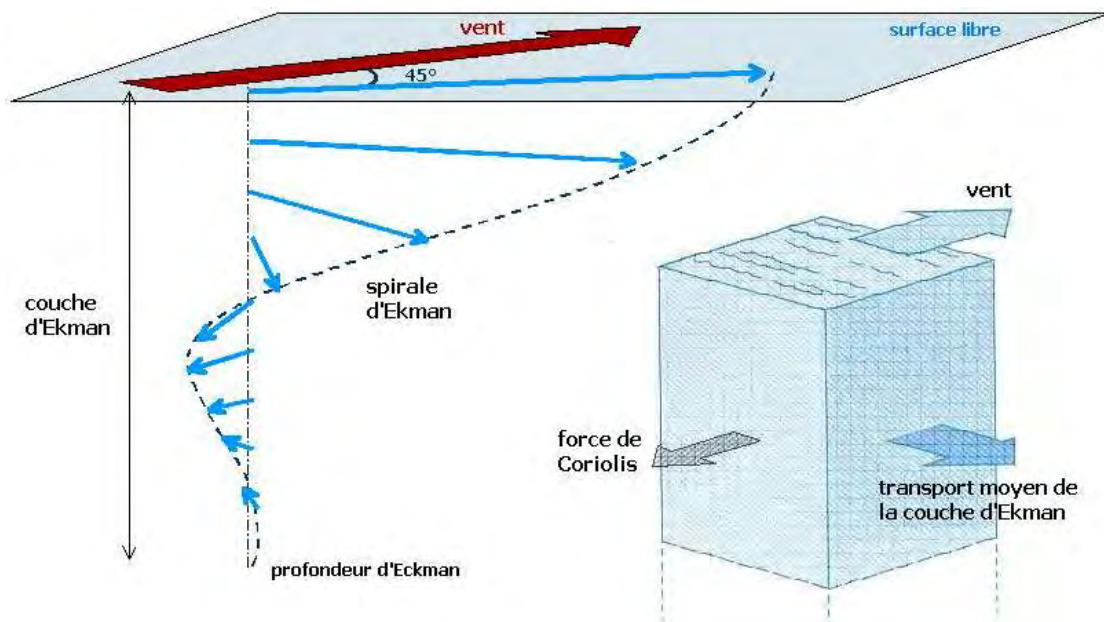


FIGURE 1.9. : Spirale d'Ekman et le courant de surface résultant du vent (JAUD, 2011).

Pour ce qui est de l'effet direct du vent sur les sargasses, généralement appelé "windage", il provient de l'effet de trainée appliqué aux parties émergées des radeaux de sargasses. Selon la fraction émergée des sargasses, le windage résultant est plus ou moins important (Figure 1.10).

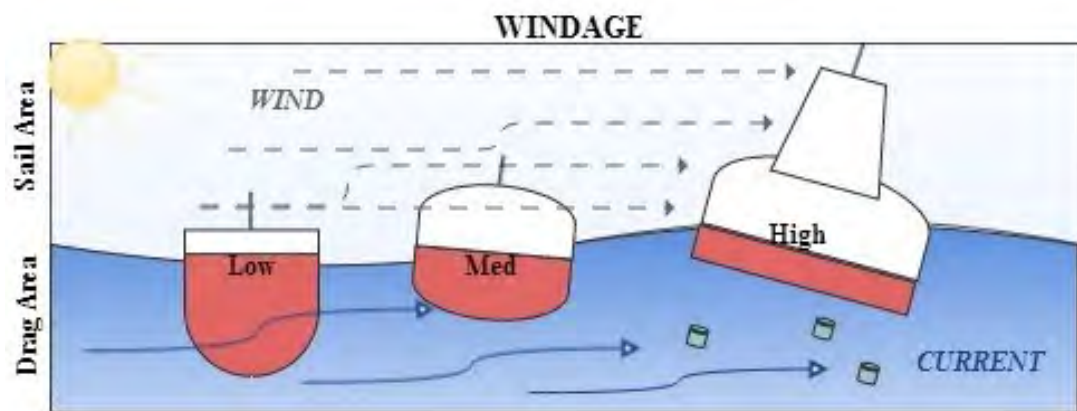


FIGURE 1.10. : Effet du vent (windage) sur la dérive dépendant de l'immersion d'un objet flottant (Schéma : National Oceanic and Atmospheric Administration)

L'effet d'entraînement des courants, géostrophique et agéostrophique, et du vent sur la dérive des sargasses peuvent être représentés par des coefficients reliant directement leur vitesse à celle des sargasses par une fonction linéaire. Ces facteurs sont jusqu'à présent encore mal déterminés par les scientifiques qui peinent à obtenir des observations précises de la dérive des sargasses. L'extraction de trajectoires de radeaux à partir d'images satellites ainsi que l'estimation de l'effet du courant et du vent sur la dérive des sargasses seront donc les sujets abordés dans le chapitre 4 de la présente thèse.

Principaux facteurs de la croissance des sargasses

Les algues sargasses étant des organismes photosynthétiques, il leur est en premier lieu nécessaire d'accéder à une source de lumière. En flottant à la surface de l'océan, elles se garantissent un ensoleillement suffisant même si celui-ci peut être légèrement restreint par une forte couverture nuageuse. Ensuite, comme tout autre organisme, les sargasses ont une gamme de conditions physiques dans laquelle elles peuvent perdurer. Notamment, des températures trop froides inhibent leur croissance tandis que des températures trop chaudes accélèrent leur dégénérescence. De ce fait, ces algues dépendent de masses d'eau tempérées afin de croître de manière optimale. De la même manière, un taux de salinité minimal est requis pour leur croissance, mais ce n'est généralement que peu contraignant dans l'océan Atlantique où elles évoluent. Enfin, les sargasses ont besoin des éléments biogéochimiques qui les composent afin de croître. Si le carbone et l'oxygène sont en abondance grâce au CO_2 et O_2 dissous dans l'eau, c'est le phosphore et l'azote qui peuvent être limitants. Les sargasses absorbent donc les ions phosphates PO_4^{3-} , ammonium NH_4^+ et nitrate NO_3^- lorsqu'ils sont disponibles. Ces derniers sont répartis inéquitablement dans l'océan Atlantique et sont largement limitants dans certains cas pour la croissance des sargasses. Cependant, leur évolution leur a permis de stocker l'azote et le phosphore au sein de leurs tissus afin de les utiliser pour leur développement ultérieur. Ainsi, elles s'assurent de croître même dans des milieux oligotrophes si elles ont au préalable absorbé des nutriments dans des eaux plus nutritives. La figure 1.11 montre un récapitulatif des facteurs déterminant la croissance des sargasses.

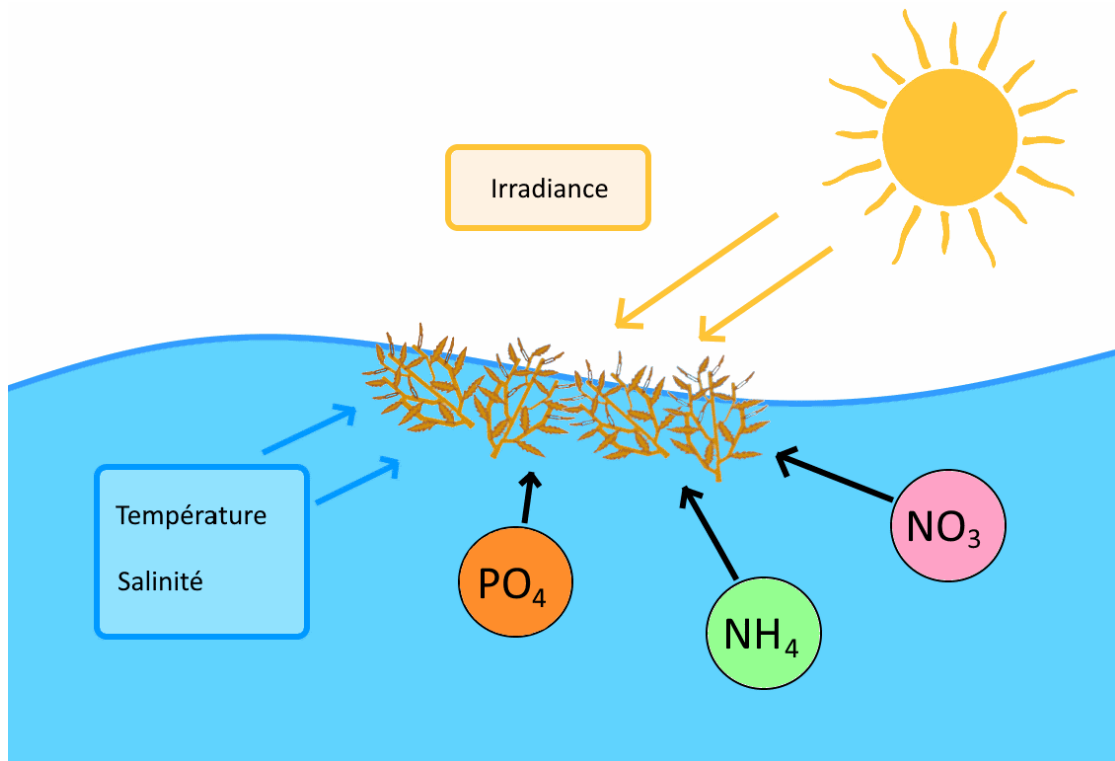


FIGURE 1.11. : Facteurs physiques et biogéochimiques nécessaires à la croissance des algues sargasses.

La combinaison de ces facteurs limitants avec leur taux de croissance nominal évalué en laboratoire donne une modélisation simple mais satisfaisante de la croissance des algues sargasses. Cependant, ces dernières ne font pas que croître indéfiniment et il faut également représenter leur mortalité dans les modèles. Comme aucune information n'est disponible sur ce phénomène précis et qu'il est de surcroît difficile à mesurer, on peut le représenter par un taux fixe de perte par jour. Il est également possible d'utiliser un taux quadratique afin de rendre compte de la compétition pour les ressources lorsque les biomasses de sargasses sont très élevées. L'analyse des résultats de cette modélisation de la croissance et de la mortalité des sargasses seront l'objet du chapitre 5 de cette thèse.

Organisation du manuscrit

Après cette introduction générale sur les algues sargasses pélagiques, sur les problèmes qui découlent de leurs échouements ainsi que sur la manière de les observer et de modéliser leur dérive et leur croissance, voici comment s'organise ce manuscrit sur la variabilité des algues sargasses.

Pour commencer, le chapitre 2 est une revue la plus exhaustive possible des travaux scientifiques traitant des sargasses depuis le siècle dernier. En traitant de tous les champs d'études appliqués aux sargasses, qu'ils soient en lien ou non aux présents

1. Introduction

travaux, cet état de l'art rend compte de l'histoire scientifique de ces algues et reflète l'évolution de l'intérêt qui leur est porté par les sociétés humaines.

Dans un second temps, le chapitre 3 et la publication scientifique associée décriront une méthodologie d'amélioration des données de télédétection. Basée sur des caractéristiques du contexte spatial des agrégats de sargasses, cette méthode utilise un algorithme d'apprentissage automatisé pour filtrer les fausses détections de sargasses et mieux quantifier leur biomasse.

Basé sur ce jeu de données corrigées, le chapitre 4 rendra compte de la méthode développée pour suivre des trajectoires d'agrégats de sargasses dans les images satellites basse résolution. Dans le même temps, il y sera décrit l'analyse statistique des trajectoires ainsi obtenues pour construire un modèle de dérive en fonction du courant et du vent.

Ce nouveau modèle de dérive sera par la suite testé dans le chapitre 5 avec une modélisation Lagrangienne de l'évolution de la distribution pluriannuelle des algues sargasses. Une fois recalibré, il s'agira également de l'associer à un modèle biogéochimique de croissance pour faire un suivi à long terme des biomasses de sargasses. Les résultats de ce modèle de dérive et de croissance fourniront les informations nécessaires à l'analyse des zones et facteurs clés afin d'expliquer la variabilité interannuelle des algues sargasses.

Pour finir, le dernier chapitre 6 établira un bilan des résultats apportés par les trois études qui composent cette thèse afin de discuter des phénomènes mis en lumière ainsi que des zones d'ombre restantes.

2. Revue de littérature

Les premiers travaux scientifiques sur les algues sargasses remontent au début du 20^{ème} siècle. En 120 ans de recherche, les thèmes abordés, reflet des problématiques de leur temps, ont largement fluctué au fil des décennies, tout comme l'intérêt qui leur est porté. Il y a encore quelques années, il s'agissait d'un sujet de niche scientifique dont les études paraissaient sporadiquement. À présent, les épisodes d'échouements massifs récurrents depuis 2011 en font un enjeu sociétal important pour les pays touchés. Les impacts sur la santé des habitants, sur les écosystèmes côtiers ainsi que sur l'économie ont conduit au financement de nombreuses nouvelles études essayant de répondre à cette problématique auparavant inexistante. On assiste depuis quelques années à une augmentation exponentielle des publications scientifiques sur les sargasses (Figure 2.1).

La temporalité de la présente thèse a rendu possible une revue bibliographique exhaustive des sujets traités par la littérature scientifique à propos des sargasses entre 1900 et 2023. Le présent chapitre rend compte de cette diversité de thèmes abordés et de son évolution temporelle.

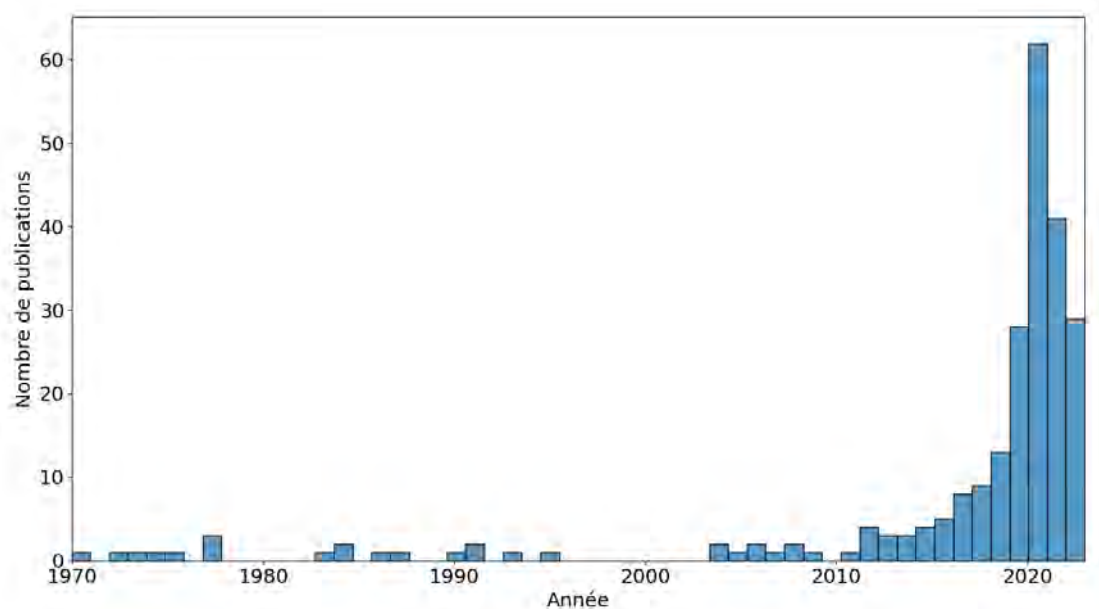


FIGURE 2.1. : Nombre annuel de publications scientifiques portant sur les sargasses pélagiques ou les organismes qui y sont associés (jusqu'en juin 2023).

2.1. Écologie

Le premier aspect des algues sargasses sur lequel s'est concentrée la communauté scientifique concerne sa capacité à créer, par leur seule présence, un nouvel écosystème à haute biodiversité (FINE, 1970). En effet, dans l'océan ouvert, habituellement dépourvu d'élément structurant, les radeaux de sargasses forment une matrice propice à l'installation d'une myriade d'autres organismes qui n'auraient pu s'y développer autrement (COSTON-CLEMENTS et al., 1991). Les sargasses agissent donc comme une espèce ingénieur autogénique sur laquelle se construit un système trophique complet ROOKER et al., 2006 (Figure 2.2). En plus de la diversité des organismes végétaux directement fixés aux sargasses (épiphytes) (K. ALLEYNE et al., 2023) de nombreuses espèces de petits organismes animaux comme des crevettes, divers gastéropodes et même des crabes trouvent refuge dans les sargasses (HACKER & MADIN, 1991 ; RUSSELL & DIERSSEN, 2015 ; STONER & GREENING, 1984 ; WEIS, 1968).

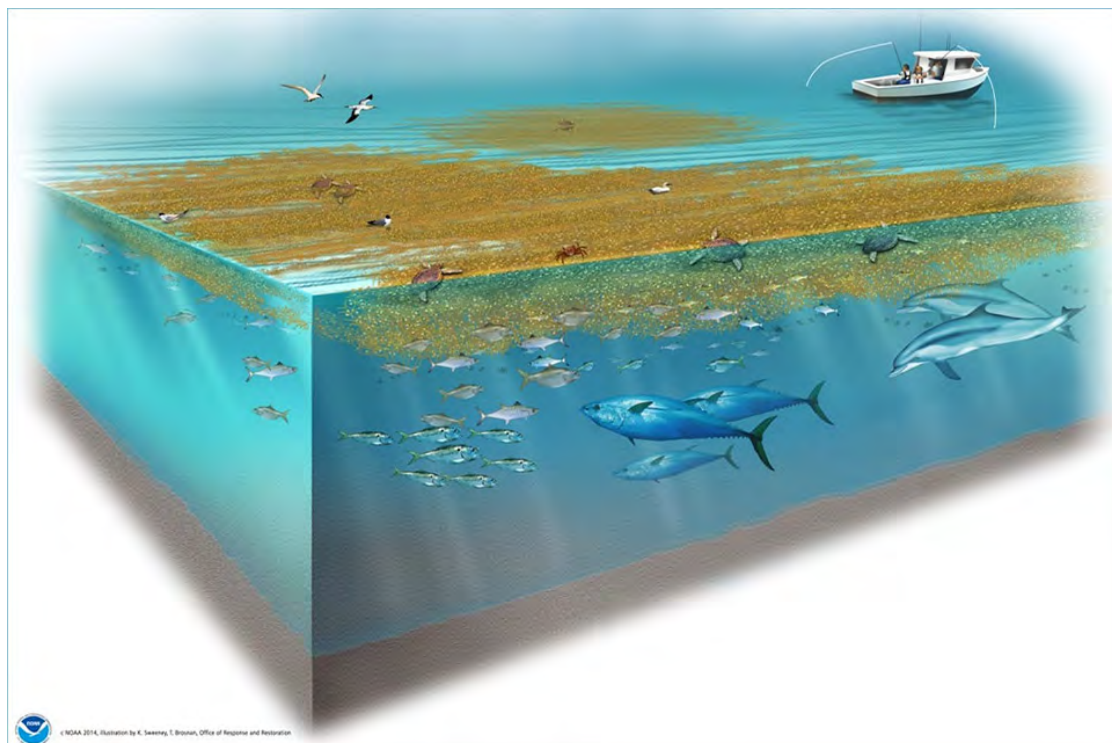


FIGURE 2.2. : L'écosystème sargasses et différents organismes associés (Photo : NOAA (National Oceanic and Atmospheric Administration)).

Les sargasses servent plus particulièrement de zones de nourricerie pour les larves ou les juvéniles de certaines espèces de poissons en offrant un abri qui les protège des prédateurs (W. R. BROOKS et al., 2007 ; CASAZZA & ROSS, 2008 ; WELLS & ROOKER, 2004). Cette abondance de proies attire également de plus gros organismes comme des poissons prédateurs (BORTONE et al., 1977 ; WELLS & ROOKER, 2004), des tortues (WITHERINGTON et al., 2012) et de nombreux oiseaux marins en chasse (MOSER &

2. Revue de littérature – 2.2. Biologie et facteurs de croissance

LEE, 2012; SHAKHOVSKOY, 2023). Ces communautés d'espèces varient assez largement dans le temps (STONER & GREENING, 1984; WELLS & ROOKER, 2004), notamment depuis le changement d'aire de répartition des sargasses ou selon le morphotype majoritaire (MARTIN et al., 2021). Certaines espèces comme *Platynereis dumerilii* (ver), *Latreutes fucorum* (crevette) ou *Portunus sayi* (crabe) sont néanmoins fortement associées à ces algues et sont systématiquement observées au sein de leurs radeaux (HUNN et al., 2022). La thématique de l'écologie des algues sargasses est l'un des rares domaines étudiés sur une longue période sans réelle variation du nombre d'études annuelles. Cette spécificité a pourvu la communauté scientifique d'une série temporelle exceptionnellement longue (HUFFARD et al., 2014).

2.2. Biologie et facteurs de croissance

L'importance des algues sargasses pour la biodiversité a suscité l'intérêt des biologistes qui ont précocement étudié leur croissance et les facteurs qui la déterminent. Plus récemment, ces études se sont avérées primordiales pour calibrer les modèles de croissance et de nouvelles études viennent affiner ces anciennes conclusions après un hiatus de presque 40 ans.



FIGURE 2.3. : Culture des algues sargasses avec un courant artificiel permanent (Photo : MAGAÑA-GALLEGOS et al., 2023a).

Les sargasses comme les autres algues brunes nécessitent du phosphore et de l'azote, de la lumière ainsi qu'une température et une salinité adéquates pour croître de manière optimale. Différents travaux scientifiques ont pu mesurer la limitation de la croissance en fonction de ces différents paramètres environnementaux en mettant

2. Revue de littérature – 2.3. Morphotypes

en place un suivi *in-situ* ou en laboratoire de leur croissance (Figure 2.3). Pour ce qui est de la limitation par le manque d'azote inorganique ou organique (NO_3^- ou NH_4^+), les croissances en laboratoire montrent une accélération dans un milieu enrichi (BAO et al., 2022; LAPOINTE et al., 2021; OVIATT et al., 2019; YAN et al., 2022). Cependant, en milieu naturel, de nombreuses sources d'azote comme sa fixation par les épiphytes (CARPENTER, 1972; CARPENTER & COX, 1974; HANSON, 1977; PHLIPS & ZEMAN, 1990) ou les excréptions des poissons suffiraient à fournir les sargasses en quantité suffisante d'azote (CHANGEUX et al., 2023; LAPOINTE, 1986). Le phosphore serait en revanche plus limitant pour la croissance des algues qui en manqueraient selon leur zone géographique (LAPOINTE, 1986). La salinité et la lumière seraient, elles aussi, des facteurs limitants, mais uniquement pour des valeurs extrêmement basses rarement atteintes dans leur milieu naturel (HANISAK & SAMUEL, 1987). Finalement, c'est la température qui pourrait être la plus contraignante, ses valeurs basses comme élevées empêchant la croissance des sargasses (HANISAK & SAMUEL, 1987; MAGAÑA-GALLEGOS et al., 2023b). Il est à noter que les morphotypes réagissent différemment à ces contraintes environnementales et de récentes études s'attachent à caractériser ces différences (CHANGEUX et al., 2023; MAGAÑA-GALLEGOS et al., 2023a).

2.3. Morphotypes

La première description des différents morphotypes des sargasses a été faite par WINGE, 1923 et raffinée par PARR, 1939. Parmi les six formes qui y sont décrites, seulement trois sont observées communément aujourd'hui (Figure 2.4). On retrouve le morphotype *Sargassum natans VIII*, rare auparavant (J. M. SCHELL et al., 2015), le morphotype *Sargassum natans I* et le morphotype *Sargassum fluitans III*, plus touffu et dense que les précédents. La distinction entre ces morphotypes se fait par analyse morphologique du thalle et des flotteurs. Il est aussi possible de les différencier par des analyses de leur composition chimique (DAVIS et al., 2021; MACHADO et al., 2022; ROSADO-ESPINOSA et al., 2020) ou bien de leur génétique (DIBNER et al., 2022). D'ailleurs, les deux formes de *Sargassum natans* sont si bien différenciées génétiquement qu'il s'agit probablement de deux espèces différentes (DIBNER et al., 2022). Les radeaux comportent le plus souvent les trois morphotypes en leur sein, mais leur abondance relative varie fortement selon le lieu et l'année (GARCÍA-SÁNCHEZ et al., 2020; IPORAC et al., 2023; J. M. SCHELL et al., 2015).

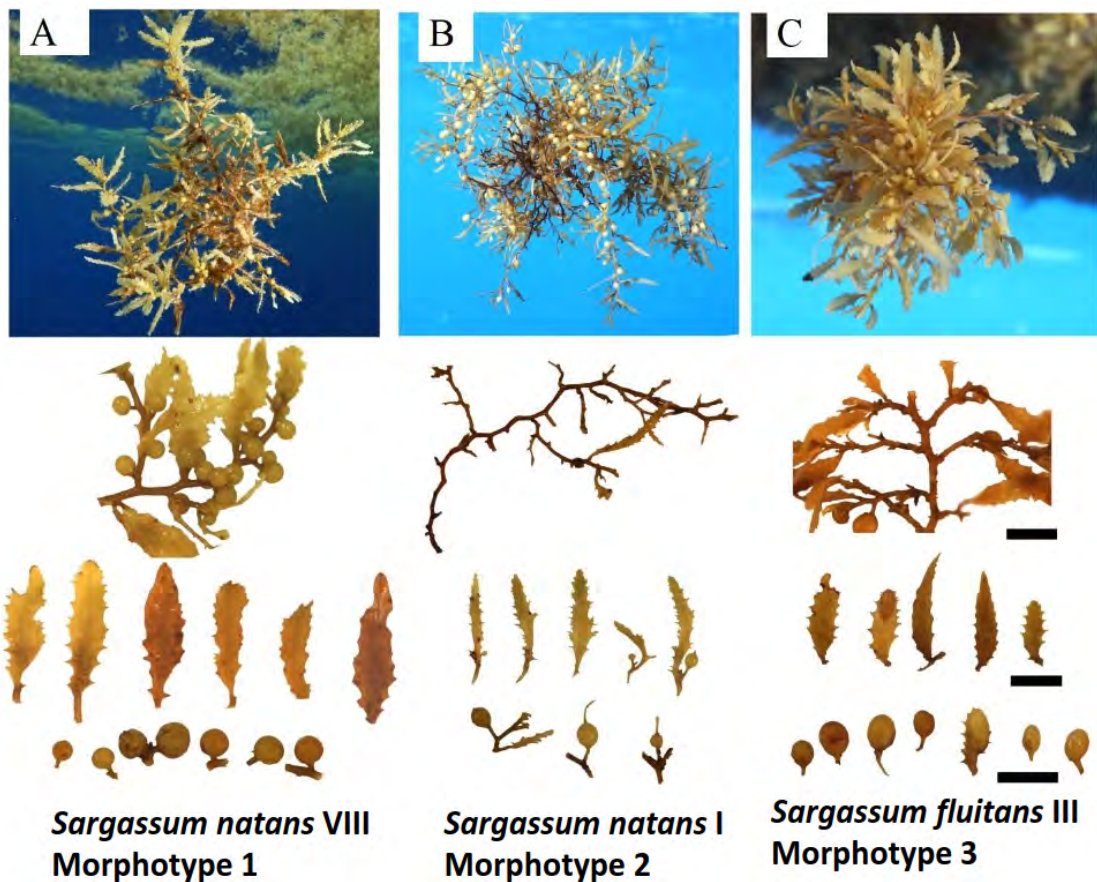


FIGURE 2.4. : Les trois morphotypes majoritaires des sargasses (Photo : Thierry Thibaut, Sandrine Ruitton).

2.4. Échouements et conséquences

Depuis 2011, les échouements massifs sur les côtes ont alerté la communauté scientifique qui s'est rapidement efforcée de caractériser les impacts de ce nouveau phénomène. En effet, en plus des impacts évidents sur le tourisme et l'économie locale (CHÁVEZ et al., 2020), l'accumulation des algues sur les plages ou dans les eaux côtières perturbe l'équilibre écologique (Figure 2.5). Leur surabondance ainsi que leur dégradation entraînent l'eutrophisation des eaux alentours ainsi que l'hypoxie voir l'anoxie (BARTLETT & ELMER, 2021; CABANILLAS-TERÁN et al., 2019; HENDY et al., 2021; RODRÍGUEZ-MARTÍNEZ et al., 2019; SÁNCHEZ et al., 2023; VAN TUSSEN BROEK et al., 2017). Cela entraîne une dégradation du milieu de vie des organismes en présence et une chute de la biomasse et de la biodiversité locale. De nombreux récifs coralliens sont touchés par ces échouements et leur dégradation, déjà induite par le tourisme, s'accélère (ANTONIO-MARTÍNEZ et al., 2020; BANASZAK, 2021; VELÁZQUEZ-OCHOA & ENRÍQUEZ, 2023). Au niveau des plages, ce sont les tortues de mer qui subissent les plus grands dommages par l'ensevelissement de leur lieu de ponte (MAURER et al.,

2. Revue de littérature – 2.5. Fixation du carbone

2022; MAURER et al., 2021; SCHIARITI & SALMON, 2022). Les populations humaines sont, elles aussi, directement touchées par l'émission de gaz toxiques due au pourrissement des algues ainsi que mise en danger par les bactéries associées aux algues sargasses ou par la contamination des ressources alimentaires marines (MERLE et al., 2021; MICHOTÉY et al., 2020; MODESTIN et al., 2022; RESIERE et al., 2021; THEIRLYNCK et al., 2023).

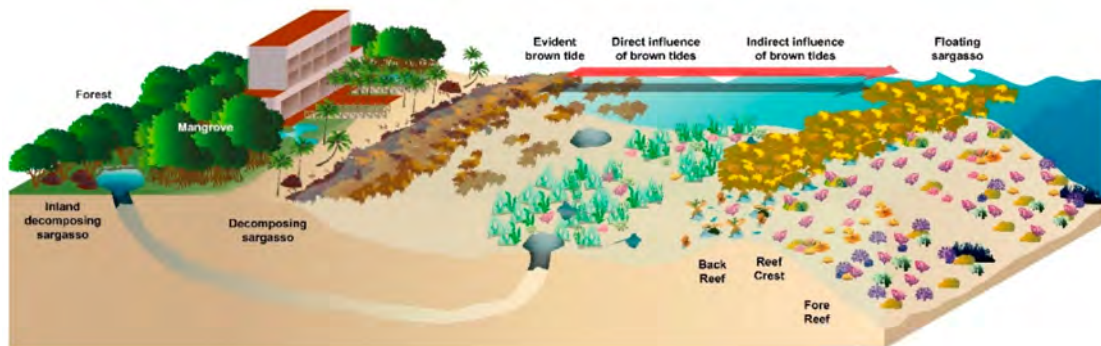


FIGURE 2.5. : L'impact des échouements sur l'écosystème côtier au Mexique (schéma : CHÁVEZ et al., 2020).

2.5. Fixation du carbone

À l'opposé de ses impacts néfastes sur les écosystèmes côtiers, les sargasses restent globalement bénéfiques à la biodiversité en plein océan. Leur accroissement soudain a également augmenté la quantité de carbone retenue dans leurs tissus. Auparavant anecdotique à l'échelle globale, leur capacité à fixer le carbone minore désormais l'augmentation du CO_2 atmosphérique dans un contexte de changement climatique (GOUVÈA et al., 2020). Leur calcification serait un vecteur important d'export du carbone vers les couches sédimentaires (PARAGUAY-DELGADO et al., 2020; SALTER et al., 2021), enrichissant par la même occasion les écosystèmes de l'océan profond (BAKER et al., 2018). Certains y voient une mise en œuvre naturelle des projets de "boisement" des océans pour limiter le carbone atmosphérique (BACH et al., 2021; RACINE et al., 2021). Cependant, la fraction effective de carbone durablement fixée reste faible et les études pointent sur la nécessité d'une gestion humaine de la fraction restante (GOUVÈA et al., 2020; ZHAO et al., 2023).

2.6. Composition chimique

La nécessité de valorisation des algues sargasses a suscité de nombreuses études d'évaluation de leur composition chimique, notamment en métaux et métalloïdes. Ces dernières ont montré l'intérêt potentiel du contenu des sargasses en nutriments exploitables (ALZATE-GAVIRIA et al., 2021; OYESIKU & EGUNYOMI, 2014; POWERS et al., 2019). Cependant, leur grande majorité alerte sur les taux d'arsenic inorganique

inhabituellement élevés (10^6 la concentration de l'océan)¹ ainsi que la contamination en pétrole (BURNS & TEAL, 1973), en mercure (MILLEEDGE et al., 2020) ou en plomb (TEJADA TEJADA et al., 2021). Similairement à leur capacité de fixation du carbone, les sargasses pourraient aussi être un agent de bioremédiation des polluants émis par les sociétés humaines (SALDARRIAGA-HERNANDEZ et al., 2020a; SALDARRIAGA-HERNANDEZ et al., 2020b).

2.7. Valorisation

Les dommages infligés aux écosystèmes et au tourisme dans les pays touchés par les échouements sont si importants qu'il leur est nécessaire à la fois de financer le nettoyage des plages et de compenser les coûts économiques par de nouveaux revenus. Il est donc venu naturellement l'idée de valoriser les sargasses en créant des filières de traitement pour les transformer en produits commercialisables. Plusieurs pistes ont été poursuivies, notamment la production de nourriture, de fertilisant, de médicaments, de biocarburant ou de plastique (Figure 2.6).

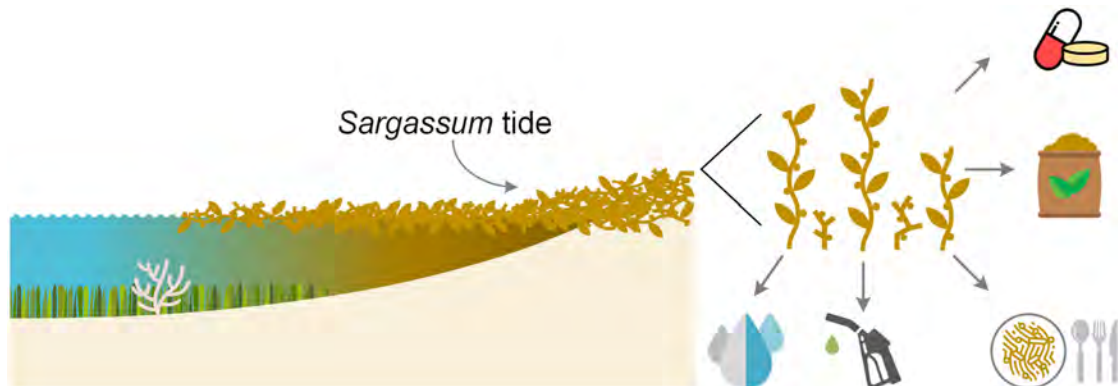


FIGURE 2.6. : Les voies de valorisation des sargasses (schéma : AMADOR-CASTRO et al., 2021).

Le tableau 2.1 résume les différents travaux qui explorent les voies possibles de valorisation des sargasses. Malheureusement, la valorisation de ces algues est entravée de manière plus ou moins problématique par différents facteurs. En premier lieu, la concentration de leurs tissus en éléments toxiques comme les métaux lourds (Arsenic) exclut leur usage alimentaire, pharmaceutique ou agricole sans une décontamination préalable (MILLEEDGE & HARVEY, 2016). Aussi, même si la production de biocarburant reste une bonne option, la discontinuité des échouements décourage l'investissement nécessaire à la mise en place des filières de production (OXENFORD et al., 2021). À cela s'ajoute les infrastructures de gestion (ramassage, stockage) des algues qui restent à

¹K. S. T. ALLEYNE et al., 2023b; CIPOLLONI et al., 2022; DASSIÉ et al., 2021; DEVAULT et al., 2021a; DEVAULT et al., 2021b; GOBERT et al., 2022; D. L. JOHNSON et BRAMAN, 1975; LIRANZO-GÓMEZ et al., 2023; ORTEGA-FLORES et al., 2023; RODRÍGUEZ-MARTÍNEZ et al., 2020; VÁZQUEZ-DELFIN et al., 2021

2. Revue de littérature – 2.8. Détection des sargasses

bâtir (RODRÍGUEZ-MARTÍNEZ et al., 2023). Plus marginalement, les algues restent un refuge de biodiversité et la question de la préservation de certaines espèces se pose lors de la collecte des algues (K. S. T. ALLEYNE et al., 2023c; IPORAC et al., 2023).

Produit valorisé	Études
Plastique	CASTAÑEDA-SERNA et al., 2021
Nourriture	MOHAMMED et al., 2020 CORDILLO SIERRA et al., 2022
Carbone actif	FRANCOEUR et al., 2021 RANGUIN et al., 2021
Asphalte et béton	SALAZAR-CRUZ et al., 2021 ROSSIGNOLO et al., 2022
Fertilisant	CHÁVEZ-GUERRERO et al., 2021 T. M. THOMPSON et al., 2020; T. THOMPSON et al., 2020 MARX et al., 2021 TRENCH et al., 2022 HERNÁNDEZ-NAVARRO et al., 2023
Bio-carburant	LÓPEZ-SOSA et al., 2020 ESCOBAR et al., 2017 APARICIO et al., 2021 T. M. THOMPSON et al., 2021a; T. M. THOMPSON et al., 2021b LÓPEZ-AGUILAR et al., 2021 AZCORRA-MAY et al., 2022 CHIKANI-CABRERA et al., 2022 RIVERA-HERNÁNDEZ et al., 2022 TOBÍO-PÉREZ et al., 2022 SALGADO-HERNÁNDEZ et al., 2023

TABLEAU 2.1. : Études scientifiques pour la valorisation économique des sargasses.

2.8. Détection des sargasses

L'apparition subite des énormes quantités d'algues a également fait apparaître la nécessité d'un suivi des masses de sargasses à court terme dans un premier temps. Puis comme le problème perdurait année après année, il s'est avéré nécessaire de pérenniser et d'automatiser cette surveillance. Le traitement d'images de télédétection est donc utilisé pour reporter et cartographier la présence des sargasses à la fois proche des côtes et à plus large échelle sur l'océan Atlantique entier.

Zones côtières et littorales

Comme les échouements surviennent sans prévenir sur une très vaste zone qui englobe plusieurs dizaines de pays, le recensement des arrivées d'algues s'est d'abord

2. Revue de littérature – 2.8. Détection des sargasses

fait sans effort de standardisation. Ce n'est que récemment que des travaux synthétisant ces archives éparses ont été publiés (FIDAI et al., 2020; URIBE-MARTÍNEZ et al., 2022). Afin de poursuivre ces efforts de standardisation, des études ont développé la détection automatique des sargasses en utilisant des images issues de caméras côtières ou de science participative (ARELLANO-VERDEJO & LAZCANO-HERNÁNDEZ, 2021; ARELLANO-VERDEJO et al., 2022; VALERIA et al., 2021). D'autres études utilisent directement des images satellites pour les détecter (LI et al., 2023; RODRÍGUEZ-MARTÍNEZ et al., 2022), notamment pour étudier leur dégradation et la contamination de l'eau proche du rivage (LEÓN-PÉREZ et al., 2023; RODRÍGUEZ-MUÑOZ et al., 2021).

Océan du large

La biomasse échouée sur les plages ne représente qu'une petite fraction de celle présente en mer (quelques pourcents) et on ne peut donc se passer d'un suivi hauturier des sargasses pour en obtenir une cartographie exhaustive. C'est donc logiquement la thématique de la télédétection des algues sargasses qui a connu le plus grand essor depuis les quinze dernières années. La télédétection des sargasses n'était encore que balbutiante au début des années 2000 avec les travaux isolés de Jim Gower en mer des sargasses qui posaient les jalons de l'actuelle méthodologie en utilisant l'outil satellite MERIS (Medium Resolution Imaging Spectrometer) et l'index radiométrique MCI (Maximum Chlorophyl Index) (J. GOWER et al., 2006; J. GOWER & KING, 2008) (voir figure 2.7). C'est d'ailleurs par cette technique que l'on a pu faire état du changement de distribution spatiale des sargasses pour la première fois (J. GOWER et al., 2013).

2. Revue de littérature – 2.8. Détection des sargasses

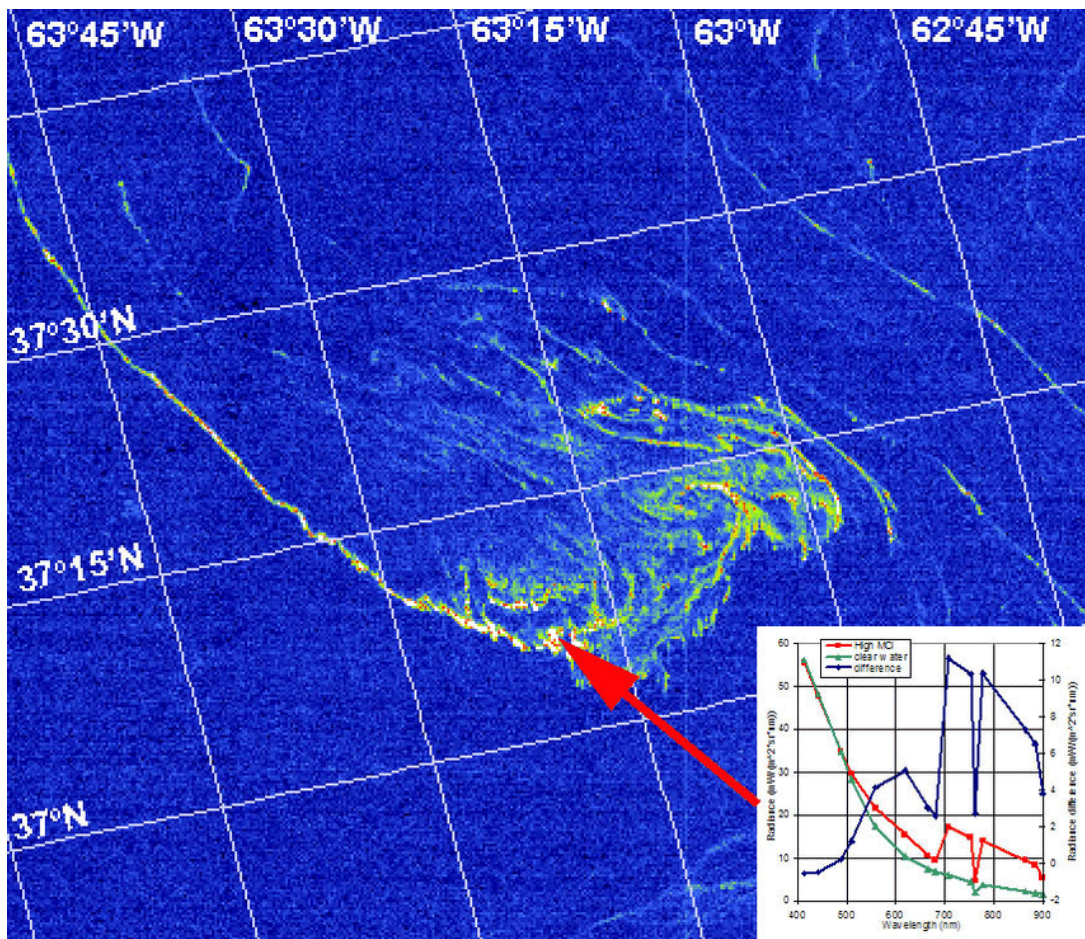


FIGURE 2.7. : Agrégat de sargasses vu par le satellite MERIS (image : J. GOWER et KING, 2008)

Avec la fin de la mission MERIS en 2012, il a fallu se tourner vers un autre outil d'observation et c'est MODIS (Moderate-Resolution Imaging Spectroradiometer) qui fut utilisé, associé à un nouvel index radiométrique spécialement conçu pour la détection des sargasses : AFAI (Alternative Floating Algae Index) (M. WANG & HU, 2016 ; M. WANG et al., 2019a ; M. WANG et al., 2018). Par la suite, les lancements des missions Sentinel-2 et Sentinel-3 motivèrent également des approches à plus haute résolution spatiale que MODIS, mais avec une moins bonne résolution temporelle (J. GOWER & KING, 2020 ; ODY et al., 2019 ; M. WANG & HU, 2020). Cette opposition entre la finesse des pixels et la fréquence d'échantillonnage est encore plus marquée avec les dernières études utilisant de la très haute résolution (HERNÁNDEZ et al., 2022 ; ZHANG et al., 2022). À l'inverse, il est également possible d'utiliser des satellites géostationnaires à une résolution spectrale et spatiale médiocres, mais à une fréquence d'échantillonnage inégalée (MINGHELLI et al., 2021 ; SHIN et al., 2021). Un récapitulatif des capteurs les plus utilisés pour l'observation des sargasses et leurs contraintes spatiale et temporelle associées est présenté dans le tableau 2.2.

2. Revue de littérature – 2.8. Détection des sargasses

Capteur	Résolution	Fréquence	Indice	Satellites	Mise en service (arrêt)
MODIS	1 km	1 jour	AFAI	2	1999 (2023), 2002
VIIRS	750 m	1 jour	AFAI	3	2011, 2017, 2021
MERIS	1.2 km	1 jour	MCI	1	2002 (2012)
MSI	20 m	10 jours	FAI	2	2015, 2017
OLCI	300 m	3 jours	MCI	2	2016, 2018
OLI	30 m	8 jours	NDVI	1	2013
ABI	500 m	15 min	NDVI	1	2016

TABLEAU 2.2. : Caractéristiques des capteurs principaux utilisés pour la détection des sargasses (LAZCANO-HERNANDEZ et al., 2023).

Une fois fait ce tour d'horizon des différents outils permettant d'observer les sargasses à distance, différentes pistes d'amélioration du traitement des images ont été poursuivies. Les fausses détections induites par d'autres objets que les sargasses comme les nuages, leur ombre ou le reflet du soleil dans l'eau gênent la cartographie des algues. Afin d'apporter une solution à ce problème, l'usage de l'apprentissage automatisé se généralise avec des méthodes ensemblistes (Random Forest, Boosting) ou des réseaux de neurones (ARELLANO-VERDEJO et al., 2019; CUEVAS et al., 2018; LAVAL et al., 2023; PODLEJSKI et al., 2022; M. WANG & HU, 2021; Y. XIAO et al., 2021). Un autre point d'amélioration concerne la synergie entre les différents capteurs. Afin de combler les lacunes des différents satellites et d'étendre leurs séries temporelles, il est possible de fusionner leurs résultats en une seule cartographie (ALMEIDA et al., 2020; DESCLOITRES et al., 2021; HU et al., 2023; M. WANG & HU, 2018). Ces outils de télédétection sont également déclinés afin de nourrir des bulletins de prévision des échouements et d'alerter la gestion des plages en intégrant des données de courantologie par exemple (de la BARREDA-BAUTISTA et al., 2023; HU et al., 2016; TRINANES et al., 2021; X. WANG et al., 2022). Enfin, quelques études contournent des problèmes inhérents à la télédétection comme la détection sous les nuages (AN et al., 2022; LAVAL et al., 2023; QI et al., 2022) ou sous la surface de l'eau (SCHAMBERGER et al., 2022). De la même manière que pour les algues sargasses d'Atlantique, le problème posé par les algues *Sargassum horneri* en mer Jaune est également suivi par télédétection (QIU et al., 2018; Z. WANG et al., 2023; XING et al., 2017), avec une nuance toutefois : les marées d'algues sargasses de mer Jaune se sont mêlées à des algues vertes (*Ulva prolifera*) et la distinction par satellite reste ardue (QI & HU, 2021; SUN et al., 2021; J. XIAO et al., 2020a; J. XIAO et al., 2020b; Y. XIAO et al., 2021). Les points d'insuffisance des méthodes de télédétection qui se démarquaient au début de la présente thèse, en 2020, concernaient notamment le manque de jeux de données en libre accès sur les sargasses, maintenant mieux pourvu avec les produits de l'université de Floride <https://optics.marine.usf.edu>, de Copernicus <https://marine.copernicus.eu/> ou du centre de données AERIS (BERLINE & DESCLOITRES, 2021). Également, la gestion des fausses détections de sargasses, dues aux nuages, aux reflets du soleil ou à la proximité des côtes par exemple, était et reste un point sensible de l'observation des sargasses par satellite et l'on manque de méthodologies claires pour résoudre ces erreurs.

2.9. Études à large échelle du transport et de la croissance des sargasses

L'intérêt des physiciens et modélisateurs pour les sargasses est resté assez limité avant l'apparition des échouements massifs et le besoin de bulletin prévisionnel qui s'ensuivit. Quelques études antérieures à 2010 ont seulement porté sur la flottaison des sargasses et leur submersion temporaire ou leur sédimentation définitive (D. L. JOHNSON & RICHARDSON, 1977; WOODCOCK, 1950, 1993). Suite aux épisodes d'échouement depuis 2011, deux questions de recherche prégnantes se sont posées à la communauté scientifique. Tout d'abord, comment anticiper et prévoir le développement des sargasses et leur dérive jusqu'aux côtes afin d'alerter au mieux les autorités en présence et les programmes de nettoyage des plages. Ensuite, plus fondamentalement, comment expliquer le bouleversement qu'ont connu la distribution des sargasses et sa grande variabilité inter-annuelle. Ces deux pistes de recherche restent néanmoins complémentaires et la plupart des nouvelles connaissances sur les sargasses viennent éclaircir ces deux questionnements.

Prévision à court terme : étude du transport

Une première étape de la prévision des échouements de sargasses a consisté à développer des bulletins à court terme de leur arrivée sur les plages en se basant sur des observations satellites fréquentes et des modèles de dérive simples basés sur les courants de surface (D. JOHNSON et al., 2020; MARÉCHAL et al., 2017a; PUTMAN et al., 2023; WEBSTER, 2013). Si ces dispositifs fonctionnent bien sur quelques jours, la précision du modèle de dérive devient rapidement essentielle à la qualité des prévisions à plus long terme. En particulier, l'effet exact du vent sur les sargasses s'est rapidement avéré être un paramètre clé du modèle de dérive. Difficilement mesurable sur le terrain, de nombreuses études l'ont testé et calibré au mieux de diverses manières. Dans un premier temps, par des analyses de sensibilité entre les résultats de modèle et des images satellites à large échelle (BERLINE et al., 2020; KWON et al., 2019). Ensuite par la comparaison avec des objets dérivants similaires bien connus (les bouées dérivantes à ancre flottante) (PUTMAN et al., 2018; PUTMAN et al., 2020; VAN SEBILLE et al., 2021) ou par la création de bouées suivies par GPS (Global positioning System) imitant directement des algues (BERON-VERA, 2021; MIRON et al., 2020). Un autre paramètre de la dérive exploré par la littérature concerne l'inertie des radeaux de sargasses. Estimé directement dans les images satellites ou pris en compte dans des modèles mécanistes complexes, il reste peu utilisé dans les modèles de prévision opérationnels (ANDRADE-CANTO et al., 2022; BERON-VERA & MIRON, 2020a; M. T. BROOKS et al., 2019). Le principal manque faisant défaut à l'étude de la dérive des sargasses est sans conteste l'absence de données de mesure directe pour enfin en inférer un modèle précis. L'imagerie satellite fournit pourtant de plus en plus de cas d'observation des sargasses à différentes résolutions et il paraît envisageable d'extraire des vitesses de sargasses depuis ces images. Cela permettrait de mieux discuter de ce paramètre effet

2. Revue de littérature – 2.9. Études à large échelle du transport et de la croissance des sargasses

du vent, encore difficilement appréhendé par la littérature, ainsi que de l'inertie des radeaux.

Variabilité interannuelle : moteur de la croissance et effet climatique

Même le meilleur modèle de dérive ne peut se passer de la prise en compte de la croissance lorsque l'échelle temporelle excède quelques mois (M. T. BROOKS et al., 2018). Or, afin de prévoir et étudier la variation interannuelle de la distribution des sargasses, il a fallu construire des modèles à plus long terme. Aussi, certaines études rendent compte du développement saisonnier des sargasses en détaillant les mécanismes de la croissance en fonction de leur environnement (M. T. BROOKS et al., 2018; JOUANNO et al., 2020; MARSH et al., 2021). La définition et la calibration de ces modèles éclairent les variables environnementales et processus déterminant la croissance des algues : nutriments (phosphore et azote), salinité, température, irradiance, fragmentation, mortalité. Ces résultats recoupent ceux pourvus par des approches statistiques qui mettent en relation les densités de sargasses observées avec des caractéristiques large-échelle de l'océan, ainsi qu'avec les téléconnexions climatiques, ou modes de variabilité climatiques (SANCHEZ-RUBIO et al., 2018; SKLIRIS et al., 2022b). Avec ces nouvelles connaissances sur les mécanismes de la dérive et les facteurs limitants la croissance des sargasses, d'autres travaux tentent d'expliquer leur implantation en Atlantique tropical et leur cycle annuel variable. Ainsi, plusieurs hypothèses sont avancées pour expliquer leur accumulation phénoménale de biomasses : l'enrichissement en nutriment des eaux de surface par les grands fleuves, en particulier l'Amazone, les remontées d'eau profonde par les upwellings, l'augmentation de la température de surface et les dépôts des vents sahariens (DJAKOURÉ et al., 2017a; JOUANNO et al., 2021b; OVIATT et al., 2019). Plus récemment, le rôle des cyclones tropicaux sur la régulation des algues au niveau saisonnier a été mis en évidence (PUTMAN & HU, 2022; SOSA-GUTIERREZ et al., 2022).

Si quelques zones d'ombre subsistent sur l'invasion des sargasses en Atlantique tropical, c'est surtout leur variabilité interannuelle qui reste mal expliquée. S'agissant d'un enjeu important pour notre capacité à anticiper le développement des biomasses de sargasses et à faire au mieux face à leurs échouements, il est essentiel de mieux étudier cette variabilité et de la relier aux facteurs déterminants de leur croissance et de leur transport.

3. Filtrage des détections MODIS avec des attributs de contexte

Le premier pas vers la compréhension de la variabilité de la distribution et de l'abondance des algues sargasses consiste naturellement à observer et quantifier leur distribution spatiale et temporelle. L'obtention de ces informations est aussi une condition *sine qua non* à la construction de modèles de transport et de croissance basés sur des observations. Malencontreusement, l'ampleur spatiale de la nouvelle aire de répartition des sargasses, qui s'étend du Golfe de Guinée jusqu'au Golfe du Mexique, entrave toute tentative d'échantillonnage représentatif sur le terrain. De ce fait, seules les observations à distance, et plus précisément par télédétection satellite, permettent de couvrir suffisamment régulièrement cette immense aire de répartition.

Il existe plusieurs méthodes pour l'observation à distance des algues sargasses. Elles s'équivalent ou se complémentent en employant divers capteurs optiques embarqués sur un ou plusieurs satellites. Leur différence notable concerne principalement leur résolution spatiale et temporelle, deux paramètres s'excluant l'un l'autre et pourtant tous les deux essentiels quant à l'observation de cette matrice d'algues aux entrelacements aussi complexes que ductiles et mouvants. Nonobstant le foisonnement d'études pour détecter les sargasses, aucune ne pourvoyait de jeu de données en libre accès, au mieux seulement une visualisation graphique de ses détections [SAWS](#).

Ce manque de données a motivé la mise en œuvre d'une chaîne de traitement de télédétection dans le cadre du projet FORESEA (FOREcasting seasonal Sargassum Events in the Atlantic) dans lequel s'inscrit la présente thèse. Cette chaîne de production, nommée SAREDA (SArgassum Evolving Distribution in the Atlantic), permet l'extraction de la présence des algues sargasses ainsi que leur quantification sur l'Océan Atlantique Nord Tropical entier. En utilisant le capteur MODIS (Moderate-Resolution Imaging Spectroradiometer) embarqué sur les satellites Aqua et Terra et en combinaison avec l'indice radiométrique AFAI (Alternative Floating Algae Index), elle produit quotidiennement et en quasi-temps réel ($j+3$) des cartes à 1 km de résolution attestant de la distribution globale des sargasses.

Les résultats provenant de cette chaîne de traitement constituent une manne providentielle pour l'étude et la modélisation de la variabilité des algues sargasses. Cependant, la validation de ces observations demeure un point crucial afin de dégager des conclusions sur la dynamique de transport et de développement de ces algues. Dans le cas présent, comme pour tout travail de télédétection, des phénomènes variés peuvent comporter des signatures radiométriques analogues à celle de l'objet d'étude et introduire des erreurs ou faux positifs dans les résultats. En particulier, la forte réflectance des algues sargasses dans le proche infrarouge (NIR, Near-InfraRed) ici

3. Filtrage des détections MODIS avec des attributs de contexte

exploitée pour les distinguer de l'eau de mer, est partagée avec divers autres objets présents dans l'Océan Atlantique Nord Tropical. Parmi ceux-ci, on retrouve notamment les nuages, les ombres portées par ces derniers, le reflet du soleil dans l'eau, la turbidité de l'eau, la contamination du signal par la végétation côtière ainsi que d'autres types d'algues comme les *Trichodesmium* ou la chlorophylle-a en suspension. Cet ensemble de phénomènes interférant avec la constitution d'un jeu de données fidèle à la réalité, les résultats de SAREDA comportaient initialement une part importante de détections erronées. Une évaluation manuelle dans les images a démontré que ces erreurs représentaient jusqu'à deux tiers de la quantité de biomasse estimée. Il était donc capital d'apporter une solution à cette contamination inopportunne des résultats en discriminant ces fausses détections des véritables sargasses.

Le premier chapitre de cette thèse se consacre donc à l'élaboration d'une méthodologie pour filtrer les faux positifs du jeu de données SAREDA. À la différence de la plupart des études qui poussent plus loin l'analyse radiométrique pour distinguer les phénomènes détectés, par exemple en utilisant des données multispectrales, je propose ici d'utiliser une nouvelle source d'information : le contexte spatial des détections. En effet, l'analyse par un expert des images résultantes de SAREDA (AFAI) permet en grande partie de trier les vraies détections des fausses en s'appuyant uniquement sur une inspection visuelle. Il s'agit donc de reproduire ce tri par une méthode de filtrage numérique reposant sur des attributs contextuels explicites. Ces derniers nourrissent un algorithme d'apprentissage automatisé préalablement entraîné pour discriminer les fausses détections.

L'article suivant détaille les étapes de cette méthodologie : la création d'un jeu de données labellisées manuellement, le choix d'un algorithme de classification ainsi que sa calibration, le développement de nouveaux attributs contextuels, la sélection du meilleur sous-ensemble d'attributs pour la classification et l'analyse du jeu de données filtrées résultant.

3. Filtrage des détections MODIS avec des attributs de contexte

Filtering out false *Sargassum* detections using context features

Witold Podlejski ^{1,2,*}, Jacques Descloitres ³, Cristèle Chevalier ², Audrey Minghelli ⁴,
Christophe Lett ¹ and Léo Berline ²

¹Marbec, Université de Montpellier, CNRS, Ifremer, IRD, Sète, France

²Aix Marseille Univ, Université de Toulon, CNRS, IRD, MIO, Marseille, France

³University of Lille, CNRS, CNES, UAR 2877 - AERIS/ICARE Data and Services Center,
F-59000 Lille, France

⁴Université de Toulon, Aix Marseille Univ, SeaTech, CNRS, LIS laboratory UMR 7020,
83041 Toulon, France

Publié : PODLEJSKI, W., DESCLOITRES, J., CHEVALIER, C., MINGHELLI, A., LETT, C., & BERLINE, L. (2022). Filtering out false Sargassum detections using context features. Frontiers in Marine Science, 9. <https://doi.org/10.3389/fmars.2022.960939>

3.1. Abstract

Since 2011, the distribution extent of pelagic *Sargassum* algae has substantially increased and now covers the whole Tropical North Atlantic Ocean, with significant inter-annual variability. The ocean colour imagery has been used as the only way to monitor regularly such a vast area. However, the detection is hampered by cloud masking, sunglint, coastal contamination and other phenomena. All together, they lead to false detections that can hardly be discriminated by classic radiometric analysis, but may be overcome by considering the shape and the context of the detections. Here, we built a machine learning model base exclusively on spatial features to filter out false detections after the detection process. Moderate-Resolution Imaging Spectroradiometer (MODIS, 1 km) data from Aqua and Terra satellites were used to generate daily map of Alternative Floating Algae Index (AFAI). Based on this radiometric index, *Sargassum* presence in the Tropical Atlantic North Ocean was inferred. For every *Sargassum* aggregations, five contextual indices were extracted (number of neighbours, surface of neighbours, temporal persistence, distance to the coast and aggregation texture) then used by a random forest binary classifier. Contextual features at large-scale were most important in the classifier. Trained with a multi-annual (2016-2020) learning set, the model performs the filtering of daily false detections with an accuracy of ~90%. This leads to a reduction of detected *Sargassum* pixels of ~50% over the domain. The method provides reliable data while preserving high spatial and temporal resolutions (1 km, daily). The resulting distribution is consistent with the literature for seasonal and inter-annual fluctuations, with maximum coverage in 2018 and minimum in 2016. This dataset will be useful for understanding the drivers of *Sargassum* dynamics at fine and large scale and validate future models. The methodology used here demonstrates the usefulness of contextual features for complementing classical remote sensing approaches. Our model could easily be adapted to other datasets containing erroneous detections.

Keywords : *Sargassum* algae; Remote sensing; Random Forest; Contextual analysis; Tropical North Atlantic; Fractional coverage ; Time series.

3.2. Introduction

For a decade, *Sargassum* stranding events have become a global concern for many countries bordering the Tropical North Atlantic Ocean. In particular, many coastlines are smeared out with *Sargassum* algae almost every year with significant impacts on the fishing industry and the tourism economy (CHÁVEZ et al., 2020). While offshore *Sargassum* aggregations are hotspots of biodiversity and provide shelter to various species (FINE, 1970; MARTIN et al., 2021), biomass accumulation on coastal waters and beaches causes ecological, economical and sanitary issues (MERLE et al., 2021; RESIERE et al., 2018). Those nuisances highlight the need of scientific research to understand and anticipate the development of *Sargassum* algae. To date, there is still no consensus about how the outbreak of *Sargassum* expansion started, nor about how

3. Filtrage des détections MODIS avec des attributs de contexte – 3.2. Introduction

to forecast accurately the annual *Sargassum* biomass growth. It was initially assumed that the increasing rivers nutrient discharge was the cause of the triggering event of 2011 (OVIATT et al., 2019; M. WANG et al., 2019b). Considering the mismatch between *Sargassum* distribution and river plumes, that hypothesis was recently revised (JOUANNO et al., 2021b). Another recent hypothesis involves an anomalous meteorological event in 2010 that may have inseminated the new *Sargassum* area (JOHNS et al., 2020). Therefore, in order to build and discuss hypotheses to explain the *Sargassum* dynamics, reliable data over a long time period are still required.

Remote sensing is a useful tool to monitor large-scale *Sargassum* distribution (ARELLANO-VERDEJO et al., 2019; CHEN et al., 2019; CUEVAS et al., 2018; J. F. GOWER & KING, 2011; ODY et al., 2019; QIU et al., 2018; SHIN et al., 2021; M. WANG & HU, 2016; XING et al., 2017) as *in-situ* approaches are costly and do not allow sufficient spatial coverage (ODY et al., 2019). *Sargassum* can be detected by satellite sensors due to its high reflectance in Near Infra-red compared to clear water. Several *Sargassum* indices using optical properties have been proposed to enhance that specific *Sargassum* signal (CUEVAS et al., 2018; DIERSSEN et al., 2015; J. GOWER et al., 2006; HU et al., 2015). Presently, Moderate-Resolution Imaging Spectroradiometer (MODIS) on board NASA's Terra and Aqua satellites, Visible Infrared Imaging Radiometer Suite (VIIRS) on board NOAA/NASA's Suomi-NPP, Ocean and Land Colour Instrument (OLCI) on board Copernicus's Sentinel-3 and MultiSpectral Instrument (MSI) on board Copernicus's Sentinel-2, are satellite sensors with adequate spectral bands for monitoring *Sargassum* algae (ODY et al., 2019).

However, *Sargassum* detection and quantification by remote sensing face numerous challenges : scarcity of the aggregations, cloud coverage, sun glint, signal contamination in the coastal areas, and large-scale fluctuations of the surrounding water reflectance. Moreover, the detection robustness is limited by the spatial resolution and revisit period of each sensor. MSI and OLCI have good spatial (20 m and 300 m respectively) and spectral resolution (J. GOWER & KING, 2020; M. WANG & HU, 2020), but their greater revisit period (5 and 2 days respectively) makes them less efficient for mapping the Tropical Atlantic considering the high cloud coverage. While MODIS and VIIRS miss some fine *Sargassum* signal because of their moderate spatial resolution (1000 m and 750 m), they both have a 1-day revisit period that provides robust time series. A processing chain was developed and described in details for MODIS and VIIRS satellite sensors (M. WANG & HU, 2016, 2018).

Regarding data availability, MODIS *Sargassum* products from M. WANG et al., 2019b are restricted to 0.5° resolution, monthly. On the SAWS website (<https://optics.marine.usf.edu/projects/saws.html>), daily Alternative Floating Algae Index (AFAI) *Sargassum* maps at native resolution are shown as images only, and restricted to the main distribution area. Consequently, there is currently no data source that combines high-frequency observations and high spatial resolution over the extended *Sargassum* distribution area (from 15°S to 50°N and from 100°W to 15°E).

Thus, in order to exploit the full potential of MODIS data and enhance further modelling use, a MODIS 1 km resolution processing chain was developed using the AFAI presented in M. WANG et al., 2016. The results showed a lot of detection er-

rors that are not mentioned in M. WANG et HU, 2016 and are likely removed by an unspecified process in the SAWS website. Those false detections are due to different phenomena, primarily by residual clouds, cloud shadows, sunglint and turbidity. As those phenomena have a spectral signature and thus AFAI similar to *Sargassum*, they produce false detections. We thus focused here on the development of an original post-processing method to filter *Sargassum* detection over the whole Tropical North Atlantic. Several machine learning models already exist for detecting *Sargassum* algae using radiometric information extensively (ARELLANO-VERDEJO et al., 2019; CUEVAS et al., 2018; QIU et al., 2018; SHIN et al., 2021). By contrast, we demonstrate here the benefit of spatial information to filter out detections as post-processing. While spatial properties of aggregations at local scale are occasionally taken into account (CHEN et al., 2019; QIU et al., 2018; M. WANG & HU, 2020) or used implicitly in neural network models (ARELLANO-VERDEJO et al., 2019; QIU et al., 2018), large-scale contextual features are still untapped. Taking the detections extracted by the remote sensing approach, our method use a random forest algorithm applied to the large-scale spatial properties for classifying true and false *Sargassum* detections. This study describes the processing scheme for filtering the false detections, the spatial features used, the learning and testing processes, and the application of the method to the MODIS time series from 2016 to 2020. Finally, the resulting filtered dataset and its variability are briefly analysed and discussed.

3.3. Materials and Methods

3.3.1. Approach overview

The study was based on Fractional Coverage (FC) products generated using a MODIS full resolution processing chain called SAREDA (*Sargassum* Evolving Distributions in the Atlantic, see Section 3.3.2, DESCLOITRES et al., 2021). It retrieved *Sargassum* detected pixels from the MODIS 1 km band and mapped them in 1 km equirectangular grid. Among these detections distributed in the whole North Atlantic Ocean, about half were likely false detections, based on visual inspection. These errors are not only restricted to the extreme parts of the Tropical North Atlantic Ocean and are mixed up with the valid detections in the new *Sargassum* area. Consequently, this issue cannot be solved using only local masks or filters. Hence, we need a global approach to filter out the data from all false detections, whatever their location.

Those false detections were caused by various phenomena (see Section 3.3.2) and can hardly be discriminated using only radiometric features (QIU et al., 2018). As a complement to FC (proportional to AFAI), we focused on shape and context characteristics of aggregations. More specifically, i) the shape of local groups of pixels, as *Sargassum* algae aggregations tend to have typical elongated shape; ii) the surrounding aggregates, as the algae are usually grouped together in clusters of aggregations close to one another; iii) the geographic location, as *Sargassum* are more likely to be present in known areas; iv) the temporal persistence, as false detections caused by

3. Filtrage des détections MODIS avec des attributs de contexte – 3.3. Materials and Methods

clouds and sun glint do not last in time while *Sargassum* true detections do. To represent those characteristics, we introduced *ad hoc* features characterising the shape of *Sargassum* aggregations and their surrounding context.

Then, using a supervised classification approach, the aggregations were classified into two classes : true or false *Sargassum* detections. The work was divided in three main tasks (Fig 3.1) : (i), the selection and extraction of features to describe the detections; (ii), the manual validation of a dataset for training the supervised algorithm; (iii), the evaluation of several machine learning algorithms and the selection of the most effective one.

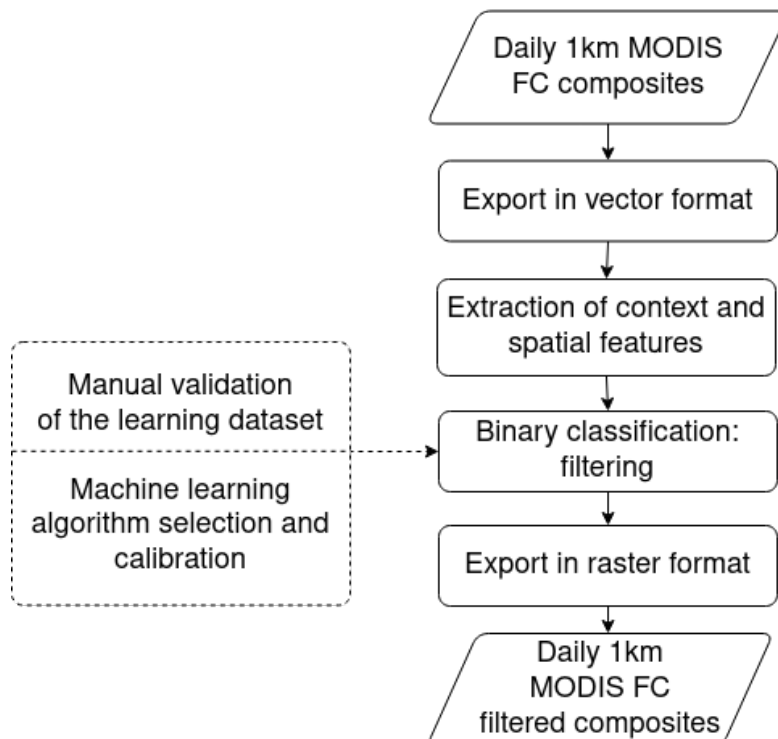


FIGURE 3.1. : Filtering method diagram. The daily images are processed to extract spatial and context features. These features feed the filtering model that discriminates between true and false detections. The manual labelling and algorithm selection are performed once (indicated in dotted line) to build the model.

As some features do not make any sense at the pixel level (e.g., shape of aggregations), the images were exported in vector format (ESRI Shapefile or GeoCSV) (CUEVAS et al., 2018). This particular step allowed each contiguous aggregation of pixels to be grouped in a single entity associated with information about shape and FC values distribution. As a result, pixels within one aggregation were assumed to belong to the same class, true or false *Sargassum* detection. This also reduced the size of the classification problem, from approximately seventy million pixels to less than two thousand aggregations per day. At the end of the classification process, the validated

3. Filtrage des détections MODIS avec des attributs de contexte – 3.3. Materials and Methods

aggregations were exported back into raster format. The Geospatial Data Abstraction Library (<https://gdal.org/>) was used to perform all spatial operations (vector/raster export and features' extraction).

3.3.2. **Sargassum dataset : SAREDA**

This study used the MODIS full resolution Level-2 (v1.20) and Level-3 (v1.21) products processed by SAREDA DESCLOITRES et al., 2021 developed at the AERIS/ICARE Data and Services Centre (<https://www.icare.univ-lille.fr>) using the AFAI (M. WANG & HU, 2016). The SAREDA pipeline is globally organised in seven main steps : 1) atmospheric correction to get Rayleigh-corrected reflectance (Rrc) (ODY et al., 2019; M. WANG & HU, 2018) using OCSSW/SeaDAS (<https://oceancolor.gsfc.nasa.gov/>) ; 2) Screening of sunglint, clouds and cloud shadows (DESCLOITRES et al., 2021; M. WANG & HU, 2016) ; 3) AFAI computation based on 1 km bands over the ocean to enhance the algae signature; 4) Evaluation of the residual AFAI signal of *Sargassum*-free ocean water due to local variations of Rrc; 5) Calculation of the AFAI deviation from the local *Sargassum*-free background; 6) Thresholding of the AFAI deviation ($1.79 * 10^{-4}$) and computing the *Sargassum* Fractional Coverage (FC) or biomass (M. WANG et al., 2018); 7) (optional) projecting and aggregating extracted data in a given area with chosen spatial and temporal resolutions.

In addition, intermediate steps were added to improve the detections extraction (Fig 3.2). Besides masking cloud, cloud shadows, sunglint and land before AFAI computation, the shallow and moderate waters (depth < 500 m) were masked. Every ensemble of contiguous detections overlapping coastal mask was excluded from the results. Most coastal areas contaminating the AFAI signal were removed from the results. After the AFAI computation, the background estimation was refined by two successive median filters with window size 401x401 and 51x51 pixels. The resulting AFAI deviation values (i.e. AFAI deviation with respect to the *Sargassum*-free background) were noisy due to the local filtering therefore an erosion-dilatation step was added to remove the small isolated detections.

3. Filtrage des détections MODIS avec des attributs de contexte – 3.3. Materials and Methods

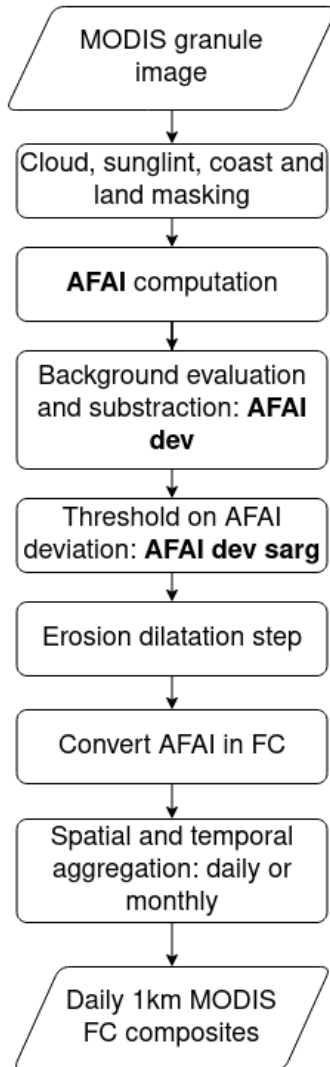


FIGURE 3.2. : SAREDA work flow. Intermediate step of the data are indicated in bold.

That work flow was applied to the full archive of MODIS Level-1B (i.e. Top-of-the-atmosphere reflectance) granules (i.e., 5-minute orbit segments, 1354x2030 pixels 2300x2030 km² each) for both satellites. From those filtered AFAI images, the FC of the *Sargassum* algae was derived from AFAI with the ratio used by M. WANG et HU, 2016. FC values retrieved from Terra/MODIS and Aqua/MODIS were then mapped to an equirectangular grid and averaged daily and monthly. The mapped area extends from 15°S to 50°N and from 100°W to 15°E. The masked pixels were discarded in the average. We called those aggregated products composites. The daily composites provide a global view of *Sargassum* state in the North Atlantic. They are not exhaustive and contain gaps because of the cloud coverage and the gaps between MODIS swaths.

In this original dataset, *Sargassum* was distributed from the Gulf of Guinea to the Gulf of Mexico going through the Caribbean Sea. However, there was a high amount of suspicious detections. At high latitudes false detections were mainly caused by

3. Filtrage des détections MODIS avec des attributs de contexte – 3.3. Materials and Methods

clouds and sun glint that were not completely removed from the data. In coastal areas, water turbidity can run over coastal mask in some cases and generate false detections (M. WANG & HU, 2021). Finally, high chlorophyll concentration or other floating algae (such as *Trichodesmium*) are responsible for the remainder of false detections. These different phenomena cause a wide spatial distribution of false detections. Some of them are scattered in time and space, especially cloud resulting detections, while others are recurrent in some areas such as offshore chlorophyll production near the Mauritanian coasts. Finally, the fraction of false detections can exceed 50%. Examples of the different types of detection are presented in Fig. 3.3.

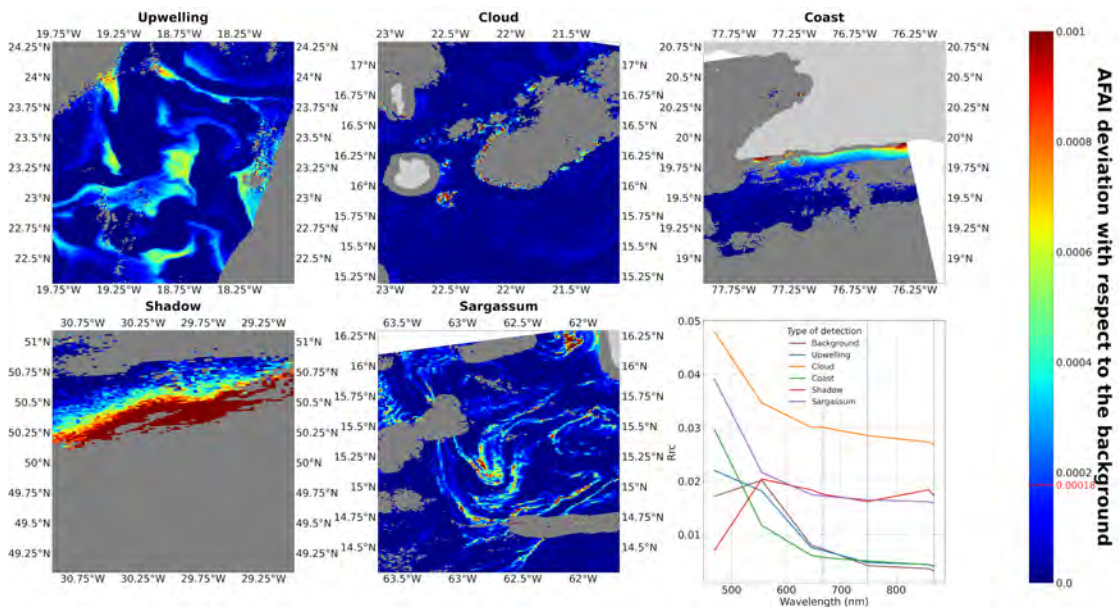


FIGURE 3.3. : Examples of true and false detections for 2020 in 2° by 2° boxes. The colour bar indicates the AFAI deviation from the background (the AFAI detection threshold is indicated in red), masked pixels : either clouds, clouds shadows sunglint or shallow waters (<500 m depth) are represented in dark grey and land in light grey. The bottom right panel shows the average of Rayleigh-corrected reflectance spectra (Rrc) of each case and the background spectrum. Rrc was averaged over the detected pixels (not-detected pixel in the case of background) for each MODIS band in the range (400 nm - 800 nm). The bands used in the AFAI computation (667, 748, 869 nm) are shown as dashed blue lines.

3.3.3. Learning dataset, "expert truth"

In order to perform the filtering, it was necessary to establish a manually labelled dataset to train the model. A manual labelling was performed over FC daily composites by visual inspection (CUEVAS et al., 2018; QIU et al., 2018; M. WANG & HU, 2016). We called that new dataset "expert truth" to differentiate it from real ground truth. To limit

3. Filtrage des détections MODIS avec des attributs de contexte – 3.3. Materials and Methods

human validation bias, results obtained by three different operators were compared. All three labelled sets were consistent, thus the operator bias was considered negligible.

The labelling process was based on daily vector images of the full North Atlantic area and set up with the graphical interface of QGIS (<https://www.qgis.org>). It was used for selecting and classifying the aggregations while displaying the AFAI images to analyse the surrounding context. Based on a daily 1 km Aqua-Terra composite and the corresponding full-resolution single-sensor non reprojected images (Level-2 products), we classified every aggregation except the ambiguous cases (< 5%).

The study focused on five years, 2016 to 2020, a period with continuous *Sargassum* presence. In order to ensure the model generalisation capability in spite of large seasonal and inter-annual variability of *Sargassum* algae, the learning dataset had to extent over a long time period to cover the different cases. The labelling process was divided evenly over the five years. Each year, we selected and validated 3 to 5 days spread out over the seasonal cycle. The dataset was thus representative of both an entire seasonal cycle and the five years of interest.

In the end, about 2000-2500 aggregations per year were labelled by the operators (Table 3.1), except for 2016 with less validated aggregations due to its lower *Sargassum* occurrence. Finally, there was about ten thousand labelled aggregations with 60 % classified as true. While the true detections were more numerous than the false ones, their spatial extent was relatively smaller and they represented only 50 % of the area.

	2016	2017	2018	2019	2020	all
Number of labelled aggregations	1586	2598	2632	2352	1953	11121
Number of true aggregations	697	1402	2147	1623	1540	7409
Ratio of true aggregations (%)	43.9	54.0	81.6	69.0	78.9	66.6
Area ratio of true aggregations (%)	20.8	29.5	71.0	57.4	68.1	48.8

TABLEAU 3.1. : Labelled aggregations per year. The aggregations were obtained by the export of FC images in vector format. The labelling was performed over the Atlantic (100°West to 15°East, 15°South to 50°North).

3.3.4. Aggregations characterisation : spatial features extraction

The first kind of features used was the shape feature. At scales lower than 1 km, *Sargassum* algae aggregate in windrows (narrow elongated rafts) and patches (ODY et al., 2019), with extent between 1 and 100 m diameter. At scales greater than 1 km, the MODIS resolution only detects aggregations in the upper range of spatial extent, mostly typical large elongated structures. These filaments are a few kilometres wide and 10–100 kilometres long. Thus, a dozen shape indicators were extracted from the aggregations to characterise them (JIAO et al., 2012). Among those, an elongation index (STOJMENOVIC & ŽUNIĆ, 2008), a roundness index, a form complexity index, the area and the perimeter were extracted :

$$Elongation = \frac{l_{max}}{l_{min}} \quad (3.1)$$

$$Roundness = 4 * \frac{a}{\pi * l_{max}^2} \quad (3.2)$$

$$Form \ complexity = \frac{4\pi * a}{p^2} \quad (3.3)$$

Where l_{max} and l_{min} are the length of the major and minor axis of the aggregation, a and p its area and perimeter. Area and perimeter metrics take aggregations inner holes into account.

A second category of features was derived from the FC values within each aggregation. While the FC value of pixels considered independently does not allow false detection screening, as FC covers a wide range of valid values, the statistical distribution of these values within one aggregation can discriminate the false and the true *Sargassum* detections. Therefore, the mean, the median, the standard deviation, the minimum, the maximum and the interquartile range of the FC values within each aggregation were extracted.

The third kind of features was composed of several indices describing the surrounding of aggregations. As *Sargassum* aggregations are often small and close to each other, we defined the Nearest Neighbours Index (NNI) that counts the number of neighbouring aggregations within a given radius around one aggregation. Additionally, the Nearest Neighbours Area Index (NNAI) measures the total area covered by those close-by neighbours. Both of these indices were extracted with different radii from the barycentre of the aggregations.

In order to give more likelihood to redundant and time-coherent detections, an original persistence index (PersI) was developed. For every aggregation, it evaluates the number of times where the aggregation is close to at least one other aggregation in the two previous days and the two next days. Finally, the Coast Shortest Distance Index (CSDI) represents the aggregation distance from a land body.

In the end, around thirty indexed features were extracted. They were highly redundant, it was thus necessary to select the minimal subset of features to ensure the simplicity, the reliability and the robustness of the classification method. The feature selection was based on different sources of information. First, it took into account the correlation between indices to select uncorrelated features. Then, when it was available, it relied on the feature frequency of use during training with machine learning algorithms. Finally, the selection maximised the performance metrics of the algorithms (Section 3.3.5). Plus, the interpretability of the features was taken into account during the selection.

3.3.5. Classification algorithms selection and tuning

The last step of the method was to select the most suitable machine learning algorithm for the filtering and tune it. In order to evaluate and compare the performance of each

3. Filtrage des détections MODIS avec des attributs de contexte – 3.3. Materials and Methods

algorithm, different scores were computed.

The classic performance scores used were the accuracy, the recall and the precision (HASTIE et al., 2009), thereafter called "overall accuracy", "overall recall" and "overall precision". These scores were obtained with k-fold cross-validation on the whole dataset. In addition, we introduced the "generalisation accuracy", the "generalisation recall" and the "generalisation precision" scores. First, the yearly accuracy, recall and precision were computed for each year using the remainder of the dataset as training dataset. The generalisation scores were defined as the average of those yearly scores. Those new metrics, needed because of the inter-annual variability of the *Sargassum* algae, represent the prediction capacity of the method over a completely unknown year. It thus gives a more realistic estimation of the method performance.

For selecting a machine learning algorithm, a benchmark was conducted over various classification algorithms. It included single model algorithms as Naive Bayes classifier (NB), Decision tree, Support Vector Machine (SVM), Linear Discriminant Analysis (LDA). Plus, some aggregated models based on decision trees were evaluated such as Adaboost, Gradient Tree Boosting (GTB), XGBoost and Random Forest (RF).

Several scores were computed to evaluate and compare the performance of each algorithm. First, the overall accuracy gives an overview of the algorithms' performance. Yet, true *Sargassum* aggregations were more important in the classification to keep as much as possible the *Sargassum* signal. As overall accuracy weights evenly the classes, the overall recall was taken into account to focus on the true positive/false positive ratio. The overall precision was also computed but with lower attention for the optimisation as the false positive matter was less important. Finally, the overall f-score summarised these last two metrics but we mainly used the overall accuracy and the overall recall for interpretability.

Finally, those metrics were computed for all the tested algorithms using the python library scikit-learn (<https://scikit-learn.org/>) (Table 3.2). They were evaluated with a cross-validation step, by performing a k-fold over the labelled dataset ($k = 50$). The inputs were the 30 extracted aggregation features (Section 3.3.4). Usual algorithm performance ranking was retrieved, with aggregated methods with higher performances than single model methods. The single model methods, with low overall accuracy and overall recall (around 85% - 90%) but higher interpretability allowed to select the right features, especially the decision tree algorithm. Aggregated methods were very efficient with around 94% of overall accuracy but not easily interpretable. The random forest algorithm showed the best performance and was thus selected. This is consistent with the literature that repeatedly employs random forest for remote sensing classification (BELGIU & DRĂGUT, 2016; CUEVAS et al., 2018).

	SVM	NB	LDA	Decision tree	Adaboost	GTB	XGBoost	RF
Accuracy	72.9	84.4	87.2	90.8	92.2	92.0	93.7	95.8
Recall	67.6	82.1	85.8	90.9	94.3	94.0	95.2	96.5
Precision	89.2	93.7	94.5	95.1	94.0	93.0	95.3	97.2

TABLEAU 3.2. : Algorithms performance computed with a k-fold operation (k=50). No particular tuning were previously performed.

After selecting the random forest algorithm, a calibration was performed on its parameters to maximise the performance. Concerning the random forest algorithms calibration itself, the models were highly configurable. However, only two main parameters were evaluated here, the numbers of bootstrapped trees and the maximum depth of trees. Although random forests are not very sensitive to overfitting, the lowest values for tree depth (12) were taken to both conserve good performances and enhance generalisation power. Similarly, the number of estimators was chosen as small as possible (24) to reduce the computation time. We evaluated here both "overall accuracy" and "generalisation accuracy". The set of input features was then reduced to a reasonable number in order to optimise performance (Section 3.3.4). For the NNI, the persistence index and the NNAI features, the radius maximising the scores for the NNI and NNAI computation was 700 km and the radius for the Persl computation was 50 km.

A learning curve was computed to check the convergence of the metrics. It was obtained by learning over an increasing fraction of the dataset, testing over the remainder, and computing both overall and generalisation scores. This was repeated 30 times to reduce random selection effect and then averaged in a single curve.

3.3.6. Time series production

The random forest classifier was applied to the daily FC composites over the time period 2016-2020 to build a filtered dataset. We obtained a complete filtered time series with one image of 1 km resolution per day.

Monthly composites were computed to overcome the extensive masking of daily products (mostly due to clouds), to enhance interpretability and for comparison with the literature (ODY et al., 2019; M. WANG & HU, 2016). Finally, the FC was converted to wet biomass using the ratio of $3,34 \text{ kg m}^{-2}$ proposed by M. WANG et al., 2018 based on field measurements in the Gulf of Mexico, the Florida Straits and Belize.

In order to summarise the whole time series (2016-2020), annual biomass averages were computed at 50 km resolution. A simplified envelope was also extracted for comparing spatial distributions between years. This envelope was obtained by first thresholding the 50 km composites ($\text{FC}=10^{-5}$). Then, the images were exported in vector format and erosion-dilation-erosion steps were applied to delete the remaining scattered aggregations and close gaps. Finally, for each pair of envelopes, the ratio between the intersected surface and the total surface was computed.

3.4. Results

The labelled dataset is shown in Fig. 3.4, it gives an overview of the spatial distribution of true and false detections.

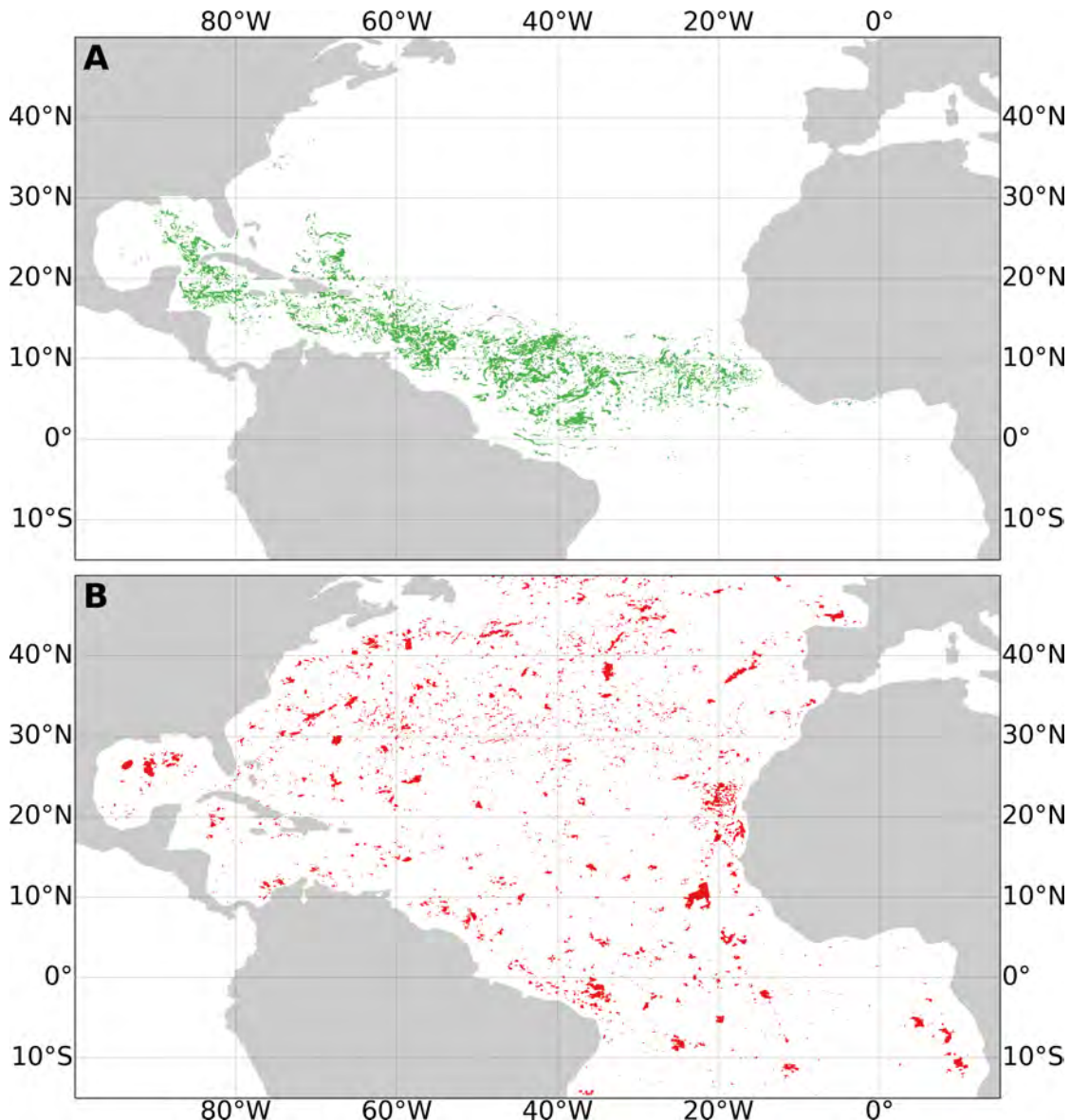


FIGURE 3.4. : Map of true (A) and false (B) *Sargassum* aggregations from the learning dataset over 5 years. All labelled aggregations were displayed at their location, with possible overlaps.

True detections are concentrated from the Gulf of Guinea to the Gulf of Mexico, going through the central Atlantic and the Caribbean Sea. The false detection distribution was more spread out over the whole area with some dense areas like offshore Mauritania.

3. Filtrage des détections MODIS avec des attributs de contexte – 3.4. Results

The whole set of features used in the classifier was reduced to five according to the performance maximisation of the filtering : NNI, CSDI, PersI, NNAI and the FC standard deviation (Tab. 3.3). Concerning the NNI, the PersI and the NNAI, they were selected regardless of the neighbourhood radius used and then calibrated.

NNI	CSDI	PersI	NNAI	FC std
44.5	15.6	15.5	14.8	9.5

TABLEAU 3.3. : Feature frequency of use (%) for the final classifier (random forest). The frequencies were averaged over 30 generated forests. The radius used for the metrics NNI, PersI and NNAI were respectively 700 km, 50 km and 700 km.

Tab. 3.3 shows the frequency of use for the five selected features. NNI is largely the most used while CSDI, PersI and NNAI are quite equivalent and the FC standard deviation is rarely used.

Concerning the classification performances, the learning curves computed on the dataset are presented in Fig 3.5. These learning curves show the fast convergence of the method performance. Both overall accuracy (recall and precision) and generalisation accuracy (recall and precision) stabilise when learning with more than half of the dataset. The generalisation accuracy (recall and precision) stabilises faster than the overall accuracy (recall and precision). The associated standard deviation was quite low thus the measurements were robust.

3. Filtrage des détections MODIS avec des attributs de contexte – 3.4. Results

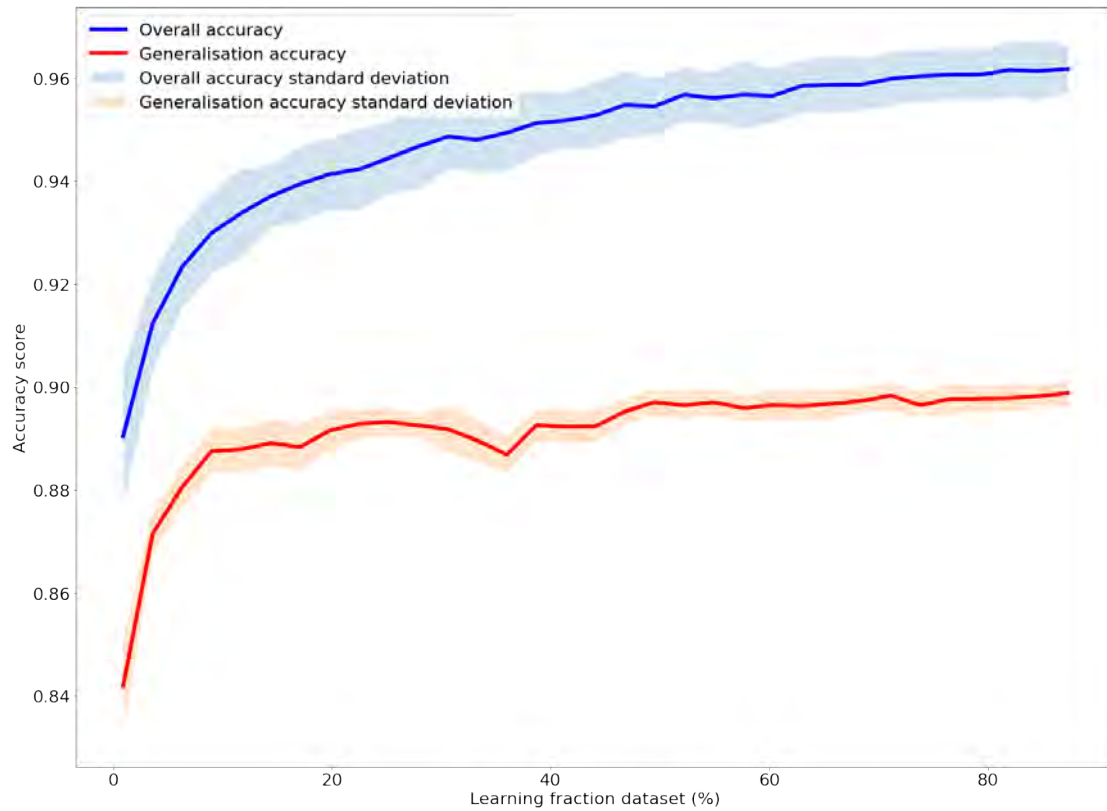


FIGURE 3.5. : Learning curve of the random forest algorithm. The dataset fraction allocated for training increases from 3% to 90%, the remaining 10% of the data are used for testing. The displayed curves are the average on 30 computed curves. The blue curve shows the overall accuracy and the red curve the generalisation accuracy (i.e. training without a year and testing on it). Similar results were observed with the recall and precision scores.

In addition, the final scores of the method are shown in Tab. 3.4. The overall performance of our approach was about 96% regardless of the predicted class. The generalisation accuracy (recall and precision) per year varied between a minimum of 84% (83% and 82% respectively) in 2016 and between a maximum of 94% (96% and 96%) in 2019. The generalisation accuracy (recall and precision) is 90% on average (92% and 91%).

3. Filtrage des détections MODIS avec des attributs de contexte – 3.4. Results

	Overall acc.	Train over the dataset except one year					Gen. acc.
		Test 2016	Test 2017	Test 2018	Test 2019	Test 2020	
Accuracy	96.28 ± 0.08	84.51 ± 0.9	84.24 ± 0.34	92.35 ± 0.35	93.98 ± 0.4	94.0 ± 0.58	89.97 ± 0.48
Recall	96.9 ± 0.06	82.55 ± 2.07	89.73 ± 0.45	95.7 ± 0.41	95.67 ± 0.19	92.65 ± 0.72	91.89 ± 0.66
Precision	97.5 ± 0.09	82.28 ± 0.88	82.58 ± 0.48	94.96 ± 0.14	95.61 ± 0.49	99.72 ± 0.72	91.23 ± 0.4

TABLEAU 3.4. : Algorithms performance scores in percentage. The computation is made 30 times to <https://fr.overleaf.com/project/62971c689b31d47b1bfe53ca> reduce random effect. The standard deviation is indicated after the scores. The generalisation scores correspond to the weighted mean of the five annual tests.

Examples of composites before and after the filtering process at 1 and 50 km spatial resolutions are presented in Fig. 3.6. A full seasonal cycle for the year 2020 at 50 km is shown in Fig. 3.7.

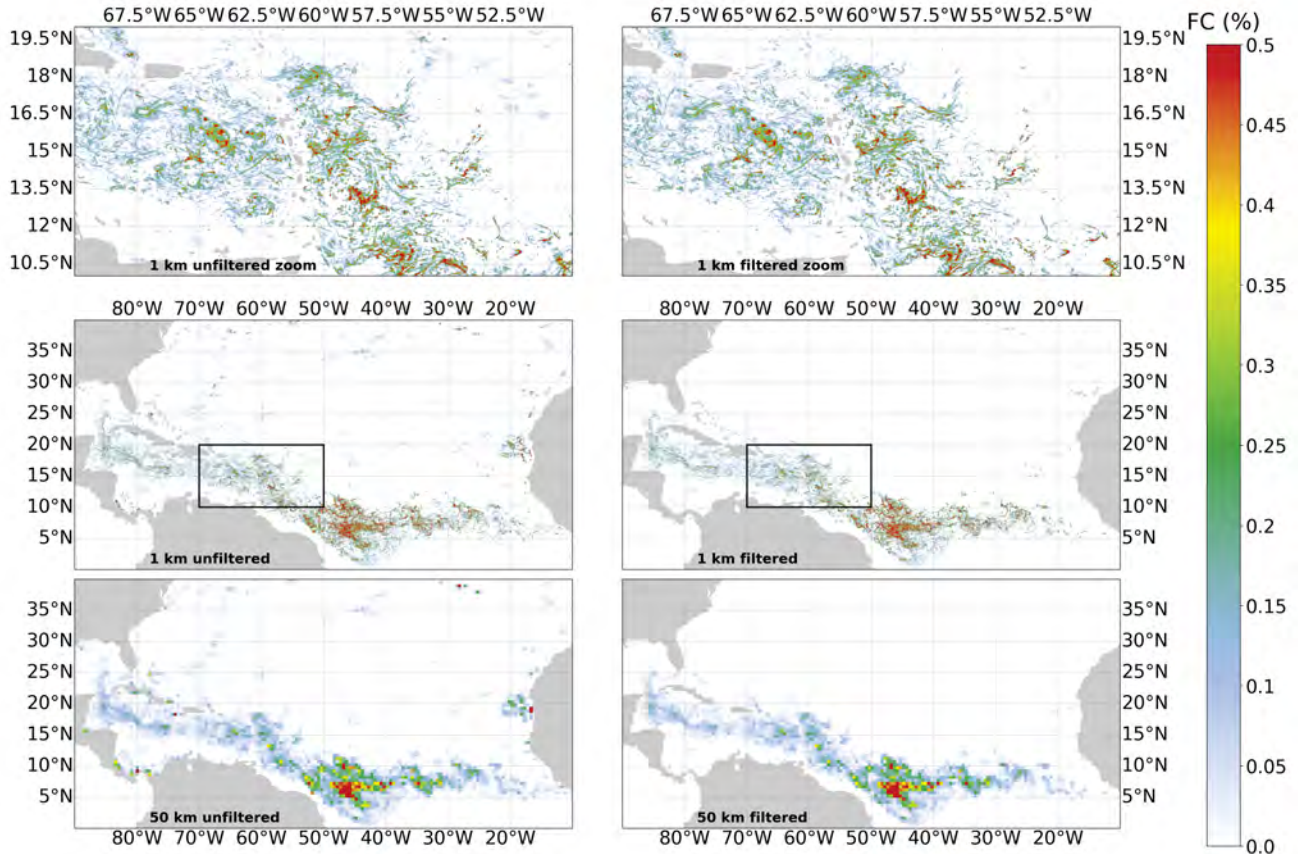


FIGURE 3.6. : Monthly composite of FC for June 2020 at 1 km and 50 km resolution for unfiltered (left) and filtered (right) data. The top panel is a zoom of the region shown on middle panel.

3. Filtrage des détections MODIS avec des attributs de contexte – 3.4. Results

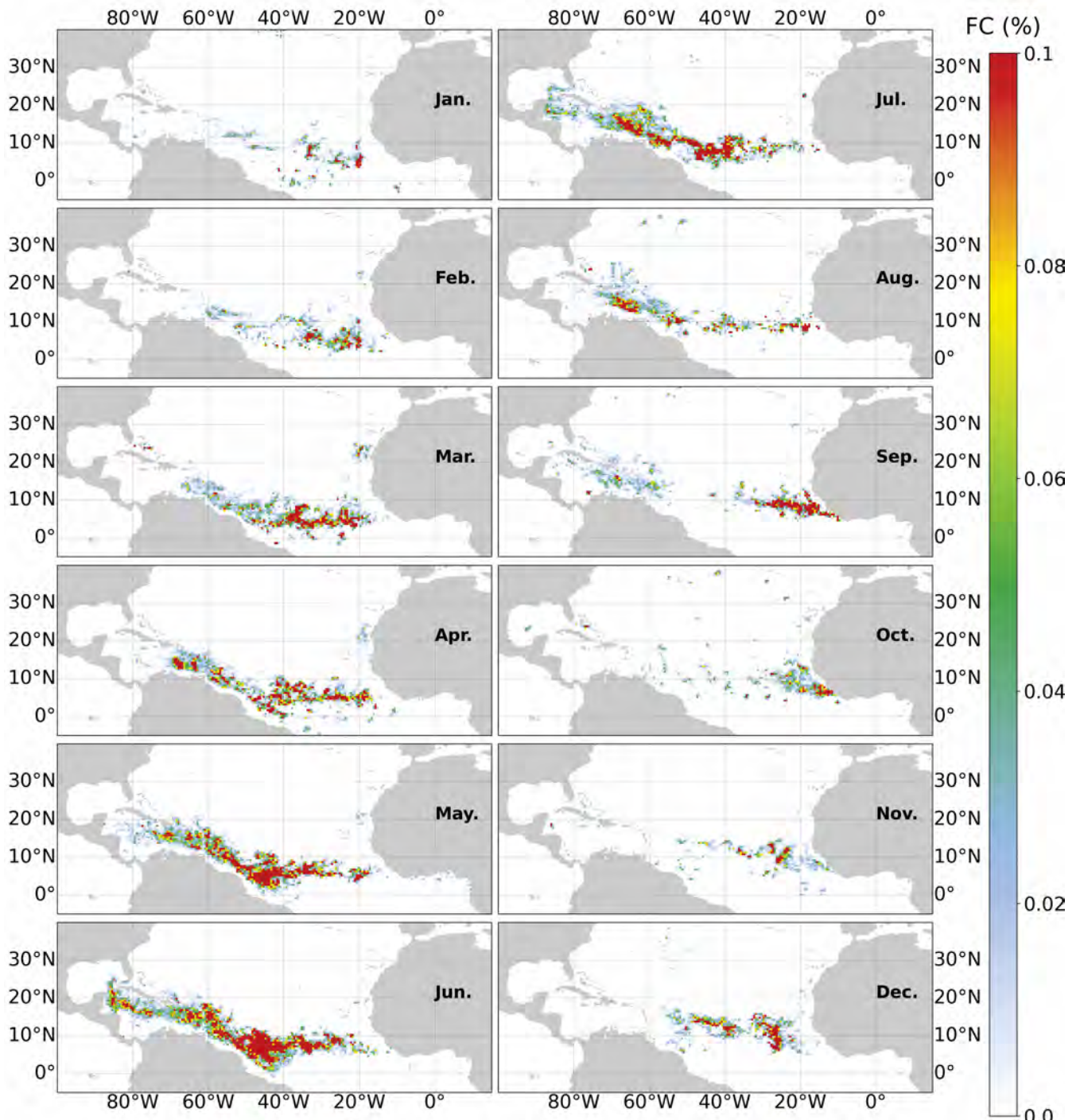


FIGURE 3.7. : Filtered FC of monthly composites for 2020 at 50 km resolution.

The filtered products showed a coherent spatial distribution over the whole time series 2016-2020 (95% of accuracy is expected). False detections were removed in the areas where no *Sargassum* algae presence was reported (for example for latitudes > 30°N and < 0°N). In the opposite, the detected aggregations in the new *Sargassum* distribution area were retained (Fig. 3.6).

3. Filtrage des détections MODIS avec des attributs de contexte – 3.4. Results

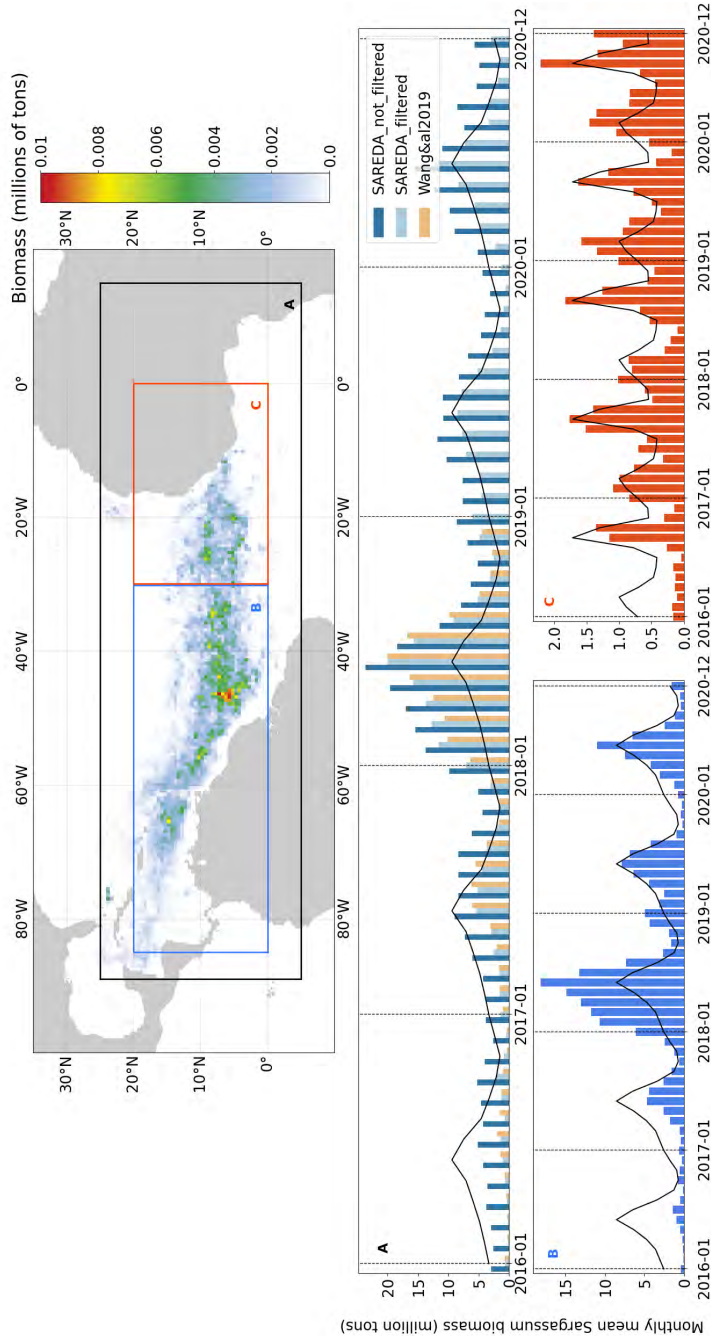


FIGURE 3.8. : *Sargassum* biomass time series averaged in different boxes during the time period 2016-2020. The top panel displays the 2020 aggregated data in 1 km-resolution and the boxes used for the biomass computation. Panel A presents the biomass time series in the same box as M. WANG et al., 2019b and compare it to their data (available until 2018 only). Panel B and C are the retrieved *Sargassum* filtered biomass for Eastern and Western Atlantic Ocean (boxes B and C on the map). The black lines on the bar-plots indicate the annual mean of filtered data computed over the five years.

3. Filtrage des détections MODIS avec des attributs de contexte – 3.4. Results

The monthly time series of biomass in three different spatial boxes are displayed in Fig. 3.8. The filtering method developed here reduced the biomass estimate by 40% in total for the whole time series and reduced the monthly estimate by 53% (average of monthly ratios). This is consistent with the estimated ratio of false detections observed in the learning dataset.

Primarily, over the North Tropical Atlantic, the seasonal cycle of biomass was rather regular (average of monthly standard deviation of 66%). The seasonal cycle of growth/decay leads to a biomass maximum in June and a minimum in November. The monthly average of biomass was estimated between 3 to 10 million tons. Biomass quantities were equivalent for 2017, 2019 and 2020 while 2016 and 2018 had respectively low and high biomass quantities. In addition to the global biomass time series, we computed separately the biomass from the Eastern and Western parts of the Tropical Atlantic Ocean to highlight their distinct dynamics. The Eastern area has lower *Sargassum* quantities with two biomass peaks in March and September. The Western area has 6 times greater biomass with only one peak in June. Concerning the boxes used for the biomass estimation in Figure 3.8, the limit of 30°W between the two areas was chosen both to maximise the differences between the two dynamics and to visually distinguish the two areas of high biomass.

For the years 2016-2018, unfiltered and filtered biomass estimates were compared to the M. WANG et al., 2019b time series. Our filtered biomass averaged over the three years was only 1% greater than M. WANG et al., 2019b estimate. Comparing month by month, there was a +4% difference on average, associated with a standard deviation of 33%. A student t-test was performed between the two datasets before and after filtering. Unfiltered data and M. WANG et al., 2019b data were significantly different with a p-value of 0.02 while filtered data was very similar to their measurements with a p-value of 0.97. Moreover, the filtered dataset was also close to their data in terms of spatial distribution (not shown). Besides, some remaining false detections and some true detections were absent in the results of M. WANG et al., 2019b, while few of their detections were removed in the filtered dataset. The detailed analysis of these discrepancies could not be achieved here and was beyond the scope of this study. Finally, the main improvement of our dataset is the spatial resolution, 1 km for SAREDA filtered against 0.5° (\approx 50 km) for M. WANG et al., 2019b composites.

3. Filtrage des détections MODIS avec des attributs de contexte – 3.5. Discussion

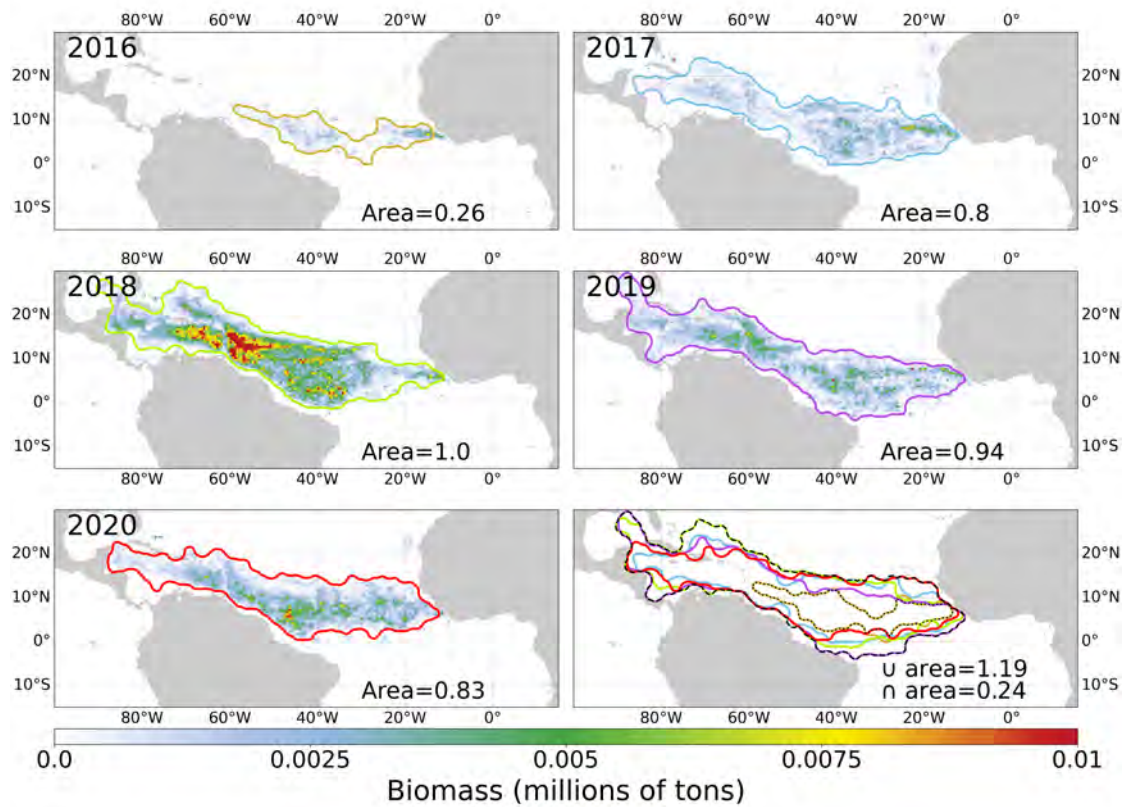


FIGURE 3.9. : Annual composites of biomass at 50 km for 2016-2020 associated with the envelope of the area of high *Sargassum* concentration. The normalised area with respect to 2018 is indicated. The last panel shows all the envelopes, its intersection (dotted line) and its union (dashed line).

Lastly, the yearly *Sargassum* spatial distribution is presented in Fig. 3.9 with simplified envelopes. By opposition to the high inter-annual biomass variations, the distribution areas do not differ much between years except in 2016. For example, the distribution area of 2018 is very similar to the area of 2017 despite the overall biomass being 3 times larger. In-depth comparison between annual distributions shows several areas of discrepancy : 1) the Gulf of Mexico, reached in 2018 and 2019 only; 2) The north of the Dominican Republic, overrun by *Sargassum* in 2017 and 2018 only; 3) The Central West Atlantic, where *Sargassum* algae usually remain above the equator except in 2019.

3.5. Discussion

3.5.1. Interpretation of features used in the classification

Among the thirty features extracted from the detected aggregations, only five were used in the final classifier. The first selected feature and the most used in the classifier

3. Filtrage des détections MODIS avec des attributs de contexte – 3.5. Discussion

was the NNI (44.5%). This selection is consistent with visual observations during labelling, as true detections were mostly concentrated together in few areas. Besides, the major use of this feature was likely responsible for the lower classifier performance in 2016 where aggregations were scarce and sparse. The CSDI, the PersI and the NNAI completed the filtering by discriminating respectively the remaining coastal false detections and the far offshore Northern cloud false detections, the time-incoherent detections and the detections neighboured by large false detections due to chlorophyll concentration. Finally, the addition of the FC standard deviation increased the generalisation accuracy and the robustness of the method by preventing overfitting.

Only context indices were retained for the classification, likely because of the too coarse spatial resolution of the data. In particular, the elongation was not selected because of the fragmentation of aggregations. The elongated structures seen in the images were often split because of the erosion-dilatation operation used during the retrieval process (Section 3.3.2). We chose here to exclude location and temporal features from the selection. A test showed that including latitude and longitude coordinates greatly improved accuracy for a single year dataset but decreased accuracy with a more extended dataset. Furthermore, since the geographic distribution of the algae changed radically in 2010, we wanted to avoid geographical constraints.

3.5.2. Accuracy of the classification and generalisation

The performance scores obtained with the classifier were between 90% and 96%. The filtering quality for new data is expected to be in the annual generalisation scores range (90%). It will depend on the consistency of new data with the 2016-2020 dataset. The only lower-performing year was 2016 where the biomass level was much lower than other years. Overall, the score should stay around 90% if the current trend of biomass distribution persists. For the filtering of the 2011-2015 period, the performance obtained for 2016 should be representative and an accuracy above 85% is expected.

The learning curve analysis showed that increasing the learning set does not greatly improve scores. From 50% to 90% of the learning set, the overall score gained less than 1% of accuracy while the generalisation score was stable. Adding data from the same years 2016-2020 to the learning set will therefore be useless. The only way to noticeably improve the method would be to add data from other years and make both scores converge.

The performance is analogous to or better than other works that used machine learning algorithms for *Sargassum* detection. CUEVAS et al., 2018 applied a random forest algorithm over a small dataset using raw reflectances and derived indices such as AFAI. Their accuracy was close to our study with a overall score of 93.4%. ARELLANO-VERDEJO et al., 2019 used deep learning on radiometric inputs from MODIS to detect *Sargassum*. Their accuracy was similar to our results (90%). Finally, studies on Yellow Sea *Sargassum* algae (QIU et al., 2018; SHIN et al., 2021) showed similar or lower performance.

3.5.3. Limits of the method and potential improvements

The choice of MODIS imagery implies rather coarse resolution but recurring observations (twice a day). We used the 1 km bands for AFAI computation to ensure good signal/noise ratio compared to 250 - 500 m bands and to better discriminate between *Sargassum* and clouds (M. WANG & HU, 2016). Comparison of AFAI with high resolution (20 m) MSI observations have shown that both estimates are consistent (DESCLOITRES et al., 2021; M. WANG & HU, 2020). MODIS appears as a trade-off between regular mapping of the *Sargassum* distribution and resolution.

The method assumed that features distribution is consistent for all aggregations regardless of their location and of their time of observation. This is mostly the case over the studied time period, as the high performance obtained by the method demonstrates a good spatial and temporal consistency. Yet, specific regions or periods may show singular distributions of features. That could be the case for areas where false detections remained after the filtering process, such as offshore Mauritania or the Amazon plume area. The global approach could be limited here and defining regional learning sets and classifiers may improve the method performance.

The learning set was built to be as representative as possible of the whole set of true and false detections. Nonetheless, in some areas (e.g., Gulf of Guinea, Sargasso Sea), discrimination between true and false detections was more strenuous for manual labelling. Both low *Sargassum* concentration and cloud coverage created ambiguous cases. This induced a lack of labelled data and most likely a lower filtering accuracy in these regions. Remote sensing imagery from other sensors with higher resolution or *in-situ* measurements could help to fill this gap and to ensure the completeness of the dataset.

Since the study focused on basin scale offshore *Sargassum* detection, coastal areas were masked. This choice does not have a large impact on *Sargassum* estimation as detections in the coastal areas were mostly false detections. Tests using our classification algorithm to filter out coastal false detections and avoid masking coastal waters were not conclusive. In coastal areas, progress in *Sargassum* detection can be made using other sensors/indices with poorer temporal resolution, such as OLCI and Maximum Chlorophyll Index (J. F. GOWER & KING, 2011), less sensitive to coastal contamination, or higher resolution sensors such as MSI (M. WANG & HU, 2020, 2021). Those sensors would be useful to complement MODIS data.

3.5.4. Uncertainties in the *Sargassum* estimates

Sargassum detection is limited by algae observability. In certain circumstances (low density, vertical mixing in the upper layer), MODIS cannot distinguish *Sargassum* from background (D. L. JOHNSON & RICHARDSON, 1977; M. WANG & HU, 2020; WOODCOCK, 1950, 1993). This limitation is outside the scope of our study.

Concerning the filtered products, clues on their uncertainties were given by the classifier performance study. For the 2016-2020 period, the expected errors fraction would be about 2.5% of false positives and 2.5% false negatives. As the false aggregations

3. Filtrage des détections MODIS avec des attributs de contexte – 3.5. Discussion

are larger than true ones, false positives would induce a greater overestimation than false negatives generate an underestimation. Thus, the filtering errors are expected to produce a small overestimation with errors on some *Sargassum* aggregations locations. For data from other years, the reasoning is the same but with around 5% of false positives and of false negatives generating an overestimation twice larger.

Concerning the aggregated products, there is an uncertainty due to the sampling, limited by the coverage of daily data. With two observations per day over the whole Tropical Ocean, only 30% of pixels were retrieved because of the different masks. The solution used to fill these gaps was to aggregate data spatially or temporally. In order to keep the best spatial resolution, temporal averaging was used. If we hypothesise a fully random mask distribution (binomial distribution for every pixel), 6 days are needed to reach a coverage of at least 90%. In practice, 12 days were needed. The temporal composites based on less than 12 days were therefore incomplete, while using more than 12 days reduce mapping accuracy because of non-negligible *Sargassum* drift.

3.5.5. *Sargassum* dynamics over 2016-2020

The biomass fluctuations resulted mainly from advection for 1-2 month timescale (BERLINE et al., 2020), while biology (growth and decay) combined to advection drives the fluctuations for longer time scales. Our results strengthened the scenario of recirculation of the *Sargassum* biomass in the North Tropical Atlantic : from the development of relatively low biomass in the Eastern Atlantic Ocean in the early months of the year, advection inseminates the Central Atlantic Ocean and leads to a biomass maximum in June-July. In addition to the bloom transport in the Caribbean Sea and the Gulf of Mexico, some *Sargassum* algae are driven back eastwards by the North Equatorial Countercurrent (NECC) causing the September peak of biomass. Finally, the algae globally decay and return to a global minimum of biomass in November. This cycle, rather stable over the studied period (2016-2020), is consistent with the time series from M. WANG et al., 2019b over 2016-2018.

The eastern and western boxes essentially distinguish the western and eastern consolidation regions from FRANKS et al., 2016. This limit also matches the transition between two distinct areas of annual biomass production, as shown on the 2020 seasonal biomass cycle (see top of Fig. 3.8). The two different dynamics and biomass quantities observed in the Eastern and Western Tropical Atlantic Ocean are consistent with the simulations from JOUANNO et al., 2021a (their figure 5) for the year 2017.

As a perspective, the 1 km resolution of our dataset may allow tracking algae aggregations over several days of observations. This tracking could provide valuable inputs on *Sargassum* drift patterns. Such an approach was recently tested with GOES (Geostationary Operational Environmental Satellite) by MINGHELLI et al., 2021 with 15-minute observations, but with a lower sensitivity. To validate the analysis of the *Sargassum* distribution dynamics and explore the anomalous 2010 event (JOHNS et al., 2020), the filtered dataset will be extended backwards to 2000, i.e. over the full MODIS archive (only Terra sensor for 2000-2001).

3.6. Conclusions

With the use of a machine learning algorithm, this study benefits from an untapped source of information : the spatial context of *Sargassum* aggregations. Those new features are complementary with radiometric data used in previous approaches and allow to screen false detections induced by various phenomena. While classic algorithms have known flaws that induce false detections, the post-processing filtering technique presented here offers a solution to identify and mitigate those flaws and produce automatically a high-quality product over a large-scale area. As the method is time and space independent and modular, it would be easily generalised to other *Sargassum* detection datasets or other application scopes. The *Sargassum* annual cycle of the filtered dataset is consistent with the literature for seasonal and inter-annual fluctuations and we provided a detailed characterisation of the spatial variability of the distribution. As a perspective, the filtering process will be implemented in the SAREDA pipeline to provide near real-time filtered products and reprocess the past time series. This dataset will be useful to understand the drivers of *Sargassum* dynamics at fine and large scale and validate future models.

3.7. Appendices

3.7.1. Neighbours indices calibration

The choice of radii used for NNI, NNAI and PersI indices was critical for their use in classification, they were thus calibrated as follow. We arbitrarily kept the same radius for the NNI and the NNAI to facilitate the interpretation of the results. The calibration thus focused on selecting a pair of radii for neighbours and persistence. Overall and generalisation accuracy (recall and precision) were then evaluated for each couple of radii (Tab. 3.5).

As the generalisation matter was critical, the radii were selected according to the best generalisation accuracy, with a small loss of overall accuracy. Finally, the radius for the NNI and the NNAI was chosen at 700 km from the barycenter of the aggregations and the PersI radius was 50 km.

3. Filtrage des détections MODIS avec des attributs de contexte – 3.7. Appendices

		Neighbours indices radius (NNI and NNAI)							
		10km	50km	100km	300km	500km	700km	1000km	
Gen. acc.	Overall acc.	10km	82.6	87.3	89.9	93.4	94.8	95.5	95.3
		50km	87.9	90.0	91.9	94.6	95.5	96.1	96.1
		100km	88.7	90.4	92.1	94.7	95.5	96.0	96.2
		300km	84.7	87.7	90.4	93.7	95.0	95.8	95.9
		500km	81.0	85.9	89.1	93.2	94.3	95.4	95.1
	Persistence index radius (PersI)	10km	77.6	82.3	84.4	88.3	88.0	89.2	86.6
		50km	83.7	85.7	86.2	89.3	88.8	89.8	88.1
		100km	85.2	86.2	86.5	89.0	89.0	89.2	86.7
		300km	78.2	81.9	83.9	87.3	87.5	88.0	84.6
		500km	75.1	80.5	83.4	86.9	86.7	87.7	85.7

TABLEAU 3.5. : Accuracy scores according to the pair of radii used for NNI-NNAI and PersI. The overall accuracy was obtained with a k-fold cross-validation on the whole dataset, the generalisation accuracy was computed by excluding a year from the training dataset and testing on it (this operation was done on each of the five years and the scores were averaged). The pair of radii yielding the best overall accuracy is indicated in blue while the pair of radii maximising the generalisation accuracy is indicated in red. Similar results were observed with overall and generalisation scores for recall and precision.

4. Suivi des agrégats de sargasses et modélisation de leur dérive

Ayant à disposition les images SAREDA purgées de la majorité de leurs scories résiduelles, il est à présent possible de s'intéresser à la dynamique et la variabilité des algues sargasses dans ce jeu de données. Comme les sargasses effectuent leur cycle saisonnier sur presque un tiers du périmètre terrestre (100° ouest à 10° est, soit 12 000 km est-ouest), leur dérive est certainement l'un des facteurs majeurs qui détermine leur répartition spatiale et temporelle. En outre, il s'agit du phénomène clé pour anticiper et idéalement prévoir les échouements de sargasses à relativement court terme (quelques dizaines de jours).

Malgré ce besoin évident de connaissances approfondies sur les mécanismes exacts de la dérive des sargasses, ceux-ci restent imparfaitement appréhendés par les études scientifiques existantes. Cela découle de la grande complexité des processus déterminant cette dérive, dont les rares données d'observation ne rendent que partiellement compte. Plusieurs obstacles rendent en effet difficile l'acquisition de données d'observation. D'une part, l'échelle des radeaux de sargasses (1 à 100 mètres) empêche la mise en œuvre d'expérimentations en laboratoire reproduisant une dérive naturelle. D'autre part, l'observation *in-situ* de la dérive, par le suivi de trajectoires par exemple, est gênée par le manque de cohésion des radeaux qui se désagrègent puis se recomposent dynamiquement. Ce manque de cohésion empêche également d'attacher des bouées GPS directement aux radeaux pour les suivre. À cela s'ajoute la complexité purement logistique de mener à bien des expérimentations de longue durée en océan ouvert. Aussi, la diversité des conditions du transport passif de ces algues évoluant dans un espace de 10 millions de kilomètres carrés nécessiterait un effort considérable d'échantillonnage.

Les quelques connaissances spécifiques aux algues sargasses, auxquelles s'ajoute le savoir bien établi concernant d'autres objets flottants similaires (comme les bouées dérivantes océanographiques), permettent néanmoins de décomposer les forces effectives de la dérive. L'effet primordial est sans conteste l'entraînement par le courant de surface environnant. Loin d'un fluide laminaire homogène, celui-ci est turbulent, dépendant de la profondeur, avec de nombreux fronts de cisaillement. Son effet est donc fort complexe à fine échelle, engendant la déformation et la scission des radeaux. Il devient plus aisément appréhendable aux échelles plus dégradées où il est assimilable à une force homogène spatialement qui entraîne les sargasses dans le sens de l'écoulement. Ce courant environnant se différencie en deux composantes principales, le courant géostrophique et agéostrophique. Le premier résulte de l'équilibre entre les gradients de pression et l'effet Coriolis à l'échelle du bassin océanique,

4. Suivi des agrégats de sargasses et modélisation de leur dérive

tandis que le second est défini localement par la juxtaposition de différents facteurs (inertie, entraînement par le vent, état de la mer et marée). Ces composantes peuvent être mesurées afin d'estimer l'effet du courant sur les sargasses en utilisant des mesures altimétriques pour le courant géostrophique et en se limitant à l'effet du vent ou courant d'Ekman pour la composante agéostrophique. Il est couramment admis que ce courant de surface advecte les sargasses à raison de sa vitesse absolue sans déperdition d'énergie.

Si les sargasses sont implicitement impactées par le vent du fait du courant d'Ekman, elles le sont également plus directement en conséquence de leur affleurement à la surface. Leur partie émergée, bien que minoritaire, est exposée à l'écoulement du vent, créant ainsi une force d'entraînement qui s'ajoute au courant. Ce facteur d'entraînement, dénommé "windage" dans la littérature scientifique spécifique aux sargasses, ou "leeway" plus généralement, constitue un point de discussion crucial pour modéliser précisément le transport des sargasses. Défini comme une petite fraction de la vitesse du vent (quelques pourcents), la communauté scientifique s'accorde sur son importance sans néanmoins conclure sur sa valeur, faute de mesures directes et absolues de ce dernier.

La seconde étude de cette thèse s'intéresse en conséquence à estimer précisément l'effet du vent sur la dérive ainsi qu'à réévaluer le rôle du courant. Dans cette optique, j'ai dans un premier temps élaboré une méthode d'extraction de trajectoires de sargasses dans les images MODIS de résolution 1 km. En utilisant des algorithmes d'appariements automatisés, il est possible de faire correspondre deux images d'agrégat de sargasses séparées de quelques heures et ainsi de calculer leur vitesse. Basée sur ces résultats d'appariements, la comparaison statistique des vitesses sargasses aux vitesses des courants de surface et du vent fournit une nouvelle interpolation des facteurs de transport des sargasses. Ce second travail se conclut donc par un nouveau modèle de dérive apportant des nuances aux inférences précédentes de la littérature.

4. Suivi des agrégats de sargasses et modélisation de leur dérive

A new *Sargassum* drift model derived from features tracking in MODIS images

Witold Podlejski^{1,2,*}, David Nerini², Andrea Doglioli², Christophe Lett¹ and Léo Berline²

¹Marbec, Université de Montpellier, CNRS, Ifremer, IRD, Sète, France

²Aix Marseille Univ, Université de Toulon, CNRS, IRD, MIO, Marseille, France

Publié : PODLEJSKI, W., BERLINE, L., NERINI, D., DOGLIOLI, A., & LETT, C. (2023). A new Sargassum drift model derived from features tracking in MODIS images. *Marine Pollution Bulletin*, 188, 114629. <https://doi.org/https://doi.org/10.1016/j.marpolbul.2023.114629>

4.1. Abstract

Massive *Sargassum* stranding events affect erratically numerous countries from the Gulf of Guinea to the Gulf of Mexico. Forecasting transport and stranding of *Sargassum* aggregates require progress in detection and drift modelling. Here we evaluate the role of currents and wind, i.e. windage, on *Sargassum* drift. *Sargassum* drift is computed from automatic tracking using MODIS 1 km *Sargassum* detection dataset, and compared to reference surface current and wind estimates from collocated drifters and altimetric products. First, we confirm the strong total wind effect of $\approx 3\%$ ($\approx 2\%$ of pure windage), but also show the existence of a deflection angle of $\approx 10^\circ$ between *Sargassum* drift and wind directions. Second, our results suggest reducing the role of currents on drift to 80% of its velocity, likely because of *Sargassum* resistance to flow. These results should significantly improve our understanding of the drivers of *Sargassum* dynamics and the forecast of stranding events.

Keywords *Sargassum* algae; Computer Vision; Regression; Tracking; Remote Sensing; Drift; Collocation; Drifter; Tropical North Atlantic; Time series.

4.2. Introduction

In recent years, the extent of the Great Atlantic *Sargassum* Belt (GASB) has stabilized to a high level of *Sargassum* biomass associated with harmful stranding events. Countries affected by stranding along their coast are struggling to face the economical, ecological and sanitary damages (CHÁVEZ et al., 2020; de LANAY et al., 2022; MERLE et al., 2021; RESIERE et al., 2018; RODRÍGUEZ-MARTIÉNEZ et al., 2019; VAN TUSSEN BROEK et al., 2017). As a consequence, strong efforts are put in monitoring *Sargassum* distribution (CUEVAS et al., 2018; DESCLOITRES et al., 2021; J. F. GOWER & KING, 2011; ODY et al., 2019; M. WANG & HU, 2016; M. WANG et al., 2019b) and modelling *Sargassum* drift and growth (BERON-VERA & MIRON, 2020b; M. T. BROOKS et al., 2018; JOUANNO et al., 2021b; PUTMAN et al., 2018).

As for several other surface drifting objects, most models of *Sargassum* drift included a windage component (BERLINE et al., 2020; JOHNS et al., 2020; JOUANNO et al., 2021a; KWON et al., 2019; PUTMAN et al., 2020) to represent the direct effect of wind and waves on drift velocity. Model results were shown to be sensitive to windage (BERLINE et al., 2020; KWON et al., 2019; MIRON et al., 2020; PUTMAN et al., 2020) and it is therefore key to estimate this factor accurately. Up to now, windage was tested in simulations and calibrated with either *in-situ* or remote sensing data (BERLINE et al., 2020; JOUANNO et al., 2021a; KWON et al., 2019; PUTMAN et al., 2020). However, except for PUTMAN et al., 2020 who used a limited number of *Sargassum* rafts tracked trajectories, there is currently no direct measure of windage.

Satellite imagery may allow tracking *Sargassum* aggregates displacement on images in order to extract velocity and estimate windage. However, *Sargassum* detection from space is hampered by the high cloud coverage and aggregates shapes change rapidly, therefore a short satellite revisit time is necessary in order to track aggregates.

4. Suivi des agrégats de sargasses et modélisation de leur dérive – 4.3. Materials and Methods

High resolution sensors (e.g., MSI, Landsat8) allow describing the fine scale structure of aggregates (DESCLOITRES et al., 2021; ODY et al., 2019) but their revisit time (5-8 days) precludes aggregate tracking from one image to the next. Moderate-Resolution Imaging Spectroradiometer (MODIS), with two daily observations separated by approximately 3 hours, is best suited for tracking *Sargassum* aggregates.

Here, we used successive MODIS *Sargassum* detection images provided by PODLEJSKI et al., 2022 over the 2015-2021 period and applied computer vision tracking algorithms to compute *Sargassum* velocity. We then used complex linear regressions to relate this velocity to estimates of currents and wind derived from altimetry and velocity of collocated drifters (LUMPKIN & PAZOS, 2007) and to assess windage. Finally, we propose a new model of *Sargassum* drift.

4.3. Materials and Methods

4.3.1. Overview

An overview of the whole approach made to extract *Sargassum* drift is shown in Fig. 4.1. First, *Sargassum* detections mapped at 1 km resolution from MODIS Aqua and Terra were collected from <https://doi.org/10.12770/8fe1cdcb-f4ea-4c81-8543-50f0b39b4eca>. The production process is described in DESCLOITRES et al., 2021 for extracting the Alternative Floating Algae Index (AFAI) and deducing *Sargassum* coverage. The filtering method developed in PODLEJSKI et al., 2022 was used to remove the false detections (false positive) caused by cloud, sunglint or coastal contamination. We used here filtered daily images at 1 km resolution. Among these images, we selected daily scenes with both Aqua and Terra clear *Sargassum* observations. For the comparison between *Sargassum* and drifters velocities, the Global Drifter Program (GDP) (LUMPKIN & PAZOS, 2007) data were collected and collocation cases (simultaneous presence in a range of 20 km) between *Sargassum* and drifters were extracted (4.6.1). The dataset of collocation was split between drogued drifters and undrogued drifters.

MODIS images were analysed with computer vision algorithms to match *Sargassum* aggregates from successive images and thereby derive their velocity (section 4.3.2). This matching process was validated manually to ensure reliability of measurements. Then, geostrophic currents and wind were interpolated at the position and time of each measurement (section 4.3.3). Finally, a statistical analysis was performed in order to infer the links between the velocities of *Sargassum* aggregates, drifters, surface current and wind, using linear regressions in the complex space (section 4.3.4).

4. Suivi des agrégats de sargasses et modélisation de leur dérive – 4.3. Materials and Methods

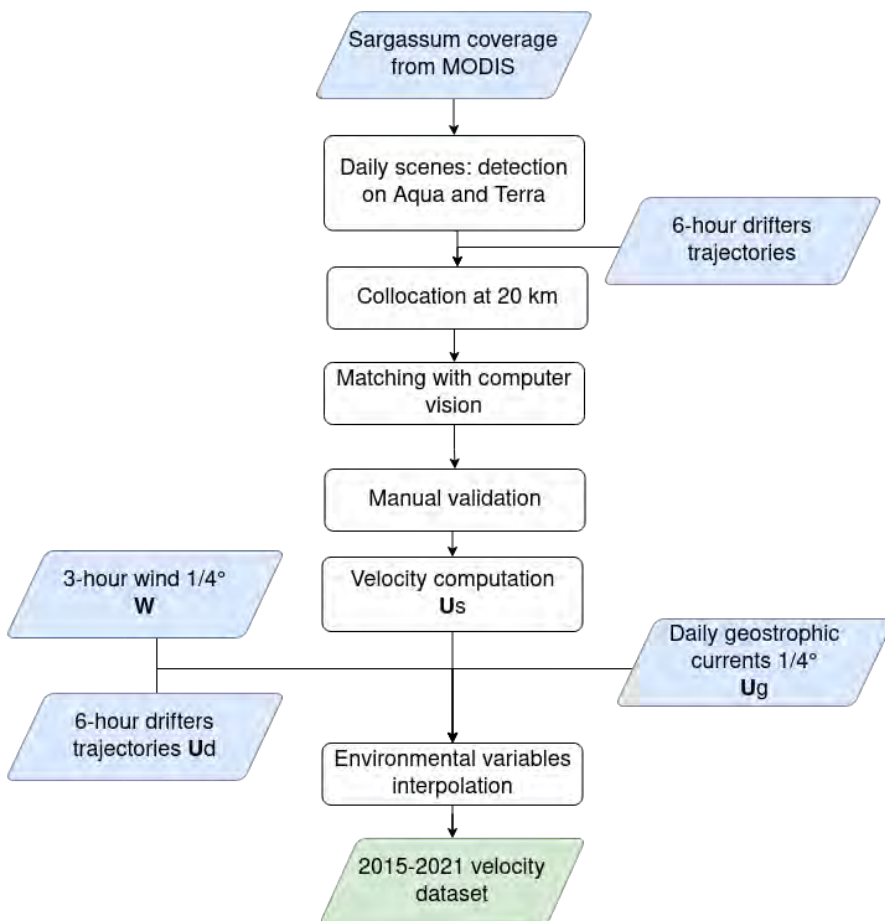


FIGURE 4.1. : Workflow of the *Sargassum* aggregates velocity extraction process, with data sources indicated in blue, results in green and processes in white. \mathbf{W} , \mathbf{U}_d , \mathbf{U}_s , \mathbf{U}_G are wind, drifter, *Sargassum* and geostrophic current velocities, respectively.

4.3.2. Images matching to derive *Sargassum* velocity

Based on the two daily MODIS images of selected *Sargassum* aggregates, a matching process was performed in order to retrieve the two successive positions of the aggregate and thereby estimate its velocity. Two different algorithms were applied on a 100×100 km AFAI images subset around the collocated drifter position (50 km range), namely Scale Invariant Feature Transform (SIFT) (LOWE, 2004) and optical flow (OF) as implemented in FARNEBÄCK, 2003. Lucas-Kanade (LUCAS, KANADE et al., 1981) and Gradient Location and Orientation Histogram (GLOH) (MIKOŁAJCZYK & SCHMID, 2005) algorithms were tested on the images, but showed lower performances. All image processing was performed with Python 3 and the OpenCV library.

SIFT was used to extract key points for describing aggregates shape based on Terra and Aqua AFAI images. Using these key points, the best subset of congruent linear 2D translations (no scaling, no rotation) was extracted, and averaged to compute

4. Suivi des agrégats de sargasses et modélisation de leur dérive – 4.3. Materials and Methods

the corresponding *Sargassum* velocity (see 4.6.2). Then, OF algorithm was applied to confirm SIFT results. Inconsistent cases between the drift directions estimated from SIFT and OF were rejected, i.e., when the absolute angle between the estimated directions was larger than 25°. We retained velocity from SIFT as it was found more robust than OF.

Finally, a manual validation was performed on all remaining cases, based on an overall visual inspection of matching cases with a focus on all matching pairs of key points to ensure they were valid.

4.3.3. Current and wind velocities

As a direct estimation of the surface current, we used drifter data. The drifter data were downloaded from the GDP website (<https://www.aoml.noaa.gov/phod/gdp/>, LUMPKIN et CENTURIONI, 2019). The Surface Velocity Program (SVP) drifters are made of a low-windage surface satellite transmitter (35 cm spherical hull) tethered by a thin cable to a semi-rigid sea anchor (the so-called “Holey-Sock” drogue) centred at 15 m depth. These properties allow drifters to follow reliably the 15 m depth currents. When a drifter loses its drogue, it tends to follow the surface current, but with a non-negligible effect of wind.

As an indirect estimation of the ocean surface current, we used the altimetry-derived geostrophic velocity at 1/4 °daily resolution available from www.aviso.altimetry.fr. Altimetry-derived current was considered as the local surface current not affected by wind.

As estimation of the surface wind velocity, we used the 10-metre wind from ECMWF ERA5 reanalysis at the 1/4 °hourly resolution (HERSBACH & DEE, 2016) (from <https://cds.climate.copernicus.eu>)

After extraction, both surface current and wind fields were interpolated at the position and time of each collocated *Sargassum* aggregate/drifter pair.

4.3.4. Statistical analyses

The overall idea here is to analyse to what extent the surface current, either from geostrophic estimates or from collocated drifters, and the wind can explain the *Sargassum* aggregate velocity measured from MODIS images.

We used the complex notation for vectors (KUNDU, 1976; POULAIN et al., 2009; SUTHERLAND et al., 2020) :

$$\mathbf{U} = r e^{i\theta} \text{ or } u + i v \quad (4.1)$$

with \mathbf{U} a velocity vector expressed as a complex number, r its norm, θ its argument (between $-\pi$ and π , anticlockwise) and u, v the eastward and northward components of the velocity.

A general model of *Sargassum* velocity \mathbf{U}_S can be written as follows (MULET et al., 2021) :

$$\mathbf{U}_S = \mathbf{U}_G + \mathbf{U}_A + \varepsilon = \mathbf{U}_G + \mathbf{U}_T + \mathbf{U}_I + \mathbf{U}_E + \mathbf{U}_{St} + \mathbf{U}_W + \varepsilon \quad (4.2)$$

where \mathbf{U}_G , \mathbf{U}_A , \mathbf{U}_T , \mathbf{U}_I , \mathbf{U}_E , \mathbf{U}_{St} , \mathbf{U}_W and ε are the *Sargassum*, the geostrophic current, the ageostrophic current, the tidal current, the inertial current, the Ekman current, the Stokes drift, the windage and the error term, respectively. The tidal current is considered negligible in the offshore cases studied. At the latitudes of interest (0 to 25°N) the Coriolis force is weak. Inspection of drifters trajectories near the collocations revealed only a few (<10) cases of inertial oscillations. As a consequence, we consider the inertial current as negligible. Following VAN SEBILLE et al., 2020, we assume that the Stokes drift and the windage can be combined. The Ekman current is also due to the wind forcing, these three terms can therefore be combined in a unique term depending on the wind :

$$\mathbf{U}_S = \alpha_G^S \mathbf{U}_G + \beta_G^S \mathbf{W} + \varepsilon \quad (4.3)$$

where \mathbf{W} is the wind and α_G^S and β_G^S are complex parameters. The parameter α_G^S represents the role of geostrophic current on *Sargassum* aggregate drift, and the parameter β_G^S represents the effect of Ekman current, Stokes drift and windage. Similarly, drifter velocity can be expressed as follows :

$$\mathbf{U}_D = \alpha_G^D \mathbf{U}_G + \beta_G^D \mathbf{W} + \varepsilon \quad (4.4)$$

with \mathbf{U}_D the drifter velocity. Here the β_G^D parameter depends largely on whether the drifter has lost its drogue or not. We thus estimated this parameter separately for drogued and undrogued drifters.

We can also relate directly *Sargassum* and drifters velocities using the following models :

$$\mathbf{U}_S = \alpha_{D,d}^S \mathbf{U}_{D,d} + \beta_{D,d}^S \mathbf{W} + \varepsilon \quad (4.5)$$

$$\mathbf{U}_S = \alpha_{D,u}^S \mathbf{U}_{D,u} + \beta_{D,u}^S \mathbf{W} + \varepsilon \quad (4.6)$$

where $\mathbf{U}_{D,d}$, $\mathbf{U}_{D,u}$ are the velocities for drogued and undrogued drifters, respectively. Here the β_D^S parameter does not include the effect of \mathbf{U}_E which is included in the α_D^S parameter.

For all models, we used linear regressions in the complex space to find the set of complex parameters minimising the error ε (4.6.3).

Also, the models were tested using Ekman-corrected velocities to distinguish between Ekman component and windage (4.6.5). Real parameters (no angle) used in the literature were tested for comparison. Each regression was evaluated with the coefficient of determination R^2 (square of the real part of the complex correlation coefficient). Significance tests were applied for both models (Fisher test) and parameters (Student test). The bootstrap method was set up to estimate robust parameters, their confidence interval and the associated coefficient of determination (see 4.6.4).

4. Suivi des agrégats de sargasses et modélisation de leur dérive – 4.4. Results

In order to further refine the regression models, outliers were isolated. Based on leave one out, the distance (error) between observations and model predictions was computed. By looking at the largest computed distance values, 4 cases were excluded where the *Sargassum* velocity direction was opposite to both wind and geostrophic currents.

4.4. Results

Over the period 2015-2021, we found 2754 cases of a *Sargassum* aggregate detected in both MODIS Terra and Aqua images and with a drifter of the Global Drifter Program passing by (see Table 4.1). Among them, for 240 cases we managed to match the *Sargassum* aggregate in Terra and Aqua images and could therefore estimate the aggregate velocity. An illustrative example of the matching process using SIFT is shown in Fig. 4.2. Our manual validation filtered out 48 more cases, and we ended up with 192 cases, 98 with a collocated drogued drifter and 94 with an undrogued drifter. This strict selection guarantees the estimates' accuracy of the drift velocity and a sufficient dataset for further statistical analysis.

Year	2015	2016	2017	2018	2019	2020	2021	All
Daily scenes	341	98	204	713	461	515	422	2754
Matching collocations	23	2	19	65	51	47	33	240
Valid drogued collocations	13	1	10	24	17	27	11	98
Valid undrogued collocations	3	1	9	26	26	14	16	94

TABLEAU 4.1. : Number of collocation cases per year at different steps of the method.

First after selection of the daily scenes with detections on Terra and Aqua, second after performing matching algorithms and finally after manual validation.

4. Suivi des agrégats de sargasses et modélisation de leur dérive – 4.4. Results

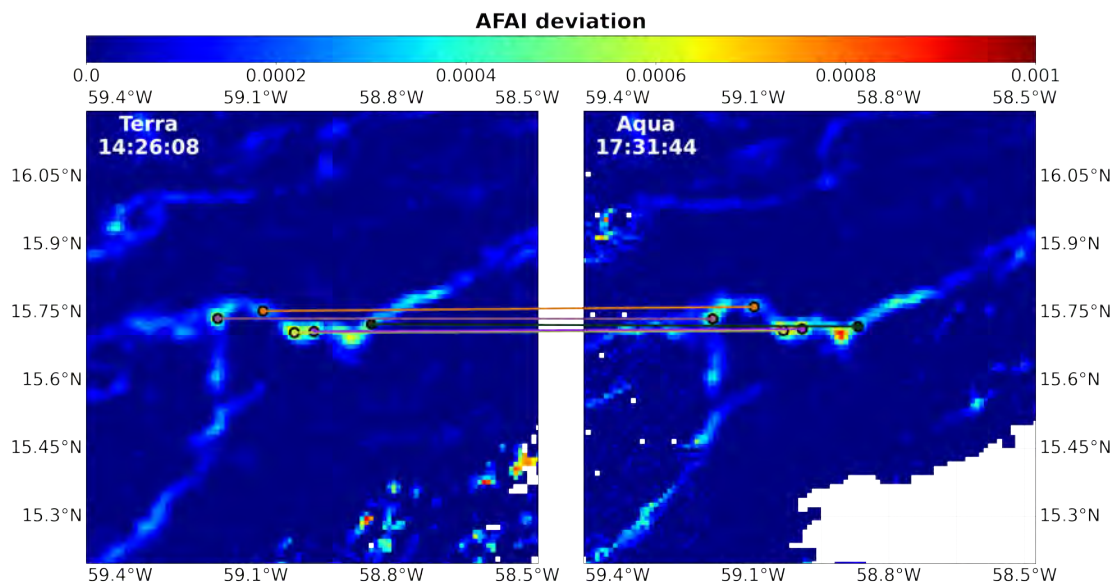


FIGURE 4.2. : Example of image matching of January 6th 2021 for a collocated case with SIFT key points extracted from Terra and Aqua 100 x 100 pixels images. The five consistent matches are shown as linked pairs of points. The colorbar refers to AFAI deviation from background (PODLEJSKI et al., 2022), the white area is the mask. The collocated drifter is located at the centre of each image (not shown).

The distribution of these cases with respect to time and space is shown in Fig. 4.3. Fig. 4.4 shows the distribution of the intensity and direction of velocities for the detected *Sargassum* aggregates, collocated drifters, and interpolated geostrophic current and wind at the time and position of the collocated drifters.

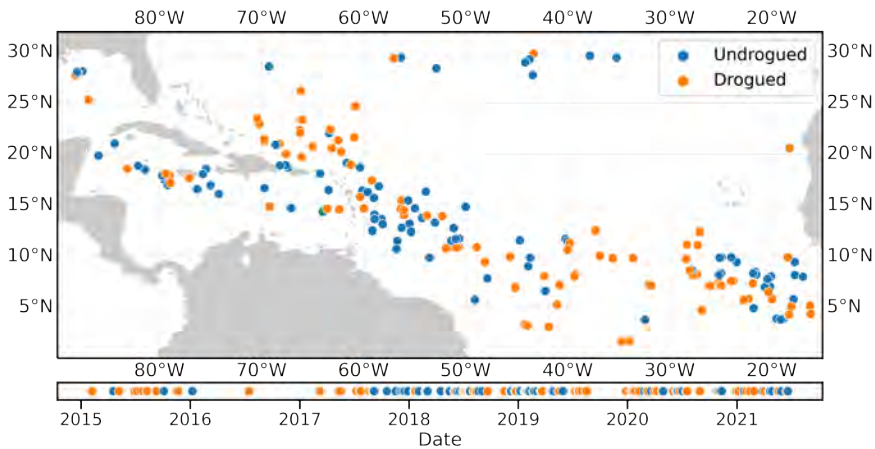


FIGURE 4.3. : Collocated *Sargassum*/drifter pairs ($n = 192$) distribution in space and time, split into drogued (orange) and undrogued (blue) drifters.

4. Suivi des agrégats de sargasses et modélisation de leur dérive – 4.4. Results

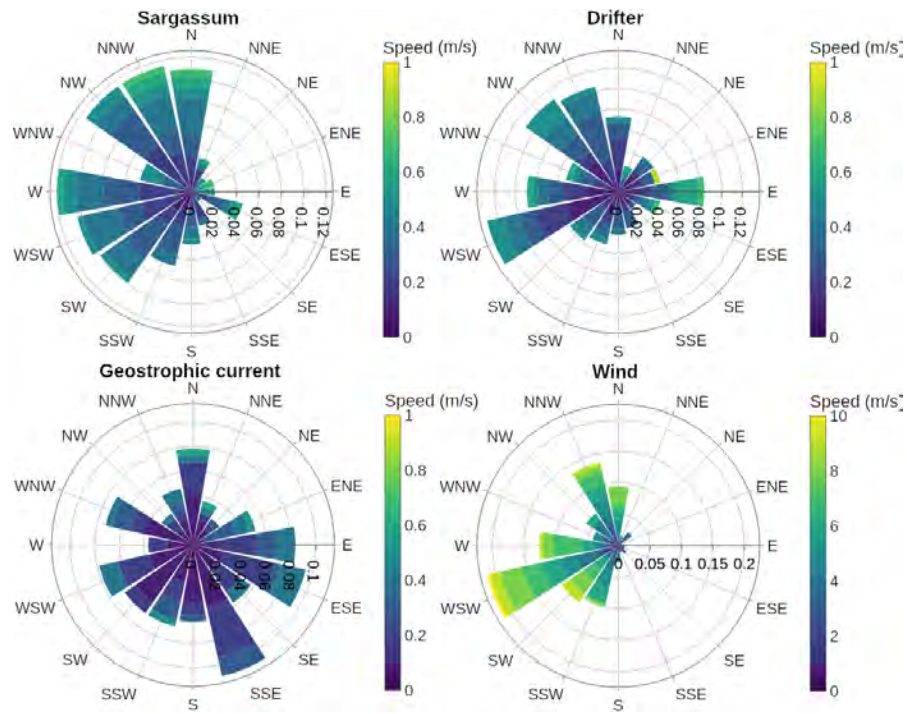


FIGURE 4.4. : Wind-rose of velocities for the detected *Sargassum* aggregates, collocated drifters (drogued and undrogued), and interpolated geostrophic current and wind at the time and location of the collocated drifters. Colours indicate the speed, and bar lengths the frequency. Note that all velocity directions are expressed in terms of vector azimuth, i.e. the direction toward which the vectors lead.

Collocated *Sargassum*/drifter pairs were homogeneously distributed in the area of *Sargassum* presence along the time series 2015-2021 (Fig. 4.3). Geostrophic currents had a rather uniform orientation distribution, whereas *Sargassum*, drifter and wind velocity orientations were primarily westward (Fig. 4.4). The 4 variables are correlated. The correlation coefficients (norm of the complex coefficients) for \mathbf{U}_S against \mathbf{U}_D and \mathbf{U}_G are 0.80 and 0.47, respectively. While \mathbf{W} against \mathbf{U}_D correlation was 0.37 and \mathbf{W} against \mathbf{U}_G correlation was only 0.18.

In a first set of regression models, we explored the relation of *Sargassum* velocity \mathbf{U}_S and drifter velocity \mathbf{U}_D against geostrophic and wind velocities \mathbf{U}_G and \mathbf{W} (Table 4.2). We obtained statistically significant correlations in all tested models, but with weak coefficients of determination R^2 (maximum of 0.47). All parameters bootstrapped means were consistent with the direct parameter estimation (not shown) and their standard deviation was approximately 10% of their value. Geostrophic current \mathbf{U}_G was projected on \mathbf{U}_S and \mathbf{U}_D with small angle values (-14° to 7°). The norm of the geostrophic current coefficient was always smaller than 1 (0.59 to 0.85). Wind velocity was projected with an angle of 15-65 ° to the right of the wind direction, the angle estimation was weakly variable ($\pm 5^\circ$). The norm of the wind coefficient corresponded to 3-4% of its velocity for *Sargassum* and undrogued drifters, whereas drogued drifters

4. Suivi des agrégats de sargasses et modélisation de leur dérive – 4.4. Results

were impacted by 1% of the wind velocity only.

Model	α	β	R ²	N _{obs}
$\mathbf{U}_S = \alpha_G^S \mathbf{U}_G + \beta_G^S \mathbf{W}$	$0.593 \pm 0.065 \exp(-14.0 \pm 8.8^\circ i)$	0	-0.02	192
	0	$0.038 \pm 0.003 \exp(-17.4 \pm 3.5^\circ i)$	0.26	192
	$0.564 \pm 0.055 \exp(1.6 \pm 5.4^\circ i)$	$0.038 \pm 0.002 \exp(-21.2 \pm 3.0^\circ i)$	0.46	192
$\mathbf{U}_{D,u} = \alpha_G^{D,u} \mathbf{U}_G + \beta_G^{D,u} \mathbf{W}$	$0.778 \pm 0.083 \exp(-11.5 \pm 8.5^\circ i)$	0	0.10	94
	0	$0.033 \pm 0.004 \exp(-14.9 \pm 5.9^\circ i)$	0.18	94
	$0.659 \pm 0.077 \exp(0.6 \pm 7.1^\circ i)$	$0.031 \pm 0.003 \exp(-21.4 \pm 5.8^\circ i)$	0.43	94
$\mathbf{U}_{D,d} = \alpha_G^{D,d} \mathbf{U}_G + \beta_G^{D,d} \mathbf{W}$	$0.8 \pm 0.073 \exp(6.3 \pm 5.2^\circ i)$	0	0.38	98
	0	$0.01 \pm 0.003 \exp(-64.2 \pm 35.1^\circ i)$	0.02	98
	$0.852 \pm 0.068 \exp(6.7 \pm 4.4^\circ i)$	$0.013 \pm 0.003 \exp(-61.4 \pm 13.7^\circ i)$	0.47	98

TABLEAU 4.2. : Regression models between measured velocities and environmental variables. \mathbf{U}_S , $\mathbf{U}_{D,d}$, $\mathbf{U}_{D,u}$, \mathbf{U}_G and \mathbf{W} are velocities for the detected *Sargassum* aggregates, collocated drogued/undrogued drifters, and interpolated geostrophic current and wind at the time and location of the *Sargassum* aggregates. Variables and estimated parameters are complex numbers, here displayed in exponential notation with angles in degrees anticlockwise. Depending on the regression model, some parameters are forced to real values (zero). The norm and the argument are associated with a standard deviation estimated over 5000 bootstrapped datasets. All regressions were statistically significant ($p < 0.01$), negative R² is due to model constraint (no intercept).

In a second set of regression models, we explored the relation of \mathbf{U}_S against \mathbf{U}_D and \mathbf{W} . (Table 4.3). We found much higher R² values (0.55-0.78) than for the first set of regressions. R² values were smaller for undrogued than for drogued drifters, and associated parameters were also generally more variable. The wind coefficient given by the regressions was 2-3%, deviated to the right of the wind.

Model	α	β	R ²	N _{obs}
$\mathbf{U}_S = \alpha_{D,u}^S \mathbf{U}_{D,u} + \beta_{D,u}^S \mathbf{W}$	$0.957 \pm 0.042 \exp(0.6 \pm 2.7^\circ i)$	0	0.62	94
	$0.681 \pm 0.048 \exp(4.3 \pm 4.1^\circ i)$	$0.021 \pm 0.003 \exp(-23.1 \pm 7.6^\circ i)$	0.66	94
	1	0.01	0.57	94
$\mathbf{U}_S = \alpha_{D,d}^S \mathbf{U}_{D,d} + \beta_{D,d}^S \mathbf{W}$	$0.889 \pm 0.048 \exp(4.9 \pm 3.4^\circ i)$	0	0.55	98
	$0.787 \pm 0.038 \exp(-2.3 \pm 2.9^\circ i)$	$0.029 \pm 0.002 \exp(-8.6 \pm 4.2^\circ i)$	0.78	98
	1	0.03	0.74	98

TABLEAU 4.3. : Regression models for *Sargassum* velocity using drifters velocity as explaining variable. Same as Table 4.2

4.5. Discussion

4.5.1. General drift patterns

We found drifter and *Sargassum* velocities directed mainly westward. Indeed, most *Sargassum* detections are located between 0 and 20°N in the tropical Atlantic (Fig. 3). In this region, trade winds are westward, as are the main surface currents (North and South Equatorial Currents and their branches). The only eastward current is the North Equatorial Counter Current at 7°N (JOHNS et al., 2020). The drifter and *Sargassum* velocities range ($< 0.9 \text{ ms}^{-1}$) is typical for offshore surface currents, with *Sargassum* median velocity slightly higher than drifters ($0.31 \text{ vs } 0.24 \text{ ms}^{-1}$).

4.5.2. Extraction of *Sargassum* velocities : method limitations

In the absence of *in situ* validation data, we assessed the velocities \mathbf{U}_S of *Sargassum* aggregates measured in MODIS successive images by comparing them with independent velocities \mathbf{U}_D of collocated surface drifters and local geostrophic currents \mathbf{U}_G . The good correlation (0.8, *p-value* < 0.01) obtained for \mathbf{U}_S against \mathbf{U}_D gives us confidence in the reliability of our method for extracting *Sargassum* velocities. The average *Sargassum* drift distance between successive images was 3.4 km. As the image's resolution was mapped at 1 km, the measurements have inherent uncertainty (MASUOKA et al., 1998), but the redundancy between matching pairs of pixels used in the images (from 4 up to 20) allowed us to stand out from noise and to ensure their robustness. Other methods to derive current velocity from satellite images (Maximum Cross Correlation, e.g. BARTON, 2002, YANG et al., 2015) used all pixels in the image with similar temporal offset (1-4 hours) and resolution (1 km) as ours. In comparison, our sparse approach (few key points instead of all pixels) with SIFT allows focusing only on relevant descriptors of the *Sargassum* shape and to easily select the velocity summarising the overall transport.

The distance used to consider *Sargassum* and drifters as collocated was set to 20 km as a compromise to obtain a significant number of collocation cases and to support the assumption that environmental variables (wind and currents) are the same for both objects. For the image matching process, we used a 50 km range around the drifter in order to benefit from more key points and context. The two distance values are smaller than the Rossby radius of deformation, i.e., the scale of current autocovariance, estimated > 60 km at latitudes < 20° (CHELTON et al., 1998).

Given these methodological choices and the 6 year-long time series of daily data, only a limited number (200) of *Sargassum* velocities were retrieved. This is mostly due to high cloud coverage (> 60% on average for daily images) in the tropical Atlantic area that prevented matching aggregates in successive images. Also, significant distortion of aggregates between images and their elongated shapes (e.g., linear aggregates provide few key points) prevented matching. Several solutions could be pursued to expand this dataset. Manual matching could be pursued to complement velocity extraction, but with presumably small amount of new scenes. The matching process

4. Suivi des agrégats de sargasses et modélisation de leur dérive – 4.5. Discussion

could be extended to others collocated tracked objects, such as Fish Aggregating Devices (IMZILEN et al., 2019). We could also try to match aggregates more distant in time. However, the match would hardly be automatic, because of the distortion increasing over time, but could be performed manually for specific regions or time of interest. Using other satellite products, such as Visible Infrared Imaging Radiometer Suite (VIIRS) or Geostationary Operational Environmental Satellite (GOES) could also be a way to expand our dataset of *Sargassum* velocities. Indeed, preliminary results suggest that VIIRS gives results analogous to MODIS (M. WANG & HU, 2020) and that GOES seems promising due to its high temporal resolution (MINGHELLI et al., 2021).

4.5.3. Physical and statistical approximations

The Stokes drift was considered combined to wind effect. Replacing \mathbf{W} by Stokes velocity from ECMWF ERA5 decreased the R^2 values (not shown). Adding Stokes velocity as an additional explanatory variable in the regressions was associated with non-significant *p-value* and negligible R^2 improvement, as Stokes velocity was highly correlated with wind velocity ($r=0.83$). More accurate data are needed to separate the effect of Stokes drift and wind in the windage, similarly to SUTHERLAND et al., 2020.

For all the models, we chose to force the regressions with no intercept (constant term) as it is hardly interpretable physically. When an intercept was included, regressions with two variables did not show major R^2 improvement nor changes of parameter values, because the intercept term was very low ($<0.05 \text{ ms}^{-1}$). This validates our hypothesis of null intercept and indicates that the results were weakly biased, and the models were linear. As the distribution of residuals is Gaussian (not shown), the remaining unexplained variability is likely due to the uncertainty of observations. Improving the result probably lies in better data accuracy.

4.5.4. Geostrophic component of *Sargassum* drift

The comparison between drifter and *Sargassum* regression models provides good indications on how *Sargassum* drift differs from drifters. First, on average, the geostrophic current component is not deviated for *Sargassum* velocity (low α_G^S angle), and this is also true for drifters. This confirms our hypothesis of negligible inertial effect for these objects at the considered timescale (3 hours). This contrasts with the results of M. T. BROOKS et al., 2019, likely because of their much larger timescale (8 days).

Second, drifter velocity is explained by a fraction of geostrophic current velocity ($\alpha_G^D=85\%$ for drogued drifters and 66% for undrogued drifters). This is also true when using Ekman-corrected drifter velocities (4.6.5). This contrasts with previous studies showing that the Ekman-corrected drifter velocities were on average 1.4 times higher than the altimeter-derived geostrophic currents (LAGERLOEF et al., 1999). These contrasting results are likely due to major progress in spatial and temporal resolutions of both altimetric product (1/4° daily data used here vs. 1° 10-day data in LAGERLOEF et al., 1999) and drifter position frequency (6-h here vs. 5-day in LAGERLOEF et al., 1999). The parameter α_G^D was found < 1 possibly because of the fine scale variability of

4. Suivi des agrégats de sargasses et modélisation de leur dérive – 4.5. Discussion

drifters velocities that are not captured by altimetry. In addition, as the α_G^S parameter was weaker than α_G^D (< 56%), this suggests a flow resistance (i.e. viscosity) of *Sargassum* aggregates that slows them down compared to local currents and nearby drifters.

4.5.5. Windage and Ekman component of *Sargassum* drift

The parameter β_G^S , i.e. the wind effect on *Sargassum* drift, was deviated to the right of the wind direction with an angle of 21° while $\beta_{D,d}^S$ is deviated with an angle of 9° (Table 4.2 and 4.3). Deviation to the right of the wind is expected from Ekman spiral theory (EKMAN, 1905). As \mathbf{U}_S and \mathbf{U}_D included the Ekman current, β_D^S is a combination of Ekman current (45° at the surface) and windage (weak deflection). This is confirmed by regressions performed on \mathbf{U}_S and \mathbf{U}_D Ekman-corrected velocities (4.6.5), where deflection angles were lower for *Sargassum*, 9° comparing to \mathbf{U}_G and 4° to $\mathbf{U}_{D,d}$.

Regressing the *Sargassum* velocity against the geostrophic current \mathbf{U}_G and wind gives the total effect of wind on *Sargassum* (Table 4.2), evaluated here at $\beta_G^S=3.8\%$ of the wind speed. This total effect includes Ekman current plus windage. Correcting *Sargassum* velocities from the Ekman currents (see 4.6.5) reduces β_G^S to 2.6%, which is pure windage. Regressing the *Sargassum* velocity against the drogued drifter velocities $\mathbf{U}_{D,d}$ (15 m depth current) and wind provides a total wind effect of $\approx 3\%$ of the wind velocity, but with a better fit ($R^2=0.78$ against 0.46). Removing the Ekman current, estimated windage is 2.1%.

This windage ($\approx 2\%$) is consistent with literature for undrogued SVP drifters (BRÜGGE & DENGG, 1991; PAZAN & NIILER, 2001; POULAIN et al., 1996) and for *Sargassum* with a windage factor that was recently reassessed between 1-3% (PUTMAN et al., 2020). Similarly to our results, studies on oil spill drift modelling highlighted the wind-induced drift corresponding to $\approx 2\%$ of the wind speed with a deviation angle on the right of $\approx 20 - 25^\circ$ (LE HÉNAFF et al., 2012). The wind effect coefficient for *Sargassum* β_D^S may not be constant. Indeed, regressions separating low and high wind cases gave values of 0.08 and 0.02 respectively (not shown). This strong dependence on wind speed may result from *Sargassum* mixing over a deeper layer as wind speed increases (ODY et al., 2019; WOODCOCK, 1993). The Ekman component varies very little over the first few meters, whereas windage may strongly decrease with the sinking of *Sargassum*.

Although the wind effect coefficient ($\beta_{D,d}^S$) is rather small, $\beta_{D,d}^S W$ represents on average 42% of the *Sargassum* drift velocity due to the high wind velocity. This result reinforces the view of a strong impact of wind on *Sargassum* and highlights the importance of including wind contribution into *Sargassum* drift models.

4.5.6. Proposed model of *Sargassum* drift

Drifters velocity is a good proxy for local currents (geostrophic plus Ekman). Undrogued drifters, supposedly more similar to *Sargassum* (VAN SEBILLE et al., 2021), were associated with higher variability and lower R^2 values than drogued drifters. Thus, the regression explaining *Sargassum* velocity with the drogued drifters and wind velocity can be exploited to better predict *Sargassum* drift. Considering the inferred

4. Suivi des agrégats de sargasses et modélisation de leur dérive – 4.6. Appendices

parameters of Table 4.3, we propose the following *Sargassum* drift model :

$$\mathbf{U}_S = 0.8\mathbf{U} + 0.03e^{-10^\circ i}\mathbf{W} \quad (4.7)$$

Where \mathbf{U}_S , \mathbf{U} and \mathbf{W} are the *Sargassum*, the total current at 15 m depth (geostrophic plus Ekman) and the wind velocities at 10 m. On average, using this model, *Sargassum* velocity of 0.36 ms^{-1} is decomposed into the contributions of current (geostrophic plus Ekman) of 0.21 ms^{-1} and wind of 0.15 ms^{-1} .

Using the complex parameters proposed here allowed a gain of 4% in the R^2 values (Table 4.3) in comparison to using real parameters ($\alpha_{D,d}^S = 1$ and $\beta_{D,d}^S = 3\%$) as in previous studies (BERLINE et al., 2020; JOHNS et al., 2020; PUTMAN et al., 2018; PUTMAN et al., 2020). However, this modest improvement corresponds on average to an error reduction of 0.13 ms^{-1} , which translates into an error reduction of 1.4 km on locations over our 3 hours measurements. These results suggest that reducing the role of current to 80% of its velocity and using a wind factor of 3% deflected 10° to the right should lead to significant improvements in further drift simulations.

4.6. Appendices

4.6.1. Collocation between *Sargassum* and drifter

A collocation was defined as a situation where a drifter was close ($< 20 \text{ km}$) from at least one detected *Sargassum* pixel, i.e., a pixel which AFAI is above the threshold defined in M. WANG et HU, 2016). More specifically, the process followed those steps : 1) the Aqua and Terra timestamp (20 km median filter) was computed at every 12 :00 UTC drifter position; 2) the drifter position was linearly interpolated at the average time between Aqua and Terra; 3) The scene was considered collocated if there was a *Sargassum* pixel in a box of 40 pixels around that interpolated position.

4.6.2. Matching on SIFT key points

In order to extract the *Sargassum* velocity, images were matched based on aggregates' shape. The SIFT algorithm allowed extracting key points to describe the *Sargassum* shape and position. Then, an ad-hoc algorithm was developed to search for the best 2D translation explaining the drift. The corresponding code, inspired from the RANdom SAmple Consensus (RANSAC) approach (DERPANIS, 2010), is detailed in the pseudo-algorithm 1. All possible translations between the two sets of points were tested, and the one maximising the counter (thus the most likely) was retained. Images pairs with less than 4 matching points were excluded. For remaining cases, matching pairs displacements in the scene were averaged to compute one value of *Sargassum* velocity that was added to the dataset.

Algorithm 1 Translation evaluation from SIFT key points

Require: T_{pts}, A_{pts} the list of SIFT key points for Terra and Aqua images

```

for each  $T_{pt} \in T_{pts}, A_{pt} \in A_{pts}$  do
     $Counter \leftarrow 0$ 
     $Translation \leftarrow A_{pt} - T_{pt}$ 
    for each  $T_{temp} \in T_{pts}, A_{temp} \in A_{pts}$  do
        if Distance( $Translation + T_{temp}, A_{temp}$ )  $\leq 500$  m then
             $Counter \leftarrow Counter + 1$ 
        end if
    end for
end for
```

4.6.3. Complex linear regression

Let \mathbf{Z} be a random complex response variable with \mathbf{X} and \mathbf{Y} complex regressors. We have a sample $E = \{(\mathbf{X}_n, \mathbf{Y}_n, \mathbf{Z}_n), 1 \cdots N\}$ of size N of these variables. It is supposed that they are connected through a linear model of the form :

$$\mathbf{Z}_n = \alpha + \beta \mathbf{X}_n + \gamma \mathbf{Y}_n + \varepsilon_n, \quad n = 1 \cdots N,$$

where α, β and γ are complex parameters that must be estimated from the sample E and ε is a (complex) remainder whose norm is hoped to be as small as possible. As usual in a regression problem, the parameter estimation is done through least squares minimization of the cost function :

$$SSE(\alpha, \beta, \gamma) = \sum_{n=1}^N (\mathbf{Z}_n - \alpha - \beta \mathbf{X}_n - \gamma \mathbf{Y}_n)(\mathbf{Z}_n - \alpha - \beta \mathbf{X}_n - \gamma \mathbf{Y}_n)_\star,$$

where \mathbf{X}_\star denotes the complex conjugate of \mathbf{X} . Let construct the design matrix $M = (\mathbb{1}, X, Y)$ where $\mathbb{1}$ is the N -vector with entries $1+i1$, $X = (\mathbf{X}_1, \dots, \mathbf{X}_N)'$ and $Y = (\mathbf{Y}_1, \dots, \mathbf{Y}_N)'$ the N -vectors of the complex regressors. In matrix form, the cost function writes :

$$SSE(a) = (Z - Ma)^\star (Z - Ma),$$

where $a = (\alpha, \beta, \gamma)'$ is the vector of parameters and $Z = (\mathbf{Z}_1, \dots, \mathbf{Z}_N)'$, the vector of the response variable and Z^\star its transpose conjugate. Solution of the complex regression is given when solving the normal equations for the complex regression :

$$\hat{a} = (M^\star M)^{-1} M^\star Z$$

An estimated value of \mathbf{Z}_n is then obtained with : $\hat{\mathbf{Z}}_n = \hat{\alpha} + \hat{\beta} \mathbf{X}_n + \hat{\gamma} \mathbf{Y}_n$. One can also compute the estimated errors with : $\hat{\varepsilon}_n = \mathbf{Z}_n - \hat{\mathbf{Z}}_n$.

4.6.4. Bootstrapped confidence intervals for parameters

Suppose now a complex regression achieved with sample E and residuals estimated with $\hat{\varepsilon}_1, \dots, \hat{\varepsilon}_N$ as above. Consider a bootstrap replicate of the initial sample denoted as $E_B = \{(\mathbf{X}_n, \mathbf{Y}_n, \mathbf{Z}_n^B), n = 1 \dots N\}$ such that $\mathbf{Z}_n^B = \hat{\alpha} + \hat{\beta}\mathbf{X}_n + \hat{\gamma}\mathbf{Y}_n + \varepsilon_n^B$, where the residuals $\varepsilon_1^B, \dots, \varepsilon_N^B$ have been drawn from an estimated distribution of the residuals that uses $\hat{\varepsilon}_1, \dots, \hat{\varepsilon}_N$ as data. As these errors are complex numbers, this distribution is bivariate. It can be estimated using a Gaussian density with mean parameter being the vector of real and imaginary parts of the empirical mean error $\bar{\varepsilon} = \frac{1}{N} \sum_n \hat{\varepsilon}_n$ and variance parameter being the empirical covariance matrix between real and imaginary parts of the $\hat{\varepsilon}_n$.

Use now a bootstrap sample E_B to compute new estimates $\hat{\alpha}^B, \hat{\beta}^B$ and $\hat{\gamma}^B$. As this procedure can be repeated at wish, one can estimate boundaries of a 95%-confidence intervals as the quantiles of the empirical distribution for both real and imaginary parts of $\hat{\alpha}, \hat{\beta}$ and $\hat{\gamma}$.

Error values are simulated using bootstrapped errors obtained by sampling an estimated distribution function of the errors in place of its real unknown distribution. Bootstrapped samples of the data are then constructed and confidence intervals can be estimated for $\hat{\alpha}, \hat{\beta}$ and $\hat{\gamma}$ considered as true coefficients of the regression instead of α, β and γ .

4.6.5. Regressions using Ekman-corrected currents

We used formulas and constants from CUSHMAN-ROISIN et BECKERS, 2011 for computing Ekman current. The eddy viscosity ν_E was $10^{-2} \text{ m}^2 \text{s}^{-1}$, the drag coefficient C_d was 1.5×10^{-3} , the air density ρ_a was 1.20 kg m^{-3} and the water density ρ_0 was $10^{-3} \text{ kg m}^{-3}$. Considering that undrogued drifters and *Sargassum* aggregates drift in the surface layer of the ocean, the Ekman current estimated at $z = 0 \text{ m}$ was removed from U_S and $U_{D,u}$. The Ekman current estimated at $z = 15 \text{ m}$ was removed from $U_{D,d}$ because of their drogue centred at 15 m depth.

4. Suivi des agrégats de sargasses et modélisation de leur dérive – 4.6. Appendices

Model	α	β	R ²	N _{obs}
$\mathbf{U}_S = \alpha_G^S \mathbf{U}_G + \beta_G^S \mathbf{W}$	$0.602 \pm 0.062 \exp(-8.6 \pm 7.1^\circ i)$	0	0.11	192
	0	$0.026 \pm 0.003 \exp(-3.2 \pm 5.5^\circ i)$	0.14	192
	$0.567 \pm 0.057 \exp(1.0 \pm 5.6^\circ i)$	$0.026 \pm 0.002 \exp(-9.0 \pm 4.8^\circ i)$	0.35	192
$\mathbf{U}_{D,u} = \alpha_G^{D,u} \mathbf{U}_G + \beta_G^{D,u} \mathbf{W}$	$0.757 \pm 0.081 \exp(-4.9 \pm 7.2^\circ i)$	0	0.22	94
	0	$0.022 \pm 0.004 \exp(2.8 \pm 9.2^\circ i)$	0.08	94
	$0.666 \pm 0.078 \exp(1.1 \pm 7.2^\circ i)$	$0.019 \pm 0.003 \exp(-5.7 \pm 10.5^\circ i)$	0.35	94
$\mathbf{U}_{D,d} = \alpha_G^{D,d} \mathbf{U}_G + \beta_G^{D,d} \mathbf{W}$	$0.828 \pm 0.07 \exp(5.5 \pm 4.7^\circ i)$	0	0.42	98
	0	$0.005 \pm 0.003 \exp(32.2 \pm 108.9^\circ i)$	-0.01*	98
	$0.844 \pm 0.071 \exp(6.0 \pm 4.4^\circ i)$	$0.005 \pm 0.002 \exp(-38.0 \pm 68.6^\circ i)$	0.44	98
$\mathbf{U}_S = \alpha_{D,u}^S \mathbf{U}_{D,u} + \beta_{D,u}^S \mathbf{W}$	$0.875 \pm 0.046 \exp(-0.7 \pm 3.3^\circ i)$	0	0.57	94
	$0.699 \pm 0.047 \exp(4.2 \pm 4.0^\circ i)$	$0.017 \pm 0.002 \exp(-16.1 \pm 8.7^\circ i)$	0.62	94
$\mathbf{U}_S = \alpha_{D,d}^S \mathbf{U}_{D,d} + \beta_{D,d}^S \mathbf{W}$	$0.81 \pm 0.044 \exp(-2.3 \pm 3.3^\circ i)$	0	0.57	98
	$0.793 \pm 0.039 \exp(-1.6 \pm 2.8^\circ i)$	$0.021 \pm 0.002 \exp(-4.0 \pm 6.0^\circ i)$	0.74	98

TABLEAU 4.4. : Same as table 4.2 except that the velocities $\mathbf{U}_S, \mathbf{U}_{D,d}$ and $\mathbf{U}_{D,u}$ are corrected from Ekman current at either 0 or 15 meter depth.

4.6.6. Wind regressions

Model	α	β	R ²	N _{obs}
$\mathbf{U}_S = \alpha \mathbf{U}_G + \beta \mathbf{W}$	0	$0.084 \pm 0.016 \exp(1.6 \pm 11.6^\circ i)$	0.23	38
	$0.721 \pm 0.125 \exp(-9.6 \pm 11.2^\circ i)$	$0.074 \pm 0.014 \exp(-2.7 \pm 11.5^\circ i)$	0.49	38
$\mathbf{U}_{D,u} = \alpha \mathbf{U}_G + \beta \mathbf{W}$	0	$0.09 \pm 0.022 \exp(5.0 \pm 15.2^\circ i)$	0.21	17
	$0.834 \pm 0.17 \exp(-7.4 \pm 17.4^\circ i)$	$0.068 \pm 0.018 \exp(18.5 \pm 16.8^\circ i)$	0.54	17
$\mathbf{U}_{D,d} = \alpha \mathbf{U}_G + \beta \mathbf{W}$	0	$0.04 \pm 0.02 \exp(35.5 \pm 172.6^\circ i)$	-0.06	21
	$1.086 \pm 0.185 \exp(-5.2 \pm 8.8^\circ i)$	$0.04 \pm 0.019 \exp(-89.3 \pm 99.2^\circ i)$	0.46	21
$\mathbf{U}_S = \alpha \mathbf{U}_{D,u} + \beta \mathbf{W}$	$0.728 \pm 0.074 \exp(-4.6 \pm 7.2^\circ i)$	$0.038 \pm 0.012 \exp(-32.9 \pm 25.0^\circ i)$	0.81	17
$\mathbf{U}_S = \alpha \mathbf{U}_{D,d} + \beta \mathbf{W}$	$0.803 \pm 0.049 \exp(-6.3 \pm 4.2^\circ i)$	$0.079 \pm 0.009 \exp(11.3 \pm 7.7^\circ i)$	0.87	21

TABLEAU 4.5. : Same as Fig. 4.2 with cases where the wind is lower than 3 m s⁻¹.

4. Suivi des agrégats de sargasses et modélisation de leur dérive – 4.6. Appendices

Model	α	β	R ²	N_{obs}
$\mathbf{U}_S = \alpha \mathbf{U}_G + \beta \mathbf{W}$	0	$0.038 \pm 0.002 \exp(-20.4 \pm 3.7^\circ i)$	0.25	154
	$0.518 \pm 0.059 \exp(4.1 \pm 6.7^\circ i)$	$0.037 \pm 0.002 \exp(-23.4 \pm 3.5^\circ i)$	0.42	154
$\mathbf{U}_{D,u} = \alpha \mathbf{U}_G + \beta \mathbf{W}$	0	$0.035 \pm 0.003 \exp(-18.2 \pm 5.6^\circ i)$	0.15	77
	$0.618 \pm 0.084 \exp(-3.0 \pm 8.3^\circ i)$	$0.032 \pm 0.003 \exp(-23.5 \pm 6.0^\circ i)$	0.35	77
$\mathbf{U}_{D,d} = \alpha \mathbf{U}_G + \beta \mathbf{W}$	0	$0.012 \pm 0.004 \exp(-67.9 \pm 30.6^\circ i)$	0.03	77
	$0.813 \pm 0.072 \exp(10.3 \pm 5.0^\circ i)$	$0.014 \pm 0.003 \exp(-60.1 \pm 12.6^\circ i)$	0.49	77
$\mathbf{U}_S = \alpha \mathbf{U}_{D,u} + \beta \mathbf{W}$	$0.645 \pm 0.054 \exp(8.3 \pm 5.1^\circ i)$	$0.021 \pm 0.003 \exp(-26.3 \pm 7.9^\circ i)$	0.57	77
$\mathbf{U}_S = \alpha \mathbf{U}_{D,d} + \beta \mathbf{W}$	$0.798 \pm 0.046 \exp(0.1 \pm 3.3^\circ i)$	$0.027 \pm 0.002 \exp(-11.4 \pm 4.7^\circ i)$	0.78	77

TABLEAU 4.6. : Same as Fig. 4.2 with cases where the wind is greater than 3 m s^{-1} .

5. Modélisation Lagrangienne et biogéochimique du transport et de la croissance des sargasses

Les conclusions du chapitre précédent suggèrent que les modèles de dérive des sargasses pourraient bénéficier significativement d'une adaptation de leur formulation et de leurs valeurs de paramètres. En particulier, le courant, jusqu'ici considéré comme agissant sur les algues à sa pleine vitesse, pourrait avoir un effet moindre résultant de l'effet de traînée des radeaux d'algues. Les sargasses feraient vraisemblablement corps face au courant environnant et ne seraient entraînées qu'à une vitesse inférieure à celle de ce dernier (de l'ordre de 80%). Aussi, l'effet du vent sur la dérive (c'est-à-dire le *windage*) pourrait être supérieur au 1% consensuel proposé par la littérature. Plus marginalement, l'effet du vent pourrait aussi être dévié légèrement vers la droite d'un angle de 10°environ.

Néanmoins, ces perspectives d'amélioration ont été déduites d'observations à fine échelle de la dérive d'agrégats de sargasses à trois heures d'intervalle. Aussi, l'amélioration des modèles à plus grande échelle par l'intégration de ces nouveaux paramètres reste prospective. La suite de la présente thèse s'intéresse donc à la mise en application des conclusions de l'étude précédente dans un modèle de dérive sur l'océan Atlantique entier et à la caractérisation des éventuels apports résultants.

La modélisation d'objets flottants peut être abordée selon deux paradigmes différents. D'une part, les modèles Eulériens permettent le suivi des quantités d'objets au sein d'une maille régulière fixe par des calculs d'advection et diffusion entre celles adjacentes. D'autre part, les modèles Lagrangiens rendent compte du suivi de particules numériques représentant les objets flottants en calculant leur trajectoire itérativement. Si l'option Eulérienne est sans doute plus adaptée aux applications prédictives à large échelle, elle ne rend pas compte de l'histoire des objets flottants et de leur parcours au cours du temps. À des fins exploratoires, l'option Lagrangienne apparaît plus adaptée pour analyser les dynamiques d'un modèle et les mécanismes physiques et biologiques sous-jacents à l'échelle de l'individu.

C'est donc un modèle Lagrangien qui sera employé ici pour reproduire la dérive des sargasses et tester les différents facteurs de vent et de courant avec des simulations de quelques dizaines de jours. Cependant, lorsque la durée des simulations excède deux ou trois mois, la dérive ne suffit plus à reproduire l'évolution de la distribution spatiale des sargasses. À ces échelles de temps, la croissance des algues s'ajoute à leur dérive et la qualité des prédictions du modèle chute sévèrement. Cela mène au cœur de cette troisième étude où il est question d'intégrer un modèle de croissance des

5. Modélisation Lagrangienne et biogéochimique du transport et de la croissance des sargasses

algues au modèle Lagrangien de leur dérive afin de reproduire leur répartition spatiale et temporelle et d'étudier les facteurs qui la déterminent.

Les contraintes régissant la croissance d'une macro-algue sont de manière générale soit physique (lumière, température, salinité) soit biogéochimique (nutriments : phosphore et azote). Le modèle présenté ci-après s'appuie sur une formalisation dite "à quota" permettant de rendre compte de la capacité des sargasses à stocker des nutriments dans leurs tissus et à les utiliser pour croître ultérieurement. En d'autres termes, les algues peuvent tirer profit d'un milieu riche en nutriments pourtant inadapté à leur croissance en absorbant phosphore et azote en son sein et en les utilisant lorsque le milieu sera devenu plus propice.

Une fois le modèle de dérive/croissance calibrés au mieux, il s'agira d'exploiter leurs résultats de manière à mettre en lumière les moteurs de la croissance. Dans cette perspective, l'article ci-dessous détaille, en fin d'étude, les zones de croissance et de décomposition des algues sargasses ainsi que leur variabilité interannuelle.

5. Modélisation Lagrangienne et biogéochimique du transport et de la croissance des sargasses

Drivers of growth and decay of *Sargassum* in the Tropical Atlantic : a Lagrangian approach

Witold Podlejski^{1,2,*}, Christophe Lett¹, Julien Jouanno³, Nicolas Barrier¹ and Léo Berline²

¹Marbec, Université de Montpellier, CNRS, Ifremer, IRD, Sète, France

²Aix Marseille Univ, Université de Toulon, CNRS, IRD, MIO, Marseille, France

³LEGOS, Université de Toulouse, IRD, CNRS, CNES, UPS, Toulouse, France

*En préparation : PODLEJSKI, W., LETT, C., JOUANNO, J., BARRIER, N., & BERLINE, L. (In prep.). Drivers of growth and decay of *Sargassum* in the Tropical Atlantic : a Lagrangian approach.*

5.1. Abstract

The proliferation of *Sargassum* in the Tropical Atlantic has almost every year since 2011, but a strong variability of biomass is observed among years. Essential knowledge about the drivers of *Sargassum* growth and decay is still lacking to explain this interannual variability. Benefiting from accurate basin scale *Sargassum* detections from remote sensing, we have developed a Lagrangian transport/growth model to simulate *Sargassum* distribution over the period 2016-2020. The resulting trajectories and biomass time series of *Sargassum* aggregates were analyzed to highlight the main limiting factors of growth and decay. The nitrogen and phosphorous concentrations are found to be weakly restrictive compared to physical limiting factors, especially the temperature. In particular, the warm waters found off northern Brazil appear to be instrumental in triggering the end of seasonal growth of *Sargassum*. The timing of the seasonal warming of this region, strongly impacts the quantities of *Sargassum* simulated each year and should be monitored to anticipate the development of *Sargassum* and resulting strandings.

Keywords : *Sargassum* algae; Lagrangian simulation; growth model; Tropical North Atlantic; Remote Sensing; Time series.

5.2. Introduction

The *Sargassum* massive proliferation in the Tropical Atlantic observed since 2011 is a profoundly dual phenomenon. It generates a tremendous shelter for biodiversity (FINE, 1970; MARTIN et al., 2021) and enhances connectivity (SEHEIN et al., 2014) while fixing large amounts of atmospheric carbon (GOUVÉA et al., 2020; M. WANG et al., 2018). But, at the same time, it is also a havoc for coastal ecosystems and related human activities (CHÁVEZ et al., 2020; MERLE et al., 2021; RESIERE et al., 2018). Various hypotheses have been put forward to explain this 2011 shift, in particular a strong climatic event occurring in 2010, long-term increase of temperature and eutrophication of large rivers, changes in upwelling and Saharan winds intensities (DJAKOURÉ et al., 2017b; JOHNS et al., 2020; MARSH et al., 2021; OVIATT et al., 2019; SKLIRIS et al., 2022a; M. WANG et al., 2019b). However, disentangling the *Sargassum* growth dynamics remains challenging and there is no consensus on what are the drivers of the seasonal growth and decay, either due to biogeochemical or physical factors, and therefore what determines the interannual variability of *Sargassum* distribution remains to be explored.

The distribution of *Sargassum* is well monitored by satellite observations, allowing the presence of algae to be extracted and biomass to be measured over time (CUEVAS et al., 2018; J. F. GOWER & KING, 2011; LAVAL et al., 2023; MINGHELLI et al., 2021; PODLEJSKI et al., 2022; M. WANG & HU, 2016). With these observations and complementary *in-situ* data, the drift of *Sargassum* has been quantified and decomposed mainly as a function of currents and wind (BERLINE et al., 2020; M. T. BROOKS et al., 2018; KWON et al., 2019; MIRON et al., 2020; PUTMAN et al., 2018; PUTMAN et al.,

5. Modélisation Lagrangienne et biogéochimique du transport et de la croissance des sargasses – 5.3. Materials and Methods

2020). Compared to previous studies, the recent drift measurements of PODLEJSKI et al., 2023 suggest a larger effect of wind (windage) and a reduced effect of currents on *Sargassum* drift. These results bring a possible improvement of drift models that needs to be further tested at large scale.

Many studies have already focused on modelling and forecasting short-term *Sargassum* stranding events (BERNARD et al., 2022; MARÉCHAL et al., 2017b; TRIÑANES et al., 2022), but few extend the forecast to a longer timescale (M. T. BROOKS et al., 2018; JOUANNO et al., 2021a; MARSH et al., 2021). While short-term forecast only requires accurate model of drift, growth can not be ignored for longer-term forecast. The growth of *Sargassum* being multifactorial, very few studies have attempted to reproduce it numerically (M. T. BROOKS et al., 2018; JOUANNO et al., 2021a; JOUANNO et al., 2021b). The most advanced model was developed by JOUANNO et al., 2021a using a growth quota approach to model both physical (temperature, salinity, irradiance) and biogeochemical (phosphorous, nitrate) limitation factors. Although accurate in its predictions, this Eulerian model did not track the history of *Sargassum* aggregates and was therefore better suited to large-scale interpretations. Conversely, Lagrangian models are commonly used to track the history of drifting objects, in particular *Sargassum* algae (BERLINE et al., 2020; FRANKS et al., 2016; PUTMAN et al., 2018), and make it possible to analyze the drivers of dynamics at the individual scale.

Here, the Lagrangian approach and JOUANNO et al., 2021a growth modelling approach were combined to simulate *Sargassum* distribution in the Tropical Atlantic over a 5-year period (2016-2020). First, we calibrated the drift model following PODLEJSKI et al., 2023's results and adapted the growth model from JOUANNO et al., 2021a to the Lagrangian approach. The simulation results were then analyzed in order to highlight the main limiting factors of growth, the areas of growth and decay and the possible causes of the interannual variability of *Sargassum*.

5.3. Materials and Methods

5.3.1. Satellite observation dataset

The Alternative Floating Algae Index (AFAI) defined by M. WANG et HU, 2016 was used according to the methodology detailed by DESCLOITRES et al., 2021 in order to detect the presence of *Sargassum* with the Moderate-Resolution Imaging Spectroradiometer (MODIS) sensor. Then the filtering method developed by PODLEJSKI et al., 2022 was applied to remove false detections due to clouds, shadows, sun glint or coastal waters. The *Sargassum* Fractional Coverage (FC) was then derived from AFAI using the ratio proposed by M. WANG et HU, 2016. FC at the native resolution of the two MODIS Aqua and Terra satellites (1 to 8 km²) was projected daily onto a 1 km resolution grid. Monthly FC composites at 50 km resolution were finally calculated by averaging these daily maps (excluding hidden and uncovered pixels in the average). FC was then converted to dry weight biomass estimates using the ratio of 3,34 kg m⁻² (M. WANG et al., 2018). Alternatively to FC maps, we also used presence maps (*p*) calculated as

5. Modélisation Lagrangienne et biogéochimique du transport et de la croissance des sargasses – 5.3. Materials and Methods

the fraction of 1-km pixels detected as *Sargassum* (N_s) over all unmasked pixels (N_u) inside each box of 50 km² ($p = N_s / N_u$, BERLINE et al., 2020). The smallest presence values ($p < 0.003$) were excluded to remove remaining isolated false detections due to clouds, shadows or sun glint.

5.3.2. *Sargassum* drift model

The *Sargassum* drift model used for the simulation was based on PODLEJSKI et al., 2023's model :

$$\mathbf{U}_S = C_f \mathbf{U} + w * \exp(i\phi) \mathbf{W} \quad (5.1)$$

where the variables \mathbf{U}_S , \mathbf{U} and \mathbf{W} are the *Sargassum* drift, the local current and the local wind expressed as complex numbers. The parameters C_f , w and ϕ are respectively the current factor, the drift factor and the deviation angle of the drift. PODLEJSKI et al., 2023 suggested $C_f = 80\%$, $w = 2\%$ and $\phi = 10^\circ$ as the best set of parameters and here we tested parameter values around these estimates in order to calibrate the drift in our Lagrangian model (see section 5.3.5.1 below). The current factor was tested between 70 and 100%, the windage between 0 and 3%, and the deviation angle between 0 and 30°.

5.3.3. *Sargassum* growth model

Based on the best set of parameters given by the drift model calibration (section 5.3.2), we extended the model to take into account the growth and decay of *Sargassum*. The growth model is based on JOUANNO et al., 2021a's nutrient quota model adapted from the Eulerian to the Lagrangian approach. The formulation of temperature and salinity limitation factors as well as mortality were revised to better match the updated version of the model by Jouanno et al. (in prep).

For each particle (aggregate) of *Sargassum*, three state variables are monitored : the carbon content (C), the nitrogen content (N) and the phosphorus content (P). These variables evolve at each simulation time step, depending on the local conditions that determine the rate of absorption and loss :

$$\begin{aligned} \frac{\partial C}{\partial t} &= U_C - \Phi_C \\ \frac{\partial N}{\partial t} &= U_N - \Phi_N \\ \frac{\partial P}{\partial t} &= U_P - \Phi_P \end{aligned} \quad (5.2)$$

where U_C , U_N and U_P are the uptake rates for carbon, nitrogen, and phosphorus content, respectively, and Φ_C , Φ_N , Φ_P are the loss rates.

The uptake of carbon is defined as follows :

$$U_C = \mu_{max} \cdot C \cdot f(T) \cdot f(I) \cdot f(S) \cdot f(Q) \quad (5.3)$$

5. Modélisation Lagrangienne et biogéochimique du transport et de la croissance des sargasses – 5.3. Materials and Methods

where μ_{max} is the maximum carbon growth rate, and $f(T)$, $f(I)$, $f(S)$ and $f(Q)$ are the limiting functions depending on temperature T , irradiance I , salinity S and nutrient quotas Q in the tissues, respectively, as detailed below.

$$f(T) = e^{-2\left(\frac{T-T_{opt}}{T_{ref}-T}\right)^2} \quad (5.4)$$

with T_{opt} the optimal temperature for *Sargassum* growth and T_{ref} a parameter equal to the minimal growth temperature T_{min} if $T \leq T_{opt}$ or to the maximal growth temperature T_{max} otherwise. Parameters T_{min} and T_{max} are the minimal temperature and maximal temperature for growth, respectively.

$$f(I) = \frac{I - I_{min}}{I_{opt}} e^{\left(1 - \frac{I - I_{min}}{I_{opt}}\right)} \quad (5.5)$$

with I_{opt} the optimal irradiance for *Sargassum* growth and I_{min} the minimal irradiance required for growth.

$$f(S) = \alpha_S S + \beta_S \quad (5.6)$$

with α_S and β_S empirical parameters set to reproduce the salinity limitation shown by HANISAK et SAMUEL, 1987.

$$\begin{aligned} f(Q) &= \min(f(Q_N), f(Q_P)) \\ f(Q_N) &= \left(\frac{1 - (Q_{Nmin}/Q_N)}{1 - (Q_{Nmin}/Q_{Nmax})} \right) \\ f(Q_P) &= \left(\frac{1 - (Q_{Pmin}/Q_P)}{1 - (Q_{Pmin}/Q_{Pmax})} \right) \end{aligned} \quad (5.7)$$

where Q_N and Q_P are the nitrogen and phosphorus quotas defined as $Q_N = N/C$ and $Q_P = P/C$, respectively. The parameters Q_{Nmin} , Q_{Nmax} , Q_{Pmin} , Q_{Pmax} correspond to the minimum and maximum quotas of nutrients in the algae. All limiting functions are restricted to the interval $[0, 1]$, therefore values outside this interval were thresholded.

At each time step, *Sargassum* takes up nutrients from surrounding waters as follows :

$$\begin{aligned} U_N &= V_{Nmax} \cdot C \cdot \left(\frac{[N]}{K_N + [N]} \right) \cdot \left(\frac{Q_{Nmax} - Q_N}{Q_{Nmax} - Q_{Nmin}} \right) \\ U_P &= V_{Pmax} \cdot C \cdot \left(\frac{[P]}{K_P + [P]} \right) \cdot \left(\frac{Q_{Pmax} - Q_P}{Q_{Pmax} - Q_{Pmin}} \right) \end{aligned} \quad (5.8)$$

with $[N]$ and $[P]$ the nitrogen and phosphorus concentration in water, V_{Nmax} and V_{Pmax} the maximal uptake rates of nutrients and K_N and K_P the half saturation constants of the absorption functions.

The loss terms in Equ. 5.2 depend on the mortality designed empirically using a quadratic function to account for high mortality when *Sargassum* accumulates :

5. Modélisation Lagrangienne et biogéochimique du transport et de la croissance des sargasses – 5.3. Materials and Methods

$$\begin{aligned}\Phi_C &= m.C \cdot \frac{C}{K_m + C} \cdot (1 + \alpha_{wind} * 3) \\ \Phi_N &= \Phi_C \cdot Q_N \\ \Phi_P &= \Phi_C \cdot Q_P\end{aligned}\tag{5.9}$$

with m the mortality rate, K_m the half saturation constant and α_{wind} a term for mortality due to wind :

$$\alpha_{wind} = \frac{1}{1 + e^{1.5(W-5)}}\tag{5.10}$$

where W is the wind speed at the sea surface. This sigmoid function amplifies mortality in case of low wind due to the absence of vertical mixing and subsequent drying of the *Sargassum* emerging part. The values of parameters used in the *Sargassum* growth model are listed in the Table 5.1 (all from Jouanno et al. (in prep)).

Name	Description	Value	Unit
μ_{max}	Maximum carbon uptake rate	0.06	d^{-1}
T_{min}	Minimum temperature value	24	°C
T_{max}	Maximum temperature value	28	°C
T_{opt}	Optimal temperature value	27.5	°C
I_{opt}	Optimal irradiance value	170	$W.m^2$
I_{min}	Minimum irradiance value	30	$W.m^2$
α_s	Slope of the limitation curve for salinity	0.0714	unitless
β_s	Origin of the limitation curve for salinity	-1.5714	$g.kg^{-1}$
Q_{Nmin}	Minimum quota value of N/C	0.014	$mgN.mgC^{-1}$
Q_{Nmax}	Maximum quota value of N/C	0.025	$mgN.mgC^{-1}$
Q_{Pmin}	Minimum quota value of P/C	0.001	$mgP.mgC^{-1}$
Q_{Pmax}	Maximum quota value of P/C	0.0014	$mgP.mgC^{-1}$
V_{Nmax}	Maximum uptake rate for nitrogen	0.015	$mgN.mgC^{-1}.d^{-1}$
V_{Pmax}	Maximum uptake rate for phosphorus	0.005	$mgP.mgC^{-1}.d^{-1}$
K_N	Half saturation term for nitrogen uptake	0.03	$mmol.m^3$
K_P	Half saturation term for phosphorus uptake	0.5	$mmol.m^3$
m	Maximum quadratic mortality rate	0.004	$mg.C^{-1}$
K_m	Half saturation term for mortality	25.10^6	$mg.C^{-1}$

TABLEAU 5.1. : Parameters used in the *Sargassum* growth model. All came from Jouanno et al. (in prep) except the K_m which was adapted here to the Lagrangian approach.

5.3.4. Model inputs : currents, wind, solar irradiation and nutrients

Our drift simulations of *Sargassum* used outputs coming from the GLORYS12 reanalysis (LELLOUCHE et al., 2021). The physical variables current velocity (\mathbf{U}), temperature

5. Modélisation Lagrangienne et biogéochimique du transport et de la croissance des sargasses – 5.3. Materials and Methods

(T) and salinity (S) were downloaded from <https://data.marine.copernicus.eu/>. Wind velocity (**W**) was taken from the reanalysis ERA5 available at <https://cds.climate.copernicus.eu> as well as the shortwave radiation (I).

The biogeochemical variables [N] and [P] were extracted from Mercator Ocean International BIO4 analysis available at <https://www.mercator-ocean.eu/>. The [N] concentration is computed as the sum of NO_3 and NH_4 while [P] concentration is equal to PO_4 .

5.3.5. Simulations setup

5.3.5.1. Drift-only simulations

Simulations were first run to find the best drift parameters set. Simulations setup from BERLINE et al., 2020 was used. From monthly *Sargassum* presence maps at 50 km resolution, particles were seeded in each pixel containing detections of *Sargassum*. The particles were evenly distributed inside the 50 km boxes, every 2 km ($N_0 = 625$ particles for each 50 km box). Each particle was associated with a weight derived from the presence of *Sargassum* ($\mu = p/N_0$).

The particles were advected with Ichthyop software (LETT et al., 2008) using Runge Kutta's 4th order numerical scheme with a 3-hour time step. Simulations started on the 15th of month *i* and lasted until the end of month *i* + 3 (≈ 105 days). Results were saved daily. A coastal 'bouncing' boundary condition was used to conserve the same quantity of simulated *Sargassum* particles along the simulation. Based on the final location particles, we built a simulated monthly composite for each month : 1) the *Sargassum* particle weights in each 50 km box were summed to create simulated daily maps; 2) the mask (clouds) of the corresponding daily MODIS images was applied to these simulated maps to ensure consistency between the simulation and the satellite observations; 3) maps were averaged monthly and binarized using the threshold $p < 0.003$ to remove weak presence value. A summary of the simulation setup is shown in Fig. 5.1.

5. Modélisation Lagrangienne et biogéochimique du transport et de la croissance des sargasses – 5.3. Materials and Methods

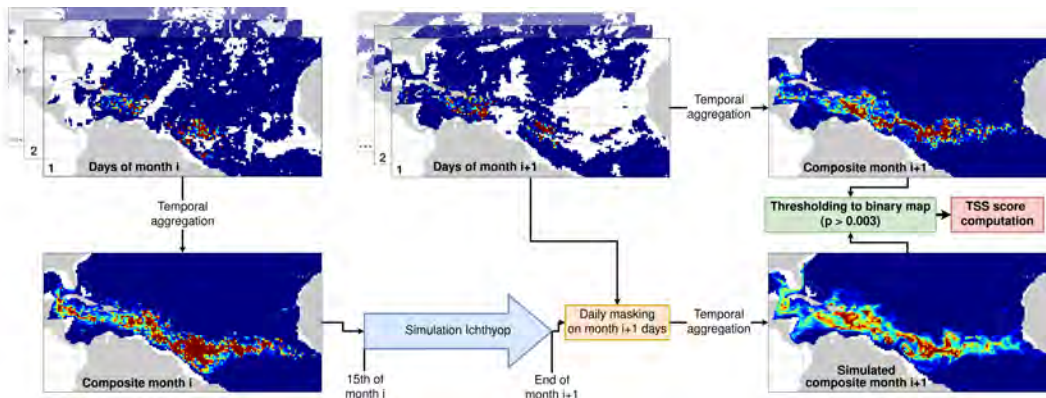


FIGURE 5.1. : Workflow of the simulation setup. The example shown is for 1-month simulations, but an identical approach was used for longer simulations (3 months, 1 year).

5.3.5.2. Assessment of model skill

The comparison between the simulated and the observed composites of *Sargassum* presence maps was performed using the True Skill Statistic (TSS, ALLOUCHE et al., 2006; BERLINE et al., 2020) in four different oceanic regions between 5°S and 35°N : i) the Caribbean Sea (90°W to 60°W); ii) the Central Atlantic Ocean (60°W to 35°W); iii) the East Atlantic Ocean (35°W to 5°W); iv) the overall region (90°W to 5°W) (see Figure 5.4). TSS makes it possible to compare presence maps giving equal weight to the absence of *Sargassum* and to the consistent/inconsistent cases of presence. This simplifies assessment of model skill by focusing on where the *Sargassum* is without considering its amount of biomass. The TSS value ranges from 0 (no skill) to 1 (perfect match).

The gain brought by the model was evaluated by comparing the TSS values with a reference, called here “persistence”, which is the TSS calculated between the satellite composites of months i and i+1. TSS values were computed for all the simulations, i.e. for all different sets of drift parameters ($4^*4^*4=64$ sets), starting each month of the time series ($12^*5=60$ times) and for a simulation period of 1, 2 and 3 months (3 periods). So the experiment ended up with $64^*60^*3=11520$ TSS values to analyze. As the different sets of parameters gave slightly different TSS values with no obvious best choice, we choose to aggregate the results for a given set of parameters, a given region and a given year, and calculated the mean and median values. For each set of parameters, we added the number of occurrences where these values were the highest to determine the most appropriate parameters according to each region.

5.3.5.3. Drift-growth simulations

The simulation set-up was identical to the drift simulation experiment, except that the simulation duration was extended to 1 year to leave sufficient time for *Sargassum* growth. Also, each particle was associated with a C content derived from the biomass

5. Modélisation Lagrangienne et biogéochimique du transport et de la croissance des sargasses – 5.4. Results

quantities of *Sargassum* using the ratio of 27% (M. WANG et al., 2018). The initial content of nitrogen and phosphorus was arbitrarily set to $C * (Q_{Nmax} - Q_{Nmin})/2$ and $C * (Q_{Pmax} - Q_{Pmin})/2$, respectively. The boundary condition used is 'beaching': any particle that touches the coast is removed from the simulation. This mimics the stranding term used in the Eulerian model of (JOUANNO et al., 2021a).

For each simulation, C content was converted back to biomass to compute monthly simulated images. The comparison of simulated biomass distribution with satellite composites on the four different ocean regions was used to assess the quality of the growth model and calibrate *Sargassum* mortality parameters (K_m , Table 5.1) manually by minimizing the difference over the four regions between simulation and satellite maps.

5.3.5.4. Time to double biomass

The Lagrangian approach enables to follow the fate of a given *Sargassum* aggregate (i.e. a particle) along its trajectory. We defined an experiment to assess the time required for an aggregate to double its biomass given its starting location. We seeded a large area (100°W to 15°E, 5°S to 35°N) with *Sargassum* particles every 5 km with 1000 kg initial biomass. After running the simulation over 1 year, the time to double (in days) was computed and associated to the starting location to obtain maps over the whole area. With all the simulations starting each month of the time series, we aggregated the maps of time to double biomass seasonally and compared it with growth limitation factors maps, both from biogeochemical and physical variables.

5.4. Results

Presence maps of *Sargassum* aggregates over the Tropical Atlantic derived from satellite and from our drift model were compared using TSS (True Skill Statistic). An example of TSS values averaged over the whole simulated domain obtained along the simulation time period is shown in Figure 5.2 for the particular case $C_f = 100\%$, $w = 1\%$, and $\phi = 0^\circ$ (blue line). In Figure 5.2 is also shown the persistence, i.e., the TSS values obtained by comparing the initial and 1-month later satellite-derived presences (orange line). The TSS curve above the persistence curve indicates that using the model prediction of *Sargassum* presence is better than assuming that *Sargassum* does not move at all over a 1-month period, and therefore that the model has some skill to simulate *Sargassum* drift (Figure 5.2). The assessed TSS values ranged between 30 and 80% with higher values in summer and lower in winter, broadly following the periods of higher and lower amounts of *Sargassum* (assessed by the fractional coverage in Figure 5.2, red line). The gain brought by the model, assessed by the difference between TSS and persistence, was between 0 and 30% and tended to be higher for the years with low amount of *Sargassum* (Figure 5.2). Overall, the influence of the deflection angle on the TSS values was small and we therefore decided to set $\phi = 0^\circ$. For this value, the values of current and windages leading to the highest average TSS

5. Modélisation Lagrangienne et biogéochimique du transport et de la croissance des sargasses – 5.4. Results

depended on time and on the considered area, being most often $C_f = 70\%$, $w = 1\%$ for the Caribbean area, $C_f = 100\%$, $w = 1\%$ for the Central Atlantic area, and $C_f = 100\%$, $w = 2\%$ for the East Atlantic area (Figure 5.3). We chose the values $C_f = 100\%$, $w = 1\%$ that lead most often to the highest TSS for the whole area (Figure 5.3).

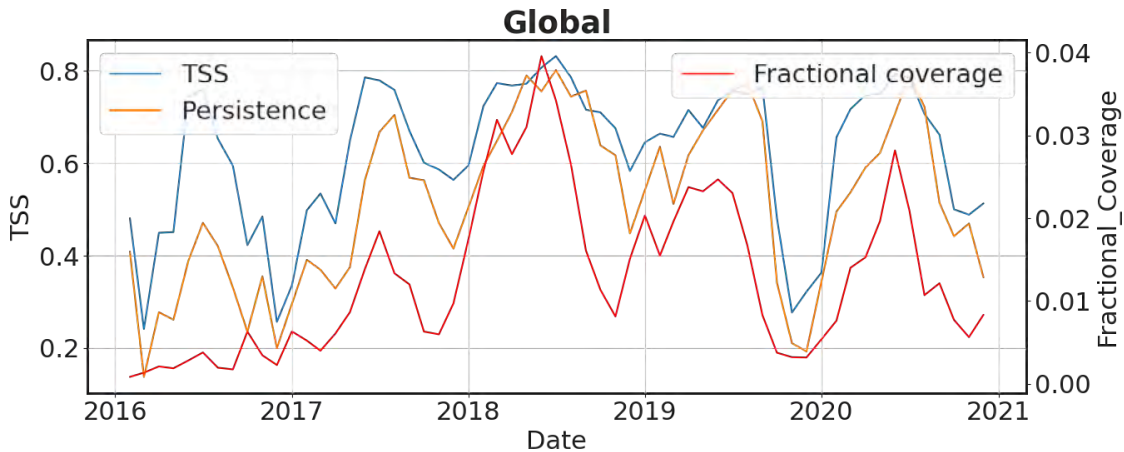


FIGURE 5.2. : TSS values computed between simulated monthly composites maps of *Sargassum* presence after 1 month of simulation and corresponding satellite images with windage set to 1%, current to 100% and deviation angle of windage to 0°. The orange curve shows the persistence, i.e. the TSS value computed between the previous satellite composite and the current one. The area between orange and blue curves gives the gain brought by the model. The red curve is the average fractional coverage in percent over of total area.

5. Modélisation Lagrangienne et biogéochimique du transport et de la croissance des sargasses – 5.4. Results

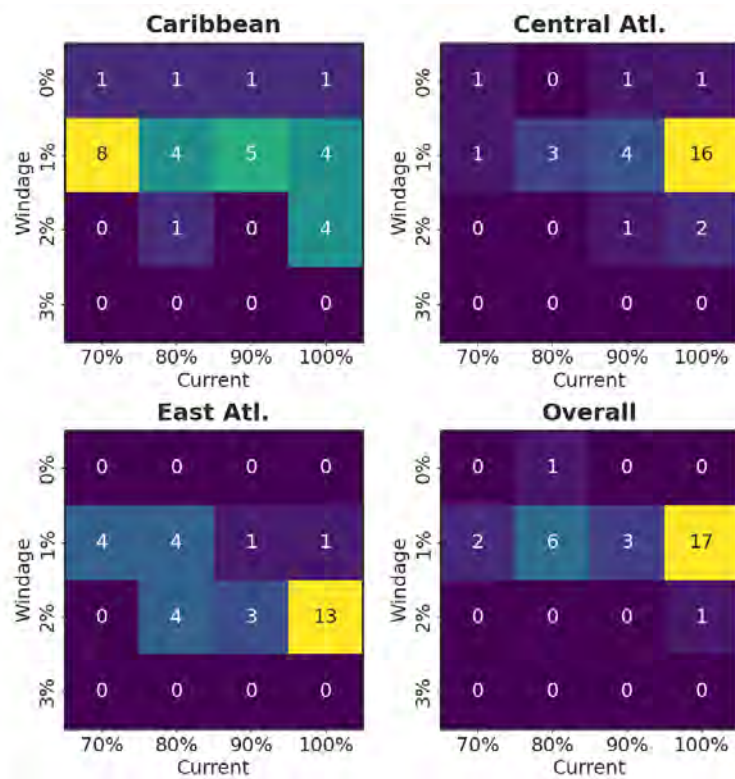


FIGURE 5.3. : Drift model skill assessment for different sets of windage and current factors in four oceanic regions. Color and values refer to the number of occurrences where the parameters set was the best performing over simulations aggregated annually. The deflection angle was here set to 0°

Simulations of the biomass growth used the best set of drift parameters. Simulations were extended to 1-year with tracking of the simulated biomass computed in four regions. The figure 5.4 shows an example of a 1-year simulation initialized on January 2017. The model faithfully reproduces the overall biomass dynamics (bottom right panel) with consistent starting and ending biomass values, as well as the local maximum and minimum of biomass found in May and in November, respectively. However, there are some spatial discrepancies after 6 months of simulation, with the biomass located more westward in the simulated composite than in the satellite composite. This can also be seen on local biomass time series like in the Caribbean where the simulated biomass does not correspond well to the satellite observations. Figure 5.5 shows the model biomass forecast compared to satellite for different leads (2, 4 and 6 months). The biomass forecast is closer to observations in the Central Atlantic and in the Caribbean compared to the East Atlantic region. The annual maximums of biomass, in particular the peak in 2018, are accurately reproduced by 2-month lead simulations and still to some extent with 4-month leads. Yet, forecast quality declines with the longer simulation times (> 4 months).

5. Modélisation Lagrangienne et biogéochimique du transport et de la croissance des sargasses – 5.4. Results

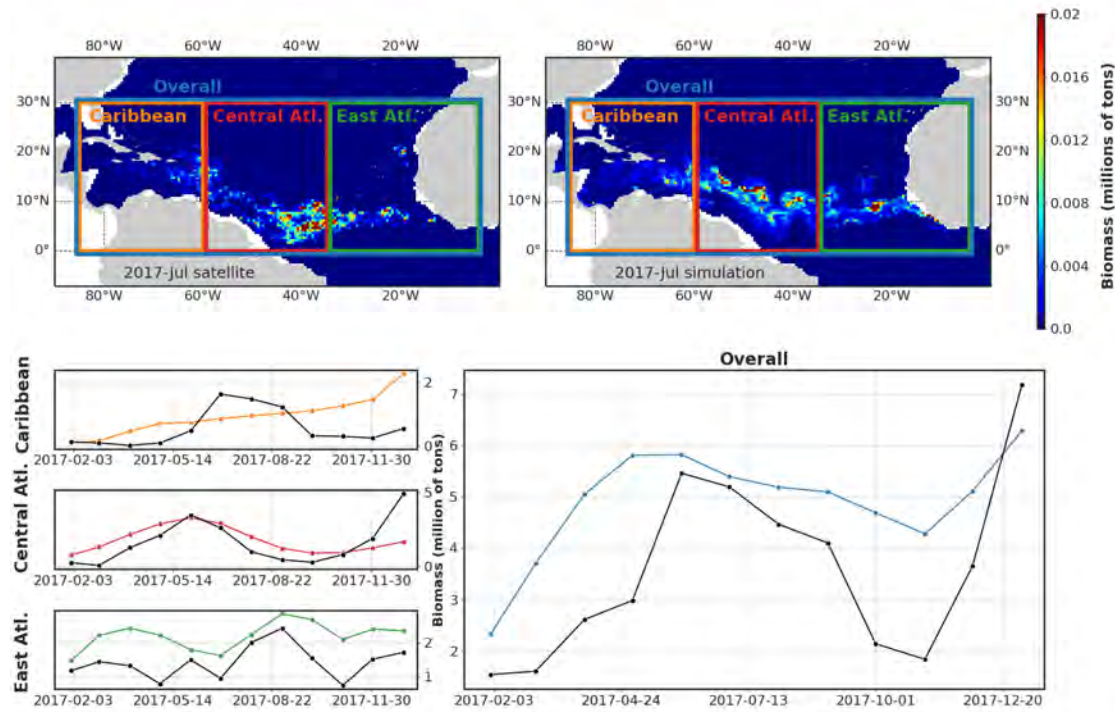


FIGURE 5.4. : Results of the drift and growth simulation starting in January 2017. The first row shows the monthly composites at 50 km resolution from satellite (left) and from the model after 6 months of simulation (right). The time series below show the evolution of *Sargassum* biomass in the four areas displayed on the top panel from satellite (black lines) and the simulation (colored lines).

5. Modélisation Lagrangienne et biogéochimique du transport et de la croissance des sargasses – 5.4. Results

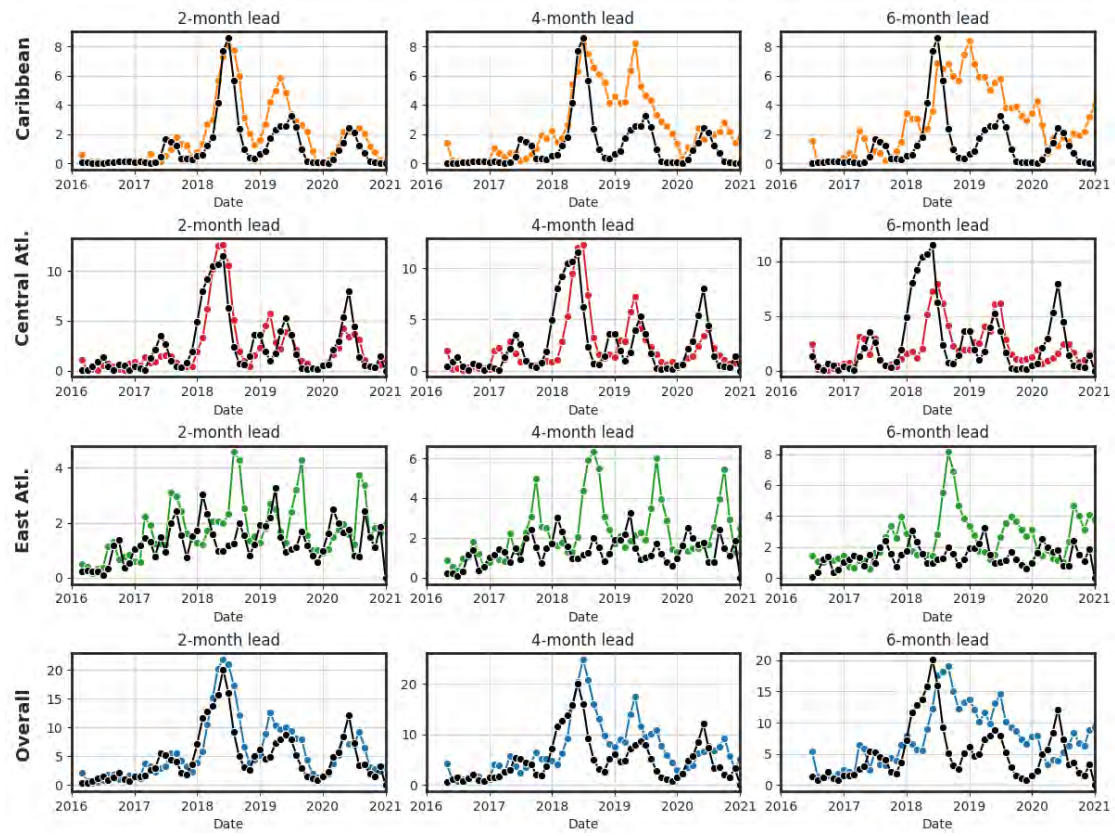


FIGURE 5.5. : Comparison between biomass (millions of tons) estimated with satellite observation (black lines) and simulated biomass (colored lines). Colors refer to the oceanic regions shown in Fig. 5.4.

The drift-growth model was used to calculate the time required for a *Sargassum* particle's biomass to double from its starting location. The resulting maps and maps of physical and biogeochemical limiting factors are shown in Figure 5.6 for the four seasons. During the major part of the year, the area of low time to double biomass values for *Sargassum* algae spans from the Gulf of Mexico to 20°W. The areas with high time to double biomass values are restricted to the North of the Atlantic Ocean (above 25°N), to the Brazilian waters and to the Gulf of Guinea. Summer stands out with high time to double biomass values in the Caribbean Sea and the Gulf of Mexico, whereas the Gulf of Guinea has lower time to double biomass values. As for the physical ($f(T) \cdot f(S) \cdot f(I)$) and biogeochemical ($\min(f(Q_N), f(Q_P))$) limiting factors, they are spatially inversely correlated. High values for the physical factor and low values for the biogeochemical factor are located in the southern Atlantic (around 10 °N) during the first half of the year, with this trend reversing in the second half of the seasonal cycle when these values are found in the northern and southern zones. The physical limitation values are largely more restrictive (0.2 in average) than the biogeochemical limitation (0.9 in average).

5. Modélisation Lagrangienne et biogéochimique du transport et de la croissance des sargasses – 5.4. Results

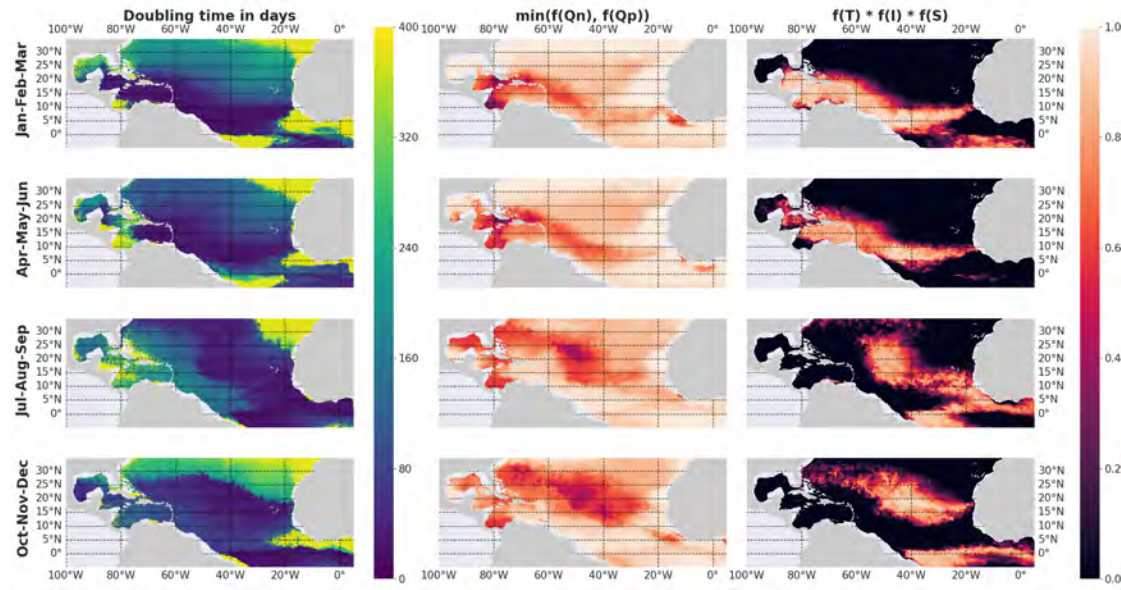


FIGURE 5.6. : Time to double biomass for *Sargassum* particles seeded at that location (left). Biogeochemical limitation factor according to the quotas of nitrogen or phosphorus in the tissues ($\min(f(Q_N), f(Q_P))$). Physical limitation factor according to temperature, irradiance and salinity ($f(T).f(S).f(I)$).

The seasonal dynamics of *Sargassum* biomass in the Caribbean Sea and its inter-annual variability are studied in more detail using biomass time series of particles crossing the Caribbean arc (Figure 5.7). In 2016 most of the biomasses stopped increasing at the beginning of May when the particles entered the Caribbean Sea, and then gradually decreased on their westward trajectory to the Gulf of Mexico. Conversely, in 2018 biomasses kept on increasing until early July, and some particles reached their biomass maximum while off the Yucatán Strait already.

5. Modélisation Lagrangienne et biogéochimique du transport et de la croissance des sargasses – 5.5. Discussion

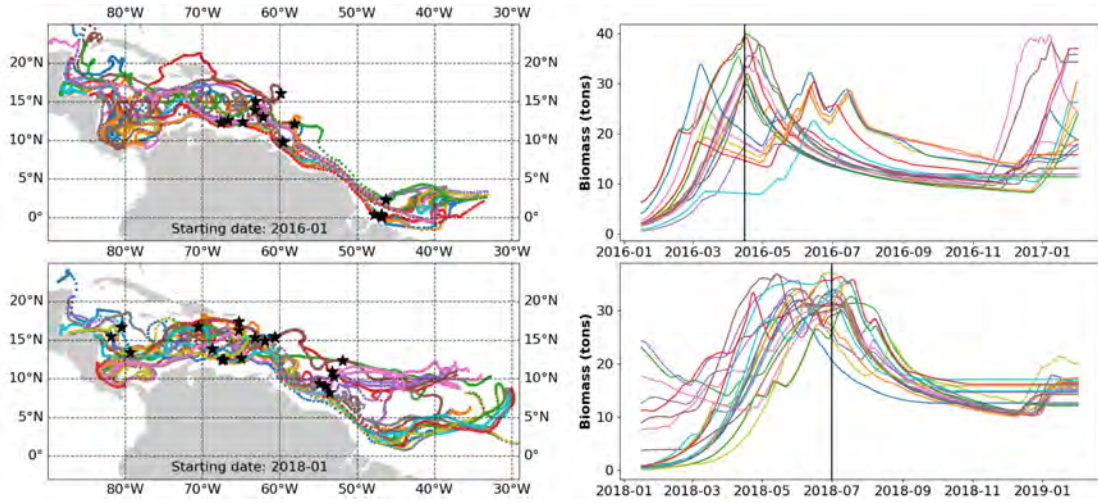


FIGURE 5.7. : Sample of simulated trajectories that cross the Caribbean arc (left) and corresponding biomass time series (right) for the years 2016 (top) and 2018 (bottom). The black vertical lines indicate the approximate average date of the biomass maximum among the time series, and the location corresponding to this date is displayed for each particle with a black star on the maps.

5.5. Discussion

5.5.1. Drift parameters variability

Our simulations have shown that the angle of deviation of the wind effect on the drift has a very small impact on the results, and we were unable to conclude on a preferred value, probably because the Ekman current is already taken into account in the GLORYS12 current. Consequently, setting it to zero for simplicity seems satisfactory. On the other hand, the windage and current factor have a significant impact on simulation performances. The three sub-regions studied each have a different set of best wind and current parameters (Figure 5.3). The Caribbean region shows the greatest variability, with a weak consensus obtained for 1% wind and 70% current. This could be explained by the high concentrations of *Sargassum* in this area, most likely associated with large *Sargassum* mat sizes, which may induce a drag effect and reduce the current effect. In the central Atlantic Ocean, the windage is estimated at 1% and the current factor at 100% consistently with previous studies (BERLINE et al., 2020; KWON et al., 2019; PUTMAN et al., 2018). In the eastern Atlantic Ocean, the best suggested current factor is again 100%, but with a higher 2% windage. This is probably due to the lower wind speed (4.2 m.s^{-1} on average in the east versus 5.9 m.s^{-1} in the central region), which leads to a higher fraction of emerged algae and therefore a proportionally stronger wind effect on drift. Despite these subsequent local variations, we chose the best set of parameters over the whole region being 1% for wind and 100% for current for the combined drift and growth simulations. The

discrepancies between these values and those suggested by PODLEJSKI et al., 2023 (2% wind and 80% current) are likely due to the difference in scales of the two studies and associated resolved physical factors acting on drift. Whereas here we used long-term simulations (several months) with a coarse resolution (50 km) to estimate the drift model parameters, the measurements by PODLEJSKI et al., 2023 were carried out on successive images separated by 3 hours only and at a 1 km resolution. GLORYS12 currents have lower accuracy than drifter-derived currents used by PODLEJSKI et al., 2023. GLORYS12 currents can also underestimate actual currents, artificially resulting in a higher current factor.

5.5.2. Main drivers of growth

The results show a weak biogeochemical limitation ($\min(f(Q_N), f(Q_P)) > 0.8$ in general). In particular, the nitrogen does not strongly constrain the growth as the associated saturation term is low ($K_N=0.03$). Algae likely always find available nitrogen, most likely because of diazotrophic fixation (LAPOINTE et al., 2021). Phosphorous is more constraining, but not dominating for the growth dynamics (see 5.8). However, the spatial pattern of the combination of these two factors shows that lower values (0.8) are found at the same location as *Sargassum* distribution in the first half of the year suggesting a slight limitation effect on *Sargassum* growth (Figure 5.6). These results highlight that biogeochemical factors are likely not primarily restrictive for *Sargassum* growth. This is consistent with recent laboratory experiments showing that *Sargassum* do not respond greatly to nutrient enrichment (MAGAÑA-GALLEGOS et al., 2023a; PHILIPPI et al., 2023). The spatial impact of environmental nutrient enrichment, either by Amazonian influx, Sahara deposition or Mauritanian upwelling as proposed in the literature (OVIATT et al., 2019; M. WANG et al., 2019b), on *Sargassum* distribution are not found critical in our results. In fact, as the limitation factors associated to those enrichment sources are rather stable between years (not shown), they are likely playing a minor role on the current interannual variability of *Sargassum* distribution.

Regarding the physical limitation of growth in simulations, low salinity can be limiting but rarely in the locations of *Sargassum* and solar radiation is always sufficient for *Sargassum* (see 5.8). It is the temperature that highly determines the dynamics of growth, depending on the area and the season. The function used for the temperature limitation was designed to inhibit growth in cold waters and to account for algae decomposition in warm waters. In particular, our interval of temperatures favorable for *Sargassum* growth (24 – 28°C) was adjusted to fit large scale growth observation from satellite data (JOUANNO et al., 2021a). These values are consistent with the observations from M. WANG et al., 2019b (Supplementary Materials). At the basin scale, the high temperatures (above 28°C) are the primary limitation factor that prevent *Sargassum* growth in the simulations. This is consistent with the large-scale negative correlation between SST and *Sargassum* concentration found in the literature (SKLIRIS et al., 2022a; M. WANG et al., 2019b). However, rather less restrictive temperature limitations were found in laboratory experiments (MAGAÑA-GALLEGOS et al., 2023a; J. SCHELL et al., 2023). This difference could be due to some environmental factors

which are not present in laboratory experiments, such as the biofouling in warm waters.

Mortality is also a key parameter, but we lack data on this particular phenomenon. The quadratic mortality function we used limits the growth for high concentrations of *Sargassum* and improves the robustness of the results by avoiding an exponential and unrealistic growth of *Sargassum*. It performs better than linear mortality, but is insufficient for low biomass particles, leading to steady slow decrease in this case.

5.5.3. Identified regions for growth and decay of *Sargassum* algae

As shown in Figure 5.6, the time to double biomass is heterogeneous at large scale both spatially and temporally, which allows us to retrieve distinct areas for *Sargassum* growth dynamics. In particular, a front is often found between 20–30°N separating the northern zone where *Sargassum* have longer time to double biomass because they grow poorly or decay due to low temperatures. The Gulf of Guinea is generally too warm for growth, except in late summer, and traps particles within it, inducing the long time to double biomass. This index can therefore be interpreted as an indication of whether a location at a given date will be favorable or not to *Sargassum* growth along its future trajectory.

An important feature appearing in our results is the band-like zone of long time to double biomass appearing in June to September from the offshore waters of northern Brazil to the Gulf of Mexico, including the entire Caribbean Sea (5.7). It is the high temperatures reached in this zone that prevent the growth of *Sargassum* (see very low values of limiting factor in this area, 5.8). Interestingly, 2018 differs from the others years on this point, with the long time to double biomass pattern delayed until late August, leading to huge biomasses. Conversely, in 2016, this happened in May, and biomasses remained low (see 5.7). Timing of the water warming in the area could explain the high variability of biomass between years and the resulting quantities of harmful strandings. This seasonal regulation is consistent with the time series of particle biomass crossing the Caribbean arc (Figure 5.7). The tipping point between growth and decline is reached when warming appears. Thus, its date in the seasonal cycle could play a major role to determine whether algae continues to grow in the Caribbean Sea, and hence the amount of *Sargassum* reaching the Yucatán coast and entering the Gulf of Mexico. Timing of warming could be linked to climate mode variability, such as the Atlantic meridional mode (AMM) or the North Atlantic Oscillation (NAO) (MARSH et al., 2023; SKLIRIS et al., 2022a; M. WANG et al., 2019b). In particular, SKLIRIS et al., 2022a showed that the AMM corresponds to high positive SST anomaly (Sea Surface Temperature) in the area between North Brazil and the Gulf of Mexico and is negatively correlated with *Sargassum* concentration. The value of the AMM appears then promising as a proxy for the long-term forecasting of the *Sargassum* biomass development and may help to improve the management of *Sargassum* strandings on the beaches.

5.6. Appendices

5.7. Interannual variability of time to double biomass values

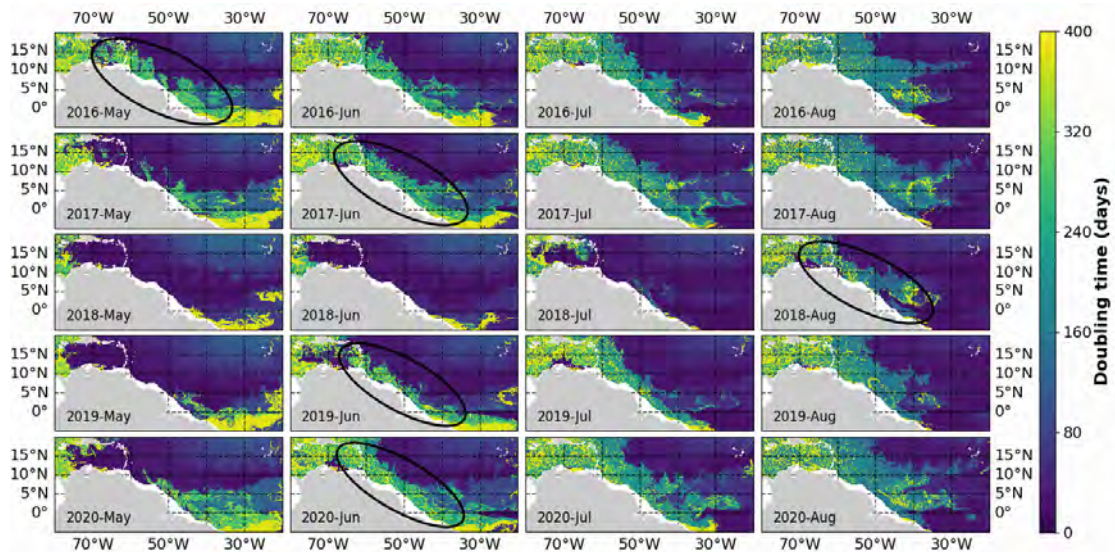


FIGURE 5.8. : The time to double biomass for years 2016 to 2020 and months May to August. The low time to double biomass values (yellow) between the North of Brazil and the Gulf of Mexico appeared in early May for 2016, in June for 2017 and 2020, in July for 2019 and in August for 2020 (rounded at the date of appearance).

5.8. Limitation factors of growth

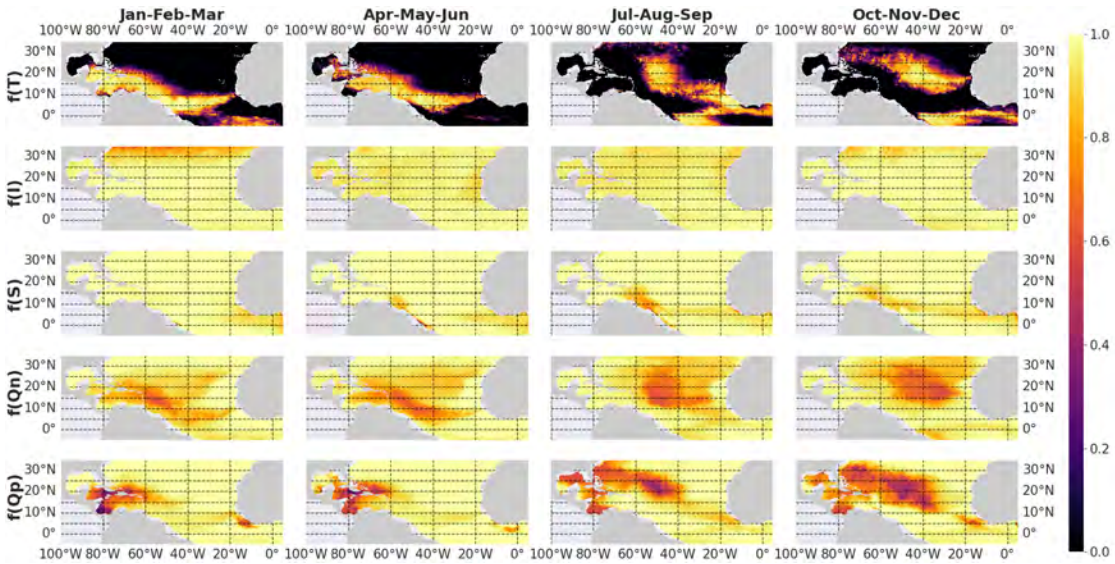


FIGURE 5.9. : Spatial and seasonal variability of the five limitation factors to *Sargassum* growth used in our model. T, I, S, Qn and Qp stand for temperature, irradiance, salinity, nitrogen quota and phosphorus quota, respectively.

5.9. Biomass time series analysis

The drift and growth simulations produce time series of biomass along the trajectories. In order to disentangle the dynamics of the annual *Sargassum* distribution, we used the functional principal component analysis (FPCA) method SHANG, 2014 applied on the biomass time series of *Sargassum* particles.

First, 1-year simulations of the drift and growth of *Sargassum* algae were initialized on each month of the time series 2016-2020 (60 simulations). The resulting biomass times series (1 per particle) were collected and defined as functional data using the python scikit-fda library (<https://fda.readthedocs.io>). After normalization, these functions were smoothed using spline basis ($n=10$) and a FPCA was applied. The 3 first components explained 90% of the variance, we thus only kept these components for our analysis. A Gaussian Mixture model was applied on this new 3-dimensional dataset to extract unsupervised classes ($n=10$) describing the different tendencies of biomass time series.

The results of this trajectory analysis are presented in figure 5.10 after grouping simulations starting in April, May or June. The rest of the simulation has similar results, with a time lag for the biomass time series due to the starting date. The obtained classes are homogeneous with low variance, and they divide the dataset into balanced parts ($\approx 10\%$ for each class). Classes number 2, 8 and 9 have stationary biomass for the last part of the time series, it corresponds to stranded particles. The average biomass found is very different depending on the class and its location.

5. Modélisation Lagrangienne et biogéochimique du transport et de la croissance des sargasses – 5.9. Biomass time series analysis

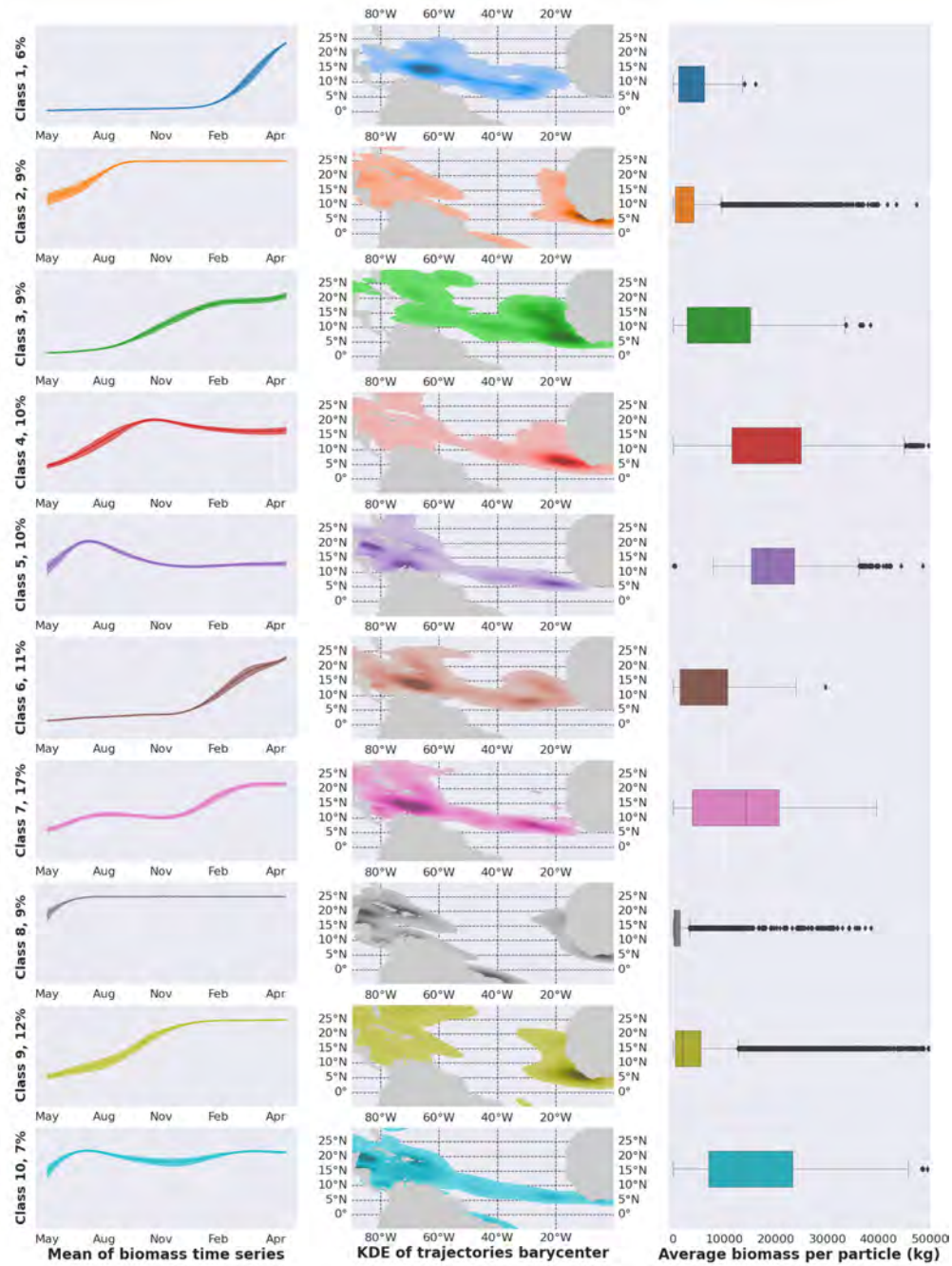


FIGURE 5.10. : The biomass time series dynamics classes for simulations starting in April, May or June. The right panel is the mean of the time series of biomass normalized according to Gaussian classes, the envelope of the curve refers to the variance. The central panel is a kernel density estimate (KDE) of the barycenter of the trajectories. The left panel is the mean biomass distribution in the class. The classes are numbered from 1 to 10 with indication of their corresponding fraction of the data set ($n_{\text{total}} = 58920$).

5. Modélisation Lagrangienne et biogéochimique du transport et de la croissance des sargasses – 5.9. Biomass time series analysis

The simulations reproduce consistently the two regions of consolidation observed in the FRANKS et al., 2016 study. The eastern consolidation region located near the coast of Liberia is characterized by a biomass maximum at the end of the year followed by a stationary regime or a slow decrease (classes 3, 4 and 9 of figure 5.10). It corresponds to approximately 30% of the trajectories with moderate amounts of biomass. On the other side of the Atlantic, the simulated trajectories consolidate in the Caribbean Sea. Maximum biomass is usually reached in late spring (classes 1, 5, 6, 7 and 10 in figure 5.10) and biomass decreases in summer due to high temperatures before growing again the next year. This represents 50% of the simulated dataset, associated with high amounts of biomass. The rest of the trajectories has stranded during the simulation. In the eastern part, stranding mainly occurs on the African coasts of the Gulf of Guinea and in the western part, mainly on the arc of the Caribbean islands and Mexican coasts. It represents 20% of trajectories but with small amounts of biomass, thus it corresponds to small fraction of the total biomass (few percents). The central area of the Atlantic does not really retain any particles. It is a transient zone crossed by the *Sargassum* algae on the way to the Caribbean Sea or on their return to the East.

6. Discussion générale

La présente thèse s'est donc focalisée, dans un premier temps, sur l'observation par télédétection des algues sargasses. En choisissant le capteur MODIS embarqué sur deux satellites à une résolution assez grossière (1 km), les travaux réalisés en amont de cette thèse ont permis d'obtenir une cartographie journalière exhaustive, nonobstant les masques, des 20 millions de kilomètres carrés de l'océan Atlantique tropical nord. La méthode d'extraction des détections, préliminaire à cette thèse, s'est appuyée sur l'index radiométrique AFAI développé dans la littérature. Celui-ci permet de détecter les concentrations de sargasses, même faibles, grâce à de leur absorbance dans le proche infrarouge, commune à tous les végétaux, ainsi que l'absorbance caractéristique des algues brunes dans le jaune (632 nm) due à leur pigment de chlorophylle c. Cependant, ce processus d'extraction génère des fausses détections en nombre équivalent aux vraies sargasses observées, principalement du fait des nuages, de leurs ombres et du reflet du soleil sur l'eau, tous similaires aux sargasses d'un point de vue radiométrique. C'est donc sur le filtrage de ces erreurs que s'est concentrée la première étude présentée dans le chapitre 3. Partant du constat qu'un opérateur averti parvient aisément à distinguer les vraies détections des fausses, cette étude vise à reproduire ce tri avec une méthode d'apprentissage automatisé. Après avoir identifié les attributs discriminant vraies et fausses détections, ici des caractéristiques de contexte spatial large échelle (nombre et surface cumulée des détections voisines, persistance temporelle, distance aux côtes), et créer un jeu de données labellisées, différents algorithmes de classification ont été testés pour sélectionner le plus performant. Ce sont les forêts aléatoires d'arbres, couramment utilisées en télédétection, qui présentaient les meilleurs résultats avec 95% de précision pour déterminer la validité d'une détection. Cette méthode de filtrage a permis de nettoyer par la suite la série temporelle 2016-2020 des détections satellites de la majorité de ses erreurs, mais a aussi permis de montrer l'intérêt des caractéristiques spatiales pour améliorer les résultats de télédétection en allant au-delà de l'analyse radiométrique classique.

Suite à ce premier travail, il a paru possible de suivre certains agrégats de sargasses sur plusieurs images MODIS successives. Or la dérive des sargasses, et en particulier l'effet du vent sur celle-ci, n'était jusqu'alors évaluée qu'empiriquement dans des modèles large échelle et il manquait de réelles mesures quantitatives pour être convenablement modélisée. Ainsi, au chapitre 4 de la présente thèse, une méthode d'extraction de trajectoires d'agrégats de sargasses a été développée afin d'en étudier la dérive. À la suite d'un important travail de sélection de cas d'intérêt, ici des paires d'images MODIS séparées de trois heures et comportant des sargasses colocalisées avec une bouée dérivante, l'algorithme de vision par ordinateur SIFT, retravaillé *ad hoc*, a permis d'extraire 200 mesures de vitesses d'agrégats de sargasses. Grâce à ce pe-

6. Discussion générale

tit jeu de données, suffisamment étoffé néanmoins pour en extraire des informations statistiquement significatives, le travail suivant a porté sur le calcul des paramètres d'un modèle physique simple reliant la vitesse des sargasses à celle des courants de surface et à celle du vent. Cette étude a bénéficié des mesures de courant précises apportées par les bouées dérivantes colocalisées aux sargasses ainsi que des mesures de vent provenant d'un modèle pour alimenter une régression linéaire multiple dans le domaine complexe. Cette approche mathématique a permis une plus grande souplesse pour la calibration des paramètres et abouti à un modèle de dérive réévaluant à la hausse l'effet du vent sur les sargasses et proposant deux nouveaux paramètres : un facteur réévaluant à la baisse l'effet du courant et un angle de déviation de l'effet du vent sur la dérive. Cette étude apporte donc un nouveau modèle de dérive de sargasses plus détaillé et précis que précédemment ainsi que des pistes d'amélioration des modèles de prédiction d'échouement à fine ou large échelle. Cela démontre aussi la capacité de l'imagerie satellite à haute fréquence à extraire des trajectoires d'objets flottants malgré sa relativement basse résolution.

Afin de mettre à l'épreuve ce nouveau modèle de dérive et de qualifier ses résultats à large échelle, le chapitre 5 commence par détailler la simulation Lagrangienne de la dérive des sargasses sur quelques mois avec différents jeux de paramètres de dérive. Les performances résultantes, mesurées à l'aide d'un score comparant les zones de distribution de sargasses observées par satellites et celles simulées par le modèle, permettent d'évaluer les performances des différentes calibrations du modèle. En utilisant les meilleurs paramètres de dérive obtenus par ce test, l'étude associe ensuite à ce modèle de dérive la modélisation de la croissance en fonction de différentes limitations du milieu, physique ou biogéochimique. Ce modèle dérive-croissance permet d'intégrer les conditions de vie sur la trajectoire des sargasses simulées et donne ainsi accès au devenir d'un agrégat selon son point de départ à un moment donné. À partir des simulations issues de ce modèle, il a été possible de calculer le temps requis par une particule pour doubler sa biomasse en fonction de son point de départ et d'ainsi montrer la prépondérance de la limitation de la croissance causée par la température sur les autres facteurs physiques (lumière, salinité) et les limitations dues aux nutriments (phosphore et azote). Ensuite, cela a permis de mettre en exergue une région climatique clé de la régulation annuelle de la croissance des sargasses. En effet, la hausse des températures saisonnières des eaux allant du nord du Brésil au golfe du Mexique est le responsable majoritaire de l'arrêt du développement des biomasses annuel dans les simulations. Ces résultats suggèrent que ce réchauffement localisé et en particulier sa temporalité saisonnière pourrait expliquer la variabilité interannuelle de la distribution de sargasses observée actuellement. Ce dernier point constitue une piste prometteuse pour mieux anticiper l'accroissement des biomasses et le risque annuel d'échouements.

Les trois études présentées ci-dessus rendent compte des étapes mises en place pour étudier la variabilité interannuelle des distributions et quantités d'algues sargasses. Ces travaux se sont succédé naturellement puisqu'il a fallu retravailler les résultats de télédétection dans le chapitre 3 pour obtenir une série temporelle fiable des biomasses de sargasses afin d'en étudier les dynamiques de dérive et de croissance.

6. Discussion générale – 6.1. Masques des données satellites

La dérive n'étant qu'imparfaitement appréhendée et modélisée, le chapitre 4 comble ensuite ce manque en proposant une reprise du modèle de dérive mesuré à partir des images satellites obtenues précédemment. Ce sont ces mêmes données de détections satellites qui ont finalement servi d'initialisation au modèle Lagrangien du chapitre 5. En se basant sur le nouveau modèle de dérive et en lui associant un modèle de croissance, ces simulations Lagrangiennes finalisent les travaux de la thèse en donnant accès au cycle saisonnier simulé des sargasses et permettent l'interprétation de leur variabilité interannuelle. Si ces trois parties se conçoivent comme trois sujets d'études distincts, voici néanmoins les points de discussion qu'ils soulèvent en commun.

6.1. Masques des données satellites

Les masques sont, pour la majorité des études de télédétection, un des obstacles majeurs à l'observation des phénomènes terrestres. Ils sont induits par différents phénomènes comme le reflet du soleil dans l'eau, la contamination côtière due à la proximité du rivage ou à la turbidité de l'eau, les phénomènes analogues à l'objet d'étude (dans notre cas d'autres algues ou des macro-plastiques) et bien sûr les masques dus aux nuages et à leur ombre, omniprésent à l'ITCZ (InterTropical Convergence Zone) et qui constituent le principal problème pour la détection des sargasses. Il est généralement nécessaire de les retirer des images et la méthode utilisée pour ce faire est un point sensible des travaux concernés. C'est d'autant plus vrai dans le cas de l'observation des sargasses qui est doublement impactée par la présence des masques. En premier lieu, ils sont source de fausses détections difficiles à isoler tant par leur couleur que par leur forme. En particulier, les nuages disposent d'un spectre de réflectance très similaire aux sargasses, notamment dans le proche infrarouge, ce qui les rend difficiles à distinguer de véritables sargasses. Qui plus est, certains nuages sont assez isolés et de forme allongée (notamment les cirrus) qui les rendent assimilables aux agrégats de sargasses et renforce la confusion entre les deux objets même en usant de leurs caractéristiques spatiales pour les différencier. Dans le cas présent, le masquage des nuages avec l'algorithme SeaDAS, doublé ensuite par le filtrage automatisé, garantissent la suppression de la majorité des nuages. Les autres études portant sur la détection des sargasses ont fait face à ce même problème et ont adopté des solutions variées. Si les images à haute résolution peuvent aider à délimiter plus finement la présence des différents masques dans les images (M. WANG & HU, 2020), c'est l'apprentissage profond qui est mis en avant dans la littérature pour résoudre ce problème (ARELLANO-VERDEJO et al., 2019 ; M. WANG & HU, 2021). Il pourrait également rendre possible la détection de sargasses au bord ou sous des nuages diffus (LAVAL et al., 2023). Un autre moyen de contourner le problème consiste à utiliser d'autres domaines de longueur d'onde, insensibles aux nuages, par exemple les capteurs radar actifs. Malheureusement, les sargasses ne sont qu'incomplètement détectables par cette technique du fait de leur légère submersion (QI et al., 2022).

6. Discussion générale – 6.2. Échelles spatiale et temporelle des images composites

6.2. Échelles spatiale et temporelle des images composites

En plus de ce problème de fausses détections, les vides laissés par le masquage des nuages réduisent d'autant la couverture des observations satellites. Or, la zone dans laquelle évoluent les algues sargasses, située près de l'ITCZ, est constamment recouverte de nombreux nuages. Aussi, même avec ses deux images journalières provenant des satellites Aqua et Terra, MODIS ne parvient à avoir une prise de vue claire que de 30% de la surface de l'océan Atlantique chaque jour dans cette zone (Figure 6.1).

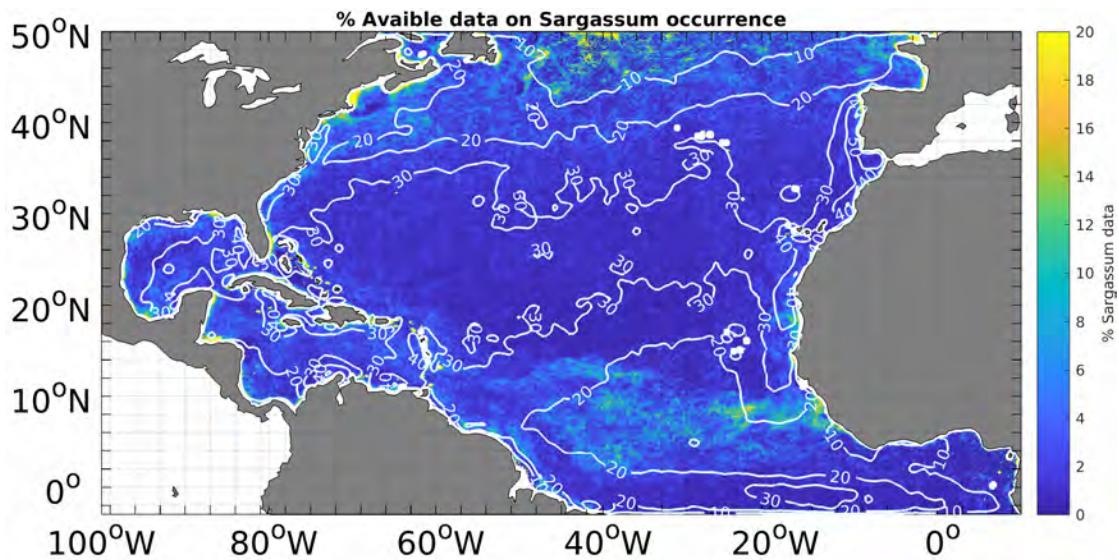


FIGURE 6.1. : Carte des fréquences d'observation des sargasses sur les zones non masquées avec MODIS à 1 km de résolution, année 2017, non filtrée. Les contours indiquent le taux moyen d'observabilité (surface sans masque) journalière en pourcentage (Figure : Madjid Hadjal).

C'est cette indisponibilité intrinsèque des données d'observation des sargasses qui rend nécessaire d'agréger temporellement les images journalières afin d'avoir un composite couvrant toute la zone de distribution des algues sargasses. Celles-ci n'étant pas immobiles, garder la même résolution spatiale avec les images agrégées (composites) induirait des duplications de la détection d'un même agrégat de sargasses. Pour éviter ce cas de figure, la solution la plus simple est de dégrader la finesse des pixels des composites. La résolution d'un pixel doit alors être diminuée proportionnellement à la distance que parcourt un agrégat de sargasses sur l'intervalle de temps de l'agrégation temporelle. La vitesse observée des sargasses étant en moyenne autour de 0.3 m.s^{-1} , la distance approximative qu'elles parcourent au cours d'un mois est de 800 km. On utilise alors, comme compromis, 50 km de résolution avec les composites mensuels pour équilibrer justesse et finesse du positionnement des détections de sargasses. Ce sont ces composites mensuels qui ont été utilisés majoritairement dans

6. Discussion générale – 6.2. Échelles spatiale et temporelle des images composites

cette thèse pour permettre la comparaison avec les résultats d'autres études. Pourtant, il pourrait sembler plus adéquat d'utiliser un intervalle de temps plus court pour limiter la dégradation de la résolution spatiale. Afin d'évaluer un intervalle d'agrégation optimal, la couverture spatiale de composites de plus ou moins longue durée a été calculée à différentes dates de la série temporelle. Les intervalles de temps garantissant une couverture d'au moins 90% sont de l'ordre de la dizaine de jours pour 5 km de résolution. C'est donc cette durée d'agrégation temporelle qui a été utilisé au cours de la présente thèse pour vulgariser les travaux effectués dans le chapitre 3 (<https://www.icare.univ-lille.fr/satellites-reveal-the-spread-of-sargassum-across-the-atlantic-february-2021/>).

Cette agrégation temporelle des images de télédétection en composites de plusieurs jours pourrait avoir des répercussions sur les simulations qui les utilisent comme conditions initiales. En effet, les simulations du chapitre 5 ont été initialisées avec des composites mensuels et la comparaison entre les résultats de simulation et les images satellites est faite avec la même agrégation temporelle. Afin de vérifier l'impact de ce choix sur les résultats de simulation, un test a été mis en œuvre sur des simulations Lagrangiennes sans croissance (pure advection). Celles-ci ont été paramétrées identiquement à celles présentées en première partie du chapitre 5 excepté pour leur initialisation. Au lieu de lâcher les particules Lagrangiennes uniquement au 15^{ème} jour du mois en se basant sur le composite mensuel (Figure 5.1 du chapitre précédent), les particules sont lâchées le jour de leur observation dans la simulation. Au cours du premier mois, les particules correspondant aux images satellites journalières sont ajoutées chaque jour à la simulation (Figure 6.2).

6. Discussion générale – 6.2. Échelles spatiale et temporelle des images composites

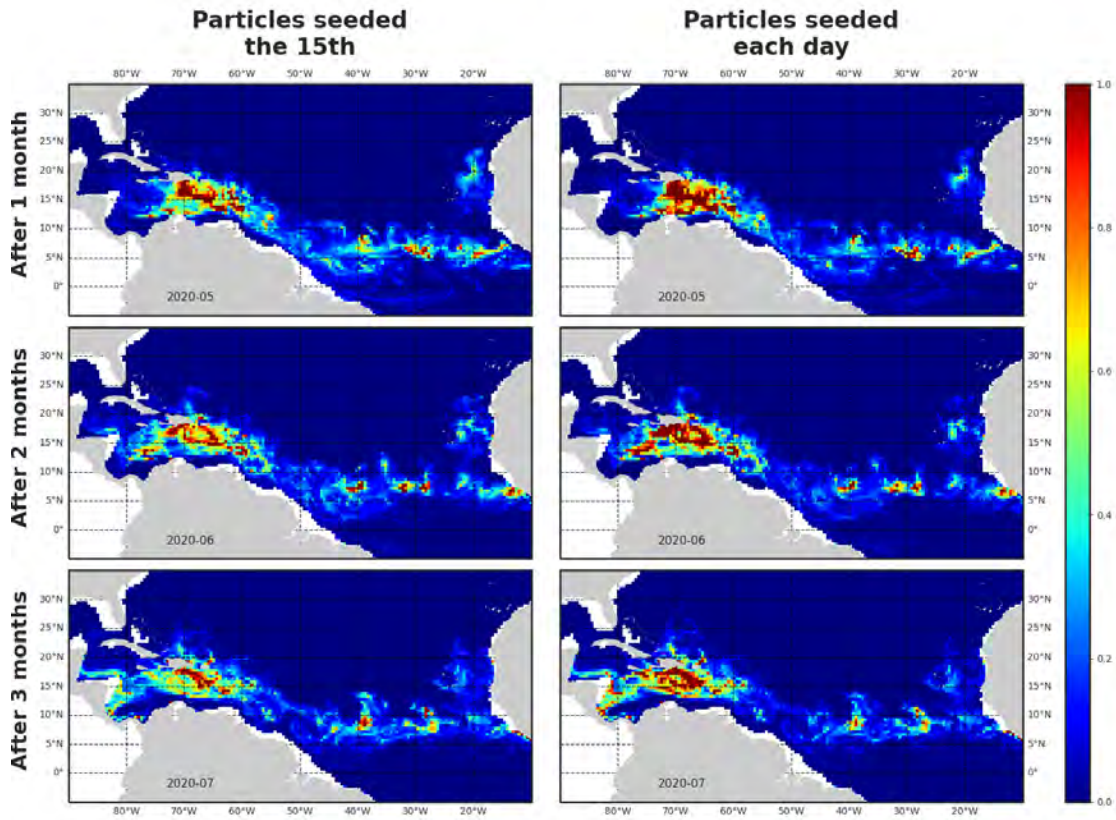


FIGURE 6.2. : Comparaison de la couverture de sargasses sous forme de composites mensuels résultant de simulations Lagrangiennes sans croissance sur des durées de 1, 2 et 3 mois. L'initialisation est basée sur une image satellite mensuelle avec les particules lâchées le 15^{ème} jour du premier mois pour la colonne de gauche. Pour la colonne de droite, les particules sont lâchées le jour d'observation des détections satellites journalières correspondantes.

Ce test a permis de montrer qu'il n'y avait pas de différence majeure entre les deux méthodes d'initialisation, les distributions spatiales obtenues étant similaires. La redondance des images journalières provoque, en revanche, la duplication de certaines particules, ce qui induit des concentrations artificiellement plus élevées avec une initialisation jour par jour. Ainsi, la perte de résolution temporelle en utilisant des composites mensuels dans les simulations a peu d'impact sur la précision des résultats et prévient du dédoublement des détections tout en simplifiant la démarche de comparaison.

6.3. Incertitude des mesures

Un point de fragilité des trois études présentées ici vient du fait qu'aucune des observations sur lesquelles elles sont construites ne sont des mesures *in-situ*. Néanmoins, de nombreux efforts ont été fournis pour valider au mieux les observations et se passer d'échantillonnage terrain, qui serait au demeurant irréalisable au vu de l'immense étendue de la zone d'étude. En premier lieu, la méthode de filtrage des détections erronées utilise un jeu de données labellisées manuellement par l'inspection visuelle des images. Si ce procédé peut être à l'origine d'erreurs, celles-ci ont été réduites au maximum grâce aux observations à la fois *in-situ* et satellites fournies par les travaux de ODY et al., 2019. Celles-ci permettent de donner une idée précise de l'aspect des agrégats de sargasses vus par les capteurs MODIS et ont aidé à déterminer les vraies et fausses détections des sargasses dans le jeu de données labellisées. Aussi, pour limiter au mieux le biais induit par l'opérateur qui a créé ce jeu de données, plusieurs images de détections ont été annotées par trois personnes différentes et un nombre très réduit de contradictions a été obtenu. Cette validation manuelle dans les images est une solution courante dans les études de télédétection, y compris pour les sargasses, si difficiles à observer directement (ARELLANO-VERDEJO et al., 2019; CUEVAS et al., 2018; LAVAL et al., 2023; M. WANG & HU, 2016). Ces précautions, associées également à la très bonne précision du modèle de classification résultant du chapitre 3, garantissent la robustesse du jeu de données de détections de sargasses obtenu.

Dans le chapitre 4, ce jeu de données de télédétection a été exploité afin d'extraire des vitesses de sargasses depuis des paires d'images. Là encore, aucune véritable mesure sur le terrain de la dérive des sargasses n'est actuellement disponible du fait du peu de cohérence structurelle des radeaux de sargasses qui gêne le suivi de leur trajectoire. C'est pourquoi cette étude s'est limitée à un nombre réduit de cas d'observation, tous colocalisés avec des bouées dérivantes. Ces dernières, situées à la surface de l'eau et suivies par GPS, donnent une mesure fidèle des courants à 15 mètres de profondeur (grâce à leur ancre flottante) ou des courants de surface (après perte de leur ancre). Dans le cas présent de l'étude des sargasses, la vitesse de ces bouées a servi à la fois à valider les mesures de vitesse de sargasses et à calculer finement leur modèle de dérive. En effet, la forte corrélation entre les vitesses des sargasses et celles des bouées assure que les observations ne sont pas aberrantes puisque l'on s'attend à ce que la dérive de ces deux objets similaires soit comparable au vu de leur proximité spatiale. Ensuite, les bouées ont servi de mesures *in-situ* des courants pour mieux inférer leur effet sur la dérive des sargasses et le différencier de l'effet du vent. C'est cette comparaison entre bouées et sargasses qui donne du crédit à la méthode d'extraction de trajectoire développée ainsi qu'au modèle de dérive résultant. Il est d'ailleurs envisagé d'étendre cette méthode à des cas de détections de sargasses non colocalisés aux bouées dérivantes afin d'enrichir le jeu de données de trajectoires.

Une autre source d'imprécision des mesures sur les sargasses concerne leurs paramètres physiologiques qui servent de base au modèle de croissance utilisé dans le chapitre 5. D'une part, certaines paramètres sur lesquels on manque d'informations,

6. Discussion générale – 6.4. Variabilité de la dérive

comme les constantes de saturation des nutriments par exemple, ont été calibrés pour forcer le modèle à obtenir des cartes de biomasses large-échelle proches de celles observées par satellite. Les valeurs de ces paramètres peuvent donc manquer de réalisme biologique. Par ailleurs, les autres paramètres du modèle, tirés en grande partie de la littérature sur la biologie des sargasses, sont pour la plupart mesurés en laboratoire. Ces expérimentations *ex-situ* permettent de maîtriser les conditions environnementales, par exemple pour mesurer la capacité de croissance en fonction de la température, mais ne correspondent qu'imparfaitement aux conditions de vie réelles des sargasses. Ainsi, si les mesures observées dans les travaux de HANISAK et SAMUEL, 1987 ou de LAPOINTE, 1986 ont été précieuses pour la création du modèle de croissance, elles ne prennent pas en compte, entre autres, la communauté microbienne de l'holobionte sargasses ainsi que les épiphytes associés qui pourtant jouent un rôle important de fixateur d'azote (CARPENTER, 1972; CARPENTER & COX, 1974). C'est ce problème qu'essayent de contourner des travaux d'expérimentation *in-situ* comme les travaux annexes à la présente thèse (Annexe B). Ils mesurent des taux de croissance de sargasses en milieu naturel, plus proche des conditions de vie réelles, mais se limitent malgré tout à des eaux côtières, assez différentes du plein océan. D'autres initiatives similaires voient le jour et la communauté scientifique devrait rapidement converger sur les valeurs effectives de ces paramètres physiologiques qui pourront être par la suite intégrées au modèle de croissance développé ici (MAGAÑA-GALLEGOS et al., 2023a; PHILIPPI et al., 2023; J. M. SCHELL et al., 2015).

6.4. Variabilité de la dérive

La dérive des sargasses a été abordée ici de deux manières différentes, dans le chapitre 4 où elle a été mesurée et modélisée directement depuis des observations satellites à fine échelle, et dans le chapitre 5 où elle a été réévaluée pour optimiser les performances à large échelle du modèle Lagrangien. Ces deux approches et leurs résultats se recoupent, mais leurs conclusions respectives ne coïncident pas. Alors que les mesures directes pointent vers une valeur du windage aux alentours de 2% et une réduction de l'effet du courant vers 80%, le consensus trouvé pour la simulation Lagrangienne correspond aux propositions précédentes de la littérature avec 1% de windage et 100% du courant (BERLINE et al., 2020; JOUANNO et al., 2020). Cette discordance est cependant nuancée par la variabilité spatiale des paramètres de dérive en ce qui concerne les résultats des simulations Lagrangiennes. En effet, selon la zone d'étude à laquelle on s'intéresse, on retrouve les valeurs de paramètres avancées par l'étude des trajectoires du chapitre 4. Le windage calculé est plus fort ($\approx 2\%$) dans la zone à l'est dans laquelle les vents sont généralement faibles et l'effet du courant dans la mer des Caraïbes est également sensiblement inférieur à 100%.

Au-delà de cette variabilité spatiale, les conclusions dissonantes sur la dérive des sargasses de ces deux études peuvent être expliquées par les différences d'échelle, de courantologie et de conditions d'observation. L'échelle de temps et la résolution spatiale utilisée pour la mesure des trajectoires (3 heures et 1 km de résolution) diffèrent

6. Discussion générale – 6.5. Modèles Lagrangien et Eulérien

largement de celles employées dans les simulations Lagrangiennes (plusieurs mois et 50 km de résolution). Aussi, le calcul de l'effet du courant sur les vitesses de sargasses provient directement des mesures *in-situ* de courant fournies par les bouées alors que la simulation Lagrangienne repose sur des données de modèles de courantologie de moindre précision. Enfin, les conditions d'observabilité qui déterminent notre capacité à extraire des trajectoires de sargasses (peu de nuages, larges agrégats) ont pu légèrement biaiser le jeu de données obtenu dans le chapitre 4. Par exemple, le fait qu'il n'y ait que de très larges agrégats qui soient observables peut expliquer que l'effet du courant sur la dérive des sargasses mesuré soit plutôt faible, l'effet de traînée étant probablement plus fort avec de grands radeaux. De manière comparable, le windage n'a probablement pas de valeur fixe et il est très certainement impacté par le taux de submersion des algues sargasses. Il a par exemple été possible de montrer que le windage estimé dans les cas de vent très faible ($< 3 \text{ m.s}^{-1}$) était bien supérieur aux valeurs de windage avec des vents plus forts (7% contre 2% respectivement, voir annexe 4.6.6). Ces considérations sur la variabilité de la dérive soulignent le besoin de multiplier les données d'observations afin d'améliorer sa modélisation et de prendre en compte de nouveaux facteurs comme la submersion et la taille des agrégats. Pour ce faire, le satellite géostationnaire GOES (Geostationary Operational Environmental Satellite), qui a déjà démontré sa capacité à permettre le suivi de sargasses, constitue une piste intéressante (MINGHELLI et al., 2021).

6.5. Modèles Lagrangien et Eulérien

La dernière étude de cette thèse présentée dans le chapitre 5 est une adaptation du modèle de croissance des sargasses développé dans les travaux JOUANNO et al., 2021a et JOUANNO et al., 2021b (Annexe A) depuis le paradigme Eulérien vers le Lagrangien. Ce dernier donne accès aux trajectoires de vie des agrégats de sargasses simulés, représentés ici par des particules. Afin de qualifier les différences de résultats de ces deux méthodes, supposément équivalentes, une comparaison sur une simulation d'une moitié d'année a été menée avec des paramètres autant que possible identiques (Figure 6.3). Les différences sont néanmoins nombreuses notamment : i) les courants d'entrée proviennent d'une réanalyse GLORYS12 pour l'approche Lagrangienne et d'une simulation NEMO au 1/4° pour l'approche Eulérienne ; ii) l'agrégation temporelle et spatiale des images satellites pour l'initialisation est de 25 km - 15 jours pour l'Eulérien et 50 km - 1 mois pour le Lagrangien ; iii) un facteur de diffusion est utilisé dans le modèle Eulérien uniquement ; iv) la mortalité est paramétrée différemment selon le modèle avec une mortalité seulement quadratique en Lagrangien alors que c'est une combinaison de mortalité quadratique et linéaire qui est employée dans l'Eulérien ; v) le report des masques nuages provenant des observations satellites est effectué sur les images simulées résultant du modèle Lagrangien et non de l'Eulérien.

6. Discussion générale – 6.5. Modèles Lagrangien et Eulérien

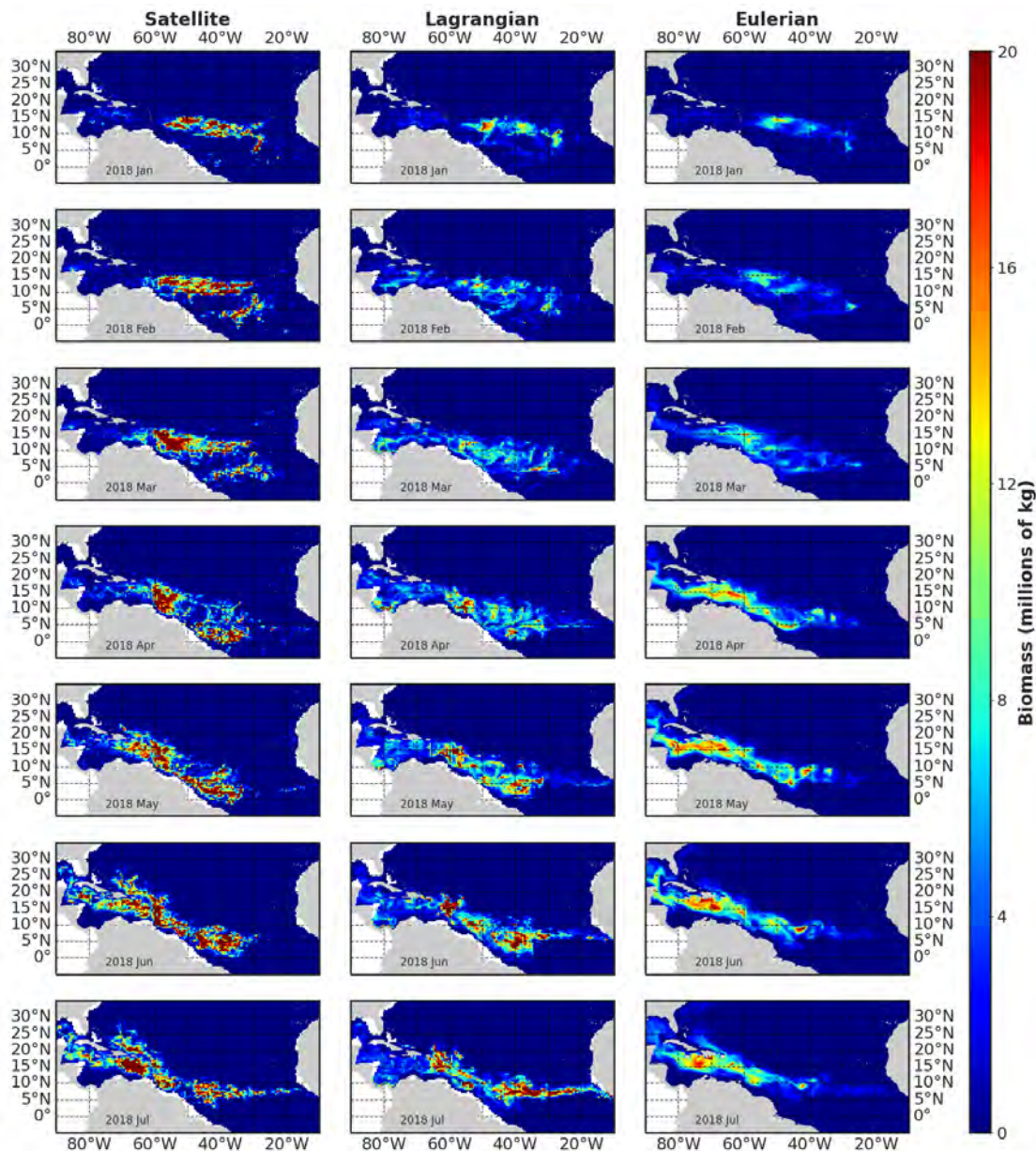


FIGURE 6.3. : Composites mensuels des biomasses de sargasses sur l'année 2018 obtenus avec une simulation de 6 mois du transport et de la croissance des sargasses. De gauche à droite, composites mensuels observés par satellite, issus du modèle Lagrangien, issus du modèle Eulérien

Cette simulation comparée a permis de montrer que si les résultats des deux modèles sont relativement analogues, ils comportent des différences et divergent avec des temps de simulation longs. Deux points principaux peuvent être relevés, les biomasses de sargasses de la simulation Eulérienne sont plus diluées et continues que celles obtenues avec le modèle Lagrangien ou les satellites, et les biomasses sont plus avancées dans le cycle saisonnier avec le modèle Eulérien (plus à l'ouest). Pour ce qui

6. Discussion générale – 6.6. Variabilité interannuelle de la distribution des sargasses

est de la rugosité apparente des composites issus des simulations Lagrangiennes, elle provient en partie des masques nuages reportés depuis les images satellites journalières qui n'ont pas été appliqués aux données Eulériennes de JOUANNO et al., 2021b. Mais il s'agit aussi du paramètre de diffusivité présent dans le modèle Eulérien qui homogénéise localement les concentrations d'algues et donne ces images lissées. Ces divergences de résultat peuvent être imputées aux différences de paramètres et d'initialisation précédemment listées, mais pourrait également dues à une potentielle différence structurelle entre simulations Eulérienne et Lagrangienne. De plus amples investigations seraient nécessaires pour conclure.

Malgré ces différences, les résultats des modèles Eulérien et Lagrangien s'équivalent et décrivent assez fidèlement la dynamique saisonnière et interannuelle des sargasses. L'intérêt premier du modèle Lagrangien est de permettre d'observer les points de basculement de la dynamique de croissance des algues sargasse et d'en étudier la temporalité et la localisation. Notamment, le travail présenté en annexe du chapitre 5 (Section 5.9) est une étude préliminaire des séries temporelles de biomasses de sargasses par analyse fonctionnelle. Les résultats de cette analyse, bien qu'encore insuffisamment conclusifs, permettent d'extraire les dynamiques de croissance des sargasses en classes différentes et de qualifier leur localisation et autres paramètres environnementaux. Une autre exploitation possible de ce modèle de croissance en Lagrangien pourrait consister à faire un rétro-suivi (backtracking) depuis des zones d'échouement. Cette approche, déjà employé par la littérature (K. S. T. ALLEYNE et al., 2023a; JOHNS et al., 2020; PUTMAN et al., 2018), bénéficierait de l'ajout du modèle de croissance développé ici et devrait permettre d'étudier l'origine des sargasses échouées, mais aussi les conditions environnementales du milieu qu'elles ont traversé.

6.6. Variabilité interannuelle de la distribution des sargasses

La distribution spatiale des sargasses et les quantités de biomasse associées connaissent des variations très contrastées d'une année à l'autre depuis leur implantation dans l'océan Atlantique tropical nord en 2010. Les premières années dans cette nouvelle aire de répartition (2011-2015) ont été assez chaotiques pour les sargasses avec l'apparition d'échouements ponctuels en 2011 et 2012 suivis d'une année exempte de sargasses et de leur recrudescence en 2014 et 2015. Depuis fin 2016, la dernière année en date comportant de faibles quantités de sargasses, elles semblent se stabiliser avec d'importants épisodes d'échouements chaque année (même si le nombre d'échouements reste hautement variable localement et peu renseigné au niveau global). Nonobstant cette relative régularité, il est des années où les sargasses envahissent avec bien plus d'ampleur leur zone estivale que sont la mer des Caraïbes et le golfe du Mexique. Les habitants de la Martinique et de la Guadeloupe se souviennent en particulier de l'été 2018 et des masses gargantuesques d'algues envahissant leurs plages. Cette variabilité entre des biomasses annuelles élevées et colossales ainsi que de leurs arrivées irrégulières soulève la question des facteurs déterminants ces différences interannuelles.

6. Discussion générale – 6.6. Variabilité interannuelle de la distribution des sargasses

Le modèle couplé de dérive et de croissance présenté dans le chapitre 5, aboutissement des travaux de la présente thèse, est bâti afin d'explorer et analyser cette variabilité interannuelle. Basé notamment sur les limitations physiques et biogéochimiques, il permet d'analyser les zones de croissance au cours du cycle saisonnier des sargasses et de l'intégrer le long de trajectoires de dérive. En premier lieu, les cartes saisonnières des facteurs limitants la pousse des sargasses ont permis de mettre en évidence la prépondérance des facteurs physiques sur les facteurs chimiques. En particulier, la température semble le facteur clé de la capacité à croître des sargasses, alors que le manque de nutriments, comme le phosphore et l'azote, semble marginal. En effet, les valeurs de paramètres, qui ont été utilisés pour modéliser la captation des nutriments et leur effet sur la croissance, sont relativement peu contraignants et les sargasses ne manquent jamais vraiment ni de nitrate ni de phosphore dans les simulations. Au contraire, les paramètres régissant la limitation par la température se sont avérés, après la calibration, beaucoup plus contraignants, en particulier la limite haute de température permettant aux sargasses de croître. Ces résultats viennent corroborer, d'une part, de récentes études en laboratoire montrant le faible effet de l'enrichissement en nutriments sur les sargasses (MAGAÑA-GALLEGOS et al., 2023a; PHILIPPI et al., 2023). D'autre part, l'anti-corrélation entre les températures de surface de l'océan et les concentrations de sargasses sont cohérents avec la forte limitation par la température proposée ici (SKLIRIS et al., 2022a; M. WANG et al., 2019a). Aussi, l'enrichissement des eaux, avancé précédemment dans la littérature (OVIATT et al., 2019; M. WANG et al., 2019b) afin d'expliquer l'accroissement des algues sargasses, semble avoir un impact minime sur les résultats des simulations. Qu'ils soient dus à des apports fluviaux (Amazone, Congo), aux vents Sahariens ou aux upwellings, ces apports en nutriments sont relativement réguliers depuis 2011 et ne correspondent donc pas à la variabilité interannuelle des sargasses. Il est alors peu probable qu'ils soient déterminants en ce qui concerne les variations de biomasse observées entre chaque année.

Parallèlement, le calcul du temps requis par une particule pour doubler sa biomasse pourvoit des informations probantes afin d'anatomiser la dynamique spatiale et temporelle des sargasses. Il en ressort en particulier un élément clé des séries annuelles de biomasses : les hautes températures du courant nord Brésil et de la mer des Caraïbes. Tempérées la plupart des mois de l'année ($\approx 25^{\circ}\text{C}$), ces eaux, par lesquelles transitent les sargasses à la fin de leur traversée saisonnière de l'Atlantique, atteignent des hautes températures ($>28^{\circ}\text{C}$) à la fin du printemps. Cette caractéristique de la circulation générale de l'Atlantique apparaît plus ou moins tardivement selon les années et l'on peut l'observer dans certains cas dès le début de mai (2016) ou qu'à partir de mi-août (2018). Ce retard plus ou moins marqué correspond très bien aux variations des quantités de sargasses observées au courant de l'été. Aussi, sachant que de fortes températures provoquent l'arrêt de la croissance des sargasses et accélèrent leur dégradation, on peut former l'hypothèse qu'il s'agit là d'un facteur prééminent de régulation annuelle des biomasses de sargasses. Ainsi, la mise en place du courant chaud au nord du Brésil et de la montée des températures au sein de la mer des Caraïbes et du golfe du Mexique détermineraient l'arrêt plus ou moins précoce de la

6. Discussion générale – 6.6. Variabilité interannuelle de la distribution des sargasses

croissance des sargasses au niveau global et partiellement les quantités de biomasse annuelles atteintes (les conditions de la distribution des sargasses en début d'année étant, elles aussi, déterminantes). Cette conclusion constitue une piste prometteuse pour expliquer et prévoir la variation interannuelle de biomasses. Il reste à expliquer les mécanismes climatiques régissants cette hausse caractéristique des températures estivales entre les eaux au large du Brésil et celles du golfe du Mexique. L'explication probable est à chercher du côté des télécorrélations atmosphériques (c'est-à-dire les modes de variabilité du climat) et plus particulièrement du mode méridional de l'Atlantique (AMM en anglais). Ce dernier, indicateur du déplacement septentrional ou méridional de l'ITCZ (InterTropical Convergence Zone), est corrélé aux anomalies de température de surface de l'océan au nord du Brésil. L'étude de SKLIRIS et al., 2022a a déjà pu montrer la corrélation négative entre l'AMM et les concentrations estivales de sargasses. Ces télécorrélations connaissent une hausse de leur variabilité sur les dernières décennies en lien avec le changement climatique, si bien qu'on peut émettre l'hypothèse que l'actuelle variabilité interannuelle des sargasses en Atlantique tropical nord est reliée aux perturbations anthropiques du climat. Pour conclure, il apparaît que les facteurs déterminant l'accumulation annuelle plus ou moins massive des algues sargasses depuis 2011 serait à chercher parmi les variations climatiques, notamment par l'intermédiaire de la température de surface de l'océan dont les extrêmes régulent la croissance saisonnière des algues sargasses dans l'Océan Atlantique tropical nord.

Bibliographie

- ALLEYNE, K., NEAT, F., & OXFORD, H. A. (2023). A baseline assessment of the epiphytic community associated with pelagic sargassum in the tropical atlantic. *Aquatic Botany*, 103635. <https://doi.org/10.1016/j.aquabot.2023.103635> (cf. p. 35)
- ALLEYNE, K. S. T., JOHNSON, D., NEAT, F., OXFORD, H. A., & VALLÈS, H. (2023a). Seasonal variation in morphotype composition of pelagic sargassum influx events is linked to oceanic origin [Number : 1 Publisher : Nature Publishing Group]. *Scientific Reports*, 13(1), 3753. <https://doi.org/10.1038/s41598-023-30969-2> (cf. p. 127)
- ALLEYNE, K. S. T., NEAT, F., & OXFORD, H. A. (2023b). An analysis of arsenic concentrations associated with sargassum influx events in barbados. *Marine Pollution Bulletin*, 192, 115064. <https://doi.org/10.1016/j.marpolbul.2023.115064> (cf. p. 40)
- ALLEYNE, K. S. T., SMALL, M., CORBIN, M., VALLÈS, H., & OXFORD, H. A. (2023c). Free-swimming fauna associated with influxes of pelagic sargassum : Implications for management and harvesting. *Frontiers in Marine Science*, 10. Récupérée 13 juillet 2023, à partir de <https://www.frontiersin.org/articles/10.3389/fmars.2023.1090742> (cf. p. 41)
- ALLOUCHE, O., TSOAR, A., & KADMON, R. (2006). Assessing the accuracy of species distribution models : prevalence, kappa and the true skill statistic (TSS). *Journal of applied ecology*, 43(6), 1223-1232 (cf. p. 103).
- ALMEIDA, K. L., CUEVAS, E., URIBE-MARTÍNEZ, A., van TUSSEN BROEK, B. I., HERNÁNDEZ-FONTES, J. V., & SILVA, R. (2020). 2 A Review of Remote Sensing Approaches to Analyse 3 the Dispersal of Pelagic Sargassum Spp., 22 (cf. p. 44).
- ALZATE-GAVIRIA, L., DOMÍNGUEZ-MALDONADO, J., CHABLÉ-VILLACÍS, R., OLGUIN-MACIEL, E., LEAL-BAUTISTA, R. M., CANCHÉ-ESCAMILLA, G., CABALLERO-VÁZQUEZ, A., HERNÁNDEZ-ZEPEDA, C., BARREDO-POOL, F. A., & TAPIA-TUSSELL, R. (2021). Presence of polyphenols complex aromatic “lignin” in sargassum spp. from mexican caribbean [Number : 1 Publisher : Multidisciplinary Digital Publishing Institute]. *Journal of Marine Science and Engineering*, 9(1), 6. <https://doi.org/10.3390/jmse9010006> (cf. p. 39)
- AMADOR-CASTRO, F., GARCÍA-CAYUELA, T., ALPER, H. S., RODRIGUEZ-MARTINEZ, V., & CARRILLO-NIEVES, D. (2021). Valorization of pelagic sargassum biomass into sustainable applications : current trends and challenges. *Journal of Environmental Management*, 283, 112013. <https://doi.org/10.1016/j.jenvman.2021.112013> (cf. p. 40)

Bibliographie

- AN, D., XING, Q., YU, D., & PAN, S. (2022). A simple method for estimating macroalgae area under clouds on MODIS imagery. *Frontiers in Marine Science*, 9. Récupérée 7 septembre 2022, à partir de <https://www.frontiersin.org/articles/10.3389/fmars.2022.995731> (cf. p. 44)
- ANDRADE-CANTO, F., BERON-VERA, F. J., GONI, G. J., KARRASCH, D., OLASCOAGA, M. J., & TRIÑANES, J. (2022). Carriers of Sargassum and mechanism for coastal inundation in the Caribbean Sea [Publisher : American Institute of Physics]. *Physics of Fluids*, 34(1), 016602. <https://doi.org/10.1063/5.0079055> (cf. p. 45)
- ANTONIO-MARTÍNEZ, F., HENAUT, Y., VEGA-ZEPEDA, A., CERÓN-FLORES, A. I., RAIGOZA-FIGUERAS, R., CETZ-NAVARRO, N. P., & ESPINOZA-AVALOS, J. (2020). Leachate effects of pelagic Sargassum spp. on larval swimming behavior of the coral Acropora palmata [Number : 1 Publisher : Nature Publishing Group]. *Scientific Reports*, 10(1), 3910. <https://doi.org/10.1038/s41598-020-60864-z> (cf. p. 38)
- APARICIO, E., RODRÍGUEZ-JASSO, R. M., PINALES-MÁRQUEZ, C. D., LOREDO-TREVINO, A., ROBLEDO-OLIVO, A., AGUILAR, C. N., KOSTAS, E. T., & RUIZ, H. A. (2021). High-pressure technology for sargassum spp biomass pretreatment and fractionation in the third generation of bioethanol production. *Bioresource Technology*, 329, 124935. <https://doi.org/10.1016/j.biortech.2021.124935> (cf. p. 41)
- ARELLANO-VERDEJO, J., LAZCANO-HERNANDEZ, H. E., & CABANILLAS-TERÁN, N. (2019). Erisnet : deep neural network for sargassum detection along the coastline of the mexican caribbean [Publisher : PeerJ Inc.]. *PeerJ*, 7, e6842. <https://doi.org/10.7717/peerj.6842> (cf. p. 44, 51, 52, 69, 119, 123)
- ARELLANO-VERDEJO, J., & LAZCANO-HERNÁNDEZ, H. E. (2021). Collective view : mapping sargassum distribution along beaches [Publisher : PeerJ Inc.]. *PeerJ Computer Science*, 7, e528. <https://doi.org/10.7717/peerj-cs.528> (cf. p. 42)
- ARELLANO-VERDEJO, J., SANTOS-ROMERO, M., & LAZCANO-HERNANDEZ, H. E. (2022). Use of semantic segmentation for mapping sargassum on beaches [Publisher : PeerJ Inc.]. *PeerJ*, 10, e13537. <https://doi.org/10.7717/peerj.13537> (cf. p. 42)
- AZCORRA-MAY, K. J., OLGUIN-MACIEL, E., DOMÍNGUEZ-MALDONADO, J., TOLEDANO-THOMPSON, T., LEAL-BAUTISTA, R. M., ALZATE-GAVIRIA, L., & TAPIA-TUSSELL, R. (2022). Sargassum biorefineries : potential opportunities towards shifting from wastes to products. *Biomass Conversion and Biorefinery*. <https://doi.org/10.1007/s13399-022-02407-2> (cf. p. 41)
- BACH, L. T., TAMSITT, V., GOWER, J., HURD, C. L., RAVEN, J. A., & BOYD, P. W. (2021). Testing the climate intervention potential of ocean afforestation using the great atlantic sargassum belt [Number : 1 Publisher : Nature Publishing Group]. *Nature Communications*, 12(1), 2556. <https://doi.org/10.1038/s41467-021-22837-2> (cf. p. 39)
- BAKER, P., MINZLAFF, U., SCHOENLE, A., SCHWABE, E., HOHLFELD, M., JEUCK, A., BRENKE, N., PRAUSSE, D., ROTHENBECK, M., BRIX, S., FRUTOS, I., JÖRGER, K. M., NEUSSER, T. P., KOPPELMANN, R., DEVEY, C., BRANDT, A., & ARNDT, H. (2018). Potential contribution of surface-dwelling Sargassum algae to deep-sea ecosystems in the southern North Atlantic. *Deep Sea Research Part II : Topical Studies*

- in Oceanography*, 148, 21-34. <https://doi.org/10.1016/j.dsr2.2017.10.002> (cf. p. 39)
- BANASZAK, A. T. (2021). Contamination of coral reefs in the mexican caribbean. In D.-P. HÄDER, E. W. HELBLING & V. E. VILLAFANE (Éd.), *Anthropogenic pollution of aquatic ecosystems* (p. 113-129). Springer International Publishing. https://doi.org/10.1007/978-3-030-75602-4_6. (Cf. p. 38)
- BAO, M., PARK, J.-S., WU, H., LEE, H. J., PARK, S. R., KIM, T.-H., SON, Y. B., LEE, T. H., YARISH, C., & KIM, J. K. (2022). A comparison of physiological responses between attached and pelagic populations of sargassum horneri under nutrient and light limitation. *Marine Environmental Research*, 173, 105544. <https://doi.org/10.1016/j.marenvres.2021.105544> (cf. p. 37)
- BARTLETT, D., & ELMER, F. (2021). The impact of sargassum inundations on the turks and caicos islands. *Phycology*, 1(2), 83-104. <https://doi.org/10.3390/phycology1020007> (cf. p. 38)
- BARTON, I. J. (2002). Ocean currents from successive satellite images : The reciprocal filtering technique. *Journal of Atmospheric and Oceanic Technology*, 19(10), 1677-1689 (cf. p. 86).
- BELGIU, M., & DRĂGUȚ, L. (2016). Random forest in remote sensing : A review of applications and future directions. *ISPRS journal of photogrammetry and remote sensing*, 114, 24-31 (cf. p. 59).
- BERLINE, L., & DESCLOITRES, J. (2021). Cartes de répartition des couvertures de Sargasses dérivées de MODIS sur l'Atlantique. <https://doi.org/10.12770/8FE1CDCB-F4EA-4C81-8543-50F0B39B4ECA>. (Cf. p. 44)
- BERLINE, L., ODY, A., JOUANNO, J., CHEVALIER, C., ANDRÉ, J.-M., THIBAUT, T., & MÉNARD, F. (2020). Hindcasting the 2017 dispersal of Sargassum algae in the Tropical North Atlantic. *Marine Pollution Bulletin*, 158, 111431 (cf. p. 45, 71, 77, 89, 97-99, 102, 103, 110, 124).
- BERNARD, D., BIABIANY, E., CÉCÉ, R., CHERY, R., & SEKKAT, N. (2022). Clustering analysis of the Sargassum transport process : application to beaching prediction in the Lesser Antilles. *Ocean Science*, 18(4), 915-935 (cf. p. 98).
- BERON-VERA, F. J. (2021). Nonlinear dynamics of inertial particles in the ocean : from drifters and floats to marine debris and sargassum. *Nonlinear Dynamics*, 103(1), 1-26. <https://doi.org/10.1007/s11071-020-06053-z> (cf. p. 45)
- BERON-VERA, F. J., & MIROU, P. (2020a). A minimal Maxey–Riley model for the drift of \emph{Sargassum} rafts [arXiv : 2003.03339]. *Journal of Fluid Mechanics*, 904, A8. <https://doi.org/10.1017/jfm.2020.666> (cf. p. 45)
- BERON-VERA, F. J., & MIROU, P. (2020b). A minimal Maxey–Riley model for the drift of Sargassum rafts. *Journal of Fluid Mechanics*, 904 (cf. p. 77).
- BORTONE, S., HASTINGS, P., & COLLARD, S. (1977). The Pelagic - Sargassum Ichthyofauna of the Eastern Gulf of Mexico. *Gulf of Mexico Science*, 1(2). <https://doi.org/10.18785/negs.0102.02> (cf. p. 35)
- BROOKS, M. T., COLES, V. J., & COLES, W. C. (2019). Inertia influences pelagic sargassum advection and distribution. *Geophysical Research Letters*, 46(5), 2610-2618. <https://doi.org/https://doi.org/10.1029/2018GL081489> (cf. p. 45, 87)

- BROOKS, M. T., COLES, V. J., HOOD, R. R., & GOWER, J. F. (2018). Factors controlling the seasonal distribution of pelagic sargassum. *Marine Ecology Progress Series*, 599, 1-18. <https://doi.org/10.3354/meps12646> (cf. p. 46, 77, 97, 98)
- BROOKS, W. R., HUTCHINSON, K., & TOLBERT, M. (2007). Pelagic Sargassum Mediates Predation Among Symbiotic Fishes and Shrimps. *Gulf of Mexico Science*, 25(2). <https://doi.org/10.18785/goms.2502.05> (cf. p. 35)
- BRÜGGE, B., & DENGG, J. (1991). Differences in drift behavior between drogued and undrogued satellite-tracked drifting buoys. *Journal of Geophysical Research : Oceans*, 96(C4), 7249-7263 (cf. p. 88).
- BURNS, K. A., & TEAL, J. M. (1973). Hydrocarbons in the pelagic Sargassum community. *Deep Sea Research and Oceanographic Abstracts*, 20(2), 207-211. [https://doi.org/10.1016/0011-7471\(73\)90051-X](https://doi.org/10.1016/0011-7471(73)90051-X) (cf. p. 40)
- CABANILLAS-TERÁN, N., HERNÁNDEZ-ARANA, H. A., RUIZ-ZÁRATE, M.-Á., VEGA-ZEPEDA, A., & SANCHEZ-GONZALEZ, A. (2019). Sargassum blooms in the Caribbean alter the trophic structure of the sea urchin Diadema antillarum [Publisher : PeerJ Inc.]. *PeerJ*, 7, e7589. <https://doi.org/10.7717/peerj.7589> (cf. p. 38)
- CARPENTER, E. J. (1972). Nitrogen Fixation by a Blue-Green Epiphyte on Pelagic Sargassum [Publisher : American Association for the Advancement of Science Section : Reports]. *Science*, 178(4066), 1207-1209. <https://doi.org/10.1126/science.178.4066.1207> (cf. p. 37, 124)
- CARPENTER, E. J., & COX, J. L. (1974). Production of pelagic Sargassum and a blue-green epiphyte in the western Sargasso Sea1. *Limnology and Oceanography*, 19(3), 429-436. <https://doi.org/https://doi.org/10.4319/lo.1974.19.3.0429> (cf. p. 37, 124)
- CASAZZA, T. L., & ROSS, S. W. (2008). Fishes associated with pelagic Sargassum and open water lacking Sargassum in the Gulf Stream off North Carolina [Number : 4]. *Fishery Bulletin*, 106(4), 348-363. Récupérée 23 mars 2021, à partir de <http://fishbull.noaa.gov/1064/casazza.pdf> (cf. p. 35)
- CASTAÑEDA-SERNA, H. U., CALDERÓN-DOMÍNGUEZ, G., DE LA PAZ SALGADO-CRUZ, M., GARCÍA-BÓRQUEZ, A., & FARRERA-REBOLLO, R. R. (2021). Pelagic sargassum as a source of micro- and nanocellulose for environmentally sustainable plastics. In D. THANGADURAI, J. SANGEETHA & R. PRASAD (Éd.), *Bioprospecting algae for nanosized materials* (p. 345-364). Springer International Publishing. https://doi.org/10.1007/978-3-030-81557-8_14. (Cf. p. 41)
- CHANGEUX, T., BERLINE, L., PODLEJSKI, W., GUILLOT, T., STIGER-POUVREAU, V., CONNAN, S., & THIBAUT, T. (2023). Variability in growth and tissue composition (CNP, natural isotopes) of the three morphotypes of holopelagic Sargassum. *Aquatic Botany*, 187, 103644 (cf. p. 3, 37).
- CHÁVEZ, V., URIBE-MARTIÉNEZ, A., CUEVAS, E., RODRÍGUEZ-MARTIÉNEZ, R. E., VAN TUSSEN BROEK, B. I., FRANCISCO, V., ESTÉVEZ, M., CELIS, L. B., MONROY-VELÁZQUEZ, L. V., LEAL-BAUTISTA, R., et al. (2020). Massive influx of pelagic Sargassum spp. on the coasts of the Mexican Caribbean 2014–2020 : Challenges and opportunities. *Water*, 12(10), 2908 (cf. p. 38, 39, 50, 77, 97).

- CHÁVEZ-GUERRERO, L., TOXQUI-TERÁN, A., RIVERA-HARO, J., LOZOYA-MÁRQUEZ, L., & LARA-BANDA, M. (2021). Management of Pelagic Sargassum spp. Landings to Atlantic Coastlines Through Direct Combustion and Further Synthesis of Highly Pure Calcium Carbonate Using the Residual Ashes. *Waste and Biomass Valorization*, 12(12), 6591-6599 (cf. p. 41).
- CHELTON, D. B., DESZOEKE, R. A., SCHLAX, M. G., EL NAGGAR, K., & SIWERTZ, N. (1998). Geographical variability of the first baroclinic Rossby radius of deformation. *Journal of Physical Oceanography*, 28(3), 433-460 (cf. p. 86).
- CHEN, Y., WAN, J., ZHANG, J., ZHAO, J., YE, F., WANG, Z., & LIU, S. (2019). Automatic Extraction Method of Sargassum Based on Spectral-Texture Features of Remote Sensing Images [ISSN : 2153-7003]. *IGARSS 2019-2019 IEEE International Geoscience and Remote Sensing Symposium*, 3705-3707. <https://doi.org/10.1109/IGARSS.2019.8898131> (cf. p. 51, 52)
- CHIKANI-CABRERA, K. D., FERNANDES, P. M. B., TAPIA-TUSSELL, R., PARRA-ORTIZ, D. L., HERNÁNDEZ-ZÁRATE, G., VALDEZ-OJEDA, R., & ALZATE-GAVIRIA, L. (2022). Improvement in methane production from pelagic sargassum using combined pretreatments. *Life*, 12(8), 1214. <https://doi.org/10.3390/life12081214> (cf. p. 41)
- CIPOLLONI, O.-A., GIGAULT, J., DASSIÉ, É. P., BAUDRIMONT, M., GOURVES, P.-Y., AMARAL-ZETTLER, L., & PASCAL, P.-Y. (2022). Metals and metalloids concentrations in three genotypes of pelagic sargassum from the atlantic ocean basin-scale. *Marine Pollution Bulletin*, 178, 113564. <https://doi.org/10.1016/j.marpolbul.2022.113564> (cf. p. 40)
- COSTON-CLEMENTS, L., SETTLE, L. R., HOSS, D. E., & CROSS, F. A. (1991). *Utilization of the Sargassum Habitat by Marine Invertebrates and Vertebrates, a Review* [Google-Books-ID : g3oeAQAAIAAJ]. U.S. Department of Commerce, National Oceanic; Atmospheric Administration, National Marine Fisheries Service, Southeast Fisheries Science Center, Beaufort Laboratory. (Cf. p. 35).
- CUEVAS, E., URIBE-MARTÍNEZ, A., & LICEAGA-CORREA, M. d. l. Á. (2018). A satellite remote-sensing multi-index approach to discriminate pelagic Sargassum in the waters of the Yucatan Peninsula, Mexico [Publisher : Taylor & Francis _eprint : <https://doi.org/10.1080/01431161.2018.1447162>]. *International Journal of Remote Sensing*, 39(11), 3608-3627. <https://doi.org/10.1080/01431161.2018.1447162> (cf. p. 44, 51-53, 56, 59, 69, 77, 97, 123)
- CUSHMAN-ROISIN, B., & BECKERS, J.-M. (2011). *Introduction to geophysical fluid dynamics : physical and numerical aspects*. Academic press. (Cf. p. 91).
- DASSIÉ, E. P., GOURVES, P.-Y., CIPOLLONI, O., PASCAL, P.-Y., & BAUDRIMONT, M. (2021). First assessment of atlantic open ocean sargassum spp. metal and metalloid concentrations. *Environmental Science and Pollution Research*. <https://doi.org/10.1007/s11356-021-17047-8> (cf. p. 40)
- DAVIS, D., SIMISTER, R., CAMPBELL, S., MARSTON, M., BOSE, S., MCQUEEN-MASON, S. J., GOMEZ, L. D., GALLIMORE, W. A., & TONON, T. (2021). Biomass composition of the golden tide pelagic seaweeds sargassum fluitans and s. natans (morphotypes i and VIII) to inform valorisation pathways. *Science of The Total*

Bibliographie

- Environment*, 762, 143134. <https://doi.org/10.1016/j.scitotenv.2020.143134> (cf. p. 37)
- de la BARREDA-BAUTISTA, B., METCALFE, S. E., SMITH, G., SJÖGERSTEN, S., BOYD, D. S., CERDEIRA-ESTRADA, S., LÓPEZ-RAMÍREZ, P., MAGALDI, A., RESSL, R., PERERA-VALDERRAMA, S., CABALLERO-ARAGÓN, H., SIORDIA, O. S., COULDIDGE, J., GRAY, P., SILVA, R., VAN TUSSEN BROEK, B. I., ESCALANTE-MANCERA, E., & FOODY, G. (2023). Monitoring holopelagic Sargassum spp. along the Mexican Caribbean coast : understanding and addressing user requirements for satellite remote sensing [Place : Lausanne, Switzerland Publisher : Frontiers Research Foundation Section : ORIGINAL RESEARCH article]. *Frontiers in Marine Science*. <https://doi.org/10.3389/fmars.2023.1166000> (cf. p. 44)
- de LANAY, D. B., MONTHIEUX, A., BANYDEEN, R., MEHDI, J.-L., RESIERE, D., DRAME, M., & NEVIERE, R. (2022). Risk of preeclampsia among women living in coastal areas impacted by sargassum strandings on the French Caribbean island of Martinique. *Environmental Toxicology and Pharmacology*, 103894 (cf. p. 77).
- DERPANIS, K. G. (2010). Overview of the RANSAC Algorithm. *Image Rochester NY*, 4(1), 2-3 (cf. p. 89).
- DESCLOITRES, J., MINGHELLI, A., STEINMETZ, F., CHEVALIER, C., CHAMI, M., & BERLINE, L. (2021). Revisited estimation of moderate resolution sargassum fractional coverage using decametric satellite data (s2-msi). *Remote Sensing*, 13(24), 5106. <https://doi.org/10.3390/rs13245106> (cf. p. 44, 52, 54, 70, 77, 78, 98)
- DEVAULT, D. A., MASSAT, F., BAYLET, A., DOLIQUE, F., & LOPEZ, P.-J. (2021a). Arsenic and chlорdecone contamination and decontamination toxicokinetics in sargassum sp. *Environmental Science and Pollution Research*. <https://doi.org/10.1007/s11356-020-12127-7> (cf. p. 40)
- DEVAULT, D. A., MODESTIN, E., COTTEREAU, V., VEDIE, F., STIGER-POUVREAU, V., PIERRE, R., COYNEL, A., & DOLIQUE, F. (2021b). The silent spring of sargassum. *Environmental Science and Pollution Research*, 28(13), 15580-15583. <https://doi.org/10.1007/s11356-020-12216-7> (cf. p. 40)
- DIBNER, S., MARTIN, L., THIBAUT, T., AURELLE, D., BLANFUNÉ, A., WHITTAKER, K., COONEY, L., SCHELL, J. M., GOODWIN, D. S., & SIUDA, A. N. S. (2022). Consistent genetic divergence observed among pelagic sargassum morphotypes in the western north atlantic [_eprint : <https://onlinelibrary.wiley.com/doi/pdf/10.1111/maec.12691>]. *Marine Ecology*, n/a(1), e12691. <https://doi.org/10.1111/maec.12691> (cf. p. 23, 37)
- DIERSSEN, H., CHLUS, A., & RUSSELL, B. (2015). Hyperspectral discrimination of floating mats of seagrass wrack and the macroalgae Sargassum in coastal waters of Greater Florida Bay using airborne remote sensing. *Remote Sensing of Environment*, 167, 247-258 (cf. p. 51).
- DJAKOURÉ, S., ARAUJO, M., HOUNSOU-GBO, A., NORIEGA, C., & BOURLÈS, B. (2017a). On the potential causes of the recent Pelagic Sargassum blooms events in the tropical North Atlantic Ocean [Publisher : Copernicus GmbH]. *Biogeosciences Discussions*, 1-20. <https://doi.org/10.5194/bg-2017-346> (cf. p. 46)

Bibliographie

- DJAKOURÉ, S., ARAUJO, M., HOUNSOU-GBO, A., NORIEGA, C., & BOURLÈS, B. (2017b). On the potential causes of the recent Pelagic Sargassum blooms events in the tropical North Atlantic Ocean. *Biogeosciences Discussions*, 1-20 (cf. p. 97).
- EKMAN, V. W. (1905). On the influence of the earth's rotation on ocean-currents. (cf. p. 88).
- ESCOBAR, B., PÉREZ-SALCEDO, K. Y., ALONSO-LEMUS, I. L., PACHECO, D., & BARBOSA, R. (2017). N-doped porous carbon from Sargassum spp. as metal-free electrocatalysts for oxygen reduction reaction in alkaline media. *International Journal of Hydrogen Energy*, 42(51), 30274-30283. <https://doi.org/10.1016/j.ijhydene.2017.06.240> (cf. p. 41)
- FARNEBÄCK, G. (2003). Two-frame motion estimation based on polynomial expansion. *Scandinavian conference on Image analysis*, 363-370 (cf. p. 79).
- FIDAI, Y. A., DASH, J., TOMPKINS, E., & TONON, T. (2020). A systematic review of floating and beach landing records of Sargassum beyond the Sargasso Sea. *Environmental Research Communications* (cf. p. 42).
- FINE, M. L. (1970). Faunal variation on pelagic sargassum. *Marine Biology*, 7(2), 112-122. <https://doi.org/10.1007/BF00354914> (cf. p. 35, 50, 97)
- FRANCOEUR, M., FERINO-PÉREZ, A., YACOU, C., JEAN-MARIUS, C., EMMANUEL, E., CHÉRÉMOND, Y., JAUREGUI-HAZA, U., & GASPARD, S. (2021). Activated carbon synthetized from sargassum (sp) for adsorption of caffeine : understanding the adsorption mechanism using molecular modeling. *Journal of Environmental Chemical Engineering*, 9(1), 104795. <https://doi.org/10.1016/j.jece.2020.104795> (cf. p. 41)
- FRANKS, J. S., JOHNSON, D. R., & KO, D. S. (2016). Pelagic sargassum in the tropical north atlantic. *Gulf and Caribbean Research*, 27(1), SC6-SC11. <https://doi.org/10.18785/gcr.2701.08> (cf. p. 71, 98, 116)
- GARCÍA-SÁNCHEZ, M., GRAHAM, C., VERA, E., ESCALANTE-MANCERA, E., ÁLVAREZ-FILIP, L., & van TUSSEN BROEK, B. I. (2020). Temporal changes in the composition and biomass of beached pelagic Sargassum species in the Mexican Caribbean. *Aquatic Botany*, 167, 103275. <https://doi.org/10.1016/j.aquabot.2020.103275> (cf. p. 37)
- GOBERT, T., GAUTIER, A., CONNAN, S., ROUGET, M.-L., THIBAUT, T., STIGER-POUVREAU, V., & WAELES, M. (2022). Trace metal content from holopelagic sargassum spp. sampled in the tropical north atlantic ocean : emphasis on spatial variation of arsenic and phosphorus. *Chemosphere*, 136186. <https://doi.org/10.1016/j.chemosphere.2022.136186> (cf. p. 40)
- GORDILLO SIERRA, A. R., AMADOR-CASTRO, L. F., RAMÍREZ-PARTIDA, A. E., GARCÍA-CAYUELA, T., CARRILLO-NIEVES, D., & ALPER, H. S. (2022). Valorization of caribbean sargassum biomass as a source of alginate and sugars for de novo biodiesel production. *Journal of Environmental Management*, 324, 116364. <https://doi.org/10.1016/j.jenvman.2022.116364> (cf. p. 41)
- GOUVÊA, L. P., ASSIS, J., GURGEL, C. F., SERRÃO, E. A., SILVEIRA, T. C., SANTOS, R., DUARTE, C. M., PERES, L. M., CARVALHO, V. F., BATISTA, M., et al. (2020). Golden

- carbon of Sargassum forests revealed as an opportunity for climate change mitigation. *Science of The Total Environment*, 729, 138745 (cf. p. 39, 97).
- GOWER, J., & KING, S. (2020). The distribution of pelagic Sargassum observed with OLCI [Publisher : Taylor & Francis _eprint : <https://doi.org/10.1080/01431161.2019.1658240>]. *International Journal of Remote Sensing*, 41(15), 5669-5679. <https://doi.org/10.1080/01431161.2019.1658240> (cf. p. 43, 51)
- GOWER, J. F., & KING, S. A. (2011). Distribution of floating Sargassum in the Gulf of Mexico and the Atlantic Ocean mapped using MERIS [Publisher : Taylor & Francis _eprint : <https://doi.org/10.1080/01431161003639660>]. *International Journal of Remote Sensing*, 32(7), 1917-1929. <https://doi.org/10.1080/01431161003639660> (cf. p. 51, 70, 77, 97)
- GOWER, J., HU, C., BORSTAD, G., & KING, S. (2006). Ocean color satellites show extensive lines of floating Sargassum in the Gulf of Mexico [Conference Name : IEEE Transactions on Geoscience and Remote Sensing]. *IEEE Transactions on Geoscience and Remote Sensing*, 44(12), 3619-3625. <https://doi.org/10.1109/TGRS.2006.882258> (cf. p. 42, 51)
- GOWER, J., & KING, S. (2008). Satellite Images Show the Movement of Floating Sargassum in the Gulf of Mexico and Atlantic Ocean [Publisher : Nature Publishing Group]. *Nature Precedings*, 1-1. <https://doi.org/10.1038/npre.2008.1894.1> (cf. p. 42, 43)
- GOWER, J., YOUNG, E., & KING, S. (2013). Satellite images suggest a new Sargassum source region in 2011. *Remote Sensing Letters*, 4(8), 764-773. <https://doi.org/10.1080/2150704X.2013.796433> (cf. p. 42)
- HACKER, S., & MADIN, L. (1991). Why habitat architecture and color are important to shrimps living in pelagic Sargassum : use of camouflage and plant-part mimicry. *Marine Ecology Progress Series*, 70, 143-155. <https://doi.org/10.3354/meps070143> (cf. p. 35)
- HANISAK, M. D., & SAMUEL, M. A. (1987). Growth rates in culture of several species of Sargassum from Florida, USA. In M. A. RAGAN & C. J. BIRD (Éd.), *Twelfth International Seaweed Symposium* (p. 399-404). Springer Netherlands. https://doi.org/10.1007/978-94-009-4057-4_59. (Cf. p. 37, 100, 124)
- HANSON, R. B. (1977). Pelagic Sargassum community metabolism : Carbon and nitrogen. *Journal of Experimental Marine Biology and Ecology*, 29(2), 107-118. [https://doi.org/10.1016/0022-0981\(77\)90042-9](https://doi.org/10.1016/0022-0981(77)90042-9) (cf. p. 37)
- HASTIE, T., TIBSHIRANI, R., & FRIEDMAN, J. (2009). *The elements of statistical learning : data mining, inference, and prediction*. Springer Science & Business Media. (Cf. p. 59).
- HENDY, I. W., WOOLFORD, K., VINCENT-PIPER, A., BURT, O., SCHAEFER, M., CRAGG, S. M., SANCHEZ-NAVARRO, P., & RAGAZZOLA, F. (2021). Climate-driven golden tides are reshaping coastal communities in quintana roo, mexico. *Climate Change Ecology*, 100033. <https://doi.org/10.1016/j.ecochg.2021.100033> (cf. p. 38)
- HERNÁNDEZ, W. J., MORELL, J. M., & ARMSTRONG, R. A. (2022). Using high-resolution satellite imagery to assess the impact of *Sargassum* inundation on coastal areas.

Bibliographie

- Remote Sensing Letters*, 13(1), 24-34. <https://doi.org/10.1080/2150704X.2021.1981558> (cf. p. 43)
- HERNÁNDEZ-NAVARRO, C., PÉREZ, S., FLÓREZ, E., ACELAS, N., & MUÑOZ-SALDAÑA, J. (2023). Sargassum macroalgae from quintana roo as raw material for the preparation of high-performance phosphate adsorbent from aqueous solutions. *Journal of Environmental Management*, 342, 118312. <https://doi.org/10.1016/j.jenvman.2023.118312> (cf. p. 41)
- HERSBACH, H., & DEE, D. (2016). ERA5 reanalysis is in production. *ECMWF newsletter*, 147(7), 5-6 (cf. p. 80).
- HU, C., FENG, L., HARDY, R. F., & HOCHBERG, E. J. (2015). Spectral and spatial requirements of remote measurements of pelagic sargassum macroalgae. *Remote Sensing of Environment*, 167, 229-246. <https://doi.org/10.1016/j.rse.2015.05.022> (cf. p. 51)
- HU, C., MURCH, B., BARNES, B., WANG, M., MARÉCHAL, J.-P., FRANKS, J., LAPOINTE, B., GOODWIN, D., SCHELL, J., & SIUDA, A. (2016). Sargassum Watch Warns of Incoming Seaweed. *Eos*, 97. <https://doi.org/10.1029/2016EO058355> (cf. p. 44)
- HU, C., ZHANG, S., BARNES, B. B., XIE, Y., WANG, M., CANNIZZARO, J. P., & ENGLISH, D. C. (2023). Mapping and quantifying pelagic sargassum in the atlantic ocean using multi-band medium-resolution satellite data and deep learning. *Remote Sensing of Environment*, 289, 113515. <https://doi.org/10.1016/j.rse.2023.113515> (cf. p. 44)
- HUFFARD, C. L., von THUN, S., SHERMAN, A. D., SEALEY, K., & SMITH, K. L. (2014). Pelagic Sargassum community change over a 40-year period : temporal and spatial variability. *Marine Biology*, 161(12), 2735-2751. <https://doi.org/10.1007/s00227-014-2539-y> (cf. p. 36)
- HUNN, D., BLANAR, C., & KERSTETTER, D. W. (2022). Evidence of Spatial Stability in Core Fauna Community Structure of Holopelagic Sargassum [Publisher : University of Puerto Rico at Mayagüez]. *Caribbean Journal of Science*, 52(2), 177-184. <https://doi.org/10.18475/cjos.v52i2.a4> (cf. p. 36)
- IMZILEN, T., CHASSOT, E., BARDE, J., DEMARcq, H., MAUFROY, A., ROA-PASCUALI, L., TERNON, J. F., & LETT, C. (2019). Fish aggregating devices drift like oceanographic drifters in the near-surface currents of the Atlantic and Indian Oceans. *Progress in oceanography*, 171, 108-127 (cf. p. 87).
- IPORAC, L. A. R., JAMES, W. R., & COLLADO-VIDES, L. (2023). Characterizing potential resource use of sargasso-dominant sea wrack by terrestrial invertebrate fauna during sargasso influxes in south florida. *Estuarine, Coastal and Shelf Science*, 108414. <https://doi.org/10.1016/j.ecss.2023.108414> (cf. p. 37, 41)
- JAUD, M. (2011). *Techniques d'observation et de mesure haute résolution des transferts sédimentaires dans la frange littorale* (thèse de doct.). (Cf. p. 10, 30).
- JIAO, L., LIU, Y., & LI, H. (2012). Characterizing land-use classes in remote sensing imagery by shape metrics. *ISPRS Journal of Photogrammetry and Remote Sensing*, 72, 46-55 (cf. p. 57).
- JOHNS, E. M., LUMPKIN, R., PUTMAN, N. F., SMITH, R. H., MULLER-KARGER, F. E., RUEDA-ROA, D. T., HU, C., WANG, M., BROOKS, M. T., GRAMER, L. J., et al. (2020).

- The establishment of a pelagic sargassum population in the tropical atlantic : biological consequences of a basin-scale long distance dispersal event. *Progress in Oceanography*, 182, 102269. <https://doi.org/10.1016/j.pocean.2020.102269> (cf. p. 25, 51, 71, 77, 86, 89, 97, 127)
- JOHNSON, D. L., & BRAMAN, R. S. (1975). The speciation of arsenic and the content of germanium and mercury in members of the pelagic Sargassum community. *Deep Sea Research and Oceanographic Abstracts*, 22(7), 503-507. [https://doi.org/10.1016/0011-7471\(75\)90023-6](https://doi.org/10.1016/0011-7471(75)90023-6) (cf. p. 40)
- JOHNSON, D. L., & RICHARDSON, P. L. (1977). On the wind-induced sinking of sargassum. *Journal of Experimental Marine Biology and Ecology*, 28(3), 255-267. [https://doi.org/10.1016/0022-0981\(77\)90095-8](https://doi.org/10.1016/0022-0981(77)90095-8) (cf. p. 45, 70)
- JOHNSON, D., FRANKS, J., OXFORD, H., & COX, S.-A. (2020). Pelagic Sargassum Prediction and Marine Connectivity in the Tropical Atlantic. *Gulf and Caribbean Research*, 31(1), GCFI20-GCFI30. <https://doi.org/10.18785/gcr.3101.15> (cf. p. 45)
- JOUANNO, J., BENSHILA, R., BERLINE, L., SOULIÉ, A., RADENAC, M.-H., MORVAN, G., DIAZ, F., SHEINBAUM, J., CHEVALIER, C., THIBAUT, T., et al. (2021a). A NEMO-based model of Sargassum distribution in the Tropical Atlantic : description of the model and sensitivity analysis (NEMO-Sarg1.0). *Geoscientific Model Development*, 14(6), 4069-4086 (cf. p. 10, 29, 71, 77, 98, 99, 104, 111, 125).
- JOUANNO, J., BENSHILA, R., BERLINE, L., SOULIÉ, A., RADENAC, M.-H., MORVAN, G., DIAZ, F., SHEINBAUM, J., CHEVALIER, C., THIBAUT, T., CHANGEUX, T., MENARD, F., BERTHET, S., AUMONT, O., ETHÉ, C., NABAT, P., & MALLET, M. (2020). A NEMO-based model of Sargassum distribution in the Tropical Atlantic : description of the model and sensitivity analysis (NEMO-Sarg1.0) [Publisher : Copernicus GmbH]. *Geoscientific Model Development Discussions*, 1-30. <https://doi.org/10.5194/gmd-2020-383> (cf. p. 46, 124)
- JOUANNO, J., MOQUET, J.-S., BERLINE, L., RADENAC, M.-H., SANTINI, W., CHANGEUX, T., THIBAUT, T., PODLEJSKI, W., MÉNARD, F., MARTINEZ, J.-M., AUMONT, O., SHEINBAUM, J., FILIZOLA, N., & N'KAYA, G. D. M. (2021b). Evolution of the riverine nutrient export to the Tropical Atlantic over the last 15 years : is there a link with Sargassum proliferation? *Environmental Research Letters*, 16(3), 034042. <https://doi.org/10.1088/1748-9326/abe11a> (cf. p. 3, 46, 51, 77, 98, 125, 127)
- KUNDU, P. K. (1976). Ekman veering observed near the ocean bottom. *Journal of Physical oceanography*, 6(2), 238-242 (cf. p. 80).
- KWON, K., CHOI, B.-J., KIM, K. Y., & KIM, K. (2019). Tracing the trajectory of pelagic Sargassum using satellite monitoring and Lagrangian transport simulations in the East China Sea and Yellow Sea [Publisher : The Korean Society of Phycology]. *ALGAE*, 34(4), 315-326. <https://doi.org/10.4490/algae.2019.34.12.11> (cf. p. 45, 77, 97, 110)
- LAGERLOEF, G. S., MITCHUM, G. T., LUKAS, R. B., & NIILER, P. P. (1999). Tropical Pacific near-surface currents estimated from altimeter, wind, and drifter data. *Journal of Geophysical Research : Oceans*, 104(C10), 23313-23326 (cf. p. 87).

Bibliographie

- LAPOINTE, B. E., BREWTON, R. A., HERREN, L. W., WANG, M., HU, C., MCGILLCUDDY, D. J., LINDELL, S., HERNANDEZ, F. J., & MORTON, P. L. (2021). Nutrient content and stoichiometry of pelagic sargassum reflects increasing nitrogen availability in the atlantic basin [Number : 1 Publisher : Nature Publishing Group]. *Nature Communications*, 12(1), 3060. <https://doi.org/10.1038/s41467-021-23135-7> (cf. p. 37, 111)
- LAPOINTE, B. E. (1986). Phosphorus-limited photosynthesis and growth of *Sargassum natans* and *Sargassum fluitans* (Phaeophyceae) in the western North Atlantic. *Deep Sea Research Part A. Oceanographic Research Papers*, 33(3), 391-399. [https://doi.org/10.1016/0198-0149\(86\)90099-3](https://doi.org/10.1016/0198-0149(86)90099-3) (cf. p. 37, 124)
- LAVAL, M., BELMOUHCINE, A., COURTRAI, L., DESCLOITRES, J., SALAZAR-GARIBAY, A., SCHAMBERGER, L., MINGHELLI, A., THIBAUT, T., DORVILLE, R., MAZOYER, C., ZONGO, P., & CHEVALIER, C. (2023). Detection of Sargassum from Sentinel Satellite Sensors Using Deep Learning Approach. *Remote Sensing*, 15(4), 1104. <https://doi.org/10.3390/rs15041104> (cf. p. 44, 97, 119, 123)
- LAZCANO-HERNANDEZ, H. E., ARELLANO-VERDEJO, J., & RODRIGUEZ-MARTINEZ, R. E. (2023). Algorithms applied for monitoring pelagic Sargassum. *Frontiers in Marine Science*, 10, 1216426 (cf. p. 14, 44).
- LE HÉNAFF, M., KOURAFALOU, V. H., PARIS, C. B., HELGERS, J., AMAN, Z. M., HOGAN, P. J., & SRINIVASAN, A. (2012). Surface evolution of the Deepwater Horizon oil spill patch : combined effects of circulation and wind-induced drift. *Environmental science & technology*, 46(13), 7267-7273 (cf. p. 88).
- LELOUCHE, J.-M., GREINER, E., BOURDALLE-BADIE, R., GARRIC, G., MELET, A., DREVILLON, M., BRICAUD, C., HAMON, M., LE, O., REGNIER, C., CANDELA, T., TESTUT, C.-E., GASPARIN, F., RUGGIERO, G., BENKIRAN, M., DRILLET, Y., & TRAON, P.-Y. (2021). The Copernicus Global 1/12° Oceanic and Sea Ice GLORYS12 Reanalysis. *Frontiers in Earth Science*, 9, 698876. <https://doi.org/10.3389/feart.2021.698876> (cf. p. 101)
- LEÓN-PÉREZ, M. C., REISINGER, A. S., & GIBEAUT, J. C. (2023). Spatial-temporal dynamics of decaying stages of pelagic sargassum spp. along shorelines in puerto rico using google earth engine. *Marine Pollution Bulletin*, 188, 114715. <https://doi.org/10.1016/j.marpolbul.2023.114715> (cf. p. 42)
- LETT, C., VERLEY, P., MULLON, C., PARADA, C., BROCHIER, T., PENVEN, P., & BLANKE, B. (2008). A Lagrangian tool for modelling ichthyoplankton dynamics. *Environmental Modelling & Software*, 23(9), 1210-1214 (cf. p. 102).
- LI, Y., GUNDERSEN, H., POULSEN, R. N., XIE, L., GE, Z., & HANCKE, K. (2023). Quantifying seaweed and seagrass beach deposits using high-resolution UAV imagery. *Journal of Environmental Management*, 331, 117171. <https://doi.org/10.1016/j.jenvman.2022.117171> (cf. p. 42)
- LIRANZO-GÓMEZ, R. E., GÓMEZ, A. M., GÓMEZ, B., GONZÁLEZ-HERNÁNDEZ, Y., & JAUREGUI-HAZA, U. J. (2023). Characterization of sargassum accumulated on dominican beaches in 2021 : analysis of heavy, alkaline and alkaline-earth metals, proteins and fats. *Marine Pollution Bulletin*, 193, 115120. <https://doi.org/10.1016/j.marpolbul.2023.115120> (cf. p. 40)

- LÓPEZ-AGUILAR, H. A., PUENTES, G. K., GÓMEZ, J. A., HUERTA-REYNOSO, E. A., PERALTA-PÉREZ, M. d. R., SERNA, F J. Z.-D. d. I., & PÉREZ-HERNÁNDEZ, A. (2021). Practical and Theoretical Modeling of Anaerobic Digestion of Sargassum spp. in the Mexican Caribbean [Publisher : HARD Publishing s.c. Jerzy Radecki, Hanna Radecka]. *Polish Journal of Environmental Studies*. <https://doi.org/10.15244/pjoes/128735> (cf. p. 41)
- LÓPEZ-SOSA, L. B., ALVARADO-FLORES, J. J., CORRAL-HUACUZ, J. C., AGUILERA-MANDUJANO, A., RODRÍGUEZ-MARTÍNEZ, R. E., GUEVARA-MARTÍNEZ, S. J., ALCARAZ-VERA, J. V., RUTIAGA-QUIÑONES, J. G., ZÁRATE-MEDINA, J., ÁVALOS-RODRÍGUEZ, M. L., & MORALES-MÁXIMO, M. (2020). A Prospective Study of the Exploitation of Pelagic Sargassum spp. as a Solid Biofuel Energy Source [Number : 23 Publisher : Multidisciplinary Digital Publishing Institute]. *Applied Sciences*, 10(23), 8706. <https://doi.org/10.3390/app10238706> (cf. p. 41)
- LOWE, D. G. (2004). Distinctive image features from scale-invariant keypoints. *International journal of computer vision*, 60(2), 91-110 (cf. p. 79).
- LUCAS, B. D., KANADE, T., et al. (1981). An iterative image registration technique with an application to stereo vision (cf. p. 79).
- LUMPKIN, R., & CENTURIONI, L. (2019). NOAA Global Drifter Program quality-controlled 6-hour interpolated data from ocean surface drifting buoys. *NOAA : Washington, DC, USA* (cf. p. 80).
- LUMPKIN, R., & PAZOS, M. (2007). Measuring surface currents with Surface Velocity Program drifters : the instrument, its data, and some recent results. *Lagrangian analysis and prediction of coastal and ocean dynamics*, 39, 67 (cf. p. 78).
- MACHADO, C. B., MADDIX, G.-M., FRANCIS, P., THOMAS, S.-L., BURTON, J.-A., LANGER, S., LARSON, T. R., MARSH, R., WEBBER, M., & TONON, T. (2022). Pelagic sargassum events in jamaica : provenance, morphotype abundance, and influence of sample processing on biochemical composition of the biomass. *Science of The Total Environment*, 152761. <https://doi.org/10.1016/j.scitotenv.2021.152761> (cf. p. 37)
- MAGAÑA-GALLEGOS, E., GARCÍA-SÁNCHEZ, M., GRAHAM, C., OLIVOS-ORTIZ, A., SIUDA, A. N. S., & van TUSSEN BROEK, B. I. (2023a). Growth rates of pelagic sargassum species in the mexican caribbean. *Aquatic Botany*, 185, 103614. <https://doi.org/10.1016/j.aquabot.2022.103614> (cf. p. 36, 37, 111, 124, 128)
- MAGAÑA-GALLEGOS, E., VILLEGAS-MUÑOZ, E., SALAS-ACOSTA, E. R., BARBA-SANTOS, M. G., SILVA, R., & van TUSSEN BROEK, B. I. (2023b). The effect of temperature on the growth of holopelagic sargassum species [Number : 1 Publisher : Multidisciplinary Digital Publishing Institute]. *Phycology*, 3(1), 138-146. <https://doi.org/10.3390/phycology3010009> (cf. p. 37)
- MARÉCHAL, J.-P., HELLIO, C., & HU, C. (2017a). A simple, fast, and reliable method to predict Sargassum washing ashore in the Lesser Antilles. *Remote Sensing Applications : Society and Environment*, 5, 54-63. <https://doi.org/10.1016/j.rsase.2017.01.001> (cf. p. 45)

Bibliographie

- MARÉCHAL, J.-P., HELLIO, C., & HU, C. (2017b). A simple, fast, and reliable method to predict Sargassum washing ashore in the Lesser Antilles. *Remote Sensing Applications : Society and Environment*, 5, 54-63 (cf. p. 98).
- MARSH, R., ADDO, K. A., JAYSON-QUASHIGAH, P.-N., OXFORD, H. A., MAXAM, A., ANDERSON, R., SKLIRIS, N., DASH, J., & TOMPKINS, E. L. (2021). Seasonal Predictions of Holopelagic Sargassum Across the Tropical Atlantic Accounting for Uncertainty in Drivers and Processes : The SARTRAC Ensemble Forecast System. *Frontiers in Marine Science*, 8, 1417. Récupérée 11 juillet 2022, à partir de <https://www.frontiersin.org/articles/10.3389/fmars.2021.722524> (cf. p. 46, 97, 98)
- MARSH, R., SKLIRIS, N., TOMPKINS, E. L., DASH, J., DOMINGUEZ ALMELA, V., TONON, T., OXFORD, H. A., & WEBBER, M. (2023). Climate-sargassum interactions across scales in the tropical Atlantic. *PLOS Climate*, 2(7), e0000253 (cf. p. 112).
- MARTIN, L. M., TAYLOR, M., HUSTON, G., GOODWIN, D. S., SCHELL, J. M., & SIUDA, A. N. (2021). Pelagic sargassum morphotypes support different rafting motile epifauna communities. *Marine Biology*, 168(7), 1-17. <https://doi.org/10.1007/s00227-021-03910-2> (cf. p. 36, 50, 97)
- MARX, U. C., ROLES, J., & HANKAMER, B. (2021). Sargassum blooms in the atlantic ocean – from a burden to an asset. *Algal Research*, 54, 102188. <https://doi.org/10.1016/j.algal.2021.102188> (cf. p. 41)
- MASUOKA, E., FLEIG, A., WOLFE, R. E., & PATT, F. (1998). Key characteristics of MODIS data products. *IEEE Transactions on Geoscience and Remote Sensing*, 36(4), 1313-1323 (cf. p. 86).
- MAURER, A. S., GROSS, K., & STAPLETON, S. P. (2022). Beached sargassum alters sand thermal environments : implications for incubating sea turtle eggs. *Journal of Experimental Marine Biology and Ecology*, 546, 151650. <https://doi.org/10.1016/j.jembe.2021.151650> (cf. p. 38)
- MAURER, A. S., STAPLETON, S. P., LAYMAN, C. A., & BURFORD REISKIND, M. O. (2021). The atlantic sargassum invasion impedes beach access for nesting sea turtles. *Climate Change Ecology*, 2, 100034. <https://doi.org/10.1016/j.ecochg.2021.100034> (cf. p. 39)
- MERLE, H., RESIÈRE, D., MESNARD, C., PIERRE, M., JEAN-CHARLES, A., BÉRAL, L., & NEVIÈRE, R. (2021). Case Report : Two Cases of Keratoconjunctivitis Tied to Sargassum Algae Emanations. *The American Journal of Tropical Medicine and Hygiene*, 104(1), 403-405 (cf. p. 39, 50, 77, 97).
- MICHOTEY, V., BLANFUNÉ, A., CHEVALIER, C., GAREL, M., DIAZ, F., BERLINE, L., LE GRAND, L., ARMOUGOM, F., GUASCO, S., RUITTON, S., CHANGEUX, T., BELLONI, B., BLANCHOT, J., MÉNARD, F., & THIBAUT, T. (2020). In situ observations and modelling revealed environmental factors favouring occurrence of Vibrio in microbiome of the pelagic Sargassum responsible for strandings. *Science of The Total Environment*, 748, 141216. <https://doi.org/10.1016/j.scitotenv.2020.141216> (cf. p. 39)

- MIKOLAJCZYK, K., & SCHMID, C. (2005). A performance evaluation of local descriptors. *IEEE transactions on pattern analysis and machine intelligence*, 27(10), 1615-1630 (cf. p. 79).
- MILLEDGE, J. J., & HARVEY, P. J. (2016). Golden tides : problem or golden opportunity? the valorisation of sargassum from beach inundations [Number : 3 Publisher : Multidisciplinary Digital Publishing Institute]. *Journal of Marine Science and Engineering*, 4(3), 60. <https://doi.org/10.3390/jmse4030060> (cf. p. 40)
- MILLEDGE, J. J., MANEEIN, S., ARRIBAS LÓPEZ, E., & BARTLETT, D. (2020). Sargassum Inundations in Turks and Caicos : Methane Potential and Proximate, Ultimate, Lipid, Amino Acid, Metal and Metalloid Analyses [Number : 6 Publisher : Multidisciplinary Digital Publishing Institute]. *Energies*, 13(6), 1523. <https://doi.org/10.3390/en13061523> (cf. p. 40)
- MINGHELLI, A., CHEVALIER, C., DESCLOITRES, J., BERLINE, L., BLANC, P., & CHAMI, M. (2021). Synergy between low earth orbit (leo)—modis and geostationary earth orbit (geo)—goes sensors for sargassum monitoring in the atlantic ocean [Number : 8 Publisher : Multidisciplinary Digital Publishing Institute]. *Remote Sensing*, 13(8), 1444. <https://doi.org/10.3390/rs13081444> (cf. p. 43, 71, 87, 97, 125)
- MIRON, P., OLASCOAGA, M., BERON-VERA, F., PUTMAN, N., TRIÑANES, J., LUMPKIN, R., & GONI, G. (2020). Clustering of marine-debris-and sargassum-like drifters explained by inertial particle dynamics. *Geophysical Research Letters*, 47(19), e2020GL089874. <https://doi.org/https://doi.org/10.1029/2020GL089874> (cf. p. 45, 77, 97)
- MODESTIN, E., DEVAULT, D. A., BAYLET, A., MASSAT, F., & DOLIQUE, F. (2022). Arsenic in caribbean bivalves in the context of sargassum beachings : a new risk for seafood consumers. *Environmental Monitoring and Assessment*, 194(8), 553. <https://doi.org/10.1007/s10661-022-10230-5> (cf. p. 39)
- MOHAMMED, A., RIVERS, A., STUCKEY, D. C., & WARD, K. (2020). Alginate extraction from Sargassum seaweed in the Caribbean region : Optimization using response surface methodology. *Carbohydrate Polymers*, 245, 116419. <https://doi.org/10.1016/j.carbpol.2020.116419> (cf. p. 41)
- MOSER, M. L., & LEE, D. S. (2012). Foraging over Sargassum by Western North Atlantic Seabirds. *The Wilson Journal of Ornithology*, 124(1), 66-72. <https://doi.org/10.1676/11-067.1> (cf. p. 35)
- MULET, S., ETIENNE, H., BALLAROTTA, M., FAUGERE, Y., RIO, M., DIBARBOURE, G., & PICOT, N. (2021). Synergy between surface drifters and altimetry to increase the accuracy of sea level anomaly and geostrophic current maps in the Gulf of Mexico. *Advances in Space Research*, 68(2), 420-431 (cf. p. 80).
- ODY, A., THIBAUT, T., BERLINE, L., CHANGEUX, T., ANDRÉ, J.-M., CHEVALIER, C., BLANFUNÉ, A., BLANCHOT, J., RUITTON, S., STIGER-POUVREAU, V., et al. (2019). From in situ to satellite observations of pelagic sargassum distribution and aggregation in the tropical north atlantic ocean (V. MÉLÉDER, Éd.). *PLOS ONE*, 14(9), e0222584. <https://doi.org/10.1371/journal.pone.0222584> (cf. p. 24, 43, 51, 54, 57, 60, 77, 78, 88, 123)

Bibliographie

- ORTEGA-FLORES, P. A., GOBERT, T., MÉNDEZ-RODRÍGUEZ, L. C., SERVIERE-ZARAGOZA, E., CONNAN, S., ROBLEDO, D., FREILE-PELEGRÍN, Y., ANDA MONTAÑEZ, J. A. d., & WAELES, M. (2023). Inorganic arsenic in holopelagic sargassum spp. stranded in the mexican caribbean : seasonal variations and comparison with international regulations and guidelines. *Aquatic Botany*, 103674. <https://doi.org/10.1016/j.aquabot.2023.103674> (cf. p. 40)
- OVIATT, C. A., HUIZENGA, K., ROGERS, C. S., & MILLER, W. J. (2019). What nutrient sources support anomalous growth and the recent sargassum mass stranding on caribbean beaches? a review. *Marine Pollution Bulletin*, 145, 517-525. <https://doi.org/10.1016/j.marpolbul.2019.06.049> (cf. p. 37, 46, 51, 97, 111, 128)
- OXENFORD, H. A., COX, S.-A., van TUSSEN BROEK, B. I., & DESROCHERS, A. (2021). Challenges of turning the sargassum crisis into gold : current constraints and implications for the caribbean. *Phycology*, 1(1), 27-48. <https://doi.org/10.3390/phycology1010003> (cf. p. 40)
- OYESIKU, O. O., & EGUNYOMI, A. (2014). Identification and chemical studies of pelagic masses of *Sargassum natans* (Linnaeus) Gaillon and *S. fluitans* (Borgesen) Borgesen (brown algae), found offshore in Ondo State, Nigeria [Number : 10]. *African Journal of Biotechnology*, 13(10). <https://doi.org/10.4314/ajb.v13i10> (cf. p. 39)
- PARAGUAY-DELGADO, F., CARREÑO-GALLARDO, C., ESTRADA-GUEL, I., ZABALA-ARCEO, A., MARTINEZ-RODRIGUEZ, H. A., & LARDIZÁBAL-GUTIERREZ, D. (2020). Pelagic *Sargassum* spp. capture CO₂ and produce calcite. *Environmental Science and Pollution Research*, 27(20), 25794-25800. <https://doi.org/10.1007/s11356-020-08969-w> (cf. p. 39)
- PARR, A. (1939). Quantitative observations on the pelagic sargassum vegetation of the western north atlantic. *Bulletin of the Bingham Oceanographic Collection*, 6 (cf. p. 37).
- PAZAN, S. E., & NIILER, P. P. (2001). Recovery of near-surface velocity from undrogued drifters. *Journal of Atmospheric and Oceanic Technology*, 18(3), 476-489 (cf. p. 88).
- PHILIPPI, M., F. HACH, P., LENA EGGLERS, S., ELMER, F., BUCK-WIESE, H., STEFELS, J., RAQUEL SALAS-ACOSTA, E., MAGAÑA-GALLEGOS, E., I. VAN TUSSEN BROEK, B., & FERNÁNDEZ-MÉNDEZ, M. (2023). Carbon fixation in holopelagic *Sargassum* is partially decoupled from nitrate and phosphate availability. *ASLO 2023* (cf. p. 111, 124, 128).
- PHLIPS, E., & ZEMAN, C. (1990). Photosynthesis, Growth and Nitrogen Fixation by Epiphytic Forms of Filamentous Cyanobacteria from Pelagic Sargassum. *Bulletin of Marine Science*, 47(3), 613-621 (cf. p. 37).
- PODLEJSKI, W., BERLINE, L., NERINI, D., DOGLIOLI, A., & LETT, C. (2023). A new Sargassum drift model derived from features tracking in MODIS images. *Marine Pollution Bulletin*, 188, 114629. <https://doi.org/https://doi.org/10.1016/j.marpolbul.2023.114629> (cf. p. 3, 76, 98, 99, 111)
- PODLEJSKI, W., DESCLOITRES, J., CHEVALIER, C., MINGHELLI, A., LETT, C., & BERLINE, L. (2022). Filtering out false Sargassum detections using context features. *Fron-*

- tiers in Marine Science*, 9. <https://doi.org/10.3389/fmars.2022.960939> (cf. p. 3, 12, 44, 49, 78, 83, 97, 98)
- POULAIN, P.-M., GERIN, R., MAURI, E., & PENNEL, R. (2009). Wind effects on drogued and undrogued drifters in the eastern Mediterranean. *Journal of Atmospheric and Oceanic Technology*, 26(6), 1144-1156 (cf. p. 80).
- POULAIN, P.-M., WARN-VARNAS, A., & NIILER, P. (1996). Near-surface circulation of the Nordic seas as measured by Lagrangian drifters. *Journal of Geophysical Research : Oceans*, 101(C8), 18237-18258 (cf. p. 88).
- POWERS, L. C., HERTKORN, N., McDONALD, N., SCHMITT-KOPPLIN, P., VECCHIO, R. D., BLOUGH, N. V., & GONSIOR, M. (2019). Sargassum sp. Act as a Large Regional Source of Marine Dissolved Organic Carbon and Polyphenols [eprint : <https://agupubs.onlinelibrary.wiley.com/doi/pdf/10.1029/2019GB006225>]. *Global Biogeochemical Cycles*, 33(11), 1423-1439. <https://doi.org/10.1029/2019GB006225> (cf. p. 39)
- PUTMAN, N. F., BEYEA, R. T., IPORAC, L. A. R., TRIÑANES, J., ACKERMAN, E. G., OLASCOAGA, M. J., APPENDINI, C. M., ARRIAGA, J., COLLADO-VIDES, L., LUMPKIN, R., HU, C., & GONI, G. (2023). Improving satellite monitoring of coastal inundations of pelagic sargassum algae with wind and citizen science data. *Aquatic Botany*, 103672. <https://doi.org/10.1016/j.aquabot.2023.103672> (cf. p. 45)
- PUTMAN, N. F., GONI, G. J., GRAMER, L. J., HU, C., JOHNS, E. M., TRINANES, J., & WANG, M. (2018). Simulating transport pathways of pelagic sargassum from the equatorial atlantic into the caribbean sea. *Progress in Oceanography*, 165, 205-214. <https://doi.org/10.1016/j.pocean.2018.06.009> (cf. p. 45, 77, 89, 97, 98, 110, 127)
- PUTMAN, N. F., & HU, C. (2022). Sinking Sargassum. *Geophysical Research Letters*, 49(17). <https://doi.org/10.1029/2022GL100189> (cf. p. 46)
- PUTMAN, N. F., LUMPKIN, R., OLASCOAGA, M. J., TRINANES, J., & GONI, G. J. (2020). Improving transport predictions of pelagic sargassum. *Journal of Experimental Marine Biology and Ecology*, 529, 151398. <https://doi.org/10.1016/j.jembe.2020.151398> (cf. p. 45, 77, 88, 89, 97)
- QI, L., & HU, C. (2021). To what extent can ulva and sargassum be detected and separated in satellite imagery? *Harmful Algae*, 103, 102001. <https://doi.org/10.1016/j.hal.2021.102001> (cf. p. 44)
- QI, L., WANG, M., HU, C., & HOLT, B. (2022). On the capacity of sentinel-1 synthetic aperture radar in detecting floating macroalgae and other floating matters. *Remote Sensing of Environment*, 280, 113188. <https://doi.org/10.1016/j.rse.2022.113188> (cf. p. 44, 119)
- QIU, Z., LI, Z., BILAL, M., WANG, S., SUN, D., & CHEN, Y. (2018). Automatic method to monitor floating macroalgae blooms based on multilayer perceptron : case study of yellow sea using goci images. *Optics Express*, 26(21), 26810-26829. <https://doi.org/10.1364/OE.26.026810> (cf. p. 44, 51, 52, 56, 69)
- RACINE, P., MARLEY, A., FROELICH, H. E., GAINES, S. D., LADNER, I., MACADAM-SOMER, I., & BRADLEY, D. (2021). A case for seaweed aquaculture inclusion

- in u.s. nutrient pollution management. *Marine Policy*, 129, 104506. <https://doi.org/10.1016/j.marpol.2021.104506> (cf. p. 39)
- RANGUIN, R., DELANNOY, M., YACOU, C., JEAN-MARIUS, C., FEIDT, C., RYCHEN, G., & GASPARD, S. (2021). Biochar and activated carbons preparation from invasive algae sargassum spp. for chlорdecone availability reduction in contaminated soils. *Journal of Environmental Chemical Engineering*, 9(4), 105280. <https://doi.org/10.1016/j.jece.2021.105280> (cf. p. 41)
- RESIERE, D., MEHDAOUI, H., FLORENTIN, J., GUEYE, P., LEBRUN, T., BLATEAU, A., VIGUIER, J., VALENTINO, R., BROUSTE, Y., KALLEL, H., MEGARBANE, B., CABIE, A., BANYDEEN, R., & NEVIERE, R. (2021). Sargassum seaweed health menace in the Caribbean : clinical characteristics of a population exposed to hydrogen sulfide during the 2018 massive stranding [Publisher : Taylor & Francis _eprint : https://doi.org/10.1080/15563650.2020.1789162]. *Clinical Toxicology*, 59(3), 215-223. <https://doi.org/10.1080/15563650.2020.1789162> (cf. p. 39)
- RESIERE, D., VALENTINO, R., NEVIÈRE, R., BANYDEEN, R., GUEYE, P., FLORENTIN, J., CABIÉ, A., LEBRUN, T., MÉGARBANE, B., GUERRIER, G., et al. (2018). Sargassum seaweed on Caribbean islands : an international public health concern. *The Lancet*, 392(10165), 2691 (cf. p. 50, 77, 97).
- RIVERA-HERNÁNDEZ, Y., HERNÁNDEZ-EUGENIO, G., BALAGURUSAMY, N., & ESPINOSA-SOLARES, T. (2022). Sargassum-pig manure co-digestion : an alternative for bioenergy production and treating a polluting coastal waste. *Renewable Energy*, 199, 1336-1344. <https://doi.org/10.1016/j.renene.2022.09.068> (cf. p. 41)
- RODRÍGUEZ-MARTÍNEZ, R. E., MEDINA-VALMASEDA, A. E., BLANCHON, P., MONROY-VELÁZQUEZ, L. V., ALMAZÁN-BECERRIL, A., DELGADO-PECH, B., VÁSQUEZ-YEOMANS, L., FRANCISCO, V., & GARCÍA-RIVAS, M. C. (2019). Faunal mortality associated with massive beaching and decomposition of pelagic Sargassum. *Marine Pollution Bulletin*, 146, 201-205. <https://doi.org/10.1016/j.marpolbul.2019.06.015> (cf. p. 38)
- RODRÍGUEZ-MARTÍNEZ, R. E., JORDÁN-DAHLGREN, E., & HU, C. (2022). Spatio-temporal variability of pelagic sargassum landings on the northern mexican caribbean. *Remote Sensing Applications : Society and Environment*, 27, 100767. <https://doi.org/10.1016/j.rsase.2022.100767> (cf. p. 42)
- RODRÍGUEZ-MARTÍNEZ, R. E., ROY, P. D., TORRESCANO-VALLE, N., CABANILLAS-TERÁN, N., CARRILLO-DOMÍNGUEZ, S., COLLADO-VIDES, L., GARCÍA-SÁNCHEZ, M., & TUSSEN BROEK, B. I. v. (2020). Element concentrations in pelagic Sargassum along the Mexican Caribbean coast in 2018-2019 [Publisher : PeerJ Inc.]. *PeerJ*, 8, e8667. <https://doi.org/10.7717/peerj.8667> (cf. p. 40)
- RODRÍGUEZ-MARTÍNEZ, R. E., TORRES-CONDE, E. G., & JORDÁN-DAHLGREN, E. (2023). Pelagic sargassum cleanup cost in mexico. *Ocean & Coastal Management*, 237, 106542. <https://doi.org/10.1016/j.ocecoaman.2023.106542> (cf. p. 41)
- RODRÍGUEZ-MUÑOZ, R., MUÑIZ-CASTILLO, A. I., EUÁN-AVILA, J. I., HERNÁNDEZ-NÚÑEZ, H., VALDÉS-LOZANO, D. S., COLLÍ-DULÁ, R. C., & ARIAS-GONZÁLEZ, J. E. (2021). Assessing temporal dynamics on pelagic sargassum influx and its relationship with water quality parameters in the mexican caribbean. *Regional*

Bibliographie

- Studies in Marine Science*, 102005. <https://doi.org/10.1016/j.rsma.2021.102005> (cf. p. 42)
- RODRÍGUEZ-MARTIÉNEZ, R., MEDINA-VALMASEDA, A., BLANCHON, P., MONROY-VELÁZQUEZ, L., ALMAZÁN-BECERRIL, A., DELGADO-PECH, B., VÁSQUEZ-YEOMANS, L., FRANCISCO, V., & GARCÍA-RIVAS, M. (2019). Faunal mortality associated with massive beaching and decomposition of pelagic Sargassum. *Marine Pollution Bulletin*, 146, 201-205 (cf. p. 77).
- ROOKER, J. R., TURNER, J. P., & HOLT, S. A. (2006). Trophic ecology of Sargassum-associated fishes in the Gulf of Mexico determined from stable isotopes and fatty acids. *Marine Ecology Progress Series*, 313, 249-259. <https://doi.org/10.3354/meps313249> (cf. p. 35)
- ROSADO-ESPINOSA, L. A., FREILE-PELEGRÍN, Y., HERNÁNDEZ-NUÑEZ, E., & ROBLEDO, D. (2020). A comparative study of Sargassum species from the Yucatan Peninsula coast : morphological and chemical characterisation [Publisher : Taylor & Francis _eprint : <https://doi.org/10.1080/00318884.2020.1738194>]. *Phycologia*, 59(3), 261-271. <https://doi.org/10.1080/00318884.2020.1738194> (cf. p. 37)
- ROSSIGNOLO, J. A., FELICIO PERES DURAN, A. J., BUENO, C., MARTINELLI FILHO, J. E., SAVASTANO JUNIOR, H., & TONIN, F. G. (2022). Algae application in civil construction : a review with focus on the potential uses of the pelagic sargassum spp. biomass. *Journal of Environmental Management*, 303, 114258. <https://doi.org/10.1016/j.jenvman.2021.114258> (cf. p. 41)
- RUSSELL, B. J., & DIERSSEN, H. M. (2015). Use of Hyperspectral Imagery to Assess Cryptic Color Matching in Sargassum Associated Crabs [Publisher : Public Library of Science]. *PLOS ONE*, 10(9), e0136260. <https://doi.org/10.1371/journal.pone.0136260> (cf. p. 35)
- SALAZAR-CRUZ, B. A., ZAPIEN-CASTILLO, S., HERNÁNDEZ-ZAMORA, G., & RIVERA-ARMENTA, J. L. (2021). Investigation of the performance of asphalt binder modified by sargassum. *Construction and Building Materials*, 271, 121876. <https://doi.org/10.1016/j.conbuildmat.2020.121876> (cf. p. 41)
- SALDARRIAGA-HERNANDEZ, S., HERNANDEZ-VARGAS, G., IQBAL, H. M., BARCELO, D., & PARRA-SALDIVAR, R. (2020a). Bioremediation potential of sargassum sp. biomass to tackle pollution in coastal ecosystems : circular economy approach. *Science of The Total Environment*, 715, 136978. <https://doi.org/10.1016/j.scitotenv.2020.136978> (cf. p. 40)
- SALDARRIAGA-HERNANDEZ, S., NÁJERA-MARTIÉNEZ, E. F., MARTIÉNEZ-PRADO, M. A., & MELCHOR-MARTIÉNEZ, E. M. (2020b). Sargassum-based potential biosorbent to tackle pollution in aqueous ecosystems—An overview. *Case Studies in Chemical and Environmental Engineering*, 2, 100032 (cf. p. 40).
- SALGADO-HERNÁNDEZ, E., ORTIZ-CEBALLOS, Á. I., MARTÍNEZ-HERNÁNDEZ, S., ROSAS-MENDOZA, E. S., DORANTES-ACOSTA, A. E., ALVARADO-VALLEJO, A., & ALVARADO-LASSMAN, A. (2023). Methane production of sargassum spp. biomass from the mexican caribbean : solid–liquid separation and component distribution [Number : 1 Publisher : Multidisciplinary Digital Publishing Institute]. *Inter-*

- national Journal of Environmental Research and Public Health*, 20(1), 219. <https://doi.org/10.3390/ijerph20010219> (cf. p. 41)
- SALTER, M., PERRY, C., RODRÍGUEZ-MARTÍNEZ, R., ALVAREZ-FILIP, L., & JORDAN-DAHLGREN, E. (2021, mars 3). *Pelagic sargassum as an emergent high-rate importer of carbonate sediment to tropical atlantic coastlines* (EGU21-15898) [Conference Name : EGU21]. Copernicus Meetings. <https://doi.org/10.5194/egusphere-egu21-15898>. (Cf. p. 39)
- SÁNCHEZ, A., GONZALEZ-JONES, P., CAMACHO-CRUZ, K. A., ANGUAS-CABRERA, D., ORTIZ-HERNÁNDEZ, M. C., & REY-VILLIERS, N. (2023). Influence of pelagic sargassum influxes on the 15n in thalassia testudinum of the mexican caribbean coastal ecosystem. *Marine Pollution Bulletin*, 192, 115091. <https://doi.org/10.1016/j.marpolbul.2023.115091> (cf. p. 38)
- SANCHEZ-RUBIO, G., PERRY, H., FRANKS, J., & JOHNSON, D. (2018). Occurrence of pelagic Sargassum in waters of the U.S. Gulf of Mexico in response to weather-related hydrographic regimes associated with decadal and interannual variability in global climate. *Fishery Bulletin*, 116. <https://doi.org/10.7755/FB.116.1.10> (cf. p. 46)
- SCHAMBERGER, L., MINGHELLI, A., CHAMI, M., & STEINMETZ, F. (2022). Improvement of atmospheric correction of satellite sentinel-3/OLCI data for oceanic waters in presence of sargassum [Number : 2 Publisher : Multidisciplinary Digital Publishing Institute]. *Remote Sensing*, 14(2), 386. <https://doi.org/10.3390/rs14020386> (cf. p. 44)
- SCHELL, J., SIUDA, A., GOODWIN, D., & VOLK, R. (2023). Environmental tolerance and growth rates of holopelagic Sargassum morphotypes. *ASLO 2023* (cf. p. 111).
- SCHELL, J. M., GOODWIN, D. S., & SIUDA, A. N. (2015). Recent Sargassum Inundation Events in the Caribbean : Shipboard Observations Reveal Dominance of a Previously Rare Form [Publisher : Oceanography Society]. *Oceanography*, 28(3), 8-11. <https://doi.org/10.5670/oceanog.2015.70> (cf. p. 37, 124)
- SCHIARITI, J. P., & SALMON, M. (2022). Impact of sargassum accumulations on loggerhead (*caretta caretta*) hatchling recruitment in SE florida, united states. *Journal of Coastal Research*, 00(0), 11 (cf. p. 39).
- SEHEIN, T., SIUDA, A. N., SHANK, T. M., & GOVINDARAJAN, A. F. (2014). Connectivity in the slender Sargassum shrimp (*Latreutes fucorum*) : implications for a Sargasso Sea protected area. *Journal of Plankton Research*, 36(6), 1408-1412 (cf. p. 97).
- SHAKHOVSKOY, I. B. (2023). Quantitative distribution of the flying fish (exocoetidae), marine mammals, birds, and sea turtles in the northern part of the central atlantic ocean (results obtained in the research cruises nos. 43–45 of the r/v “akademik nikolaj strakhov”). *Journal of Ichthyology*, 63(3), 435-468. <https://doi.org/10.1134/S0032945223030141> (cf. p. 36)
- SHANG, H. L. (2014). A survey of functional principal component analysis. *AStA Advances in Statistical Analysis*, 98, 121-142 (cf. p. 114).
- SHIN, J., LEE, J.-S., JANG, L.-H., LIM, J., KHIM, B.-K., & JO, Y.-H. (2021). Sargassum detection using machine learning models : a case study with the first 6 months

- of goci-ii imagery. *Remote Sensing*, 13(23), 4844. <https://doi.org/10.3390/rs13234844> (cf. p. 10, 28, 43, 51, 52, 69)
- SKLIRIS, N., MARSH, R., APPEANING ADDO, K., & OXFORD, H. (2022a). Physical drivers of pelagic sargassum bloom interannual variability in the Central West Atlantic over 2010–2020. *Ocean Dynamics*, 72(6), 383-404 (cf. p. 97, 111, 112, 128, 129).
- SKLIRIS, N., MARSH, R., APPEANING ADDO, K., & OXFORD, H. (2022b). Physical drivers of pelagic sargassum bloom interannual variability in the central west atlantic over 2010–2020. *Ocean Dynamics*. <https://doi.org/10.1007/s10236-022-01511-1> (cf. p. 46)
- SOSA-GUTIERREZ, R., JOUANNO, J., BERLINE, L., DESCLOITRES, J., & CHEVALIER, C. (2022). Impact of tropical cyclones on pelagic sargassum [eprint : https://onlinelibrary.wiley.com/doi/pdf/10.1029/2021GL097484]. *Geophysical Research Letters*, 49(6), e2021GL097484. <https://doi.org/10.1029/2021GL097484> (cf. p. 46)
- STOJMENOVĆ, M., & ŽUNIĆ, J. (2008). Measuring elongation from shape boundary. *Journal of Mathematical Imaging and Vision*, 30(1), 73-85 (cf. p. 57).
- STONER, A., & GREENING, H. (1984). Geographic variation in the macrofaunal associates of pelagic Sargassum and some biogeographic implications. *Marine Ecology Progress Series*, 20, 185-192. <https://doi.org/10.3354/meps020185> (cf. p. 35, 36)
- SUN, D., CHEN, Y., WANG, S., ZHANG, H., QIU, Z., MAO, Z., & HE, Y. (2021). Using landsat 8 OLI data to differentiate sargassum and ulva prolifera blooms in the south yellow sea. *International Journal of Applied Earth Observation and Geoinformation*, 98, 102302. <https://doi.org/10.1016/j.jag.2021.102302> (cf. p. 44)
- SUTHERLAND, G., SOONTIENS, N., DAVIDSON, F., SMITH, G. C., BERNIER, N., BLANKEN, H., SCHILLINGER, D., MARCOTTE, G., RÖHRS, J., DAGESTAD, K.-F., et al. (2020). Evaluating the leeway coefficient of ocean drifters using operational marine environmental prediction systems. *Journal of Atmospheric and Oceanic Technology*, 37(11), 1943-1954 (cf. p. 80, 87).
- TEJADA TEJADA, P., RODRÍGUEZ-RODRÍGUEZ, Y., RODRÍGUEZ DE FRANCISCO, L., PERDOMO, O., & BOLUDA, C. (2021). Lead, chromium, nickel, copper and zinc levels in Sargassum species reached the coasts of Dominican Republic during 2019 : A preliminary evaluation for the use of algal biomass as fertilizer and animal feeding. *Tecnología y Ciencias del Agua*, 12, 01-32. <https://doi.org/10.24850/j-tyca-2021-03-04> (cf. p. 40)
- THEIRLYNCK, T., MENDONÇA, I. R. W., ENGELEN, A. H., BOLHUIS, H., COLLADO-VIDES, L., van TUSSEN BROEK, B. I., GARCÍA-SÁNCHEZ, M., ZETTLER, E., MUYZER, G., & AMARAL-ZETTLER, L. (2023). Diversity of the holopelagic sargassum microbiome from the great atlantic sargassum belt to coastal stranding locations. *Harmful Algae*, 122, 102369. <https://doi.org/10.1016/j.hal.2022.102369> (cf. p. 39)

- THOMPSON, T. M., RAMIN, P., UDUGAMA, I., YOUNG, B. R., GERNAEY, K. V., & BAROUTIAN, S. (2021a). Techno-economic and environmental impact assessment of biogas production and fertiliser recovery from pelagic sargassum : a biorefinery concept for barbados. *Energy Conversion and Management*, 245, 114605. <https://doi.org/10.1016/j.enconman.2021.114605> (cf. p. 41)
- THOMPSON, T. M., YOUNG, B. R., & BAROUTIAN, S. (2020). Efficiency of hydrothermal pretreatment on the anaerobic digestion of pelagic Sargassum for biogas and fertiliser recovery. *Fuel*, 279, 118527. <https://doi.org/10.1016/j.fuel.2020.118527> (cf. p. 41)
- THOMPSON, T. M., YOUNG, B. R., & BAROUTIAN, S. (2021b). Enhancing biogas production from caribbean pelagic sargassum utilising hydrothermal pretreatment and anaerobic co-digestion with food waste. *Chemosphere*, 275, 130035. <https://doi.org/10.1016/j.chemosphere.2021.130035> (cf. p. 41)
- THOMPSON, T., YOUNG, B., & BAROUTIAN, S. (2020). Pelagic sargassum for energy and fertiliser production in the caribbean : a case study on barbados. *Renewable and Sustainable Energy Reviews*, 118, 109564. <https://doi.org/10.1016/j.rser.2019.109564> (cf. p. 41)
- TOBÍO-PÉREZ, I., ALFONSO-CARDERO, A., DÍAZ-DOMÍNGUEZ, Y., POHL, S., PILOTO-RODRÍGUEZ, R., & LAPUERTA, M. (2022). Thermochemical conversion of sargassum for energy production : a comprehensive review. *BioEnergy Research*. <https://doi.org/10.1007/s12155-021-10382-1> (cf. p. 41)
- TRENCH, C., THOMAS, S.-L., THORNEY, D., MADDIX, G.-M., FRANCIS, P., SMALL, H., MACHADO, C. B., WEBBER, D., TONON, T., & WEBBER, M. (2022). Application of Stranded Pelagic Sargassum Biomass as Compost for Seedling Production in the Context of Mangrove Restoration. *Frontiers in Environmental Science*, 10. Récupérée 27 février 2023, à partir de <https://www.frontiersin.org/articles/10.3389/fenvs.2022.932293> (cf. p. 41)
- TRINANES, J., PUTMAN, N. F., GONI, G., HU, C., & WANG, M. (2021). Monitoring pelagic Sargassum inundation potential for coastal communities [Publisher : Taylor & Francis _eprint : <https://doi.org/10.1080/1755876X.2021.1902682>]. *Journal of Operational Oceanography*, 0(0), 1-12. <https://doi.org/10.1080/1755876X.2021.1902682> (cf. p. 44)
- TRIÑANES, J., HU, C., PUTMAN, N., OLASCOAGA, M., BERON-VERA, F., GONI, G., & ZHANG, S. (2022). An Integrated Observing Effort for Sargassum Monitoring and Warning in the Caribbean Sea, Tropical Atlantic, and Gulf of Mexico (cf. p. 98).
- URIBE-MARTÍNEZ, A., BERRIEL-BUENO, D., CHÁVEZ, V., CUEVAS, E., ALMEIDA, K. L., FONTES, J. V. H., van TUSSEN BROEK, B. I., MARIÑO-TAPIA, I., LICEAGA-CORREA, M. d. l. Á., OJEDA, E., CASTAÑEDA-RAMÍREZ, D. G., & SILVA, R. (2022). Multiscale distribution patterns of pelagic rafts of sargasso (*Sargassum* spp.) in the Mexican Caribbean (2014–2020). *Frontiers in Marine Science*, 9. Récupérée 7 septembre 2022, à partir de <https://www.frontiersin.org/articles/10.3389/fmars.2022.920339> (cf. p. 42)

Bibliographie

- VALERIA, U.-A. A., IRVING, V.-G. J., HIND, T., ANDRES, G.-F., & ELIAS, V.-M. (2021). Coast sargassum level estimation from smartphone pictures. *arXiv* :2109.10390 [cs]. Récupérée 28 septembre 2021, à partir de <http://arxiv.org/abs/2109.10390> (cf. p. 42)
- VAN SEBILLE, E., ALIANI, S., LAW, K. L., MAXIMENKO, N., ALSINA, J. M., BAGAEV, A., BERGMANN, M., CHAPRON, B., CHUBARENKO, I., CÓZAR, A., et al. (2020). The physical oceanography of the transport of floating marine debris. *Environmental Research Letters*, 15(2), 023003 (cf. p. 81).
- VAN SEBILLE, E., ZETTLER, E., WIENDERS, N., AMARAL-ZETTLER, L., ELIPOT, S., & LUMPKIN, R. (2021). Dispersion of surface drifters in the Tropical Atlantic [Publisher : Frontiers]. *Frontiers in Marine Science*, 7, 607426. <https://doi.org/10.3389/fmars.2020.607426> (cf. p. 45, 88)
- VAN TUSSEN BROEK, B. I., ARANA, H. A. H., RODRÍGUEZ-MARTÍNEZ, R. E., ESPINOZA-AVALOS, J., CANIZALES-FLORES, H. M., GONZÁLEZ-GODOY, C. E., BARBA-SANTOS, M. G., VEGA-ZEPEDA, A., & COLLADO-VIDES, L. (2017). Severe impacts of brown tides caused by *Sargassum* spp. on near-shore Caribbean seagrass communities. *Marine pollution bulletin*, 122(1-2), 272-281 (cf. p. 38, 77).
- VÁZQUEZ-DELFIN, E., FREILE-PELEGRÍN, Y., SALAZAR-GARIBAY, A., SERVIERE-ZARAGOZA, E., MÉNDEZ-RODRÍGUEZ, L. C., & ROBLEDO, D. (2021). Species composition and chemical characterization of sargassum influx at six different locations along the mexican caribbean coast. *Science of The Total Environment*, 795, 148852. <https://doi.org/10.1016/j.scitotenv.2021.148852> (cf. p. 40)
- VELÁZQUEZ-OCHOA, R., & ENRÍQUEZ, S. (2023). Environmental degradation of the mexican caribbean reef lagoons. *Marine Pollution Bulletin*, 191, 114947. <https://doi.org/10.1016/j.marpolbul.2023.114947> (cf. p. 38)
- VERLAQUE, M., RUITTON, S., MINEUR, F., BOUDOURESQUE, C., & BRIAND, F. (2015). *CIESM Atlas of Exotic Species in the Mediterranean. Volume 4. Macrophytes.* (Cf. p. 21).
- WANG, M., & HU, C. (2016). Mapping and quantifying sargassum distribution and coverage in the central west atlantic using modis observations. *Remote Sensing of Environment*, 183, 350-367. <https://doi.org/10.1016/j.rse.2016.04.019> (cf. p. 43, 51, 52, 54-56, 60, 70, 77, 89, 97, 98, 123)
- WANG, M., & HU, C. (2018). On the continuity of quantifying floating algae of the Central West Atlantic between MODIS and VIIRS [Publisher : Taylor & Francis _eprint : <https://doi.org/10.1080/01431161.2018.1447161>]. *International Journal of Remote Sensing*, 39(12), 3852-3869. <https://doi.org/10.1080/01431161.2018.1447161> (cf. p. 44, 51, 54)
- WANG, M., & HU, C. (2020). Automatic extraction of sargassum features from sentinel-2 msi images. *IEEE Transactions on Geoscience and Remote Sensing*, PP, 1-19. <https://doi.org/10.1109/TGRS.2020.3002929> (cf. p. 43, 51, 52, 70, 87, 119)
- WANG, M., & HU, C. (2021). Satellite remote sensing of pelagic sargassum macroalgae : the power of high resolution and deep learning. *Remote Sensing of Environment*, 264, 112631. <https://doi.org/10.1016/j.rse.2021.112631> (cf. p. 44, 56, 70, 119)

Bibliographie

- WANG, M., HU, C., BARNES, B. B., MITCHUM, G., LAPOINTE, B., & MONTOYA, J. P. (2019a). The great atlantic *Sargassum* belt. *Science*, 365(6448), 83-87. <https://doi.org/10.1126/science.aaw7912> (cf. p. 10, 26, 43, 128)
- WANG, M., HU, C., BARNES, B. B., MITCHUM, G., LAPOINTE, B., & MONTOYA, J. P. (2019b). The great Atlantic Sargassum belt. *Science*, 365(6448), 83-87 (cf. p. 51, 66, 67, 71, 77, 97, 111, 112, 128).
- WANG, M., HU, C., CANNIZZARO, J., ENGLISH, D., HAN, X., NAAR, D., LAPOINTE, B., BREWTON, R., & HERNANDEZ, F. (2018). Remote sensing of sargassum biomass, nutrients, and pigments. *Geophysical Research Letters*, 45(22), 12-359. <https://doi.org/https://doi.org/10.1029/2018GL078858> (cf. p. 43, 54, 60, 97, 98, 104)
- WANG, X., WANG, L., CHEN, L., ZHANG, F., CHEN, K., ZHANG, Z., ZOU, Y., & ZHAO, L. (2022). AlgaeMask : an instance segmentation network for floating algae detection. *Journal of Marine Science and Engineering*, 10(8), 1099. <https://doi.org/10.3390/jmse10081099> (cf. p. 44)
- WANG, Z., ZHANG, X., LIU, Y., FU, M., XIAO, J., & YUAN, C. (2023). Interannual variations of sargassum blooms in the yellow sea and east china sea during 2017-2021. *Harmful Algae*, 102451. <https://doi.org/10.1016/j.hal.2023.102451> (cf. p. 44)
- WEBSTER, R. K. (2013). Development and implementation of Sargassum Early Advisory System (SEAS). 81(3), 6 (cf. p. 45).
- WEIS, J. S. (1968). Fauna Associated with Pelagic Sargassum in the Gulf Stream [Publisher : University of Notre Dame]. *The American Midland Naturalist*, 80(2), 554-558. <https://doi.org/10.2307/2423550> (cf. p. 35)
- WELLS, R. J. D., & ROOKER, J. R. (2004). Distribution, age, and growth of young-of-the year greater amberjack (*Seriola dumerili*) associated with pelagic Sargassum [Number : 3]. *Fishery Bulletin*, 102(3), 545-554. Récupérée 23 mars 2021, à partir de <http://fishbull.noaa.gov/1023/wells.pdf> (cf. p. 35)
- WELLS, R. D., & ROOKER, J. R. (2004). Spatial and temporal patterns of habitat use by fishes associated with Sargassum mats in the northwestern Gulf of Mexico. *Bulletin of Marine Science*, 74(1), 81-99 (cf. p. 35, 36).
- WINGE, O. (1923). The sargasso sea, its boundaries and vegetation. *Oceanographical Expeditions 1908-10 to the Mediterranean and Adjacent Seas*, 3 (cf. p. 37).
- WITHERINGTON, B., HIRAMA, S., & HARDY, R. (2012). Young sea turtles of the pelagic Sargassum-dominated drift community : habitat use, population density, and threats. *Marine Ecology Progress Series*, 463, 1-22. <https://doi.org/10.3354/meps09970> (cf. p. 35)
- WOODCOCK, A. H. (1950). Subsurface pelagic sargassum. *J. mar. Res.*, 9(2), 77-92 (cf. p. 45, 70).
- WOODCOCK, A. H. (1993). Winds subsurface pelagic sargassum and langmuir circulations. *Journal of Experimental Marine Biology and Ecology*, 170(1), 117-125. [https://doi.org/10.1016/0022-0981\(93\)90132-8](https://doi.org/10.1016/0022-0981(93)90132-8) (cf. p. 45, 70, 88)
- XIAO, J., FAN, S., WANG, Z., FU, M., SONG, H., WANG, X., YUAN, C., PANG, M., MIAO, X., & ZHANG, X. (2020a). Decadal characteristics of the floating *Ulva* and Sargassum in the Subei Shoal, Yellow Sea. *Acta Oceanologica Sinica*, 39(10), 1-10. <https://doi.org/10.1007/s13131-020-1655-4> (cf. p. 44)

Bibliographie

- XIAO, J., WANG, Z., SONG, H., FAN, S., YUAN, C., FU, M., MIAO, X., ZHANG, X., SU, R., & HU, C. (2020b). An anomalous bi-macroalgal bloom caused by Ulva and Sargassum seaweeds during spring to summer of 2017 in the western Yellow Sea, China. *Harmful Algae*, 93, 101760. <https://doi.org/10.1016/j.hal.2020.101760> (cf. p. 44)
- XIAO, Y., LIU, R., KIM, K., ZHANG, J., & CUI, T. (2021). A Random Forest-Based Algorithm to Distinguish Ulva prolifera and Sargassum From Multispectral Satellite Images [Conference Name : IEEE Transactions on Geoscience and Remote Sensing]. *IEEE Transactions on Geoscience and Remote Sensing*, 1-15. <https://doi.org/10.1109/TGRS.2021.3071154> (cf. p. 44)
- XING, Q., GUO, R., WU, L., AN, D., CONG, M., QIN, S., & LI, X. (2017). High-resolution satellite observations of a new hazard of golden tides caused by floating Sargassum in winter in the Yellow Sea [Conference Name : IEEE Geoscience and Remote Sensing Letters]. *IEEE Geoscience and Remote Sensing Letters*, 14(10), 1815-1819. <https://doi.org/10.1109/LGRS.2017.2737079> (cf. p. 44, 51)
- YAN, F., JIANG, H., MA, Y., CUI, C., QIN, H., LIU, L., ZANG, S., XING, H., XU, Z., & WU, H. (2022). Combined influences of light and nitrogen enrichment on the physiological performance of a golden tide alga (sargassum horneri). *Journal of Marine Science and Engineering*, 10(9), 1195. <https://doi.org/10.3390/jmse10091195> (cf. p. 37)
- YANG, H., ARNONE, R., & JOLLIFF, J. (2015). Estimating advective near-surface currents from ocean color satellite images. *Remote Sensing of Environment*, 158, 1-14 (cf. p. 86).
- ZHANG, S., HU, C., BARNES, B. B., & HARRISON, T. N. (2022). Monitoring Sargassum inundation on beaches and nearshore waters using PlanetScope/Dove observations [Conference Name : IEEE Geoscience and Remote Sensing Letters]. *IEEE Geoscience and Remote Sensing Letters*, 1-1. <https://doi.org/10.1109/LGRS.2022.3148684> (cf. p. 43)
- ZHAO, C., SUN, J., SHEN, Y., XIA, Z., HU, M., WU, T., ZHUANG, M., LI, Y., TONG, Y., YANG, J., ZHANG, J., & HE, P. (2023). Removable carbon and storage carbon of golden tides. *Marine Pollution Bulletin*, 191, 114974. <https://doi.org/10.1016/j.marpolbul.2023.114974> (cf. p. 39)

ANNEXES

A. Apports en nutriments des grands fleuves et prolifération des sargasses

L'article ci-dessous est une analyse de l'effet des apports en nutriments des grands fleuves (Amazon, Congo, Orénoque) sur la croissance des algues sargasses. Basé sur la corrélation spatiale entre les plumes des grands fleuves (zone d'influence) et entre les concentrations de sargasses, il montre que ceux-ci n'ont probablement que peu d'influence sur l'actuelle dynamique de croissance des algues. La présente thèse a participé à cette étude en fournissant les données d'observation de sargasses filtrées des fausses détections avec la méthode développée dans le chapitre 3.

ENVIRONMENTAL RESEARCH LETTERS**OPEN ACCESS****RECEIVED**
14 September 2020**REVISED**
15 January 2021**ACCEPTED FOR PUBLICATION**
28 January 2021**PUBLISHED**
1 March 2021

Original content from this work may be used under the terms of the Creative Commons Attribution 4.0 licence.

Any further distribution of this work must maintain attribution to the author(s) and the title of the work, journal citation and DOI.

**LETTER**

Evolution of the riverine nutrient export to the Tropical Atlantic over the last 15 years: is there a link with *Sargassum* proliferation?

Julien Jouanno¹ , Jean-Sébastien Moquet² , Léo Berline³ , Marie-Hélène Radenac¹, William Santini⁴ , Thomas Changeux³ , Thierry Thibaut³ , Witold Podlejski³, Frédéric Ménard³ , Jean-Michel Martinez¹ , Olivier Aumont⁵ , Julio Sheinbaum⁶ , Naziano Filizola⁷ and Guy Dieudonne Moukandi N'Kaya⁸

¹ LEGOS, Université de Toulouse, IRD, CNRS, CNES, UPS, Toulouse, France

² CNRS/INSU, ISTO, UMR, 7327 Orléans, France

³ Aix-Marseille University, Université de Toulon, CNRS/INSU, IRD, MIO UM 110, Mediterranean Institute of Oceanography (MIO), Campus of Luminy, 13288 Marseille, France

⁴ GET, UMR5563, CNRS/IRD/Université de Toulouse-3, Toulouse, France

⁵ Laboratoire d'Océanographie et de Climatologie: Expérimentation et Approches Numériques, IRD-IPSL, 4 Place Jussieu, 75005 Paris, France

⁶ CICESE, Ensenada, Mexico

⁷ Amazonas State Federal University—UFAM, Geoscience Department, Manaus, Brazil

⁸ LMEI/CUSI/ENSP/Marien Ngouabi University, BP 69 Brazzaville, Congo

E-mail: julien.jouanno@ird.fr

Keywords: *Sargassum*, hydrology, Amazon

Supplementary material for this article is available [online](#)

Abstract

The Tropical Atlantic is facing a massive proliferation of *Sargassum* since 2011, with severe environmental and socioeconomic impacts. As a contribution to this proliferation, an increase in nutrient inputs from the tropical rivers, in response to climate and land use changes or increasing urbanization, has been often suggested and widely reported in the scientific and public literature. Here we discuss whether changes in river nutrient inputs could contribute to *Sargassum* proliferation in the recent years or drive its seasonal cycle. Using long-term *in situ* and satellite measurements of discharge, dissolved and particulate nutrients of the three world largest rivers (Amazon, Orinoco, Congo), we do not find clear evidences that nutrient fluxes may have massively increased over the last 15 years. Moreover, focusing on year 2017, we estimate that along the year only 10% of the *Sargassum* biomass occurred in regions under river plume influence. While deforestation and pollution are a reality of great concern, our results corroborate recent findings that hydrological changes are not the first order drivers of *Sargassum* proliferation. Besides, satellite observations suggest that the major Atlantic river plumes suffered a decrease of phytoplankton biomass in the last two decades. Reconciling these observations requires a better understanding of the nutrient sources that sustain *Sargassum* and phytoplankton growth in the region.

1. Context

Before 2010, holopelagic *Sargassum* spp. were preferentially found in the Sargasso Sea and in the Gulf of Mexico. They now develop in large quantities on the southern part of the North Atlantic between 0° N and 10° N forming a ‘*Sargassum* belt’ stranding in millions of tons on the coasts of the Lesser Antilles, Central America, Brazil and West Africa. (e.g. Smetacek and Zingone 2013, Wang and Hu 2016, Langin 2018, Wang et al 2019).

Satellite imagery pointed to the presence of large amounts of *Sargassum* in areas under seasonal influence of the Amazon plume (Gower et al 2013, Sissini et al 2017, Oviatt et al 2019, Wang et al 2019) raising the hypothesis that river nutrient fluxes might play a role in this proliferation (Langin 2018, Oviatt et al 2019, Wang et al 2019). A possible influence of the Congo has also been invoked in several studies (Djakouré et al 2017, Oviatt et al 2019). A recent study by Johns et al (2020), however, did not find strong evidence to support this hypothesis as there

appears to be a spatiotemporal mismatch between *Sargassum* occurrence and these riverine sources of nutrients. Given the importance of this question and the present discrepancies in the scientific literature we find it important to examine to which extent the riverine source of nutrients may contribute to the proliferation of pelagic *Sargassum*. Indeed, several elements give support to a possible influence of the riverine sources of nutrients. First, rivers export nitrogen (N) and phosphorus (P), which are key limiting nutrients required for *Sargassum* growth (Lapointe 1986, 1995). Specifically, the Amazon also contains important concentrations of dissolved organic substrates that could be an important source of nutrient for *Sargassum* growth as reviewed in Oviatt *et al* (2019). Second, the Tropical Atlantic receives the fresh and nutrient rich waters of the three largest rivers on the planet—in terms of flow (Amazon, 209 000 m³ s⁻¹, Congo, 42 000 m³ s⁻¹ and Orinoco, 35 000 m³ s⁻¹), which alone represent 21% of the total global riverine flow (Milliman and Farnsworth 2011). Their low-saline and productive plumes extend thousands of kilometers far offshore (Muller-Karger *et al* 1988, Signorini *et al* 1999). Third, the watersheds undergo strong climatic and anthropogenic pressures that are thought to have the potential to modify oceanic biogeochemical systems. For instance, Seitzinger *et al* (2010) estimated that the total river input of N to the coastal seas has approximately doubled since the 70s, with South America representing ~20% of the global increase. The Amazon basin already shows some signs of a transition to a disturbance-dominated regime in response to agricultural expansion and climate variability (Davidson *et al* 2012). The region experiences a strong anthropogenic pressure associated with a rapid urbanization (Richards and Vanwey 2015), intense hydropower dam construction (Latrubesse *et al* 2017), and increase of mining and oil extraction contamination (e.g. Moquet *et al* 2014). The overall consequences of these changes in terms of nutrient budget remain uncertain since they can act as a source or a sink of nutrients.

In this context, the long-term evolution of the continental nutrient export to the Tropical Atlantic is investigated on the basis of *in situ* observations of the major dissolved and particulate nutrients exported by the three main rivers of the basin (Amazon, Orinoco and Congo). Satellite estimates of chlorophyll provide an independent set of observations to monitor the long-term changes of biological activity in the large river plumes. Finally, the large-scale seasonal distribution of *Sargassum* for year 2017 is confronted to numerical experiments of river plume dispersal. We focused on this year because basin scale *Sargassum* fractional coverage observations from MODIS were available (Berline *et al* 2020), with concurrent observations carried out during two cruises in the Tropical

Atlantic (Ody *et al* 2019). Year 2017 was the third most important year of the decade in terms of quantity of *Sargassum* (as inferred from time series in Wang *et al* 2019), with a seasonal pattern that closely mirrors the averaged seasonal pattern from Wang *et al* (2019).

2. River nutrient fluxes

The productivity of the *Sargassum* is enhanced by N and P availability (Lapointe 1995). At global scale, the rivers carry N to oceanic coastal zone in dissolved and particulate forms in almost equal proportion (Joo *et al* 2013) while P is mainly exported as particulate form (90%–95% of the total P flux to the ocean; Ruttenberg 2004). About 25%–45% of the particulate P (Ruttenberg 2004) and a significant proportion of particulate N are reactive in the sea water and bioavailable for marine organisms including the seaweed. The dissolved and particulate N and P fluxes measured or estimated at the seaward-most stations for the Amazon, Orinoco, and Congo basins are shown in figure 1 for the last two decades. These data were collected by the SO-HYBAM observatory and are presented together with riverine flux calculation methods in the supplementary material.

For the three rivers, the largest input of N is provided by the dissolved organic matter. Dissolved organic nitrate delivered by the Amazon is thought to become bioavailable in the offshore fraction of the plume through bacterial and photochemical transformations (Medeiros *et al* 2015). For the Amazon, this flux appears to regularly increase from 2004, apart from maxima in years 2007 and 2008. Observations for the Orinoco suggest a doubling of this flux over the last 15 years (figure 1). The particulate fluxes of N, estimated from remote sensing, is also expected to contribute to nutrient supply through desorption of the shelf (Demaster and Aller 2000). It is stable for the three rivers. The dissolved inorganic N flux, computed from NO₃⁻ *in situ* measurements, show larger values during the last decade for the three rivers (figures 1(a)–(c)). Before 2013, values above the detection limit (0.01 mg l⁻¹) were of similar magnitude than independent Amazon (Richey *et al* 2009, Ward *et al* 2015, Doherty *et al* 2017), Orinoco (Lewis and Saunders 1989) and Congo (Descy *et al* 2017) water analyses. They did not show a marked evolution over this period. From the years 2013–2014, the average concentration of NO₃⁻ has increased for the three rivers. On the one hand, the scatter of the measured concentrations is so high that it is difficult to determine how significant the NO₃⁻ increase really is. On the other hand, the more frequent recording of high NO₃⁻ fluxes is of concern and suggests a potential evolution of the dissolved NO₃⁻ export that needs to be investigated. However, it should be noted that the marked changes in terms of NO₃⁻ for the different

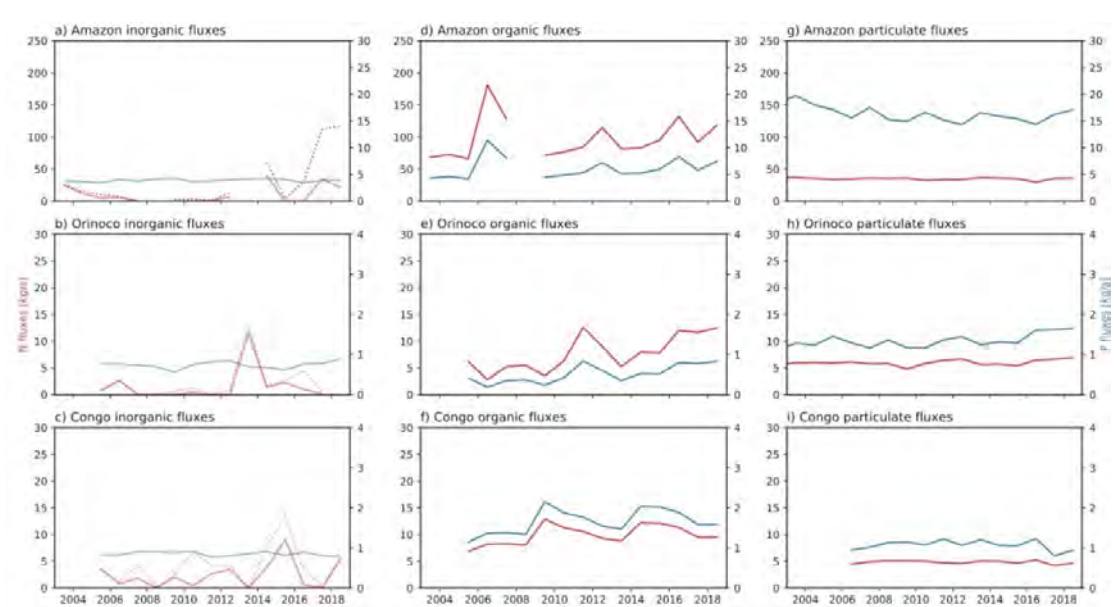


Figure 1. Interannual variations of dissolved inorganic N (red) and P (blue) fluxes (left column), dissolved organic N and P fluxes (central column) and particulate N and P fluxes (right column). Data are from 2003 to 2018 and include the three largest rivers of the Tropical Atlantic: (a), (d), (g) the Amazon at Óbidos station, (b), (e), (h) the Orinoco at Ciudad Bolívar station and (c), (f), (i) the Congo at Brazzaville station. Fluxes were computed from different data sources (*in-situ*, satellite, literature) and details are given in supplementary material. In (a)–(c), the annual mean N flux has been computed considering all the available Hybam monthly measured NO_3^- concentrations (dashed line) but also removing the 10% extreme values for each year (continuous line).

rivers occurred 2–3 years after the first massive proliferation of 2011.

In the Amazon river, the largest amount of P is delivered in particulate form (figure 1(g)). The importance of the particulate P is in line with observations by Berner and Rao (1994) who conclude that the solubilization of P from bacterial decomposition of river-transported organic matter and desorption from ferric oxide/hydroxide may result in an effective flux of reactive P about three times greater than that carried only in dissolved form. This particulate flux shows a slight decrease over the last two decades, while the inorganic and organic dissolved fluxes remained stable. The P fluxes for the Orinoco and Congo are one order of magnitude smaller than those of the Amazon.

So, observations show different long-term trends of inorganic, organic and particulate fluxes of N and P. No direct and clear relationship with *Sargassum* growth can be drawn, neither in terms of long-term evolution, nor in terms of interannual variability (e.g. no major peak of nutrient fluxes was observed during the record *Sargassum* years 2015 and 2018, and there is no clear relation with the basin scale *Sargassum* biomass time series from Wang *et al* 2019). Large uncertainties remain in the nutrient fluxes estimation and the fate of these nutrients in the open ocean, but these results already question whether the order of magnitude of the observed trends and variability are large enough to contribute to the inter-annual variability of the oceanic biological response.

3. Link with changes in plume productivity and *Sargassum* distribution

The diversity of the nutrient trends and the lack of knowledge on the lability of the dissolved and particulate riverine material render uncertain the assessment of the long-term evolution of the riverine fertilization of the ocean. As an independent marker of possible changes in the nutrient export by the large Tropical Atlantic rivers, the long-term evolution of surface chlorophyll estimated from satellite ocean color is now analyzed. Chlorophyll is the main pigment in phytoplankton and here we use chlorophyll as a proxy of phytoplankton biomass. As it has been evidenced for the Mississippi in the northern Gulf of Mexico (Lohrenz *et al* 1997, Rabalais *et al* 2002, Wysocki *et al* 2006), we expect that fluctuations in riverine nutrients alter the dynamics of phytoplankton growth and thus phytoplankton biomass in the large tropical river plumes. The difference between the ‘*Sargassum* period’ (2011–2018) and the years before (2003–2010) reveals an overall decrease of the chlorophyll concentration in the Tropical Atlantic (figure 2(b)). This decline is sharper in the Amazon, Orinoco, and Congo plume regions. Since Chlorophyll retrieval from space is subject to large discrepancies between the different available products, we compared five monthly chlorophyll products from three different groups (GlobColour, NOAA, and CCI). For the three rivers considered, four out of the five different products show a consistent decrease of chlorophyll concentration in the plume areas

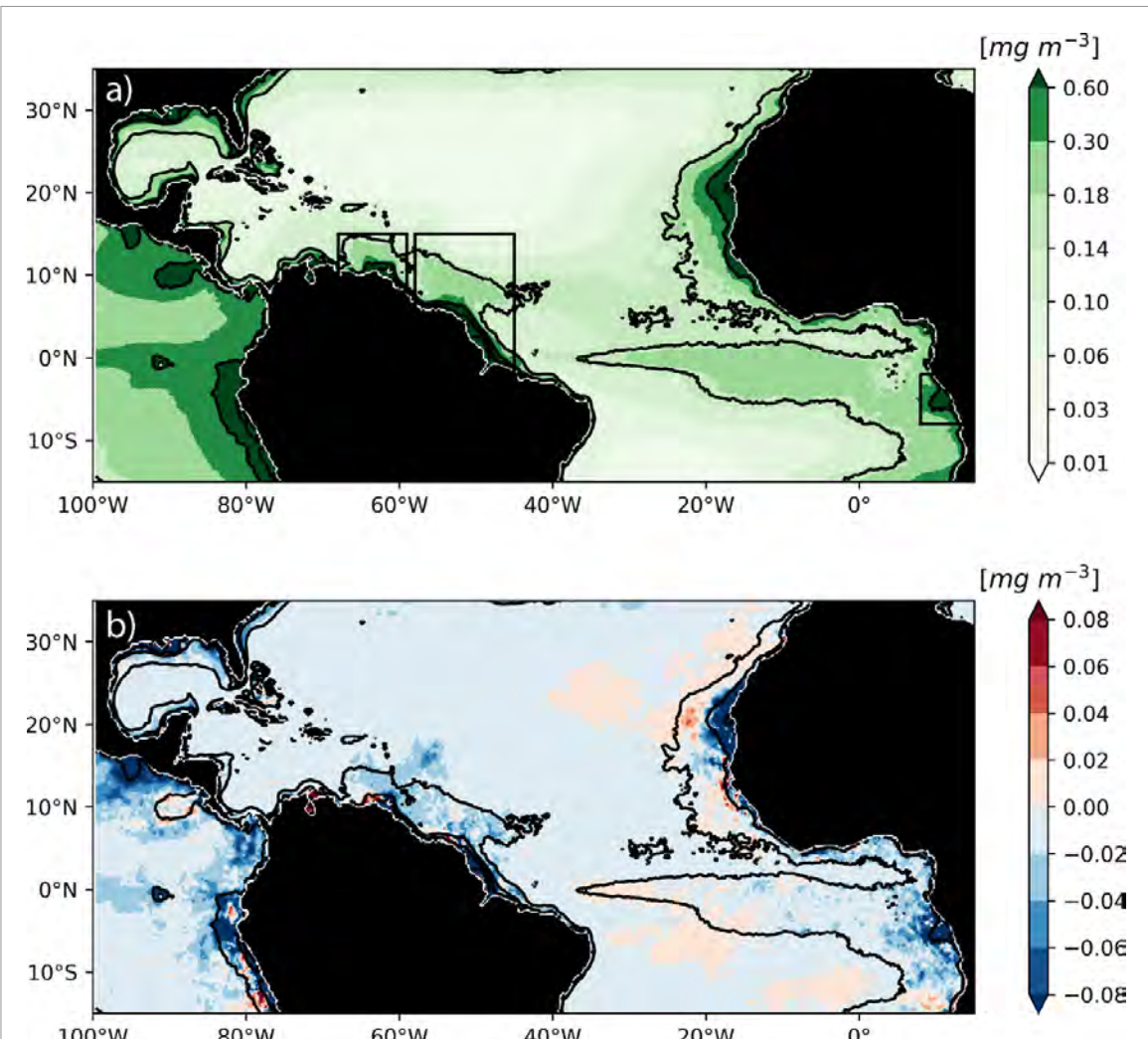


Figure 2. (a) Mean chlorophyll concentrations (in mg m^{-3}) from GlobColour monthly MODIS GSM product at $1/4^\circ$ horizontal resolution for the period 2003–2018. (b) Difference of chlorophyll concentration between the period 2011–2018 and the period 2003–2010. Black contours indicate the 0.3 and 0.6 mg m^{-3} chlorophyll concentration iso-contours. The boxes indicate the extent of the regions used to computed the chlorophyll time series in figure S5.

(figure S5 (available online at stacks.iop.org/ERL/16/034042/mmedia)).

The basin scale decrease of chlorophyll evidenced in figure 2(b) is in line with the study by Gregg and Rousseau (2019) that suggested that global net ocean primary production has experienced a small but significant decline in the 18 year satellite records from 1998 to 2015, in response to shallowing surface mixed layer depth, decreasing nitrate supply and changes in the phytoplankton communities. Chlorophyll concentrations in river plumes exhibit a larger decrease. The underlying cause of these changes in the chlorophyll content of the plumes is difficult to ascertain from observations only. It is worth mentioning that (a) colored detrital material contributes to total light attenuation in the blue region of the spectrum where chlorophyll-a also absorbs strongly (Fournier *et al* 2015) which could lead to large errors in ocean color retrievals, (b) the response of the productive plumes may not only depend on the riverine nutrient flux

but on other variables such as temperature, stratification, turbidity, or dust deposition. But this decrease, whether it is caused by a decrease of plume productivity or weaker discharge of dissolved colored material (which is not observed in SO-HYBAM observations of organic and particulate nutrient fluxes, figure 1) is difficult to reconcile with the hypothesis of an overall increase in fertilization by tropical rivers in recent years. A better understanding of the river plume biogeochemistry is required, together with analysis of possible competing growth dynamics between phytoplankton and *Sargassum*.

The seasonal distribution of *Sargassum* for year 2017 is shown in figure 3 together with the chlorophyll concentrations. The *Sargassum* bloom during the first 6 months of the year occurs preferentially in the Intertropical Convergence Zone (ITCZ; located between the equator and 10° N), where chlorophyll is relatively high compared to the surrounding subtropical oligotrophic area. To our knowledge,

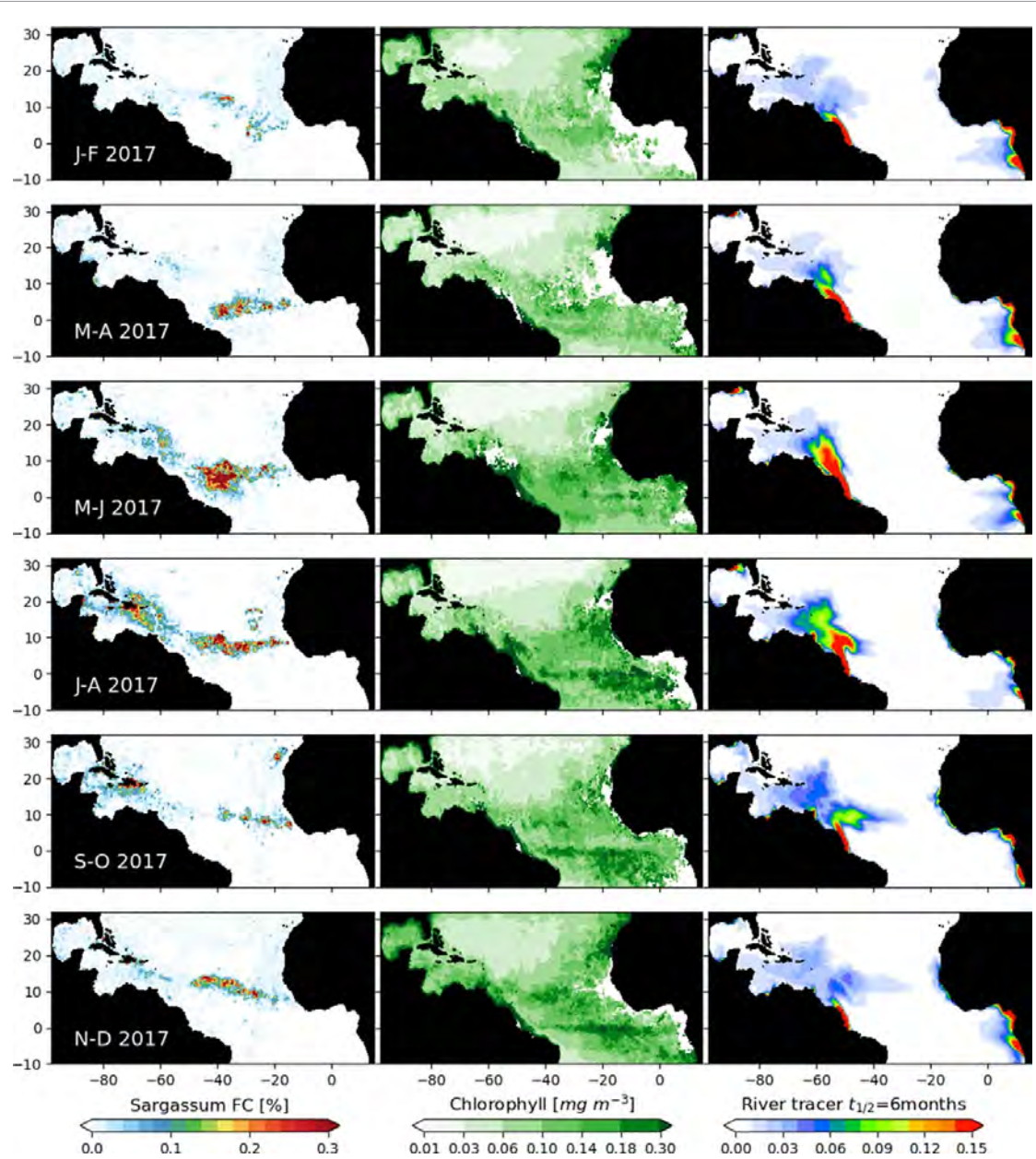


Figure 3. (a) Fractional Coverage (%) of *Sargassum*, (b) chlorophyll from monthly GlobColour GSM merged product (mg m^{-3}), (c) river tracer surface distribution (no unit, initialized at 1 at the river mouth) with half-life time scale of 6 month from a $1/4$ degree NEMO regional simulation. Data are all for year 2017 and have been averaged over 2 month periods.

the causes of the high chlorophyll level have not been identified, but could be the result of diatoms-diazotroph assemblages (Subramaniam *et al* 2008, Schlosser *et al* 2014), atmospheric deposition of dust (Yu *et al* 2015), or biomass burning emissions (Barkley *et al* 2019). Yet, the presence of relatively high chlorophyll concentration indicates nutrient availability that may participate to sustain *Sargassum* growth.

Interestingly, we remark that during September–October, when the North Brazil Current retroflects and transports the Amazon riverine freshwater to the east, the abundance of *Sargassum* in the plume area between 60°W and 40°W , is drastically reduced relative to the two previous months. The North Brazil Current is mainly fed by waters originating from the

equatorial area and the southern Tropical Atlantic (Johns *et al* 1998) where no massive proliferation of *Sargassum* was observed in the previous months. Our interpretation is that the weak abundance of *Sargassum* in the plume at this time is mainly controlled by advection of low *Sargassum* water in the region. The low salinity of the plume could also limit the proliferation of *Sargassum* there. Indeed, culture experiments of *Sargassum natans* and *Sargassum fluitans* described in Hanisak and Samuel (1987) revealed some dependence of their growth rate to salinity. A reduction in salinity from 36 to 30 caused a reduction in the growth rates by almost half, and no growth was observed for salinity below 18. This effect may likely limit the fertilizing effect of the nutrient rich river plumes.

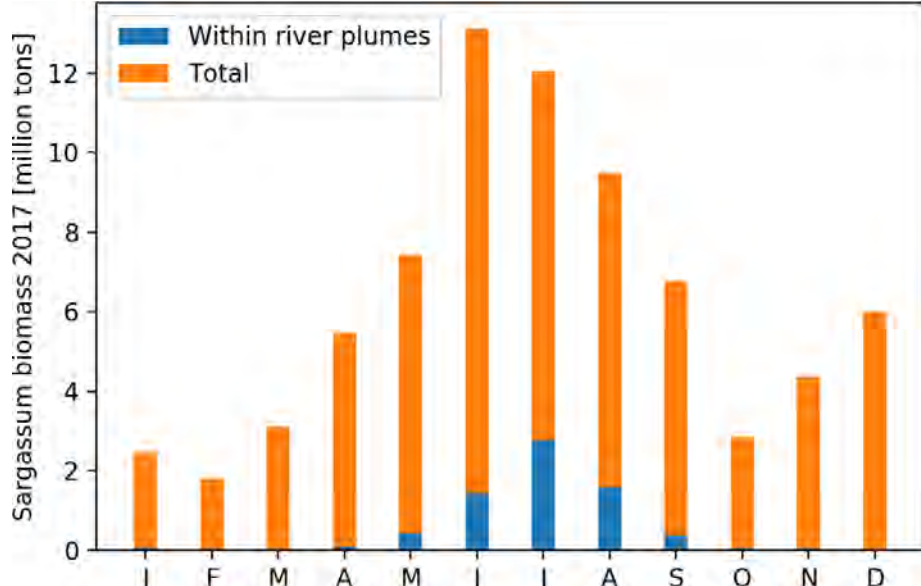


Figure 4. Monthly mean *Sargassum* biomass for year 2017 estimated from MODIS in the Caribbean and Central Atlantic (5° S– 25° N, 89° W– 15° E). The blue bar marks the fraction of the biomass which is colocated with the model river plume (defined as areas with surface concentration of riverine waters >0.05 , i.e. more than 5% of kg of water with riverine origin per kg of ocean water; the spatial distribution of the river tracer is shown in figure 3(c)).

The river plume dispersion numerical experiment (figure 3) also reveals that the central Atlantic is not under the influence of the Amazon plume during the first half of the year. The largest coincidence between the plume and *Sargassum* distribution occurs in June–July–August (figure 4), when the Amazon plume extends toward the Lesser Antilles. This is in line with the analysis by Gouveia *et al* (2019) that showed that the Amazon plume fingerprints on oceanic primary productivity spatio-temporal variability are restricted to the western Tropical Atlantic. The first 6 months of the year appear to be crucial for the occurrence of *Sargassum* along the south American and Caribbean coasts a few months later (Wang and Hu 2017, Putman *et al* 2018, Wang *et al* 2019, Berline *et al* 2020). Even if Amazon river fertilization could contribute to the seasonal growth in the portion of western Tropical Atlantic under seasonal influence of the Amazon plume (an area between 60° W and 40° W and between 0° N and 20° N), this analysis further suggests that it does not drive the large-scale seasonal bloom. At the annual scale, we found that only 9% of the *Sargassum* biomass occurred in the river plume area in 2017, with occurrence below 5% from September to May and peak at 23% in July when the plume is well extended toward the Lesser Antilles. It is even more unlikely that the Congo and Orinoco rivers could contribute to the large-scale bloom due to the limited imprint of the plumes on the chlorophyll distribution and remoteness of the river plumes from the main *Sargassum* bloom areas.

As a conclusion, while increasing inputs of N and P in the watershed from human activity, predominantly from land-based activities, are thought to have

the potential to significantly increase the nutrient fluxes toward the ocean and have been proposed as contributors of the *Sargassum* proliferation, this analysis suggests that riverine fertilization is unlikely a key controlling factor of both seasonal and interannual variability of the *Sargassum* biomass. In agreement with recent findings by Johns *et al* (2020), it fails to explain the *Sargassum* distribution shift that occurred after 2010. Instead, Johns *et al* (2020) proposed that an extreme negative phase of the North Atlantic Oscillation triggered the 2011 event and that vertical mixing dynamics below the ITCZ sustains *Sargassum* growth in the Central Tropical Atlantic. This is in line with the enhanced chlorophyll concentrations observed below the ITCZ (figure 4). However, the forcing processes sustaining the productivity there remain to be clarified. This study also reminds us that advection is instrumental in controlling the seasonal distribution of *Sargassum*, as already revealed by several studies (Brooks *et al* 2018, Wang *et al* 2019, Berline *et al* 2020). Although much progress has been made recently on how *Sargassum* advection responds to currents and winds (Berline *et al* 2020, Putman *et al* 2020, Miron *et al* 2020), this issue has yet to be fully evaluated and understood. That key aspects of growth and movement are missing from our ability to understand and forecast spatiotemporal variability in the distribution of pelagic *Sargassum*.

4. Methods

Methods and associated references are available in the supplementary material.

Data availability statement

The data that support the findings of this study are openly available at the following URL/DOI: <https://hybam.obs-mip.fr>.

Acknowledgments

This study was supported by IRD, the French Ministère de la Transition Écologique, the ANR project FORESEA (<https://sargassum-foresea.cnrs.fr>), and project TOSCA-SAREDA_DA. Supercomputing facilities were provided by GENCI project GEN7298. We thank the HyBAm research group, especially A Laraque, for open access to the hydrological, sedimentary and geochemical data, CNES for funding project TOSCA-SAREDA_DA, and the NASA, GlobColour and CCI for providing chlorophyll data. We acknowledge J Bouchez for providing hydrogeochemistry Amazon River data.

Authors contributions

All authors contributed to the interpretation of the results and writing of the manuscript. J J and J S M designed the study. J J implemented the numerical simulations, and conducted the comparison with observations. G M M and F M participated to the long-term hydrological measurements. J S M, W S and J M M performed the hydrological analysis. L B and W P produced the basin scale *Sargassum* observations. M H R contributed to the ocean color analysis.

ORCID iDs

Julien Jouanno  <https://orcid.org/0000-0001-7750-060X>

Jean-Sébastien Moquet  <https://orcid.org/0000-0003-1925-9306>

Léo Berline  <https://orcid.org/0000-0002-5831-7399>

William Santini  <https://orcid.org/0000-0003-0098-9755>

Thomas Changeux  <https://orcid.org/0000-0002-0418-3321>

Thierry Thibaut  <https://orcid.org/0000-0001-8530-9266>

Frédéric Ménard  <https://orcid.org/0000-0003-1162-660X>

Jean-Michel Martinez  <https://orcid.org/0000-0003-3281-8512>

Olivier Aumont  <https://orcid.org/0000-0003-3954-506X>

Julio Sheinbaum  <https://orcid.org/0000-0001-7031-5225>

Naziano Filizola  <https://orcid.org/0000-0001-7285-7220>

Guy Dieudonne Moukandi N'Kaya  <https://orcid.org/0000-0002-9115-1896>

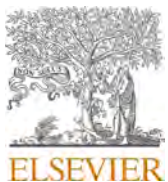
References

- Barkley A E et al 2019 African biomass burning is a substantial source of phosphorus deposition to the Amazon, Tropical Atlantic Ocean, and Southern Ocean *Proc. Natl Acad. Sci.* **116** 16216–21
- Berline L, Ody A, Jouanno J, Chevalier C, André J-M, Thibaut T and Ménard F 2020 Hindcasting the 2017 dispersal of *Sargassum* algae in the Tropical North Atlantic *Mar. Pollut. Bull.* **158** 11431
- Berner R A and Rao J L 1994 Phosphorus in sediments of the Amazon River and estuary: implications for the global flux of phosphorus to the sea *Geochim. Cosmochim. Acta* **58** 2333–9
- Brooks M T, Coles V J, Hood R R and Gower J F 2018 Factors controlling the seasonal distribution of pelagic *Sargassum* *Mar. Ecol. Prog. Ser.* **599** 1–18
- Davidson E A et al 2012 The Amazon basin in transition *Nature* **481** 321
- Demaster D J and Aller R C 2000 Biogeochemical processes on the Amazon shelf: changes in dissolved and particulate fluxes during river/ocean mixing *The Biogeochemistry of the Amazon Basin* ed M E McClain, R Victoria and J E Richey (Oxford: Oxford University Press) pp 328–57
- Desy J-P, Darchambeau F, Lambert T, Stoyneva-Gaertner M P, Bouillon S and Borges A V 2017 Phytoplankton dynamics in the Congo River *Freshwater Biol.* **62** 87–101
- Djakouré S, Araujo M, Hounsou-Gbo A, Noriega C and Bourlès B 2017 On the potential causes of the recent Pelagic *Sargassum* blooms events in the tropical North Atlantic Ocean *Biogeosci. Discuss.* submitted (<https://doi.org/10.5194/bg-2017-346>)
- Doherty M et al 2017 Bacterial biogeography across the Amazon River-ocean continuum *Front. Microbiol.* **8** 882
- Fournier S, Chapron B, Salisbury J, Vandemark D and Reul N 2015 Comparison of spaceborne measurements of sea surface salinity and colored detrital matter in the Amazon plume *J. Geophys. Res.: Oceans* **120** 3177–92
- Gouveia N A, Gherardi D F M, Wagner F H, Paes E T, Coles V J and Aragão L E O C 2019 The salinity structure of the Amazon River plume drives spatiotemporal variation of oceanic primary productivity *J. Geophys. Res.: Biogeosci.* **124** 147–65
- Gower J, Young E and King S 2013 Satellite images suggest a new *Sargassum* source region in 2011 *Remote Sens. Lett.* **4** 764–73
- Johns E M et al 2020 The establishment of a pelagic *Sargassum* population in the tropical Atlantic: biological consequences of a basin-scale long distance dispersal event *Prog. Oceanogr.* **182** 102269
- Johns W E, Lee T N, Beardsley R C, Candela J, Limeburner R and Castro B 1998 Annual cycle and variability of the North Brazil Current *J. Phys. Oceanogr.* **28** 103–28
- Joo Y J, Li D D and Lerman A 2013 Global nitrogen cycle: pre-anthropocene mass and isotope fluxes and the effects of human perturbations *Aquat. Geochem.* **19** 477–500
- Langin K 2018 Seaweed masses assault Caribbean islands *Science* **360** 1157–8
- Lapointe B E 1986 Phosphorus-limited photosynthesis and growth of *Sargassum natans* and *Sargassum fluitans* (Phaeophyceae) in the western North Atlantic *Deep Sea Res. A* **33** 391–9
- Lapointe B E 1995 A comparison of nutrient-limited productivity in *Sargassum natans* from neritic vs. oceanic waters of the western North Atlantic Ocean *Limnol. Oceanogr.* **40** 625–33
- Latrubesse E M et al 2017 Damming the rivers of the Amazon basin *Nature* **546** 363–9
- Lewis W M and Saunders J F 1989 Concentration and transport of dissolved and suspended substances in the Orinoco River *Biogeochemistry* **7** 203–40
- Lohrenz S E, Fahnenstiel G L, Redalje D G, Lang G A, Chen X and Dagg M J 1997 Variations in primary production of northern Gulf of Mexico continental shelf waters linked to

- nutrient inputs from the Mississippi River *Mar. Ecol. Prog. Ser.* **155** 45–54
- Medeiros P M, Seidel M, Ward N D, Carpenter E J, Gomes H R, Niggemann J, Krusche A V, Richey J E, Yager P L and Dittmar T 2015 Fate of the Amazon River dissolved organic matter in the tropical Atlantic Ocean *Glob. Biogeochem. Cycles* **29** 677–90
- Milliman J D and Farnsworth K L 2011 *River Discharge to the Coastal Ocean—A Global Synthesis* (Cambridge: Cambridge University Press)
- Miron P, Olascoaga M J, Beron-Vera F J, Putman N E, Trinanes J, Lumpkin R and Goni G J 2020 Clustering of Marine-Debris- and Sargassum -Like Drifters Explained by Inertial Particle Dynamics *Geophys. Res. Lett.* **47** e2020GL089874
- Moquet J S, Maurice L, Crave A, Viers J, Aravelo N, Lagane C, Lavado Casimiro W and Guyot J L 2014 Cl and Na fluxes in an Andean foreland basin of the Peruvian Amazon: an anthropogenic impact evidence *Aquat. Geochem.* **20** 613–37
- Muller-Karger F E, McClain C R and Richardson P L 1988 The dispersal of the Amazon's water *Nature* **333** 56
- Ody A et al 2019 From *In Situ* to satellite observations of pelagic *Sargassum* distribution and aggregation in the Tropical North Atlantic Ocean *PLoS One* **14** e0222584
- Oviatt C A, Huizenga K, Rogers C S and Miller W J 2019 What nutrient sources support anomalous growth and the recent *Sargassum* mass stranding on Caribbean beaches? A review *Mar. Pollut. Bull.* **145** 517–25
- Putman N F, Goni G J, Gramer L J, Hu C, Johns E M, Trinanes J and Wang M 2018 Simulating transport pathways of pelagic *Sargassum* from the Equatorial Atlantic into the Caribbean Sea *Prog. Oceanogr.* **165** 205–14
- Putman N F, Lumpkin R, Olascoaga M J, Trinanes J and Goni G J 2020 Improving transport predictions of pelagic *Sargassum* *J. Exp. Mar. Biol. Ecol.* **529** 151398
- Rabalais N N, Turner R E, Dortch Q, Justic D, Bierman V J and Wiseman W J 2002 Nutrient-enhanced productivity in the northern Gulf of Mexico: past, present and future *Nutrients and Eutrophication in Estuaries and Coastal Waters* (Berlin: Springer) pp 39–63
- Richards P and Vanwey L 2015 Where deforestation leads to urbanization: how resource extraction is leading to urban growth in the Brazilian Amazon *Ann. Am. Assoc. Geogr.* **105** 806–23
- Richey J E, Victoria R L, Hedges J I, Dunne T, Martinelli L A, Mertes L and Adams J 2009 Pre-LBA carbon in the Amazon River Experiment (CAMREX) data ORNL DAAC
- Ruttenberg K C 2004 The global phosphorus cycle *Treatise on Geochemistry* ed W H Schlesinger vol 8 (Amsterdam: Elsevier) pp 585–643
- Schlosser C, Klar J K, Wake B D, Snow J T, Honey D J, Woodward E M S, Lohan M C, Achterberg E P and Moore C M 2014 Seasonal ITCZ migration dynamically controls the location of the (sub)tropical Atlantic biogeochemical divide *Proc. Natl Acad. Sci.* **111** 1438–42
- Seitzinger S P et al 2010 Global river nutrient export: a scenario analysis of past and future trends *Glob. Biogeochem. Cycles* **24** GB0A08
- Signorini S R, Murtugudde R G, McClain C R, Christian J R, Picaut J and Busalacchi A J 1999 Biological and physical signatures in the tropical and subtropical Atlantic *J. Geophys. Res.: Oceans* **104** 18367–82
- Sissini M N et al 2017 The floating *Sargassum* (Phaeophyceae) of the South Atlantic Ocean—likely scenarios *Phycologia* **56** 321–8
- Smetacek V and Zingone A 2013 Green and golden seaweed tides on the rise *Nature* **504** 84–88
- Subramaniam A et al 2008 Amazon River enhances diazotrophy and carbon sequestration in the tropical North Atlantic Ocean *Proc. Natl Acad. Sci.* **105** 10460–5
- Wang M and Hu C 2016 Mapping and quantifying *Sargassum* distribution and coverage in the Central Western Atlantic using MODIS observations *Remote Sens. Environ.* **183** 350–67
- Wang M and Hu C 2017 Predicting *Sargassum* blooms in the Caribbean Sea from MODIS observations *Geophys. Res. Lett.* **44** 3265–73
- Wang M, Hu C, Barnes B B, Mitchum G, Lapointe B and Montoya J P 2019 The great Atlantic *Sargassum* belt *Science* **365** 83–87
- Ward N D, Krusche A V, Sawakuchi H O, Brito D C, Cunha A C, Moura J M S, da Silva R, Yager P L, Keil R G and Richey J E 2015 The compositional evolution of dissolved and particulate organic matter along the lower Amazon River—Óbidos to the ocean *Mar. Chem.* **177** 244–56
- Wysocki L A, Bianchi T S, Powell R T and Reuss N 2006 Spatial variability in the coupling of organic carbon, nutrients, and phytoplankton pigments in surface waters and sediments of the Mississippi River plume *Estuar. Coast. Shelf Sci.* **69** 47–63
- Yu H et al 2015 The fertilizing role of African dust in the Amazon rainforest: a first multiyear assessment based on data from Cloud-Aerosol Lidar and Infrared Pathfinder Satellite Observations *Geophys. Res. Lett.* **42** 1984–91

B. Croissance différenciée des trois morphotypes de sargasses

L'article suivant détaille les résultats principaux d'une expérimentation hybride, à moitié en milieu naturel (eaux littorales de la Martinique) et à moitié en laboratoire, sur les algues sargasses. Il y a été question de la croissance des trois morphotypes courants actuellement dans différentes conditions d'enrichissement en nutriments. Si l'article ne se focalise qu'exclusivement sur les taux de croissance qui diffèrent selon les morphotypes, l'apport de la présente thèse concerne l'analyse de ces taux de croissance en fonction d'enrichissement en phosphore et en nitrate. Du fait d'événements météo imprévus, les résultats de cette partie de l'étude ne sont pas exploitables et n'ont pas été valorisés dans cette publication. Il en est néanmoins ressorti que l'enrichissement en phosphore a un effet significatif sur la croissance au contraire de l'enrichissement en azote, ce qui a nourri les travaux de modélisation de la croissance du chapitre 5.



Short communication

Variability in growth and tissue composition (CNP, natural isotopes) of the three morphotypes of holopelagic *Sargassum*

T. Changeux ^{a,*^{1,2}}, L. Berline ^a, W. Podlejski ^a, T. Guillot ^b, V. Stiger-Pouvreau ^c, S. Connan ^c, T. Thibaut ^a

^a Aix Marseille Univ, Université de Toulon, CNRS, IRD, MIO, Marseille, France

^b Ifremer Martinique, 79 route de Pointe Fort, 97231 Le Robert, France

^c Univ Brest, CNRS, IRD, Ifremer, LEMAR, F-29280 Plouzane, France

ARTICLE INFO

Keywords:

Seaweed
Brown macroalgae
Sargasso
Carbon
Nitrogen
Phosphorus
Algal bloom
In-situ culture

ABSTRACT

Holopelagic *Sargassum* blooms in the tropical North Atlantic since 2011 are composed of two species, *Sargassum natans* and *S. fluitans*, and three morphotypes: *S. natans* VIII, *S. natans* I and *S. fluitans* III. The distinct morphology and the variations in space and time of the proportion of these three morphotypes suggest that they may have different physiology. For the first time, we have quantified the growth rates of these three morphotypes through in situ 9-day experiments on the coast of Martinique Island (French West Indies). Despite the non-optimal conditions for growth for these pelagic species and the short time of the experiment, we have observed that *Sargassum fluitans* III was growing faster (approximately twice as fast) than *S. natans* VIII and *S. natans* I. *Sargassum natans* I exhibited the slowest growth. The differences in tissue composition (CNP and CN natural isotopes) of morphotypes point to a greater benefit for *S. fluitans* III from the coastal localization of our experiment than for the two *S. natans* morphotypes, and suggest that *S. natans* I had achieved its last growth further offshore before our experiment. These contrasting growth performances are consistent with the dominance of *S. fluitans* III in recent observations in the Caribbean region and along the path from the *Sargassum* belt. This also makes this last morphotype the best candidate for cultivation. Making the distinction between the growth performances of morphotypes may improve the current predictive models about dispersal of these species.

1. Introduction

Since 2011, the tropical North Atlantic Ocean has been the site of seasonal blooms of holopelagic *Sargassum*, rooted in the North Equatorial Recirculation Region. Holopelagic *Sargassum* are currently forming the Great Atlantic *Sargassum* Belt that can be observed from space (Wang et al., 2019), and causes strandings westwards, along the whole of the North Atlantic coast of South America and the Caribbean area, including the Gulf of Mexico, and eastwards along the West African coasts (Berline et al., 2020).

These strandings are composed of three distinct morphotypes: *Sargassum natans* VIII Parr, *S. natans* I Parr, and *S. fluitans* III Parr (Schell et al., 2015). Each morphotype shows a distinct morphology especially blade size, number of blades and air bladders (floats) per stem, and

presence of thorns on the stem (García-Sánchez et al., 2020; Schell et al., 2015) suggesting that the three morphotypes may have different biological characteristics. This is confirmed by the recent growth rates observed in-situ and ex-situ for *S. natans* VIII and *S. fluitans* III (Magaña-Gallegos et al., 2023a), and ex-situ for the three morphotypes (Magaña-Gallegos et al., 2023b).

Since the beginning of *Sargassum* blooms in 2011, significant variations of the abundance in morphotype composition have been observed. Initially, *S. natans* VIII was dominant in the south (Antilles Current, Eastern Caribbean and Western Tropical Atlantic) and *S. natans* I in the north (south of the Sargasso Sea) (Schell et al., 2015; November 2014 to May 2015). In 2017, during two open ocean campaigns along a latitudinal gradient from Guyana to the Sargasso Sea (<https://doi.org/10.17600/17004300>) in May/June and following a longitudinal

* Corresponding author.

E-mail address: thomas.changeux@ird.fr (T. Changeux).

¹ ORCID 0000-0002-0418-3321

² Postal address: Institut Méditerranéen d'Océanologie (MIO), Campus de Luminy, Case 901, Océanomed, Bât. Méditerranée 26M/102, 13288 Marseille Cédex 9, France.

transatlantic route (<https://doi.org/10.17600/17016900>) in October from Cabo Verde Island to Guadeloupe, *S. fluitans* III appeared to be dominant north of Guadeloupe for the first cruise and everywhere for the second cruise. More recently, studies have shown a quasi-permanent dominance of *S. fluitans* III in *Sargassum* strandings on Mexican Caribbean shores from 2016 to 2020 (Vázquez-Delfín et al., 2021; García-Sánchez et al., 2020), along the Jamaican coast (Machado et al., 2022), and on the Caribbean, Florida and Bahamas coasts (Iporac et al., 2022) as well as on a transatlantic cruise in 2022 (<https://energieaugrandlarg.wixsite.com/website>).

Biological models of *Sargassum* dynamics in the Atlantic Ocean (Brooks et al., 2018; Jouanno et al., 2021) use parameters based on physiological studies that do not differentiate between morphotypes (Hanisak and Samuel, 1987; Lapointe, 1995; Lapointe et al., 2014). However in macroalgae, the life traits are often taxon-dependent (Vranken et al., 2022) and therefore could explain the variations in dominance between morphotypes with time and across the North Atlantic Ocean. Taking into account differential growth rate may improve the model simulations.

Differential physiology would also impact tissue composition of *Sargassum* in CNP including C:N, N:P, C:P ratios and $\delta^{13}\text{C}$, $\delta^{15}\text{N}$ isotopes, as it integrates *Sargassum* environmental history along its drift path (Lapointe et al., 2021; Vázquez-Delfín et al., 2021).

The aim of this work was then to quantify the growth rates and tissue CNP composition of the three morphotypes through in situ short term experiments in Martinique Island (French West Indies).

2. Materials and methods

2.1. Location of experimental site and *Sargassum* sampling

Experiments were performed on the east coast of Martinique Island, in Baie du Robert, close to the Ifremer marine station, where a meteorological station is located. It took place in May-June 2021, when the Island is frequently supplied with *Sargassum* (Johns et al., 2020). This shallow bay (<30 m depth) faces the Atlantic Ocean and receives *Sargassum* pushed by the northeast trade winds after passing over the continental shelf, which extends for more than 15 km offshore (Fig. S1).

The nutrient concentrations (NO_3^- , NO_2^- , NH_4^+ , PO_4^{2-}) of surface seawater in the bay was monitored once every 2 months since 2017 as part of an extension of Ifremer's REPHY network (Belin et al., 2021) to the French overseas territories. The values (mean \pm SD) measured at the REPHY station, situated 400 m from our experimental site (S1), were low for a coastal station, especially when considering the different forms of N, $\text{NO}_3^- + \text{NO}_2^-$ ($0.3 \pm 0.3 \mu\text{mol/L}$) and NH_4^+ ($0.3 \pm 0.3 \mu\text{mole/L}$), with regard to PO_4^{2-} ($0.07 \pm 0.05 \mu\text{mol/L}$). This absence of pollution is confirmed by a previous detailed study of the bay (De Rock et al., 2019).

2.2. Growth experiment

Sargassum individuals were collected off the coast within the bay selecting the young clumps following the criteria of Stoner and Greening (1984) to age the clumps. For each morphotype, we cut fragments of 5–20 cm length from the apical part, free from visible epiphytes. To be consistent with field observations, the three morphotypes were grown together. Approximately 20 g of wet weight of each morphotype (5–10 fragments, 60 g in total) hereinafter called a batch, were placed in 5 L transparent plastic bottles, perforated with one hundred holes to allow good water circulation (see Fig. S2 showing cultivation device). The density of 60 g for 5 L was chosen after trials to increase the time before first signs of degradation while maintaining a sufficient quantity of *Sargassum* for the analyses. These bottles were attached to mooring cables at 2 m depth to avoid destruction of the devices by wave effect. Temperature and light inside two of the four bottles was recorded with UA-002-08 (HOBO) data loggers.

The entire experiment lasted 9 days, from May 25th to June 3rd

2021. The wet weight was measured every 3 days both for batches and individuals. The wet weight of each batch was measured on a BAXTRAN BR balance (0.1 g readability) after dewatering using absorbent paper in a salad spinner. Inside each batch, three individuals per morphotype ($n = 36$) were identified with colored beads strung on a nylon thread attached to the fragment. The wet weight of each individual ($n = 12$ per morphotype) was obtained as for the batch but by using a more accurate balance (PRECISA 321LT, 0.1 mg readability). In addition, the number of floats was counted for each individual.

2.3. Water, tissue, and data analysis

At the beginning of the experiment, and before each measurement session, we sampled the water in 200 mL plastic bottles to measure nutrient composition. The sample was fixed with 100 μL HgCl_2 per bottle, and then stored in a cool place protected from light. The analyses were carried out by automated colorimetry for NO_3^- , NO_2^- , NH_4^+ , PO_4^{2-} (Aminot and Kérouel, 2007) and for NH_4^+ (Holmes et al., 1999).

At the end of the experiment, eight samples (mix of individuals) of 5 g wet weight of each morphotype were analyzed for C, N, P, $\delta^{13}\text{C}$ and $\delta^{15}\text{N}$ tissue composition. These samples were dried in an oven at 60 °C during 48 h, reduced into powder, acidified to eliminate mineral sources of carbon, and analyzed by spectrometry following Raimbault et al. (2008).

The growth rate (GR) in weight was calculated in d^{-1} following:

$$GR_d = \frac{1}{d} \ln \left(\frac{W_d}{W_0} \right)$$

where d = number of days ($d = 9$ for the entire experiment) and W_d = wet weight at day d , W_0 = wet weight at day 0.

The floats ratio (FR) was calculated (in %) with reference to the initial number of floats for the entire experiment following:

$$FR = \frac{N_9}{N_0} \cdot 100$$

where N_9 = number of floats at day 9 and N_0 = number of floats at day 0.

Non parametric Kruskal-Wallis test (KW test) followed by Dunns post-hoc test were used to test the morphotype effect on *Sargassum* GR, FR and tissue composition with a significance level of 0.05.

3. Results

3.1. Field conditions

During the 9 days of experiment, water temperature inside the bottles varied from 28 °C at night to 31 °C during the day (06:00 AM-6:00 PM) when light inside the bottle varied from 74 to 740 $\mu\text{mol photons m}^{-2} \text{s}^{-1}$ with a mean value of 137 $\mu\text{mol photons m}^{-2} \text{s}^{-1}$. The nutrient concentrations were high and variable compared to REPHY measurements (respectively 1.7 ± 2.0 vs $0.3 \pm 0.3 \mu\text{mol/L}$ for $\text{NO}_3^- + \text{NO}_2^-$, 2.1 ± 1.7 vs $0.3 \pm 0.3 \mu\text{mol/L}$ for NH_4^+ and 0.3 ± 0.3 vs $0.07 \pm 0.05 \mu\text{mol/L}$ for PO_4^{2-}).

The daily rainfall, including one day before the start of the experiment, varied from 0 to 10.6 mm, with a mean of 1.52 mm which is below the average of 2.07 mm from May to June 2021 at the station. The wind speed and direction were regular for the season (9.73 m.s^{-1} oriented WNW (67.27°)). The high nutrient values compared to REPHY station were mainly related to the location of our experimental site closer to the coast and human activities.

3.2. Patterns of change in the *Sargassum* weight and floats ratio

The increase in *Sargassum* weight along the experiment was clearly visible when considering the batches (Fig. S3). After 9 days, the initial 20 g were exceeded by all morphotypes, reaching about 25 g for

S. natans VIII and *S. natans* I and approaching 30 g for *S. fluitans* III (see pictures Fig. S4). After 6 days, the weight increase slowed down for all morphotypes. In contrast, this increase was lower and more variable in the individual measurements (Fig. S3). The floats ratio (FR) after 9 days was overall below 100 %, showing a loss of floats for all morphotypes (Fig. S5). This was especially the case for *S. natans* I.

3.3. Growth rate

For all morphotypes, the GR over every 3-day period decreased overall over time from the beginning of the experiment (Fig. 1 A). The median value of batch GR varied from 0.063 to 0.022 d⁻¹ after 3 days, from 0.044 to 0.018 d⁻¹ after 6 days, and from 0.019 to –0.006 d⁻¹ after 9 days. *Sargassum fluitans* III had always the highest GR values and *S. natans* I the lowest. *Sargassum natans* VIII GR was intermediate. After 9 days, the individual GR showed a significant variation between morphotypes (KW test $\chi^2 = 16.244$, df = 2, p-value = 0.0002969). The Dunn's post hoc test gives two significant results: *S. fluitans* III vs *S. natans* I (p = 0.0000678 ***) and *S. fluitans* III vs *S. natans* VIII (p = 0.0313 *). Even if the mean individual GR of *S. natans* I was negative, linked with the first signs of senescence, the mean batch GR of this morphotype was positive (Fig. 1 B).

3.4. Tissue elemental composition (C, N, P, $\delta^{13}\text{C}$, $\delta^{15}\text{N}$) of *Sargassum*

The effect of morphotype was significant only for %N, $\delta^{15}\text{N}$, $\delta^{13}\text{C}$ and C:N (Table S1). For other elements, the median values were %C = 23.52 %, %P = 0.07 %, N:P = 30.33 and C:P = 827.43.

The post hoc Dunn tests (Fig. 2; Table S1) showed that *S. fluitans* III was characterized by a high %N, $\delta^{15}\text{N}$ and low C:N and $\delta^{13}\text{C}$. In contrast, *S. natans* VIII showed low %N, $\delta^{15}\text{N}$ and high C:N and $\delta^{13}\text{C}$ and *S. natans* I was essentially characterized by a low $\delta^{15}\text{N}$.

4. Discussion

4.1. Changes in growth performance during the experiment

For the three morphotypes, GR (0.02–0.04 d⁻¹ for batches) were in the low range of literature growth data reported by Brooks et al. (2018), i.e. [0.029–0.11] d⁻¹ relying on in situ (Lapointe, 1986; Lapointe et al., 2014) and laboratory experiments (Hanisak and Samuel, 1987). In addition, GR decreased with time for all morphotypes. This does not align with the neritic origin of our samples, generally associated with low nutrient limitation and high GR following Lapointe (1995). These results, for both batches and individuals, indicate that algae were not in optimal growth conditions. This decrease of GR may be due:

- to excessively high seawater temperatures [28–31 °C] observed during the experiment, as decrease in growth after 24 °C was observed by Hanisak and Samuel (1987) for *S. natans*;
- to light limitation since our mean light measurement of 137 μmol photons m⁻² s⁻¹ in the bottle corresponds to intermediate GR of 0.02 d⁻¹ (Hanisak and Samuel, 1987);
- to stress related to the confinement in the bottles despite the numerous holes made in order to renew the water. On the one hand, pelagic *Sargassum* are known to produce large quantities of dissolved organic carbon (Powers et al., 2019) that promote, together with high nutrient level, bacterial growth (Michotey et al., 2020). On the other hand, the lack of ventilation may lead to micronutrient depletion.

GR did not correspond to maximum growth values, taking into account both the phenomenon of growth and senescence over 9 days. Although culture conditions may be limiting, our results clearly show contrasting performances among morphotypes.

4.2. Differential growth between the 3 morphotypes and implications

Sargassum fluitans III was growing faster, approximately twice as fast as *S. natans* VIII and *S. natans* I. This is consistent with lab experiment results of Hanisak and Samuel (1987), and ex-situ experiments of Magaña-Gallegos et al. (2023b), but differs from ex-situ and in-situ experiments for only two morphotypes of Magaña-Gallegos et al. (2023a). Moreover, *S. natans* I exhibited the slowest growth rate. This suggests that growth is morphotype dependent. When exposed to high temperature, high nutrient concentration and a slight light limitation, *S. fluitans* III does better than *S. natans* I.

These differences may have implications with regard to the relative abundance of morphotypes observed at sea and in strandings. However GR cannot be simply translated into abundances. The coexistence of the three morphotypes suggests that processes other than growth maintain competitive success of the *S. natans* morphotypes despite lower GR. Morphotypes may have differing environmental niches that were not spanned by our experimental conditions. For instance, in a more oligotrophic and colder environment than ours, *S. natans* I dominated during 2014 and 2015 north of 24°N (Schell et al., 2015). Magaña-Gallegos et al. (2023b) also found that morphotypes had distinct temperature optima.

Future measurements of growth in contrasted conditions may help to explain field observations of morphotype composition and the dominance of *S. fluitans* III in the Caribbean region and along the path from the *Sargassum* belt.

4.3. Significance of CNP and isotope composition

Our results showed significant differences of %N, $\delta^{15}\text{N}$, $\delta^{13}\text{C}$ and C:N between morphotypes while no difference has been found between *S. natans* and *S. fluitans* in the large (n = 488) and long-term dataset of Lapointe et al. (2021). Even if the tissue composition prior to experiment is unknown this discrepancy can be explained by the particular environmental history of our samples.

Overall, %N and %P cannot explain the different GR among morphotypes. Both *S. fluitans* III and *S. natans* I have similar %N and %P values, but different GR. It may be related to nutrient uptake that occurred before the experiment. To improve interpretations, future experiments should include isotopes analyses on freshly arrived *Sargassum* before starting the experiment.

The high N:P (30.33) and C:P value (827) of all morphotypes in our experiment suggests a limitation in P, as pointed out by Lapointe et al. (2021) for samples collected after 2010 s. This P limitation may explain why %N differences do not result in growth rate variations.

The value of %C (23.5 %) was low compared to the recent Mexican samples of Vázquez-Delfín et al. (2021). Conversely, %N values were high in agreement with the Lapointe et al. (2021) data for the 2010 s, except for *S. natans* VIII which were lower in our study. The high C:N values (36) of *S. natans* VIII suggest that this morphotype was not in good growing conditions.

The isotopic composition showed high values in $\delta^{13}\text{C}$ which are footprints of the continental origin of C as a consequence of the coastal situation of our samples. The low values of $\delta^{15}\text{N}$ of *S. natans* I may be indicative of diazotrophic fixation, common in pelagic *Sargassum* (Carpenter, 1972; Philips and Zeman, 1990) while higher values may indicate enrichment by NO₃⁻ present along the coast (Lapointe et al., 2021; Montoya, 2008). It is interesting to note that $\delta^{15}\text{N}$ order among morphotypes follow the GR. This suggests that higher $\delta^{15}\text{N}$ indicate more recent growth fueled by coastal NO₃⁻. That implies that the last growth of *S. natans* I was achieved at a greater distance in time and offshore. However, we would need the composition before the experiment to conclude with certainty on this point.

Thus, the significant variations of the elemental composition point to a greater benefit for *S. fluitans* III from the coastal situation of our experiment than for the two *S. natans* morphotypes.

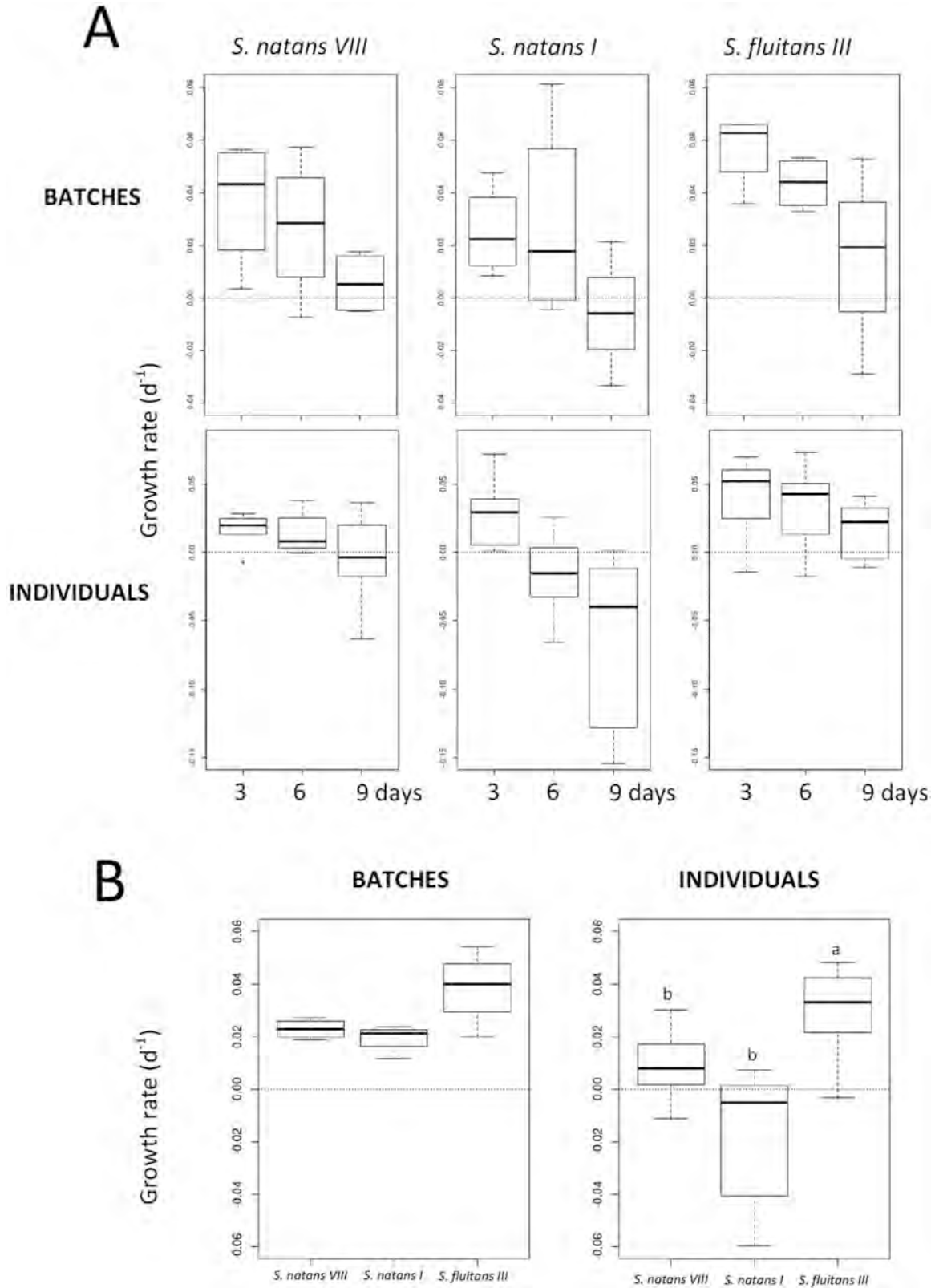


Fig. 1. Holopelagic *Sargassum* growth rate (d^{-1}) for each morphotype measured on batches ($n = 4$) and individuals ($n = 12$ per morphotype) every 3 days (A.) and over the 9 days of the experiment (B.). Box shows the sample median and the first and third quartiles. Whiskers extend to the last data point which is no more than 1.5 times the interquartile range. Outliers are shown as dots. The letter identifies the significant differences (p -value < 0.05).

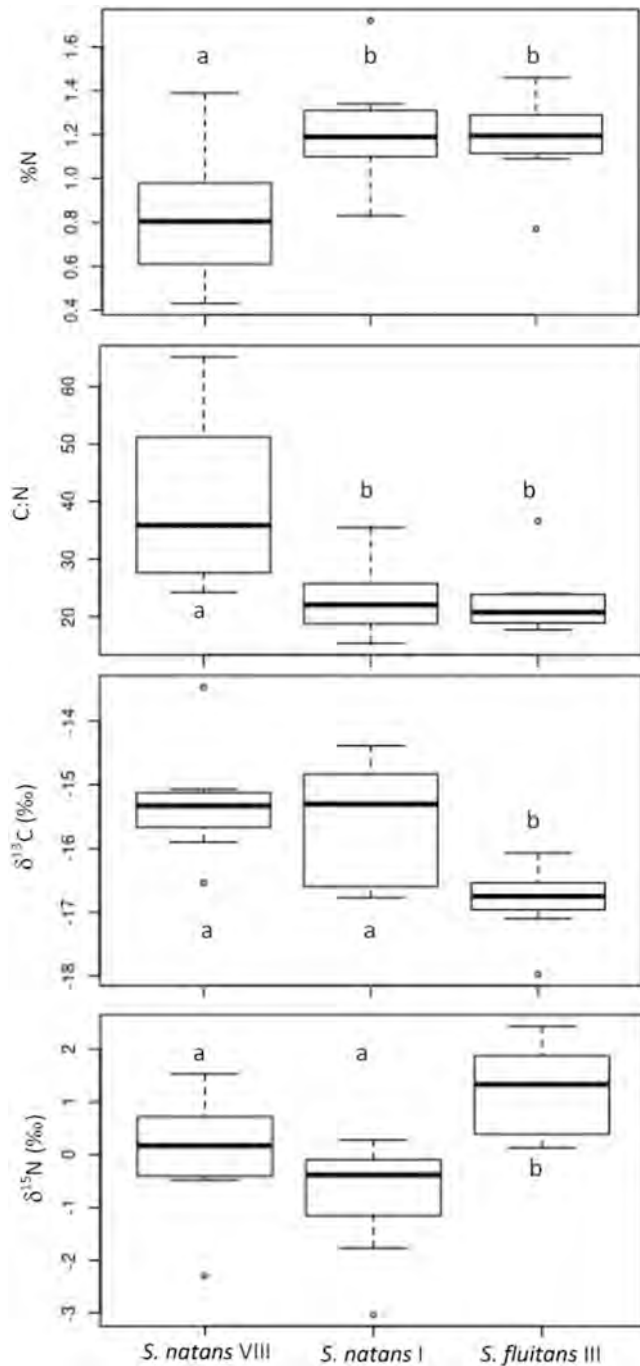


Fig. 2. Tissue composition (%N, C:N, $\delta^{15}\text{N}$, $\delta^{13}\text{C}$) between *Sargassum* morphotypes. Box, whiskers and letters are shown as in Fig. 1.

In conclusion, despite the non optimal conditions encountered in this in situ experiment, it shows for the first time contrasting growth performances between the three morphotypes that are consistent with their abundance in the field. Current models including algal growth, which do not distinguish between morphotypes, can be improved by taking these morphotype growth differences into account. These differences in growth are probably linked to photosynthetic processes between morphotypes that will have to be specified with new experiments. *Sargassum fluitans* III appears here as the most tolerant morphotype, best candidate for nearshore and indoor cultivation.

Funding

This research was supported by the French Agence Nationale de la Recherche *Sargassum* grants FORESEA, France (ANR-19-SARG-0007-01) and SAVE-C, France (ANR-19-SARG-0008) and by the French Institut de Recherche pour le Développement Long-term Mission funding, France.

CRediT authorship contribution statement

Conceptualization, Data curation, Methodology, Software, Supervision, Validation, Visualization (TC, LB), Formal analysis (TC, LB, WP), Funding acquisition, Project administration, Resources (TC, LB, TT), Investigation (TC, TG), Writing (TC, LB, SC, VSP, TT).

Declaration of Competing Interest

The authors declare that they have no known competing financial interests or personal relationships that could have appeared to influence the work reported in this paper.

Data availability

Data will be made available on request.

Acknowledgements

We are grateful to Emmanuel Thouard, Ifremer Martinique, who gave access to Ifremer station facilities and meteorological data, Jean-Pierre Allenou, Ifremer Martinique, for the REPHY data and Samson Devillers, Ifremer Martinique, for his operational assistance. Tissue analysis was performed by PACEM Mediterranean Institute of Oceanography (MIO) intern platform. Patrick Rimbault, from the MIO, helped with interpretation. The map in Fig. S1 was partly produced by Felix Navarro MIO internship from AgroParisTech.

Appendix A. Supporting information

Supplementary data associated with this article can be found in the online version at doi:10.1016/j.aquabot.2023.103644.

References

- Aminot, A., Kérouel, R., 2007. Dosage automatique des nutriments dans les eaux marines: méthodes en flux continu. Ifremer, France.
- Belin, C., Soudant, D., Amzil, Z., 2021. Three decades of data on phytoplankton and phycotoxins on the French coast: Lessons from REPHY and REPHYTOX. Harmful Algae 102, 101733. <https://doi.org/10.1016/j.hal.2019.101733>.
- Berline, L., Ody, A., Jouanno, J., Chevalier, C., André, J.-M., Thibaut, T., Ménard, F., 2020. Hindcasting the 2017 dispersal of *Sargassum* algae in the Tropical North Atlantic. Mar. Pollut. Bull. 158, 111431 <https://doi.org/10.1016/j.marpolbul.2020.111431>.
- Brooks, M., Coles, V., Hood, R., Gower, J., 2018. Factors controlling the seasonal distribution of pelagic *Sargassum*. Mar. Ecol. Prog. Ser. 599, 1–18. <https://doi.org/10.3354/meps12646>.
- Carpenter, E.J., 1972. Nitrogen fixation by a blue-green epiphyte on pelagic *Sargassum*. Science 178, 1207–1209. <https://doi.org/10.1126/science.178.4066.1207>.
- De Rock, P., Cimentera, N., Allenou, J.-P., 2019. Réalisation d'un suivi du milieu marin en vue de la mise en oeuvre de la nouvelle station d'épuration (Pontaléry) au Robert - Caractérisation de l'état initial (Rapport Ifremer). Le Robert (Martinique).
- García-Sánchez, M., Graham, C., Vera, E., Escalante-Mancera, E., Álvarez-Filip, L., van Tussenbroek, B.I., 2020. Temporal changes in the composition and biomass of beached pelagic *Sargassum* species in the Mexican Caribbean. Aquat. Bot. 167, 103275 <https://doi.org/10.1016/j.aquabot.2020.103275>.
- Hanisak, M.D., Samuel, M.A., 1987. Growth rates in culture of several species of *Sargassum* from Florida, USA. In: Ragan, M.A., Bird, C.J. (Eds.), Twelfth International Seaweed Symposium. Springer, Netherlands, Dordrecht, pp. 399–404. https://doi.org/10.1007/978-94-009-4057-4_59.
- Holmes, R.M., Aminot, A., Kérouel, R., Hooker, B.A., Peterson, B.J., 1999. A simple and precise method for measuring ammonium in marine and freshwater ecosystems. Can. J. Fish. Aquat. Sci. 56, 1801–1808. <https://doi.org/10.1139/f99-128>.
- Iporac, L.A.R., Hatt, D.C., Bally, N.K., Castro, A., Cardet, E., Mesidor, R., Olszak, S., Duran, A., Burkholder, D.A., Collado-Vides, L., 2022. Community-based monitoring reveals spatiotemporal variation of sargasso inundation levels and morphotype

- dominance across the Caribbean and South Florida. *Aquat. Bot.* 182, 103546 <https://doi.org/10.1016/j.aquabot.2022.103546>.
- Johns, E.M., Lumpkin, R., Putman, N.F., Smith, R.H., Muller-Karger, F.E., T. Rueda-Roa, D., Hu, C., Wang, M., Brooks, M.T., Gramer, L.J., Werner, F.E., 2020. The establishment of a pelagic Sargassum population in the tropical Atlantic: Biological consequences of a basin-scale long distance dispersal event. *Prog. Oceanogr.* 182, 102269 <https://doi.org/10.1016/j.pocean.2020.102269>.
- Jouanno, J., Benshila, R., Berline, L., Soulié, A., Radenac, M.-H., Morvan, G., Diaz, F., Sheinbaum, J., Chevalier, C., Thibaut, T., Changeux, T., Menard, F., Berthet, S., Aumont, O., Ethé, C., Nabat, P., Mallet, M., 2021. A NEMO-based model of Sargassum distribution in the tropical Atlantic: description of the model and sensitivity analysis (NEMO-Sarg1.0). *Geosci. Model Dev.* 14, 4069–4086. <https://doi.org/10.5194/gmd-14-4069-2021>.
- Lapointe, B.E., 1995. A comparison of nutrient-limited productivity in *Sargassum natans* from neritic vs. oceanic waters of the western North Atlantic Ocean. *Limnol. Oceanogr.* 40, 625–633. <https://doi.org/10.4319/lo.1995.40.3.0625>.
- Lapointe, B.E., West, L.E., Sutton, T.T., Hu, C., 2014. Ryther revisited: nutrient excretions by fishes enhance productivity of pelagic Sargassum in the western North Atlantic Ocean. *J. Exp. Mar. Biol. Ecol.* 458, 46–56. <https://doi.org/10.1016/j.jembe.2014.05.002>.
- Lapointe, B.E., Brewton, R.A., Herren, L.W., Wang, M., Hu, C., McGillicuddy, D.J., Lindell, S., Hernandez, F.J., Morton, P.L., 2021. Nutrient content and stoichiometry of pelagic Sargassum reflects increasing nitrogen availability in the Atlantic Basin. *Nat. Commun.* 12, 3060. <https://doi.org/10.1038/s41467-021-23135-7>.
- Machado, C.B., Maddix, G.-M., Francis, P., Thomas, S.-L., Burton, J.-A., Langer, S., Larson, T.R., Marsh, R., Webber, M., Tonon, T., 2022. Pelagic Sargassum events in Jamaica: provenance, morphotype abundance, and influence of sample processing on biochemical composition of the biomass. *Sci. Total Environ.* 817, 152761 <https://doi.org/10.1016/j.scitotenv.2021.152761>.
- Magaña-Gallegos, Edén, García-Sánchez, M., Graham, C., Olivos-Ortiz, A., Siuda, A.N.S., van Tussenbroek, B.I., 2023a. Growth rates of pelagic Sargassum species in the Mexican Caribbean. *Aquat. Bot.* 185, 103614 <https://doi.org/10.1016/j.aquabot.2022.103614>.
- Magaña-Gallegos, Edén, Villegas-Muñoz, E., Salas-Acosta, E.R., Barba-Santos, M.G., Silva, R., van Tussenbroek, B.I., 2023b. The Effect of Temperature on the Growth of Holopelagic Sargassum Species. *Phycology* 3, 138–146. <https://doi.org/10.3390/phycology3010009>.
- Michotey, V., Blanfuné, A., Chevalier, C., Garel, M., Diaz, F., Berline, L., Le Grand, L., Armougom, F., Guasco, S., Ruitton, S., Changeux, T., Belloni, B., Blanchot, J., Ménard, F., Thibaut, T., 2020. In situ observations and modelling revealed environmental factors favouring occurrence of *Vibrio* in microbiome of the pelagic *Sargassum* responsible for strandings. *Sci. Total Environ.* 748, 141216 <https://doi.org/10.1016/j.scitotenv.2020.141216>.
- Montoya, J.P., 2008. Nitrogen stable isotopes in marine environments. In: Nitrogen in the Marine Environment. Elsevier, pp. 1277–1302. <https://doi.org/10.1016/B978-0-12-372522-6.00029-3>.
- Philips, E., Zeman, C., 1990. Photosynthesis, growth and nitrogen-fixation by epiphytic forms of filamentous cyanobacteria from pelagic *Sargassum*. *Bull. Mar. Sci.* 47 (3), 613–621.
- Powers, L.C., Hertkorn, N., McDonald, N., Schmitt-Kopplin, P., Del Vecchio, R., Blough, N.V., Gonsior, M., 2019. *Sargassum* sp. Act as a Large Regional Source of Marine Dissolved Organic Carbon and Polyphenols. *Glob. Biogeochem. Cycles* 33, 1423–1439. <https://doi.org/10.1029/2019GB006225>.
- Raimbault, P., Garcia, N., Cerutti, F., 2008. Distribution of inorganic and organic nutrients in the South Pacific Ocean – evidence for long-term accumulation of organic matter in nitrogen-depleted waters. *Biogeosciences* 5, 281–298. <https://doi.org/10.5194/bg-5-281-2008>.
- Schell, J., Goodwin, D., Siuda, A., 2015. Recent Sargassum inundation events in the Caribbean: shipboard observations reveal dominance of a previously rare form. *Oceanogr* 28, 8–10. <https://doi.org/10.5670/oceanog.2015.70>.
- Stoner, A., Greening, H., 1984. Geographic-variation in the macrofaunal associates of pelagic *Sargassum* and some biogeographic implications. *Mar. Ecol. -Prog. Ser.* 20, 185–192. <https://doi.org/10.3354/meps020185>.
- Vázquez-Delfín, E., Freile-Pelegrín, Y., Salazar-Garibay, A., Serviere-Zaragoza, E., Méndez-Rodríguez, L.C., Robledo, D., 2021. Species composition and chemical characterization of *Sargassum* influx at six different locations along the Mexican Caribbean coast. *Sci. Total Environ.* 795, 148852 <https://doi.org/10.1016/j.scitotenv.2021.148852>.
- Vranken, S., Robuchon, M., Dekeyzer, S., Bárbara, I., Bartsch, I., Blanfuné, A., Boudouresque, C.-F., Decock, W., Destombe, C., de Reviers, B., Diaz-Tapia, P., Herbst, A., Julliard, R., Karez, R., Kersen, P., Krueger-Hadfield, S.A., Kuhlenkamp, R., Peters, A.F., Peña, V., Pineiro-Corbeira, C., Rindi, F., Rousseau, F., Rueness, J., Schubert, H., Sjötun, K., Sansón, M., Smale, D., Thibaut, T., Valero, M., Vandepitte, L., Vanhoorne, B., Vergés, A., Verlaque, M., Vieira, C., Le Gall, L., Leliaert, F., De Clerck, O., 2022. AlgaeTraits: a trait database for (European) seaweeds. *ESSD – Ocean/Biol. Oceanogr.* <https://doi.org/10.5194/essd-2022-329>.
- Wang, M., Hu, C., Barnes, B.B., Mitchum, G., Lapointe, B., Montoya, J.P., 2019. The great Atlantic Sargassum belt. *Science* 365, 83–87. <https://doi.org/10.1126/science.aaw7912>.

Bibliographie – B. Croissance différenciée des trois morphotypes de sargasses